Distribution unlimited.

Near and Far-Field Acoustic Scattering through and from Two Dimensional Fluid-Fluid Rough Interfaces

by John Einar Moe

Technical Report
APL-UW TR 9606
October 1996

ONR Grant N00014-96-1-0121

DISCLAIMER NOTICE

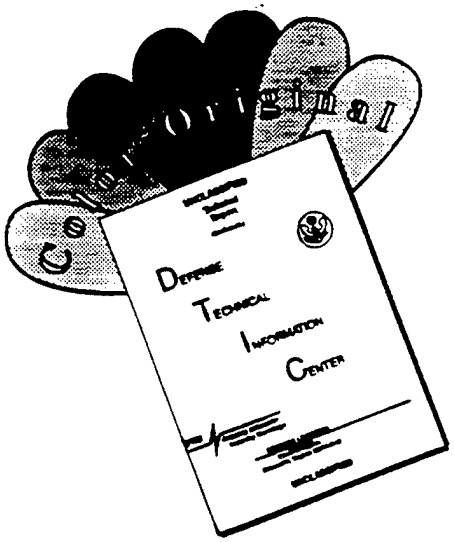

THIS DOCUMENT IS BEST QUALITY AVAILABLE. THE COPY FURNISHED TO DTIC CONTAINED A SIGNIFICANT NUMBER OF COLOR PAGES WHICH DO NOT REPRODUCE LEGIBLY ON BLACK AND WHITE MICROFICHE.

Distribution unlimited.

Near and Far-Field Acoustic Scattering through and from Two Dimensional Fluid-Fluid Rough Interfaces

by John Einar Moe

Technical Report
APL-UW TR 9606
October 1996

Applied Physics Laboratory University of Washington
1013 NE 40th Street Seattle, Washington 98105-6698

ONR Grant N00014-96-1-0121

Near and Far-Field Acoustic Scattering through and from Two Dimensional Fluid-Fluid Rough Interfaces

by

John Einar Moe

A dissertation submitted in partial fulfillment
of the requirements for the degree of

Doctor of Philosophy

University of Washington

1996

Program Authorized
to offer Degree Department of Electrical Engineering

Date July 15, 1996

University of Washington

Abstract

Near and Far-Field Acoustic Scattering through and from Two Dimensional Fluid-Fluid Rough Interfaces

Recent experimental results [F. E. Boyle and N. P. Chotiros, J. Acoust Soc. Am. 91, 2615-2619, 1992; N. P. Chotiros, J. Acoust Soc. Am. 97, 199-214, 1995] reveal acoustic penetration from water into sandy sediments at grazing angles below the compressional critical angle in relation to the mean surface. These authors interpret their results to indicate the excitation of a Biot slow wave in the sediment. Another explanation is considered here. Modeling the ocean as a homogenous fluid and the sediment as a lossy homogenous fluid, computer simulations of these experiments based on analytical derivations in this work show that roughness of the water-sediment interface causes propagation of acoustical energy from water into the sediment at grazing angles below the compressional critical grazing angle; these simulations indicate that the experimental results can be explained in terms of diffraction of an ordinary longitudinal wave. These simulations use an analytical expression for the time-dependent mean square incoherent field scattered through (and from) a rough 2-D fluid-fluid interface that is derived in terms of the bistatic scattering cross section per unit area per unit solid area (differential cross section) of the rough interface. First-order perturbation theory is used to derive an expression for the differential cross section. The coherent field is calculated using the flat-surface result (zero-order perturbation theory) and compared to the coherent component of the second-order perturbation theory result. Effects of sound-speed gradients on the field scattered from the rough water-sediment interface are also shown using the first-order perturbation derivations.

Table of Contents

List of Figures

Acknowledgments

This work would not have been possible without the support and guidance of several people. I am extremely thankful to my advisor, Dr. Darrell Jackson, for the many hours of discussion that we had over the years. I have gained valuable insight from his guidance and extensive experience, and credit him for my working in this area. I am indebted to Dr. Eric Thorsos for his advice concerning focus, organization, and content of this work. I have benefited immensely from his in-depth understanding of the subject matter, and I am very grateful to him. I have also benefited a great deal from the advice of Dr. Dale Winebrenner, whose suggestions have contributed considerably to this work. I am very grateful to him as well. I am grateful to Professor Akira Ishimaru for his excellent teaching of wave propagation and scattering theory and for making his expertise available. His comments and help are very much appreciated. I am truly grateful to have been given the opportunity to learn directly from the experts in the area of wave propagation and scattering theory. Their contributions are evident throughout this dissertation. I am also grateful to Professor Russell McDuff for his contribution as a committee member.

I would also like to thank the University of Washington Applied Physics Laboratory staff, specifically Dr. Kevin Williams, Dr. Peter Kaczkowski, Garfield Mellema, Chris Jones, and Miguel Nathwani for helpful discussions, Monty Bolstad and Al Brookes for very efficient administrative help, Jamie Jamison and Distributed Computing Services for their very timely computer help, and Priscilla Schneider and the library staff.

Dedication

To my wife, Michele, and son, Alex, for their never ending support, sacrifice, patience, and faith.

CHAPTER 1

Introduction

1.1 Purpose

A current area of considerable interest in ocean acoustics is the penetration of acoustical energy from a source in water into the seafloor (Williams, Satkowiak, and Bugler, 1989; Chotiros, 1995). Recent experimental results (Boyle and Chotiros, 1992; Chotiros, 1995) reveal acoustic penetration from water into sandy sediments at grazing angles below the compressional critical angle in relation to the mean surface. In addition, energy appears to propagate in the sediment at speeds slower than the compressional wave speed, in a direction concurring with Snell's law. These authors interpret their results to indicate the excitation of a Biot slow wave in the sediment.

A primary goal of this work is to demonstrate that their experimental results can be explained in terms of diffraction of an ordinary longitudinal wave, rather than refraction of a slow wave. The effect of roughness on penetration of the seafloor is demonstrated by developing a rough surface scattering model that provides a solution to scattering into the rough seafloor. In order to provide a tractable model, simplifying assumptions about the ocean and seafloor are made, and an approach for solving the corresponding time-dependent rough surface scattering problem is taken that leads to simple analytical results. The ocean acoustic model used and the methods of solution are discussed in the following sections. Although the main problem is acoustic scattering *through* the rough fluid-fluid interface for an incident field in the water, analytical results derived in this work also include scattering *from* the rough fluid-fluid interface. Furthermore, these analytical results are general, and can be applied to other rough surface scattering problems.

1.2 Ocean acoustic model

The propagation of sound in the ocean is very complicated (see for example, Urick, 1975; Brekhovskikh and Lysanov, 1991; Burdic, 1991). Sound speed is not constant, but varies as a function of temperature, salinity, and depth. In addition, acoustical energy propagating in the ocean is attenuated by absorption and by scattering due to inhomogeneities in the water. However, for the examples considered here, the propagation distances in the water are short enough so that the sound speed does not vary appreciably. Furthermore, at the frequencies of interest (300 Hz - 60 kHz) attenuation of acoustical energy over these short distances is also negligible. For this reason, the water is modeled as a lossless homogenous fluid.

The ocean seafloor is in general an inhomogeneous porous, viscoelastic medium, possibly supporting the propagation of Biot slow waves (Biot, 1956a, 1956b; Biot, 1962a, 1962b) and transverse, or shear, waves (e.g., Brekhovskikh and Lysanov, 1991) in addition to longitudinal, or compressional, waves. The seafloor has a roughness spectrum approximating that of a power law (Fox and Hayes, 1985; Goff and Jordan, 1989; Briggs, 1989). Acoustical energy incident on the seafloor will be scattered from this rough interface back into the water, and through this rough interface into the sediment.

The main purpose of this work is to show the effect of roughness in the seafloor on scattering into the sediment. Although volume inhomogeneities in the sediment can be a significant source of scattering (Ivakin and Lysanov, 1981; Jackson, Winebrenner, and Ishimaru, 1986; Jackson and Briggs, 1992), volume scattering is beyond the scope of this work. However, the effect of vertical stratification of the sediment below the rough interface on the scattered field is discussed. Boyle and Chotiros (1992) and Chotiros (1995) neglect the effects of roughness in their interpretation of sediment penetration experiments, and suggest that penetration of acoustical energy into a sandy sediment at shallow

grazing angles (below the compressional critical angle) can be explained by Biot wave propagation — provided nonstandard Biot parameters are used (Chotiros, 1995). We show that their experimental results can be reproduced in a computer simulation that models the sandy sediment as a fluid and the interface between the water and the sediment as randomly rough. Ivakin and Jackson (in preparation) show that for the case of sandy sediments, the component of energy propagating as shear waves is small, and can therefore be neglected. Attenuation of acoustical energy is not negligible in the sediment for even very short distances, and the sediment is therefore modeled as a lossy fluid.

Since it is not feasible to obtain an exact analytical description of even a relatively small portion of the seafloor, a probabilistic analysis is most practical. A statistical quantity of particular interest to rough surface scattering is the bistatic scattering cross section per unit area per unit solid angle (Ishimaru, 1978b). For convenience, this quantity will be referred to as the differential cross section. It is useful to represent solutions for scattered acoustical energy in terms of differential cross section. However, exact analytical expressions for the differential cross section are not available.

1.3 Rough interface scattering solution techniques

Determining the field scattered *from* or *through* (penetrating) a rough interface given an arbitrary incident field is a problem with applications in several research areas, in addition to ocean acoustics (e.g., remote sensing, solid state physics, astronomy, optics). In the area of ocean acoustics, rough surface scattering is viewed as a contributor to propagation loss for sound propagating in shallow water (e.g., Kuperman and Ingenito, 1977) and a source of interfering reverberation in active sonar systems. In the acoustic detection of subsurface scatterers, the rough seafloor can be considered a source of interfering reverberation and signal loss (Nagy and Rose, 1993), and in medical imaging applications, rough interfaces in intervening tissue layers often lead to distorted

images (Berkhoff, Thijssen, and van den Berg, 1996). Although the rough interface scattering problem has been of interest for several decades, there is no exact solution method for the statistical problem.

Solutions of the rough interface scattering problem are obtained by means of either numerical or approximate analytical methods. Although numerical methods can result in accurate calculations for the scattered field, statistical results require a numerically intensive "Monte Carlo" approach. In addition, numerical methods are very computer intensive for the three dimensional problem (Tsang, Chan, and Pak, 1993, 1994; Pak *et al.*, 1995).

A classical analytical technique applied to acoustic scattering by Brekhovskikh (1952) and by Eckart (1953) is the Kirchhoff approximation, or tangent plane approximation. Although this approximation has a useful region of validity for Dirichlet boundary conditions (Thorsos, 1988a, 1988b, 1990; Thorsos and Jackson, 1989, 1991; Ishimaru and Chen, 1990), it is not as suitable for obtaining statistics of the scattered field for more general seafloor boundary conditions, such as fluid-fluid, where the reflection coefficient is a function of angle. However, as shown by Thorsos (1996b), the Kirchhoff approximation can be very accurate for scattering *through* a rough fluid-fluid interface near the Snell's law direction.

More recent approximate methods include the phase perturbation method (Winebrenner, 1985; Winebrenner and Ishimaru, 1985a, 1985b), the small slope approximation (Voronovich, 1985), and the operator expansion method (Milder, 1991). A summary of all of these approximate methods is given in Kaczkowski (1994). See also Thorsos and Broschat (1995) for a description of the small slope method. Although the phase perturbation method can provide an accurate approximation to the scattered field for Dirichlet and Neumann surfaces (Broschat *et al.*, 1987; Broschat, Thorsos, and Ishimaru, 1989), it does not readily provide tractable solutions for the fluid-fluid seafloor scattering problem.

The operator expansion method is accurate in several scattering regimes for Dirichlet surfaces (Kaczkowski, 1994; Kaczkowski and Thorsos, 1994), but has not been developed for other boundary conditions and does not allow for formal averaging. A Monte Carlo approach is therefore required for obtaining field statistics. The small slope approximation can yield statistical solutions to the scattering problem with a fluid-solid boundary condition (Yang and Broschat, 1994), using a separate supporting analytical technique in a region of known validity. The analytical technique commonly used with the small slope approximation is perturbation theory (Rayleigh, 1945).

Perturbation theory, first used by Rice (1951) for randomly rough surfaces, is a straightforward technique for obtaining solutions to the scattering problem with complicated boundary conditions (Kuo, 1964; Dacol and Berman, 1988; Winebrenner, Farmer, and Joughin, 1995; Ivakin, 1994). The Rayleigh-Rice method (Rice, 1951) is a classical perturbative approach that uses the Rayleigh hypothesis as a starting point. In this approach, the incident and scattered fields are each expressed in terms of a Weyl, or a plane wave, representation. The Rayleigh hypothesis assumes that the scattered field can be represented everywhere in terms of a superposition of plane waves traveling away from the surface. Although this assumption is generally not valid close to the surface, Jackson, Winebrenner, and Ishimaru (1988) have established that the Rayleigh-Rice method and another more rigorous form of perturbation theory based on the extinction theorem (Nieto-Vesperinas and Garcia, 1981) yield identical solutions for the special case of a Dirichlet boundary condition through at least fifth order. They conjecture that the two perturbation methods yield identical results for all orders and all boundary conditions, and that the Rayleigh hypothesis is irrelevant to perturbation theory.

The conditions for validity of the perturbation solution depend on the root mean square (RMS) height h of the rough surface as well as the wave number

k_1 of the incident wave. It is generally accepted that for values of $k_1 h$ much smaller than one, a first-order perturbation solution will usually, but not always, represent the scattered field with sufficient accuracy (Thorsos and Jackson, 1989). For this reason, first-order perturbation theory is widely used for low frequency scattering from rough surfaces. Kuo (1964) has presented an expression for the differential cross section of a randomly rough interface separating two fluids based on first-order Rayleigh-Rice perturbation theory. This result has been frequently used to model the seafloor (Crowther, 1983; Jackson, Winebrenner, and Ishimaru, 1986; Stanic *et al.*, 1988, 1989; Mourad and Jackson, 1989, 1993; Jackson and Briggs, 1992). Dacol and Berman (1988), Kuperman and Schmidt (1986), Liu, Schmidt, and Kuperman (1993), and Essen (1994) have applied perturbation theory to a rough shear-supporting sea-floor.

Comparisons of first-order perturbation approximations with exact numerical results for the 2-D problem (1-D surface) have been made by Chen and Fung (1988) and Thorsos and Jackson (1989) for surfaces with a Gaussian roughness spectrum. These comparisons indicate that perturbation theory can be valid for values of $k_1 h$ as high as 0.25. Thorsos (1990) shows by comparisons with exact integral equation results for scattering from a 1-D rough fluid-fluid interface, that first-order perturbation theory accurately determines the differential cross section for scattering from a "Pierson-Moskowitz" roughness spectrum with $k_1 h = 0.45$. Using a truncated power-law roughness spectrum and sound-speed profile appropriate to the examples in this dissertation, Thorsos (1996a) shows by comparisons with exact integral equation results for scattering through a 1-D rough fluid-fluid interface, that first-order perturbation theory accurately determines the differential cross section over a wide range of scattering angles with $k_1 h = 2$. For scattering from a 1-D rough fluid-fluid interface, Thorsos shows that perturbation theory is valid for $k_1 h = 0.35$. Since a goal of this work is to

provide a tractable analytical model for seafloor scattering that is particularly accurate for scattering *through* a rough interface, perturbation theory is used.

1.4 Overview

Representing the ocean as a homogenous fluid, and the sediment as a lossy homogenous fluid separated by a rough interface, an analytical model based on perturbation theory is used to create computer simulations of the penetration experiments conducted by Boyle and Chotiros (1992) and Chotiros (1995) — even though these authors suggest that their results can be explained in terms of slow wave propagation in sediment that is a Biot medium. The general formalism for scattering of a pulse through a rough interface as well as from a rough interface is derived in chapter 2 of this dissertation. First-order fluid-fluid perturbation theory results used to approximate the rough interface scattering problem in the simulations are derived in chapter 3. In chapter 4, the results of the corresponding simulations of the experiments are given and compared with the experimental results of Boyle and Chotiros (1992) and Chotiros (1995). The simulations use the first-order perturbation model developed in chapters 2 and 3 to calculate the incoherent scattered intensity at a receiver in the sediment, and use the flat surface, zero-order field to calculate the coherent intensity. Using the zero-order field to represent the coherent intensity is valid for small amounts of surface roughness; however, the surface roughness used in the ocean experiment simulations is $k_1 h = 1$. The second-order component of the coherent intensity is derived in chapter 5, and compared with the zero-order component of the coherent intensity for the sediment roughness parameters used in the ocean experiment simulation.

The simulation model also neglects gradients in sound speed in the sediment. In the approach taken in chapter 5, the medium below the interface is constrained to be a fluid only down to the lowest point of the rough interface. Below this point, the sediment can be an arbitrary vertically stratified medium,

characterized by its flat surface reflection coefficient. An application of the derivations in this chapter shows the effect of an upward refracting sound-speed gradient on the field scattered back into the water. This result is further generalized in chapter 6, where the sediment parameters below the lowest point on the rough interface are taken to be random. Although results showing the effect of gradients on scattering through a rough interface are not presented in chapter 6, this case can also be examined using the analytical approach in this chapter and chapter 5. Overviews of chapters 2 through 6 are presented in sections 1.4.1 through 1.4.5.

1.4.1 Time-dependent mean square scattered field

The total propagation time from source to receiver can be experimentally determined when the source signal is a pulse. For a known propagation path and known propagation speed, the distance of an object can be determined from the propagation time of a scattered pulse. Likewise, if the propagation speed is unknown, but the propagation path and locations of the source and receiver are known, the propagation speed can be determined from the pulse propagation time. In Boyle and Chotiros (1992), the propagation speed in the sediment is inferred from the arrival of signal energy. The main purpose of chapter 2 is to derive a near-field expression for the *time-dependent* mean square scattered field (average of square of field magnitude) due to a narrowband point source, including dispersion due to scattering and frequency dependence of wave speed. These results (Moe and Jackson 1996a, 1996b) are applied to the simulation of tank experiments (Boyle and Chotiros, 1992) and ocean experiments (Chotiros, 1995); the results of these simulations are discussed in chapter 4.

The time-dependent mean square scattered field can be expressed in terms of a two-dimensional integral over the two-frequency mutual coherence function, $\Gamma(\omega_1,\omega_2)$ (see Ishimaru, 1978a, or Ishimaru *et al.*, 1994a). Scattering of a pulse

from the ocean surface is addressed in Ziomek (1982a, 1982b), where $\Gamma(\omega_1,\omega_2)$ is presented in terms of a Kirchhoff representation. Ishimaru *et al.* (1994a) derive an analytical expression for $\Gamma(\omega_1,\omega_2)$ for scattering from rough surfaces based on the Kirchhoff approximation, and Ishimaru *et al.* (1994b) use a second-order Kirchhoff approximation with shadowing corrections (Ishimaru and Chen, 1990, 1991) to obtain an analytical expression for $\Gamma(\omega_1,\omega_2)$ that includes backscattering enhancement effects. In chapter 2, we obtain a general expression for $\Gamma(\omega_1,\omega_2)$ appropriate for rough interface scattering for a narrowband incident plane wave that does not depend on a particular scattering approximation.

In order to obtain simple analytic expressions for the time-dependent mean square scattered field, Ishimaru *et al.* (1994a, 1994b) assume the scattering channel is a WSSUS (wide-sense stationary uncorrelated scattering) channel (Ishimaru, 1978a) — the two-frequency mutual coherence function, $\Gamma(\omega_1,\omega_2)$ is only dependent on the frequency difference, $\omega_d=\omega_2-\omega_1$, and not on $(\omega_1+\omega_2)/2$. Because of frequency dependent attenuation in the sediment, we do not assume that $\Gamma(\omega_1,\omega_2)$ is only dependent on ω_d. However, in chapter 2, we assume that the incoherent T-matrix correlation function varies slowly over the source frequency range, and expand phase terms in a power series in frequency. Both the incoherent T-matrix correlation function approximation and the power series expansion require that the source signal be narrowband. This approach is used to derive a general analytical expression for the time-dependent mean square incoherent field scattered *from* and *through* a 2-D fluid-fluid rough interface due to a narrowband incident plane wave which is expressed in terms of the second moment of the T-matrix. At distances sufficiently far from the rough interface to neglect the evanescent waves, this expression for the time-dependent mean square incoherent field is given in terms of the differential cross section of the rough interface. This derivation leads to

the usual sonar equation in the limit as the narrowband signal approaches the CW (continuous wave) case. For the special case of a CW incident plane wave, this result becomes essentially exact for distances greater than about a wavelength from the interface. This result is surprising because the differential cross section is defined as a far-field entity (Ishimaru, 1978b; Winebrenner and Ishimaru, 1986). The expression for the time-dependent mean square incoherent field due to an incident plane wave is used to obtain the expression for the scattered field due to a narrowband point source heuristically. A simple analytical expression is obtained for the case of a Gaussian shaped source pulse, also in terms of the differential cross section.

First-order perturbation calculations (first-order perturbation results are derived in chapter 3) for the case of a baseband Gaussian shaped source pulse illustrate narrowband pulse dispersion effects of the incoherent field due to forward scattering into a lossy sediment. For the case of incidence below the critical grazing angle, first-order perturbation computations also show that the incoherent field scattered through a rough surface can be much greater than the zero-order field transmitted below the corresponding flat surface depending on loss and receiver depth. These computations for the mean square incoherent field penetrating the rough interface are compared to the flat-surface result, for both plane wave and point sources.

1.4.2 First-order perturbation theory

Derivations for the first-order perturbation expressions used for the numerical computations in chapter 2 and in the computer simulations (chapter 4) are presented in chapter 3. Rayleigh-Rice perturbation theory is derived in chapter 3 for the simple case of a rough interface separating two homogenous fluids. The water above the rough interface is modeled as a homogenous lossless fluid, and the sediment below the interface is modeled as a homogenous lossy fluid. The results of chapter 3 are equivalent to those published by Kuo (1964) and Mourad

and Jackson (1989), except that the field scattered into the second medium is also considered here. Although these results are derived for the two homogenous fluid case, this form of the first-order scattered field solution is shown to be more general in chapter 5. First-order perturbation theory solutions for this case are also used in the simulations of sediment penetration experiments in chapter 4. As in Moe and Jackson (1994c), a truncated or filtered power law is used for the roughness spectrum. This filter is shown to be equivalent to subtracting a moving average (Papoulis, 1984) from a 2-D surface with power-law roughness spectrum.

1.4.3 Computer simulations of recent experiments

A recent tank experiment (Boyle and Chotiros, 1992) and a recent ocean experiment (Chotiros, 1995) reveal acoustic penetration from water into sandy sediments at grazing angles below the compressional critical angle in relation to the mean surface. In their tank experiment (Boyle and Chotiros, 1992), a receiver buried in sand measures the intensity of a signal transmitted in water above the sand. The propagation time of the transmitted pulse is the same as that of slow refracted wave. Since only a single receiver is used in Boyle and Chotiros' tank experiments, no information about direction of the propagating energy in the sediment is available. In an attempt to determine both direction and speed of the energy propagating in the sediment, a buried array of receivers was used in an ocean experiment (Chotiros, 1995) that measures the intensity at an array of receivers in the sediment due to an acoustical source in the water. They use a simple algorithm to determine the speed and direction of the intensity front propagating in the sediment. The results of their experiments seem to suggest propagation of energy at speeds slower than the compressional speed of the sediment, in a direction concurring with Snell's law.

Assuming a small amount of roughness at the water-sediment interface, and using the 3-D scattering model developed in chapter 2 with the first-order

perturbation theory results for 2-D fluid-fluid rough interfaces derived in chapter 3, we reproduce the results of the tank experiments, indicating that the acoustic penetration of the surface may be due to scattering (diffraction) from low levels of roughness (Moe *et al.*, 1995) rather than slow-wave refraction. Assuming roughness parameters appropriate to the ocean experiment reported by Chotiros (1995), our goal is to reproduce his results with the model developed in this dissertation. An explanation by Thorsos (1995) of how diffraction can mimic a slow wave is given in chapter 4, along with discussions of simulation results (Moe *et al.*, 1995). Some of the results presented in this chapter have been presented in Moe *et al.* (1995) and again in Jackson *et al.* (1996).

1.4.4 Perturbation theory results for a fluid-fluid rough interface including gradients

Moe and Jackson (1994a) follow the approach used by Winebrenner, Farmer, and Joughin (1995) in their treatment of electromagnetic scattering from rough dielectric surfaces, and constrain the sediment below the rough interface, down to the lowest point on the interface, to be a fluid. However, the medium below the lowest point on the interface is only constrained to be vertically stratified (e.g., sound speed can vary with depth, but not horizontal position) and is represented by its reflection coefficient. The derivation in chapter 5 takes this approach, allowing the sediment below the lowest point on the surface to be viscoelastic, or porous, supporting shear or Biot slow waves as well as gradients in physical properties. A first-order solution for scattering from a rough interface is also given in Ivakin (1994). Multiple layered rough interfaces in layered sediments are also considered in his presentation.

First-order perturbation theory is valid for obtaining the incoherent field scattered into the sediment for the roughness parameters used in the simulations (Thorsos, 1996a), but generally, there is a need for higher order results to test validity and to correct lower orders. Also, sediments tend to be stratified, so the

assumption of spatial homogeneity of the second medium is sometimes questionable. Using Rayleigh-Rice perturbation theory, Nth-order recursion equations are derived in chapter 5 that provide a starting point for evaluating the Nth-order scattered field in terms of lower orders. The validity of using the zero-order result to represent the coherent intensity is shown in chapter 5, where an expression for the second-order coherent field is derived.

1.4.5 Formal average with random sediment parameters

In the simulation discussed in chapter 4, the sediment is taken to be a homogenous fluid. The perturbation derivations in chapter 5 allow for the effects of sound-speed gradients on the field scattered through and from the rough water-sediment interface. Strong gradients and discontinuities in density and sound speed on scales of several cm are often observed in shallow water environments (Briggs, Richardson, and Young, 1985; Richardson, 1986; Stanic *et al.,* 1988, 1989; Jackson and Briggs, 1992; Lyons, Anderson, and Dwan, 1994; Jackson *et al.*, 1996), and gradients on scales of hundreds of meters are observed in deep ocean environments (Hamilton, 1979, 1980). Although the approach taken in chapter 5 includes the effects of layering and gradients in seafloor parameters below the rough interface, it does not allow for the inherent randomness of these parameters, which will sometimes "wash out" rapid angular variations in scattering caused by constructive and destructive interference. Perfect vertical stratification leads to interference effects which may not always appear. By allowing stratification parameters to be random, these interference effects can be averaged to reveal more robust features of the differential cross section. Note that this approach does not model volume scattering, since there is no horizontal dependence of sediment properties.

In chapter 6, the first-order expression for the differential cross section derived in chapters 2 and 5 is generalized to account for randomness in the medium below the lowest point on the rough interface by expressing the

differential cross section in terms of moments of the stochastic flat surface reflection coefficient. Upward refraction or reflection due to large sound-speed gradients in the sediment results in increased scattering strength over the non-gradient case. This scattering gain occurs for various sediment types over a wide range of bistatic angles, but has a relative maximum when the incident and scattered grazing angles are equal (backscattering enhancement). Backscattering enhancement is observed and predicted in scattering from rough interfaces (e.g., Maradudin and Mendez, 1993; Ishimaru *et al.*, 1994b), but it is not manifest in first-order perturbation theory calculations that involve only scattering from a single rough interface with no additional specular or refracted path. Hanson and Zavorotny (1995) show that backscattering enhancement is apparent using first-order perturbation theory in a two-scale model for electromagnetic scattering from a rough ocean surface. In Hanson and Zavorotny, the energy path consists of a single scattering event and specular reflection; in the sound-speed gradient problem addressed in chapter 6, the energy path consists of a single scattering event and refraction.

CHAPTER 2

Near field scattering through and from a 2-D fluid-fluid rough interface

2.1 Introduction to chapter 2

In this chapter, a general analytical expression for the time-dependent mean square scattered field (average of square of incoherent field magnitude) due to an incident narrowband plane wave is derived and expressed in terms of the second order T-matrix statistics, as well as in terms of the bistatic scattering cross section per unit area per unit solid angle (differential cross section) of the rough interface. This novel approach yields an analytical expression that is not dependent on a particular scattering solution technique. In addition, the effect of loss in the medium below the interface is included in the result. Even though the differential cross section is typically considered a far-field entity (Ishimaru, 1978a), the form of this result in terms of the differential cross section is valid for distances on the order of a wavelength from the interface. This rigorously derived result is used to derive the scattered field due to a narrowband point source heuristically. This derivation leads to the usual sonar equation in the limit as the narrowband signal approaches the CW (continuous wave) case. The results of this chapter, along with the two-fluid perturbation theory results of chapter 3, are used in the simulation of sediment penetration experiments (Boyle and Chotiros, 1992; Chotiros, 1995), discussed in chapter 4. The results of this chapter are also presented in Moe and Jackson (1996a, 1996b).

Figure 2.1 shows a 2-D slice of the 3-D ocean model. A time-dependent incident field in a homogenous fluid (water) above a rough water-sediment interface results in energy scattered from the interface back into the water and

through the rough interface into the sediment. The sediment is represented by a homogenous lossy fluid. The effect of depth-dependent sediment parameters on the time-dependent scattered field is not considered in this formalism. However, in the general perturbation theory derivation in chapter 5, as well as in the formally averaged sediment parameters derivation in chapter 6, the effect of sound-speed gradients on the intensity scattered back into the water for the CW case is discussed. General background for the scattering problem is given in the next section.

The solution for a time-dependent scattered field requires obtaining the solution for the two-frequency mutual coherence function, $\Gamma(\omega_1,\omega_2)$ (Ishimaru, 1978a). A general expression for $\Gamma(\omega_1,\omega_2)$ for an incident plane wave is derived by assuming the T-matrix correlation function is a slowly varying function of frequency. Dispersion effects due to frequency-dependent phase speed are treated by expanding phase terms in a power series about the center frequency. The validity of this expansion and the frequency-independence assumption both depend on the source signal bandwidth. The validity of the frequency-independence assumption for the T-matrix correlation function is shown in chapter 3 to also depend on the distance from the interface. Using this approximate expression for $\Gamma(\omega_1,\omega_2)$, we obtain a near-field expression for the time-dependent mean square incoherent field (average of incoherent field magnitude squared) for narrowband source signals in terms of the second moment of the T-matrix. Neglecting the evanescent field components in this result, we obtain a useful expression for the time-dependent mean square incoherent field in terms of the differential cross section. This result is remarkable in that a near field result is obtained in terms of what is generally considered to be a far field quantity. First-order perturbation results (derived in the following chapter) depict the contribution of the evanescent component to the incoherent scattered field for a CW plane wave source. The resulting profiles of

mean square incoherent field versus depth are compared with the flat-surface case, also illustrating the effect of roughness on the field penetrating a fluid-fluid interface.

Using the narrowband time-dependent mean square incoherent field result for an incident plane wave, we heuristically obtain an analytical expression for the time-dependent mean square incoherent field due to a point source. First-order perturbation results illustrate dispersion of a pulse with Gaussian envelope due to forward scattering into a lossy sediment. These computations are carried out using a low-frequency cutoff for the bottom relief spectrum, and are compared to the flat-surface case.

2.2 Scattering problem background

The general scattering geometry is shown in Fig. 2.1. An arbitrary pressure field, $\psi_i(\mathbf{r})$, is incident on a 2-D rough interface separating the homogenous lossless fluid in medium 1 (water) from the lossy fluid in medium 2 (sediment). The zero-mean rough interface is defined by

$$z = hf(\mathbf{R}), \tag{2.1}$$

where $\mathbf{R}$ is the transverse component of the three-dimensional position vector $\mathbf{r}$, and h is the root mean square (RMS) height of the rough interface. The total field, $\psi_1(\mathbf{r})$, above the rough interface is a sum of an arbitrary incident field, $\psi_i(\mathbf{r})$, and the resulting scattered pressure field, $\psi_f(\mathbf{r})$:

$$\psi_1(\mathbf{r}) = \psi_i(\mathbf{r}) + \psi_f(\mathbf{r}). \tag{2.2}$$

The boundary conditions on the interface consist of the continuity of pressure,

$$\psi_1(\mathbf{r})\big|_{z=f(\mathbf{R})} = \psi_2(\mathbf{r})\big|_{z=hf(\mathbf{R})}, \tag{2.3}$$

and the continuity of normal velocity,

$$\frac{1}{\rho_1}\hat{n}\cdot\nabla\psi_1(\mathbf{r})\big|_{z=f(\mathbf{R})}=\frac{1}{\rho_2}\hat{n}\cdot\nabla\psi_2(\mathbf{r})\big|_{z=hf(\mathbf{R})}, \tag{2.4}$$

where ψ_2 is the pressure field in the sediment, $\hat{n}$ is the unit vector normal to the interface, ρ_1 is the density of the water, and ρ_2 is the density of the sediment The scattered field, $\psi_f(\mathbf{r})$, in the region above the highest point on the interface and the incident field are expressed in terms of the following (Weyl) plane wave expansions (Devaney and Sherman, 1973):

$$\psi_f(\mathbf{r})=\int d^2K\Psi_f(\mathbf{K})e^{ik_1\beta_1(\mathbf{K})z}e^{i\mathbf{K}\cdot\mathbf{R}} \tag{2.5}$$

and

$$\psi_i(\mathbf{r})=\int d^2K\Psi_i(\mathbf{K})e^{-ik_1\beta_1(\mathbf{K})z}e^{i\mathbf{K}\cdot\mathbf{R}}, \tag{2.6}$$

where $\mathbf{K}$ is the two-dimensional transverse wave vector with magnitude K, k_1 is the wave number in the medium above the interface, and

$$\beta_1(\mathbf{K})=\sqrt{1-K^2/k_1^2}\,. \tag{2.7}$$

The square root in Eq. (2.7) is chosen so that β_1 is either positive or positive imaginary. For the CW (continuous wave) case, a factor of $e^{-i\omega t}$ is suppressed, but in general the above equations are the Fourier transforms of the time domain field,

$$\psi_1(\mathbf{r})\equiv\psi_1(\mathbf{r},\omega)=\int dt\,\psi_1(\mathbf{r},t)e^{i\omega t}. \tag{2.8}$$

The field below the rough interface is expressed as a plane wave expansion of waves traveling in the negative z direction,

$$\psi_2(\mathbf{r})=\psi_{2-}(\mathbf{r})\equiv\int d^2K\Psi_{2-}(\mathbf{K})e^{-ik_2\beta_2(\mathbf{K})z}e^{i\mathbf{K}\cdot\mathbf{R}}, \qquad z<0, \tag{2.9}$$

where

$$\beta_2(\mathbf{K})=\sqrt{1-K^2/k_2^2} \tag{2.10}$$

and

$$k_2 = \frac{(1+i\delta)\omega}{\nu c_1} \tag{2.11}$$

is the complex wave number in the lossy medium below the interface with frequency-independent loss parameter, δ. The speed ratio, ν, is the ratio of the sound speed in the sediment, c_2, to the sound speed in the water, c_1. Although the definition of k_2 in Eq. (2.11) violates causality (Aki and Richards, 1980; Wingham, 1985), we show these noncausal effects are negligible and consistent with the approximations made in deriving the analytical result. The square root in Eq. (2.10) is chosen such that β_2 is in the first quadrant of the complex plane. The field scattered back into medium 1 can be expressed in terms of the incident field and the T-matrix, T_{11}:

$$\Psi_f(\mathbf{K}) = \int d^2K' T_{11}(\mathbf{K},\mathbf{K}')\Psi_i(\mathbf{K}'). \tag{2.12}$$

Likewise, the downward component of the scattered field penetrating below the interface is expressed in terms of the T-matrix, T_{12}:

$$\Psi_{2-}(\mathbf{K}) = \int d^2K' T_{12}(\mathbf{K},\mathbf{K}')\Psi_i(\mathbf{K}'). \tag{2.13}$$

The scattered field for the case of an incident plane wave is found by substituting

$$\Psi_i(\mathbf{K}) = \delta(\mathbf{K}-\mathbf{K}_i) \tag{2.14}$$

into Eq. (2.12) and the result into Eq. (2.5), yielding

$$\psi_f(\mathbf{r}) = \int d^2K T_{11}(\mathbf{K},\mathbf{K}_i)\mathrm{e}^{ik_1\beta_1(\mathbf{K})z}\mathrm{e}^{i\mathbf{K}\cdot\mathbf{R}}. \tag{2.15}$$

The scattered field penetrating the interface for the incident plane wave case is found in the same way from Eqs. (2.9), (2.13), and (2.14):

$$\psi_{2-}(\mathbf{r}) = \int d^2K T_{12}(\mathbf{K},\mathbf{K}_i)\mathrm{e}^{-ik_2\beta_2(\mathbf{K})z}\mathrm{e}^{i\mathbf{K}\cdot\mathbf{R}}. \tag{2.16}$$

For convenience, let $\psi(\mathbf{r})$ represent both $\psi_f(\mathbf{r})$ and $\psi_{2-}(\mathbf{r})$. Define

$$\tilde{\psi}(\mathbf{r}) \equiv \psi(\mathbf{r}) - \langle \psi(\mathbf{r}) \rangle, \tag{2.17}$$

where $\langle \psi(\mathbf{r}) \rangle$ is the mean of the field averaged over the ensemble of rough interfaces. Similarly, define

$$\tilde{T}(\mathbf{K}, \mathbf{K}_i) = T(\mathbf{K}, \mathbf{K}_i) - \langle T(\mathbf{K}, \mathbf{K}_i) \rangle \tag{2.18}$$

to be the incoherent T-matrix. Using the above definitions, $\tilde{\psi}(\mathbf{r})$ is expressed as

$$\tilde{\psi}(\mathbf{r}) = \int d^2K \tilde{T}(\mathbf{K}, \mathbf{K}_i) \mathrm{e}^{-ik_2\beta_2(\mathbf{K})z} \mathrm{e}^{i\mathbf{K}\cdot\mathbf{R}}. \tag{2.19}$$

2.3 General result for incident plane wave

The purpose of this section is to derive an expression for the time-dependent mean square incoherent field at the receiver position, $\mathbf{r}$, due to a narrowband plane wave source. Although the following derivation considers the more general case of scattering *through* a rough interface, it also applies to scattering *from* a rough interface.

2.3.1 Time domain received signal

A narrowband source signal, $s(t)$, with units of pressure and with Fourier transform

$$S(\omega) = \int_{-\infty}^{\infty} dt\, s(t) \mathrm{e}^{i\omega t} \tag{2.20}$$

can be represented as

$$s(t) = \mathrm{Re}\left\{ u(t) \mathrm{e}^{-i\omega_c t} \right\}, \tag{2.21}$$

where $u(t)$ is the corresponding complex baseband input signal with Fourier transform $U(\omega)$, and ω_c is the carrier frequency, or center frequency of the pulse (see, for example, Ishimaru, 1978a; Proakis, 1989). An incident plane wave pulse with direction denoted by the transverse unit vector, $\hat{\alpha}_i$, and incident grazing angle, θ_i, is expressed in terms of its 2-D Fourier transform as

$$\Psi_i(\mathbf{K},\omega) = S(\omega)\delta(\mathbf{K}-\mathbf{K}_i)e^{i\omega z_s \sin\theta_i/c_1}, \qquad \omega > 0, \tag{2.22}$$

where

$$\mathbf{K}_i = \frac{\omega}{c_1}\cos\theta_i\hat{\alpha}_i \tag{2.23}$$

is the incident transverse wave vector, and z_s is taken to be an arbitrary source height. Using Eqs. (2.9), (2.13), (2.17), (2.18), (2.20), (2.21), and (2.22) and chapter 5 of Ishimaru (1978a), we express the incoherent field $\tilde{\psi}_{bb}(\mathbf{r},t)$ at a position $\mathbf{r} = (\mathbf{R},z)$ below the interface as

$$\tilde{\psi}_{bb}(\mathbf{r},t) = \frac{1}{2\pi}\int d\omega' U(\omega')\mathcal{H}_{12}(\omega'+\omega_c)e^{-i\omega' t}, \tag{2.24}$$

where

$$\begin{aligned}\mathcal{H}_{12}(\omega'+\omega_c) = \int d^2K \Big\{ &\tilde{T}_{12}(\mathbf{K},\mathbf{K}_i,\omega'+\omega_c)e^{i\sin\theta_i z_s(\omega'+\omega_c)/c_1} \\ &\times e^{-i\kappa\beta_2(\mathbf{K},\omega'+\omega_c)z(\omega'+\omega_c)/c_1} e^{i\mathbf{K}\cdot\mathbf{R}}\Big\}\end{aligned} \tag{2.25}$$

is the Fourier transfer of the impulse response of the incoherent field, generally known as the transfer function. The complex wave number ratio is given by

$$\kappa \equiv k_2/k_1 = \frac{(1+i\delta)}{\nu} \tag{2.26}$$

and

$$\mathbf{K}_i = \frac{\omega' + \omega_c}{c_1} \cos\theta_i \hat{\alpha}_i. \tag{2.27}$$

We have explicitly shown the dependence of $\beta_2(\mathbf{K})$ on frequency and $\mathbf{K}$.

2.3.2 Time-dependent mean square incoherent field

The time-dependent mean square incoherent field at position $\mathbf{r}$ can be expressed as (Ishimaru 1978a, chapter 4)

$$I_2(\mathbf{r},t) = \left\langle \left| \tilde{\psi}_{bb}(\mathbf{r},t) \right|^2 \right\rangle. \tag{2.28}$$

Combining Eqs. (2.24) and (2.28) yields Ishimaru's (1978a) Eq. (5-17):

$$I_2(\mathbf{r},t) = \left(\frac{1}{2\pi}\right)^2 \int d\omega' \int d\omega'' \left\{ U(\omega') U^*(\omega'')\, \mathrm{e}^{-i\omega' t}\, \mathrm{e}^{i\omega'' t} \times \Gamma(\omega' + \omega_c, \omega'' + \omega_c) \right\}, \tag{2.29}$$

where

$$\Gamma(\omega' + \omega_c, \omega'' + \omega_c) = \left\langle \mathscr{H}_{12}(\omega' + \omega_c) \mathscr{H}_{12}^*(\omega'' + \omega_c) \right\rangle \tag{2.30}$$

is defined by Ishimaru (1978a) as the two-frequency mutual coherence function. Using the expression for $\mathscr{H}_{12}$ in Eq. (2.25), Eq. (2.30) is equivalent to

$$\begin{aligned} &\Gamma(\omega' + \omega_c, \omega'' + \omega_c) \\ &= \int d^2K'' \int d^2K' \left\langle \tilde{T}_{12}(\mathbf{K}', \mathbf{K}_i', \omega' + \omega_c) \tilde{T}_{12}^*(\mathbf{K}'', \mathbf{K}_i'', \omega'' + \omega_c) \right\rangle \\ &\times \mathrm{e}^{i\mathbf{K}'\cdot\mathbf{R}} \mathrm{e}^{-i\mathbf{K}''\cdot\mathbf{R}} \mathrm{e}^{i \sin\theta_i z_s \omega'/c_1} \mathrm{e}^{-i \sin\theta_i z_s \omega''/c_1} \\ &\times \left. \mathrm{e}^{-i\kappa\beta_2(\mathbf{K}', \omega' + \omega_c) z(\omega' + \omega_c)/c_1} \mathrm{e}^{i\left(\kappa\beta_2(\mathbf{K}'', \omega'' + \omega_c)\right)^* z(\omega'' + \omega_c)/c_1} \right\}, \end{aligned} \tag{2.31}$$

where the transverse wave vectors for the incident field at the angular frequencies ω'' and ω' are

$$\mathbf{K}_i''=\frac{\omega_c+\omega''}{c_1}\cos\theta_i\hat{\alpha}_i \quad \text{and} \quad \mathbf{K}_i'=\frac{\omega_c+\omega'}{c_1}\cos\theta_i\hat{\alpha}_i. \tag{2.32}$$

Define $\mathcal{C}_{12}(\mathbf{K}',\mathbf{K}'',\mathbf{K}_i',\mathbf{K}_i'',\omega_c+\omega',\omega_c+\omega'')$ (see, for example, Zipfel and DeSanto, 1972; Voronovich, 1995) such that

$$\begin{aligned}&\left\langle \tilde{T}_{12}(\mathbf{K}',\mathbf{K}_i',\omega'+\omega_c)\tilde{T}_{12}^*(\mathbf{K}'',\mathbf{K}_i'',\omega''+\omega_c)\right\rangle \\ &\equiv \mathcal{C}_{12}(\mathbf{K}',\mathbf{K}'',\mathbf{K}_i',\mathbf{K}_i'',\omega_c+\omega',\omega_c+\omega'')\delta(\mathbf{K}''-\mathbf{K}'+\mathbf{K}_i'-\mathbf{K}_i'').\end{aligned} \tag{2.33}$$

We refer to $\mathcal{C}_{12}$ as the incoherent T-matrix correlation function. In the above expression, the subscript is used to represent scattering into the sediment and the dependence of $\tilde{T}_{12}$ on ω is included in the argument. Substituting Eq. (2.33) and

$$\mathbf{K}_i''-\mathbf{K}_i'=\frac{\omega''-\omega'}{c_1}\cos\theta_i\hat{\alpha}_i\equiv\mathbf{K}_d \tag{2.34}$$

into Eq. (2.31), and changing the integration variable $\mathbf{K}'$ to

$$\mathbf{K}=\mathbf{K}'+\mathbf{K}_d/2, \tag{2.35}$$

yields

$$\begin{aligned}&\Gamma(\omega'+\omega_c,\omega''+\omega_c)\\ &=\int d^2K\left\{\mathcal{C}_{12}(\mathbf{K}-\mathbf{K}_d/2,\mathbf{K}+\mathbf{K}_d/2,\mathbf{K}_i',\mathbf{K}_i'',\omega_c+\omega',\omega_c+\omega'')\right.\\ &\times e^{-i\mathbf{K}_d\cdot\mathbf{R}}e^{i\sin\theta_i z_s\omega'/c_1}e^{-i\sin\theta_i z_s\omega''/c_1}\\ &\times e^{-i\kappa\beta_2(\mathbf{K}-\mathbf{K}_d/2,\omega_c+\omega')z\omega'/c_1}\\ &\left.\times e^{i\left(\kappa\beta_2(\mathbf{K}-\mathbf{K}_d/2,\omega_c+\omega'')\right)^* z(\omega_c+\omega'')/c_1}\right\}.\end{aligned} \tag{2.36}$$

Equation (2.36) is now evaluated by making a few approximations. We assume $\mathcal{C}_{12}$ is a slowly varying function of frequency, and for the case of a narrowband source signal,

$$\mathscr{C}_{12}(\mathbf{K}-\mathbf{K}_d/2,\mathbf{K}+\mathbf{K}_d/2,\mathbf{K}_i',\mathbf{K}_i'',\omega_c+\omega'',\omega_c+\omega')$$

$$\cong \mathscr{C}_{12}(\mathbf{K},\mathbf{K},\mathbf{K}_i,\mathbf{K}_i,\omega_c,\omega_c)$$
$$\equiv \mathscr{C}_{12}(\mathbf{K},\mathbf{K}_i,\omega_c), \tag{2.37}$$

where the relation (Thorsos and Jackson, 1989; Berman, 1992)

$$\mathscr{C}_{12}(\mathbf{K},\mathbf{K}_i,\omega_c)\delta(\mathbf{K}-\mathbf{K}'') \equiv \left\langle \tilde{T}_{12}(\mathbf{K},\mathbf{K}_i,\omega_c)\tilde{T}_{12}^*(\mathbf{K}'',\mathbf{K}_i,\omega_c)\right\rangle \tag{2.38}$$

is a special case of Eq. (2.33), and $\mathbf{K}_i$ is evaluated at the center frequency:

$$\mathbf{K}_i = \frac{\omega_c}{c_1}\cos\theta_i\hat{\alpha}_i. \tag{2.39}$$

It is easy to show using first-order perturbation theory (see chapter 3) that the approximation in Eq. (2.37) is valid for $K+|\mathbf{K}_d|/2 < k_1$, or

$$K < k_1 - \pi f_d \cos\theta_i/c_1, \tag{2.40}$$

where $2\pi f_d = |\omega''-\omega'|$ can be taken to be the source signal bandwidth. For larger K, the phase of the quantity on the left side of Eq. (2.37) cannot be considered independent of frequency. The first-order T-matrix representing scattering from the water into the sediment, T_{12}, is derived in chapter 3 and given in Eqs. (3.41) and (3.45), and the first-order approximation of the incoherent T-matrix correlation function is given in Eq. (3.50).

Define the vertical component of the wave vector in medium 2 as

$$B_2(K,\omega_c+\omega',\omega_c+\omega'') \equiv \left((\omega_c+\omega')/c_1\right)\kappa\beta_2(\mathbf{K}-\mathbf{K}_d/2,\omega_c+\omega'). \tag{2.41}$$

Analytical expressions for dispersion in a waveguide can be found by expanding the propagation constant of the time-dependent field in a power series (for example, see Ishimaru, 1991, chap. 4). Similarly, with reference to Eq. (2.36), $(\omega'/c_1)\kappa\beta_2$ is expanded in a power series in ω' and ω''. For the case of a narrowband signal,

$$B_2(K,\omega_c+\omega',\omega_c+\omega'') \cong B_{2c}(K)+\frac{\partial B_2}{\partial \omega'}\omega'+\frac{\partial B_2}{\partial \omega''}\omega'' + \frac{1}{2}\left[\frac{\partial^2 B_2}{\partial \omega'^2}\omega'^2+2\frac{\partial^2 B_2}{\partial \omega \partial \omega''}\omega'\omega''+\frac{\partial^2 B_2}{\partial \omega''^2}\omega''^2\right], \tag{2.42}$$

where the derivatives are evaluated at $\omega' = \omega'' = 0$, and

$$B_{2c}(K) \equiv \kappa k_1 \beta_2(\mathbf{K},\omega_c), \tag{2.43}$$

where the wave number, k_1, in the above equation and all following equations is evaluated at the center frequency ($k_1 = \omega_c/c_1$). Solving for the derivatives in Eq. (2.42) (see Appendix A), combining like powers of ω' and ω'' in Eq. (2.36), and substituting the result into Eq. (2.29) yields

$$\begin{aligned} I_2(\mathbf{r},t) \cong \int d^2K \Big\{ & \mathcal{C}_{12}(\mathbf{K},\mathbf{K}_i,\omega_c) e^{2k_{1c}\,\mathrm{Im}(\kappa\beta_2(\mathbf{K},\omega_c))z} \\ & \times \frac{1}{2\pi}\int d\omega'' U^*(\omega'') e^{i\omega''(t-t_1-t_2)^*} e^{i\omega''^2 P^*/4} \\ & \times \frac{1}{2\pi}\int d\omega' U(\omega') e^{-i\omega'(t-t_1-t_2)} e^{-\omega'\omega'' P} e^{-i\omega'^2 P/4} \Big\}, \end{aligned} \tag{2.44}$$

where

$$t_1 = \frac{\mathbf{R}\cdot\hat{\alpha}_i}{c_1}\cos\theta_i + \frac{z_s}{c_1}\sin\theta_i + z\frac{\hat{\alpha}_i\cdot\mathbf{K}\cos\theta_i}{c_1 k_1}\mathrm{Re}\left(\frac{1}{\kappa\beta_2(\mathbf{K},\omega_c)}\right) \tag{2.45}$$

and

$$t_2 = \frac{-z\kappa/c_1}{\beta_2(\mathbf{K},\omega_c)}. \tag{2.46}$$

The physical significance of these parameters will be discussed later. Note that t_1 is real and t_2 is complex. The complex coefficient,

$$\begin{aligned} P = \Big\{ & \left(2\kappa^2/B_{2c}^3\right)\left(\hat{\alpha}_i\cdot\mathbf{K}\omega_c\cos\theta_i/c_1^3 - (K/c_1)^2\right) - i\,\mathrm{Im}(1/B_{2c})(\cos\theta_i/c_1)^2, \\ & -i\,\mathrm{Im}\left(1/B_{2c}^3\right)(\hat{\alpha}_i\cdot\mathbf{K}\cos\theta_i/c_1)^2 \Big\} z \end{aligned} \tag{2.47}$$

and the real coefficient,

$$\not{P} = \mathrm{Im}\left\{\left(\hat{\alpha}_i \cdot \mathbf{K}\cos\theta_i / B_{2c}^3\right)\left(\kappa^2\omega_c / c_1^3 - \hat{\alpha}_i \cdot \mathbf{K}\cos\theta_i / \left(2c_1^2\right)\right) - \cos^2\theta_i / \left(2c_1^2 B_{2c}\right)\right\} z, \quad (2.48)$$

can represent the contribution to pulse dispersion of the frequency-dependent phase term. This result is simplified by setting

$$g^2(t) \equiv \frac{1}{2\pi}\int d\omega'' U^*(\omega'') \mathrm{e}^{i\omega'' t^*} \mathrm{e}^{i\omega''^2 P^*/4} \times \frac{1}{2\pi}\int d\omega' U(\omega') \mathrm{e}^{-i\omega' t} \mathrm{e}^{-i\omega'\omega''\not{P}} \mathrm{e}^{-i\omega'^2 P/4}. \quad (2.49)$$

The above definition leads to a simple expression for the time-dependent mean square incoherent field in medium 2:

$$I_2(\mathbf{r},t) \cong \int d^2K \mathcal{C}_{12}(\mathbf{K},\mathbf{K}_i,\omega_c) \mathrm{e}^{2k_1 \mathrm{Im}(\kappa\beta_2(\mathbf{K},\omega_c))z} g^2\left(t - t_d\right). \quad (2.50)$$

In addition to being a function of the complex argument, t, $g(t)$ is a function of K, the incident field direction, and fluid-sediment parameters. Note that

$$t_d \equiv t_1 + t_2 \quad (2.51)$$

is also a complex function of K. For an arbitrarily small pulse bandwidth (CW), P, $\not{P}$, $\mathrm{Im}(t_2)$ are arbitrarily small, and $g(t) \to u(t)$.

The definition of κ in Eq. (2.25) violates causality (see Aki and Richards, 1980, chap 5, and Wingham, 1985). When a corrected version of Eq. (8) from Wingham (1985) is used, causality will not be violated if $\kappa - 2\delta \ln\left|(\omega_c + \omega')/\omega_c\right|/(\pi v)$ is substituted for κ in (A2). Using this substitution, and following the derivation in Appendix A, results in causal versions of the parameters $P, \not{P}, t_1$, and t_2. Since $\delta << 1$ for ocean sediment, the difference between the causal representation of $P, \not{P}, t_1$, and t_2 and Eqs. (2.45) - (2.48) is negligible.

While Eq. (2.50) involves an integral over the transverse wave vector, it can be converted to an integral over the scattering interface through the change of variable,

$$\mathbf{R}' = \mathbf{R} - \nu r_d \mathbf{K}/k_1 . \tag{2.52}$$

As shown in Fig. 2.2, $\mathbf{R}'$ is the location of a small scattering patch on the interface, and $r_d = |\mathbf{r}_d|$ is the distance from this patch to the field point, $\mathbf{r}$.

$$r_d = \sqrt{|\mathbf{R} - \mathbf{R}'|^2 + z^2} . \tag{2.53}$$

We constrain $\mathbf{K}$ to the range $K < k_1/\nu$ in Eq. (2.52), that is, we neglect evanescent waves. This constraint is justified later when the contribution of evanescent waves on the mean square scattered incoherent field is illustrated using first-order perturbation computations for an incident plane wave. This constraint is also consistent with the frequency-independence assumption of the T-matrix correlation function. This assumption is invalid for arbitrarily large integration variable K in Eq. (2.50) (see Eq. 2.40). The Jacobian follows from Eq. (2.52).

$$\left(\frac{\partial K}{\partial R'}\right) = \frac{k_1^2}{\nu^2 r_d^6}\begin{vmatrix} y_d^2 + z^2 & x_d y_d \\ x_d y_d & x_d^2 + z^2 \end{vmatrix} = \frac{k_1^2}{\nu^2 r_d^4} z^2 , \tag{2.54}$$

where x_d and y_d are the transverse coordinates of $\mathbf{r}_d$. The geometric significance of these definitions is apparent when one assumes that the loss parameter is small $(\delta << 1)$. Then

$$\begin{aligned} k_1 \kappa \beta_2(\mathbf{K}, \omega_c) &= \sqrt{(\kappa k_1)^2 - K^2} \\ &\cong (k_1 \sin\theta_2/\nu)\left(1 + i\delta/\sin^2\theta_2\right), \end{aligned} \tag{2.55}$$

where

$$\sin\theta_2 = \sqrt{1 - K^2 \nu^2/k_1^2} = |z|/r_d \tag{2.56}$$

is the sine of the scattered grazing angle defined in Fig. 2.2. When terms of second order and higher in the loss parameter are dropped, the significance of t_1 and t_2 becomes apparent, as

$$t_1 = \mathbf{R}' \cdot \hat{\alpha}_i \cos\theta_i / c_1 + z_s \sin\theta_i / c_1 \tag{2.57}$$

is the time required for the incident plane wave front with direction $(\hat{\alpha}_i \cos\theta_i, \sin\theta_i)$ to travel from the source reference point, $(0,0,z_s)$, to the scattering patch, $(\mathbf{R}',0)$, and

$$\mathrm{Re}(t_2) = r_d / c_2 \tag{2.58}$$

is the time required for a spherical wave scattered from the patch at $(\mathbf{R}',0)$ to travel through the sediment to the field point $(\mathbf{R},z)$, $z<0$. According to Eq. (2.55), the absorption exponent in medium 2 is given by

$$\mathrm{Im}\left(k_1 \kappa \beta_2\left(K,\omega_c\right)\right)|z| = \frac{k_1 \delta}{\nu}|z| / \sin\theta_2 = \mathrm{Im}(k_2) r_d . \tag{2.59}$$

Substituting Eqs. (2.54) and (2.59) into Eq. (2.50) results in

$$I_2(\mathbf{r},t) = \int d^2R' \, \frac{k_1^2 \sin^2(\theta_2)}{\nu^2 r_d^2} \mathcal{C}_{12}(\mathbf{K},\mathbf{K}_i,\omega_c) \mathrm{e}^{-2\,\mathrm{Im}(k_2) r_d} \, g^2(t - t_d). \tag{2.60}$$

Substituting the following quantities,

$$\sigma_{12}(\hat{\alpha},\hat{\alpha}_i) \equiv \frac{k_1^2 \sin^2(\theta_2)}{\nu^2} \mathcal{C}_{12}(\mathbf{K},\mathbf{K}_i,\omega_c), \tag{2.61}$$

$$\hat{\alpha} = \mathbf{K}/K, \text{ and } \hat{\alpha}_i = \mathbf{K}_i / K_i \tag{2.62}$$

into Eq. (2.60) yields

$$I_2(\mathbf{r},t) \cong \int d^2R' \, \frac{\sigma_{12}(\hat{\alpha},\hat{\alpha}_i)}{|\mathbf{r}-\mathbf{r}'|^2} \mathrm{e}^{-2\,\mathrm{Im}(k_2)|\mathbf{r}-\mathbf{r}'|} \, g^2(t - t_d). \tag{2.63}$$

The interpretation of σ_{12} as a differential cross section will be justified later in this section. Since $\mathbf{K} = k_1(\mathbf{R}-\mathbf{R}')/(\nu r_d)$, t_1, t_2, g, and therefore P and $\not{P}$ are functions of $|\mathbf{R}-\mathbf{R}'|$. Note that the CW result follows from Eq. (2.63) by simply setting $g(t-t_d)=1$. For this case of an arbitrarily narrowband source signal, the result in Eq. (2.50) for the mean square incoherent field is exact, and Eq. (2.63) approaches the exact result at distances at least a few wavelengths from the interface, where the evanescent waves contribute very little to the mean square incoherent field.

Although the mean square incoherent field scattered into the water, $I_1(\mathbf{r},t)$, is similarly derived, the corresponding expression for $I_1(\mathbf{r},t)$ is most easily obtained as a special case of Eq. (2.63) by substituting medium 1 parameters for medium 2 parameters. For example, k_1 is substituted for k_2, β_1 for $\kappa\beta_2$, etc. For this special case, Eq. (2.63) simplifies to

$$I_1(\mathbf{r},t) \cong \int d^2R' \frac{\sigma_{11}(\hat{\alpha},\hat{\alpha}_i)}{|\mathbf{r}-\mathbf{r}'|^2} g_{11}^2(t-t_d), \tag{2.64}$$

where from Eq. (2.61)

$$\sigma_{11}(\hat{\alpha},\hat{\alpha}_i) = k_1^2 \sin^2(\theta_2)\left|\mathcal{C}_{11}(\mathbf{K},\mathbf{K}_i,\omega_c)\right|^2. \tag{2.65}$$

In this case, θ_2 is also the scattered field grazing angle measured from the mean horizontal plane, $|z|/r_d = \sin(\theta_2)$. Again, the quantity $\mathcal{C}_{11}$ is found from the relation (Eq. 2.38)

$$\mathcal{C}_{11}(\mathbf{K},\mathbf{K}_i,\omega_c)\delta(\mathbf{K}-\mathbf{K}'') \equiv \left\langle \tilde{T}_{11}(\mathbf{K},\mathbf{K}_i,\omega_c)\tilde{T}_{11}^*(\mathbf{K}'',\mathbf{K}_i,\omega_c)\right\rangle. \tag{2.66}$$

There is no loss in this case: $\not{P}=0$, and therefore,

$$g_{11}^2(t) \equiv \left|\frac{1}{2\pi}\int d\omega' U(\omega') e^{-i\omega' t} e^{-i\omega'^2 P_{11}/4}\right|^2, \tag{2.67}$$

$$P_{11} \equiv \left(2/B_{11c}^3\right)\left(\omega_c K \cos\theta_i \cos\phi / c_1^3 - \left(K/c_1\right)^2\right), \tag{2.68}$$

and

$$B_{1c}(K) \equiv k_1 \beta_1(K, \omega_c). \tag{2.69}$$

Note that t_d is still given by Eq. (2.51), but the propagation time from the surface patch to the receiver/observation point above the interface is a real quantity.

$$t_2 = \frac{z/c_1}{\beta_1(K, \omega_c)}. \tag{2.70}$$

As given in Voronovich (1994), the quantity $\sigma_{11}(\hat{\alpha}, \hat{\alpha}_i)$ in Eq. (2.65) is actually the differential cross section defined in Ishimaru (1978b).

$$\sigma_{11}(\hat{\alpha}, \hat{\alpha}_i) = \frac{|\mathbf{r} - \mathbf{r}'|^2}{\Delta A} \frac{\left\langle |\tilde{\psi}_f|^2 \right\rangle}{|\psi_i|^2}, \tag{2.71}$$

where ψ_i is a plane-wave field incident on a surface patch of area ΔA, and $\hat{\alpha}_i$ is the unit vector in the direction of propagation of the incident field; $\tilde{\psi}_f$ is the scattered coherent field at a long distance $|\mathbf{r} - \mathbf{r}'|^2$ from the interface, in the direction denoted by the unit vector, $\hat{\alpha}$. Similarly, σ_{12} is the differential cross section relating the mean square incident field to the mean square scattered incoherent field in medium 2 (the sediment), defined as

$$\sigma_{12}(\hat{\alpha}, \hat{\alpha}_i) = \frac{|\mathbf{r} - \mathbf{r}'|^2}{\Delta A} \frac{\left\langle |\tilde{\psi}_{2-}|^2 \right\rangle}{|\psi_i|^2} e^{2\,\mathrm{Im}(k_2)|\mathbf{r} - \mathbf{r}'|}, \tag{2.72}$$

where $\tilde{\psi}_{2-}$ is the incoherent field at the receiver in the sediment, a distance $|\mathbf{r} - \mathbf{r}'|$ from the surface patch, and the unit vector $\hat{\alpha}$ represents the transverse direction of the scattered field in the lower medium. The result given in Eq. (2.63) (or Eq. 2.64) is remarkable, as the differential cross section is a far-field entity. Close inspection of Eq. (2.63) shows that it is the sonar equation when $u(t)$ is

substituted for $g(t)$, in which the mean square scattered incoherent field is obtained by integrating the differential cross section over the interface with appropriate attenuation due to spreading and sediment loss. Equations (2.38) and (2.61) are a convenient way to find σ_{12} in theoretical developments; Eqs. (2.65) and (2.66) are a convenient way to find σ_{11}.

2.3.3 Dispersion of a Gaussian input pulse

Two types of pulse dispersion occur in this problem. One type is simply due to scattering and is treated by the integral in Eq. (2.63) over the scattering surface. The other type of dispersion is due to the frequency dependence of the propagation constant and is embodied in Eq. (2.49). This subsection focuses on the latter form of dispersion. Consider the case of a pulse with a peak pressure, p_{peak}, and Gaussian envelope,

$$u(t) = p_{\text{peak}}\, \mathrm{e}^{-t^2/t_s^2}. \tag{2.73}$$

Its Fourier transform is given by

$$U(\omega) = p_{\text{peak}} t_s \sqrt{\pi}\, \mathrm{e}^{-t_s^2 \omega^2/4}. \tag{2.74}$$

The parameter t_s is chosen to vary the width of this input pulse, and therefore the pulse bandwidth and energy. Substituting Eq. (2.74) into Eq. (2.49) (see Appendix B) and integrating over ω' and ω'' yields

$$g^2(t) = p_{\text{peak}}^2 \frac{t_s^2}{q' q''} \mathrm{e}^{-t^2/q'^2}\, \mathrm{e}^{-\left(t^* + 2tP/q'^2\right)^2 / q''^2}, \tag{2.75}$$

where

$$q' \equiv \sqrt{t_s^2 + iP}, \tag{2.76}$$

$$q'' \equiv \sqrt{t_s^2 - iP''}, \tag{2.77}$$

and

$$P'' \equiv P^* - i(2\not{P}/q')^2, \tag{2.78}$$

Substituting Eqs. (2.76) and (2.77) into Eq. (2.75), and simplifying, yields an expression equivalent to Eq. (2.75):

$$g^2(t) = p_{\text{peak}}^2 \frac{t_s^2}{\sqrt{\left|t_s^2 - iP^*\right|^2 - (2\not{P})^2}} \exp\left(\frac{-2\,\text{Re}\left\{\left(t_s^2 - iP^*\right)t^2\right\}}{\left|t_s^2 - iP^*\right|^2 - (2\not{P})^2} \right). \tag{2.79}$$

As mentioned, $\text{Re}(t_d) = \text{Re}(t_2) + t_1$ represents the propagation delay of the pulse. The imaginary part of t_2 is a result of modeling the sediment as lossy. Since higher frequency signals are attenuated more than lower frequency signals, the lower frequency components of a narrowband signal will be less attenuated than the center frequency. The imaginary component of t_2, along with $\not{P}$, and the imaginary component of P compensate for typically excessive loss in the CW loss term — the exponential term in Eq. (2.50) or Eq. (2.63). In addition, P is a frequency dispersion term that results in pulse broadening of the signal below the rough interface. Note that for the zero loss case, the parameter $\not{P} = 0$. The effect of loss and the parameters P and $\not{P}$ is seen in Fig. 2.3 for $g^2(t - t_d)$ from Eq. (2.79) evaluated at

$$g^2(t - t_d)\Big|_{t=\text{Re}(t_d)} = g^2(-t_{2i}), \quad t_{2i} = \text{Im}(t_d) = \text{Im}(t_2) \tag{2.80}$$

and plotted as a function of scattered grazing angle. In Fig. 2.3, the pulse length parameter, t_s, is equal to two periods of the center, or carrier, frequency for both cases shown. When the loss and dispersion are small, $|g(-t_{2i})|$ approaches $u(0) = 1$. The smaller the scattered grazing angle, the greater the dispersion, and the smaller one would expect the pulse peak amplitude. However, the loss of the CW signal represented by the term $e^{-2\,\text{Im}(k_2)|\mathbf{r}-\mathbf{r}'|}$ is greater than the loss of the

narrowband signal, and the propagation distance becomes large for small scattered grazing angles (z is fixed). Even though there is dispersion, the loss for the narrowband case is significantly less than the CW case, and $|g(-t_{2i})|>1$. In the case of Fig. 2.3, with depth of 0.3 m, $|g(-t_{2i})|$ is greater than one for very small grazing angles since the propagation distance becomes very large. An example with zero loss always has $P''=P^*$ and $t_{2i}=0$, and it is always true that $|g(0)|\leq 1$.

2.4 Applications and calculations

Although the theoretical results in this dissertation are general and include scattering back into the water, the examples deal with scattering through a rough fluid-fluid interface ($z<0$). Both plane-wave and point sources are considered, and the mean square scattered incoherent field is computed for both the flat surface case and the rough surface case.

In the examples of the following section, the mean square scattered field in medium 2 is divided into coherent and incoherent parts. The incoherent component is treated using first-order perturbation theory, and the coherent component is treated in zeroth order — the flat surface solution is used. There is a slight inconsistency in this approach, in that the mean square incoherent field is proportional to the second power of k_1h, while the square of the coherent field magnitude is only computed to an accuracy of zeroth order. As Rice (1951) has shown, the square of the coherent field magnitude to second order in k_1h is obtained by subtracting the power carried by the mean square incoherent field. For small k_1h, this correction is necessarily slight. In chapter 5, the second-order perturbation scattered field and second-order coherent field are derived.

2.4.1 Continuous plane wave source

The contribution of the evanescent waves to the field scattering through a rough interface is shown in the following CW incident plane wave examples. In Fig. 2.4a, the first-order field penetrating through a rough interface, with roughness spectrum given in Eq. (3.66) and $k_1 h = 0.2545$, is calculated using Eqs. (3.70) in Eq. (2.50) and setting $g(t - t_d) = 1\text{Pa}$. The solid line in the plot represents the first-order result including evanescent waves, and the dashed line is the first-order result excluding evanescent waves, which is the result in Eq. (2.63). Since the grazing angle in this example is below critical, the zero-order field (dotted line) is evanescent. Near the interface, the mean square incoherent field decays with increasing depth at a rate comparable to the square of the magnitude of the zero-order field, but decays at a rate dictated by the sediment loss farther from the interface. Including the evanescent waves ($K > k_1/\nu$) does not make a significant difference at a distance greater than about a wavelength (7.5 cm) below the interface. The sediment parameters used in the plot in Fig. 2.4b are the same as Fig. 2.4a, except the roughness parameters are chosen such that $k_1 h = 1.0$. Perturbation theory is shown valid for $k_1 h = 1$ by Thorsos (1996a) for scattering through a rough interface with truncated power-law roughness spectrum. In this case, including the evanescent waves of the integral ($K > k_1/\nu$) does not make a significant difference at a distance greater than about 12cm below the interface.

These examples show that including the evanescent waves in the calculation of the first-order mean square incoherent field is only necessary close to the interface, and the contribution of evanescent waves to the mean square incoherent field is dependent on the interface roughness. It is important to note that in the region below the interface where the incoherent evanescent contribution is significant, the zero-order coherent contribution to the mean square field is typically much greater.

2.4.2 Mean square incoherent field due to a point source

Starting with the plane wave result in Eq. (2.63) and expressing the 2-D integral in terms of a summation over the interface yields

$$I_2(\mathbf{r},t) \cong \Delta A \sum_{n} \frac{\sigma_n\left(\hat{\alpha}_{fn},\hat{\alpha}_i\right)}{r_{2n}^2} g^2\left(t - t_{1n} - t_{2n}\right) e^{-2\,\mathrm{Im}(k_2) r_{2n}}\,, \tag{2.81}$$

where

$$r_{2n} = \left|\mathbf{r} - \mathbf{r}_n'\right| \tag{2.82}$$

is the distance from surface patch n at position $\mathbf{r}_n'$ of size ΔA to the observed field point, $\mathbf{r}$, and

$$\hat{\alpha}_{fn} = \frac{\mathbf{R} - \mathbf{R}'}{\left|\mathbf{R} - \mathbf{R}'\right|}. \tag{2.83}$$

The propagation time from this surface patch to the receiver, $\mathrm{Re}(t_{2n})$, is also given by

$$\mathrm{Re}(t_{2n}) = r_{2n}/c_2\,. \tag{2.84}$$

As the area of each surface patch, ΔA, approaches zero, the summation in Eq. (2.81) approaches the exact integral in Eq. (2.63).

An expression for the first-order mean square field below the interface due to a point source follows heuristically from Eq. (2.81). Here, the surface patch (area ΔA) is chosen sufficiently small in relation to the distance, r_{1n}, from the point source to surface patch n, to ensure that the field incident on the interface is a plane wave. However, the size of this patch cannot be chosen arbitrarily small, and the distance between the source and interface is therefore constrained to be greater than some minimum value. Limitations of this approximation remain an issue. The scattered or penetrating mean square incoherent field is given by

$$I_2(\mathbf{r},t) \cong \Delta A \sum_n \frac{\sigma_n\left(\hat{\alpha}_{fn},\hat{\alpha}_{in}\right)}{r_{1n}^2 r_{2n}^2} r_0^2 g^2(t-t_{dn}) e^{-2\,\mathrm{Im}(k_2) r_{2n}}, \tag{2.85}$$

where

$$\hat{\alpha}_{in} = \frac{\mathbf{R}_n' - \mathbf{R}_s}{|\mathbf{R}_n' - \mathbf{R}_s|}, \tag{2.86}$$

$\mathbf{R}_s$ is the transverse coordinate vector of the source, $g(t)$ is the pressure at 1 m from the source, and $r_0 = 1\,\mathrm{m}$. The total propagation time is given by the real part of

$$t_{dn} = \frac{r_{1n}}{c_1} + t_{2n}, \tag{2.87}$$

with

$$r_{1n} = \sqrt{|\mathbf{R}_n' - \mathbf{R}_s|^2 + z_s^2}. \tag{2.88}$$

When the approximation $g(t) = u(t)$ is made, Eq. (2.85) is in the form of a convolution with reduced computation time.

Using the expression for the first-order differential cross section given in Eq. (3.77), the approximate mean square incoherent field pulse in lossy sediment below a rough interface due to a Gaussian narrowband point source above the interface is found for two cases. In Fig. 2.5a, the time-dependent mean square incoherent field at a position below a rough interface in a lossy medium due to a point source is found using Eq. (2.79) for $g^2(t)$ in Eq. (2.85), and is compared to the result obtained setting P and $\hat{P}$ to zero — $g(t) = u(t)$. Although the resulting pulse shapes are close in magnitude, as well as peak arrival time, using $g(t)$ does result in an incoherent pulse that has a smaller peak magnitude. In this example, the parameter t_s in Eq. (2.73) is equal to two cycles of the center frequency of $f_c = 20\,\mathrm{kHz}$. This frequency results in $k_1 h = 0.25$, which is within the region of accuracy for first-order perturbation theory (Thorsos and Jackson,

1989; Thorsos, 1990; Thorsos, 1996a). In Fig. 2.5b, the point source is farther from the interface, but the incident angle is the same. The incident grazing angle is defined here to be the angle between the mean surface and the line containing the source and receiver points.

2.4.3 Zero-order calculations

Setting

$$\Psi_{2-}(\mathbf{K}) = \mathrm{T}(\mathbf{K})\Psi_i(\mathbf{K}) \tag{2.89}$$

and

$$\Psi_i(\mathbf{K}) = \frac{ir_0 U}{2\pi k_1 \beta_1(\mathbf{K})} \mathrm{e}^{-i\mathbf{K}\cdot\mathbf{R}_s} \mathrm{e}^{ik_1\beta_1(\mathbf{K})z_s} \tag{2.90}$$

in Eq. (2.9) results in an expression for the field penetrating a flat fluid-fluid interface due to a point source at $(\mathbf{R}_s, z_s)$ with unit pressure magnitude at $1\,\mathrm{m}$ from the source. The quantity U has unit magnitude and dimensions of pressure $\times$ time. The resulting integral simplifies to

$$\psi_{2-}(\mathbf{r}) = i\int_0^\infty dK \frac{K\mathrm{T}(\mathbf{K})Ur_0}{k_1\beta_1(\mathbf{K})} \mathrm{e}^{i(z_s k_1\beta_1(\mathbf{K}) - z k_2\beta_2(\mathbf{K}))} J_0(KR), \tag{2.91}$$

where J_0 is the Bessel function of order zero. For comparison purposes, the square of the time-dependent zero-order, or flat-surface coherent field magnitude,

$$I(\mathbf{r},t) = \left| \int_{-\infty}^{\infty} d\omega U(\omega) r_0 \mathrm{e}^{-i\omega t} \int_0^\infty dK \frac{K\mathrm{T}(\mathbf{K})}{k_1\beta_1(\mathbf{K})} \mathrm{e}^{i(z_s k_1\beta_1(\mathbf{K}) - z k_2\beta_2(\mathbf{K}))} J_0(KR) \right|^2, \tag{2.92}$$

is plotted in Fig. 2.6a along with the time-dependent first-order mean square incoherent field using the same parameters as in Fig 2.5a. In this example, the incident field is below the critical angle. Although the zero-order component can

be approximated from Eq. (2.91) using the method of stationary phase to solve the resulting integral (see for example Brekhovskikh, 1980; Ishimaru, 1991) when the incident field is above the critical angle, a numerical method is more suitable when the incident grazing angle is close to critical (Westwood, 1989). Figure 2.6a shows an "exact" solution of the square of the flat-surface transmitted coherent field magnitude, along with the first-order mean square incoherent field from Fig. 2.5a. For this example, the zero-order coherent pulse arrives earlier and with greater magnitude than the first-order incoherent pulse. In Fig. 2.6b, the source is moved farther from the surface than the previous two examples. Even though the sediment parameters, receiver point, and incident angle (the angle between the mean surface and the line containing the source and receiver points) are unchanged from Fig. 2.6a, the incoherent first-order pulse is greater in magnitude than the zero-order pulse. As the source is moved further from the surface, the stationary phase path for the zero-order pulse is longer, and the zero-order pulse amplitude is more attenuated in the lossy sediment. Since Fig. 2.4 is a plane wave CW version of this same example, one would expect that the first-order mean square incoherent field would be greater than the zero-order field squared for the source point far from the rough interface.

2.5 Summary

A general analytic expression for the time-dependent narrowband mean square incoherent field scattered from and through a fluid-fluid rough interface is expressed in terms of the second moment of the T-matrix, and in terms of the differential cross section. This result is valid for narrowband source signals when the T-matrix correlation function is a slowly varying function of frequency over the source signal frequencies. Using the exact CW incident plane wave result, along with first-order perturbation theory, and sediment parameters characteristic of a sandy seafloor, we show that the evanescent component of the scattered

incoherent field in the sediment becomes insignificant about a wavelength from the surface, depending on the surface roughness. These examples show that the expression in terms of the differential cross section is valid except within one or two (depending on the roughness spectrum) wavelengths of the surface. This result is surprising since the differential cross section is a far field entity.

The above formalism applied to the scattering through a rough surface shows the effect of roughness on penetration through a surface. When the grazing angle of a plane wave incident field is below the critical angle in relation to the mean surface, the zero-order component of the transmitted field is evanescent, and does not penetrate deeply into the seafloor. Higher order components contain downward traveling waves, which can increase the depth of penetration of sound relative to the flat-surface case (Moe and Jackson, 1994b; Moe *et al.*, 1995).

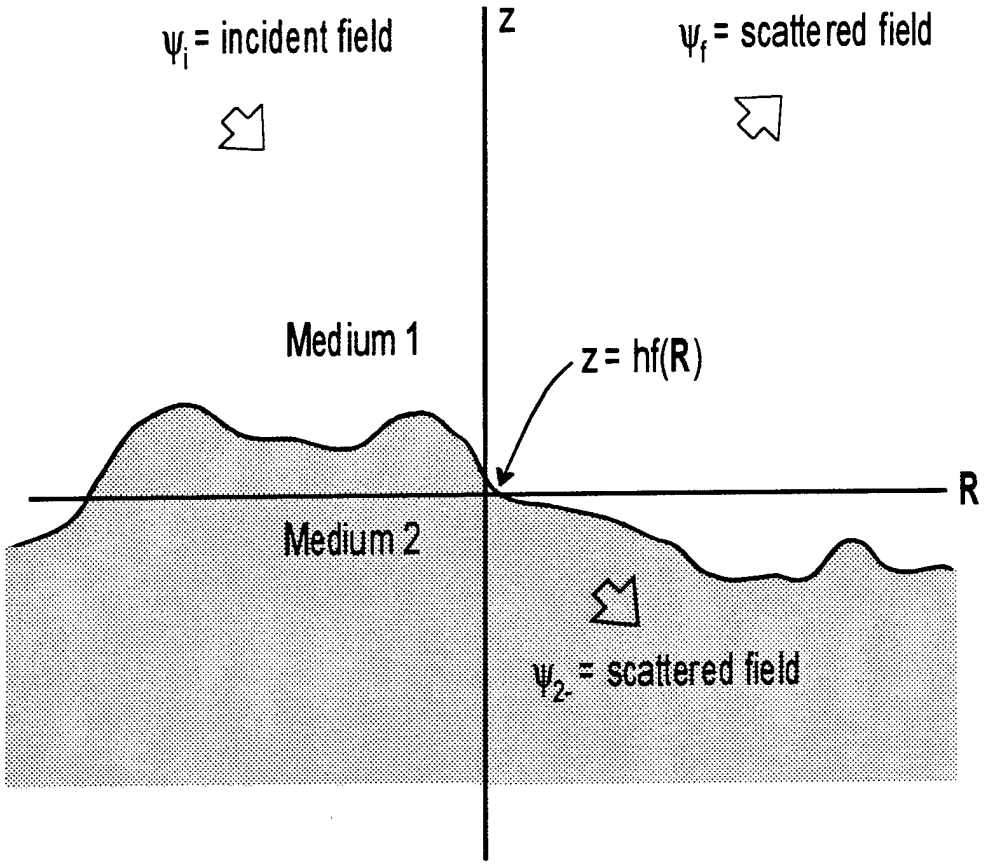

Figure 2.1 : Scattering problem geometry for rough interface separating a lossless fluid in medium 1 $(z > hf(\mathbf{R}))$ from a lossy fluid in medium 2 $(z < hf(\mathbf{R}))$. This diagram can be viewed as a slice through a two-dimensional surface.

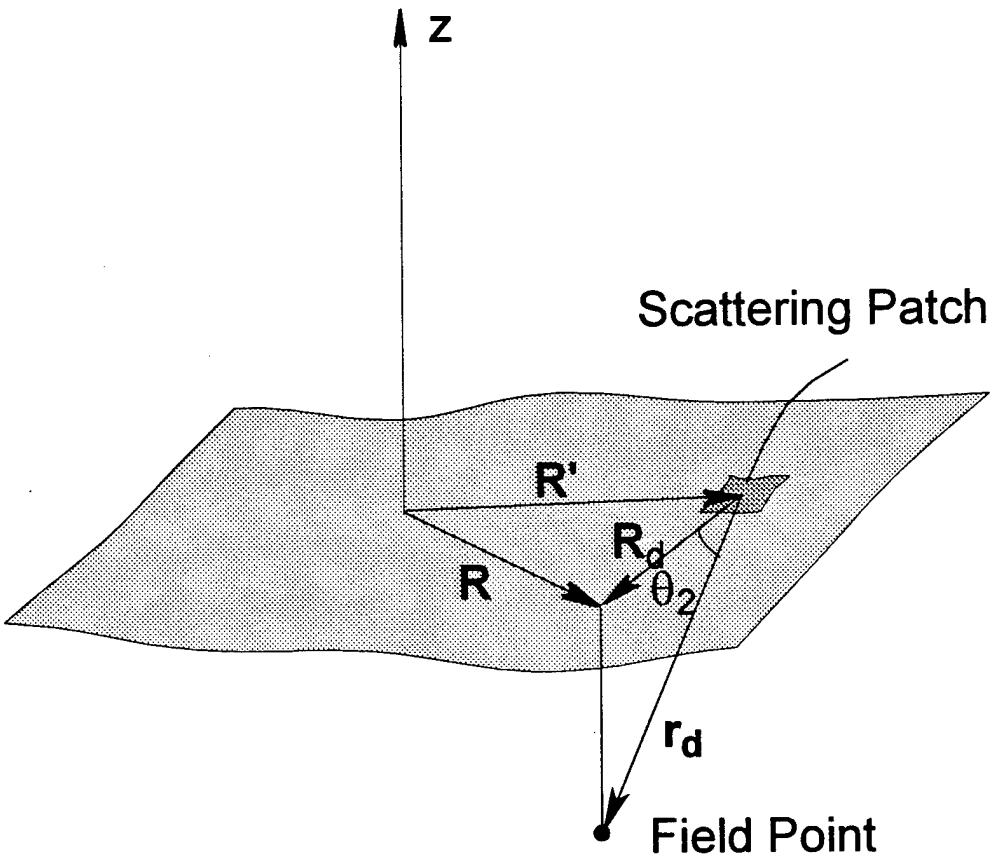

Figure 2.2 : Diagram describing transverse position variables.

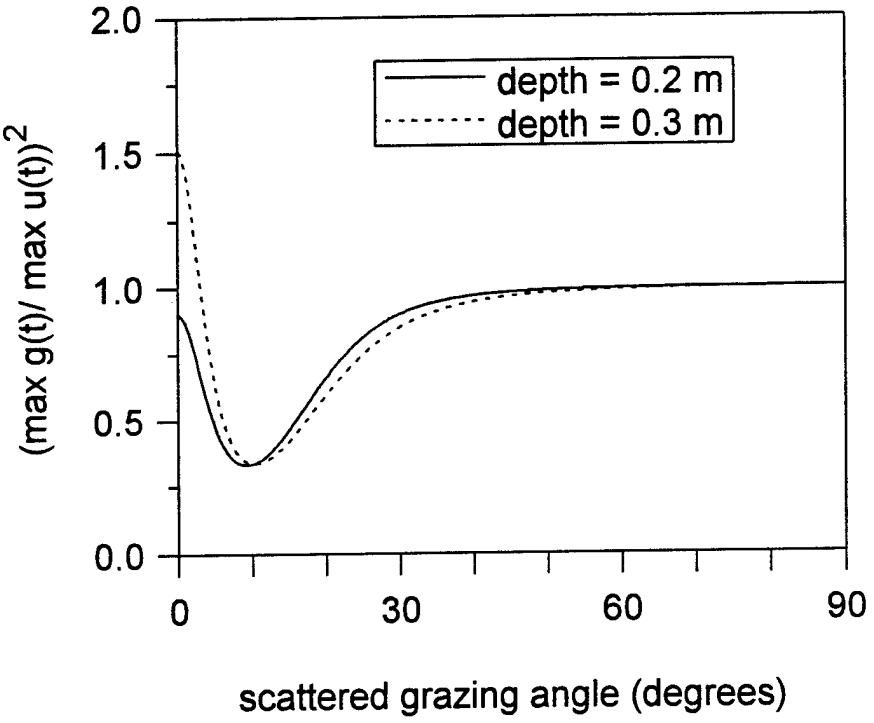

Figure 2.3 : Illustration of effect of dispersion on peak mean square incoherent field. Peak of $g^2(t)$, normalized with respect to $\max\left(u^2(t)\right)$ as a function of grazing angle. $\delta = 0.0163$, $f = 20\,\text{kHz}$, $c_1 = 1500\,\text{m s}$, $\nu = 1.13$, $t_s = 100\mu s$.

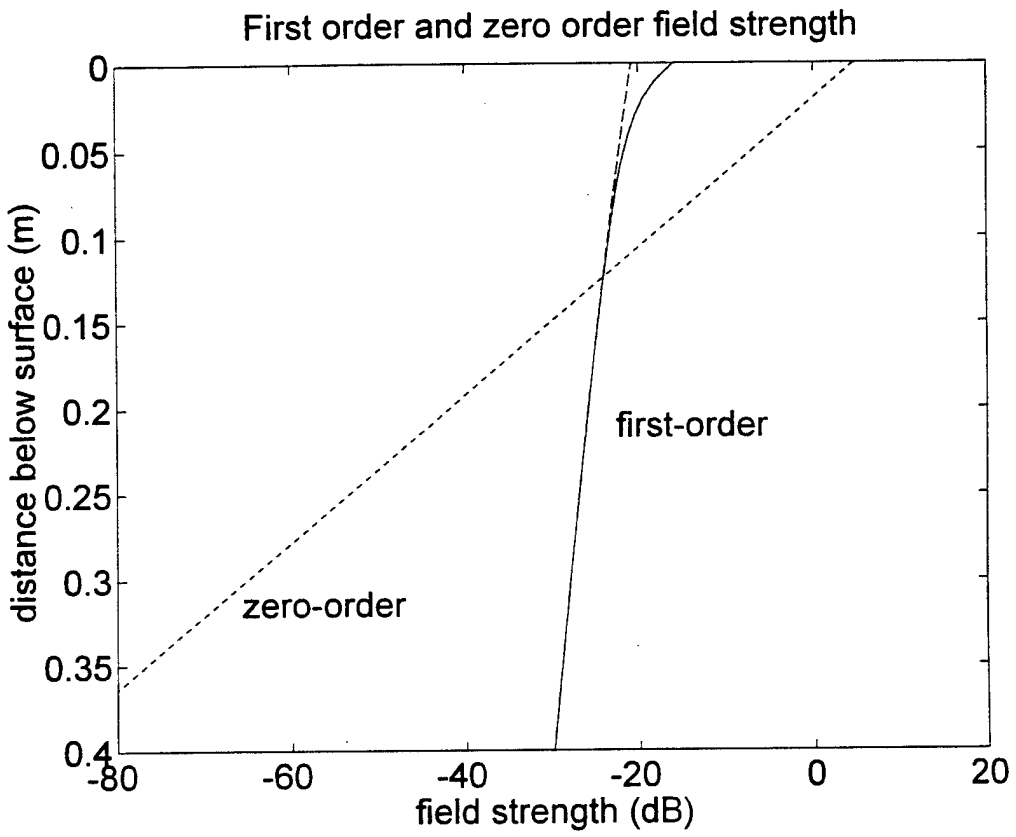

Figure 2.4a : First-order and zero-order field strength as a function of depth. Field strength is given in dB with respect to incident pressure. Solid line includes evanescent component in first-order calculation, dashed line does not include evanescent component in first-order calculation. Incident angle is 20°. Critical angle is 27.75°, $f = 20\,\text{kHz}$, $a = 0.1\,\text{m}$, $\gamma = 3$, $w_2 = 2\times10^{-5}\,\text{m}$, $\rho = 2$, $\delta = 0.019$, $c_1 = 1500$ m/s, $\nu = 1.13$, $k_1 h = 0.254$.

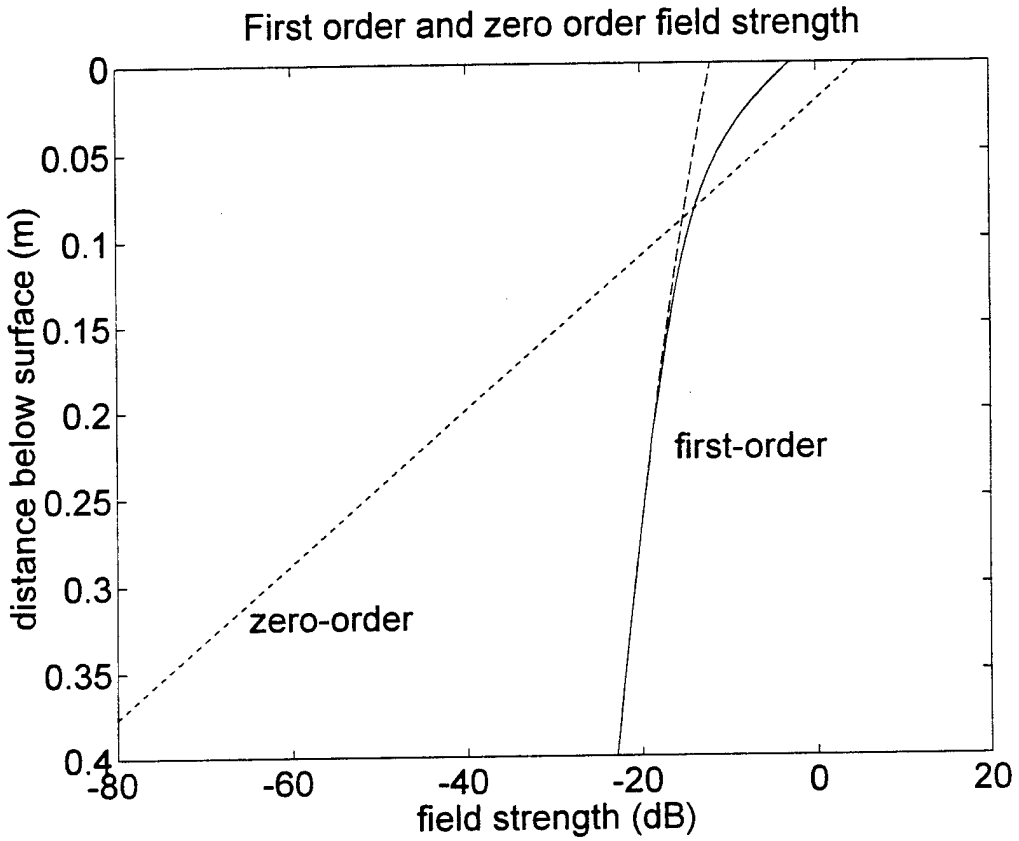

Figure 2.4b : First-order and zero-order field strength as a function of depth. Field strength is given in dB with respect to incident pressure. Solid line includes evanescent component in first-order calculation, dashed line does not include evanescent component in first-order calculation. Incident angle is 20°. Critical angle is 27.75°, $f = 20\,\text{kHz}$, $a = 0.5\,\text{m}$, $\gamma = 3$, $w_2 = 6.2 \times 10^{-5}\,\text{m}$, $\rho = 1.96$, $\delta = 0.0163$, $c_1 = 1500$ m/s, $\nu = 1.126$, $k_1 h = 1.00$.

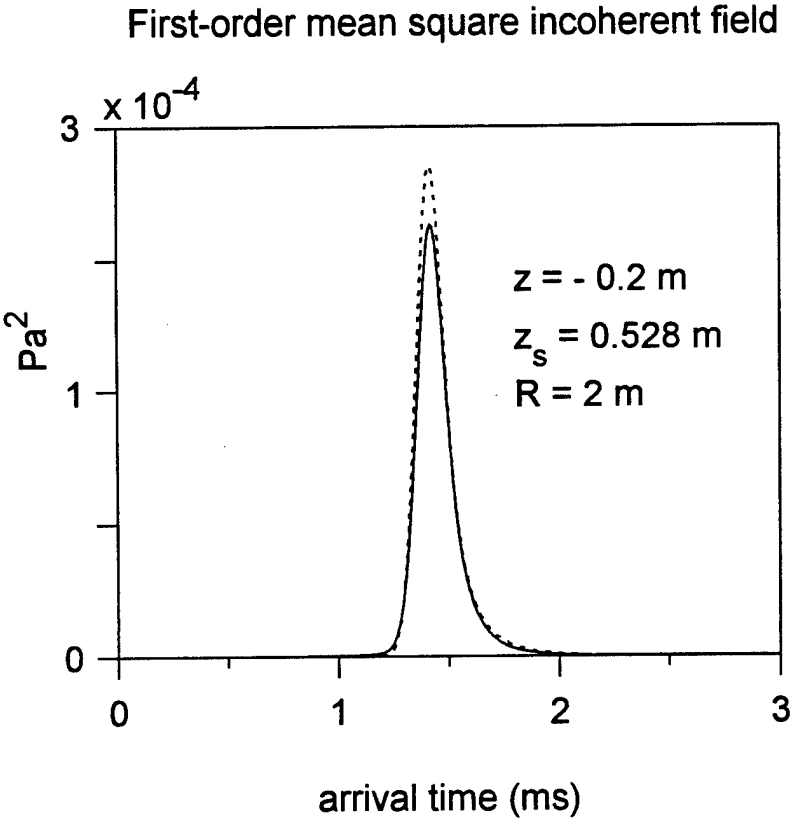

Figure 2.5a : Time-dependent mean square incoherent field at depth $0.2\,\mathrm{m}$ below the mean interface. Point source height above interface is $0.528\,\mathrm{m}$; transverse distance between source and receiver: $2\,\mathrm{m}$. Source frequency = $20\,\mathrm{kHz}$, $t_s = 100\mu s$. Solid line uses Eq. 2.85; dotted line is obtained from setting $g(t) = u(t)$. Same sediment parameters and incident angle as Fig. 2.4a.

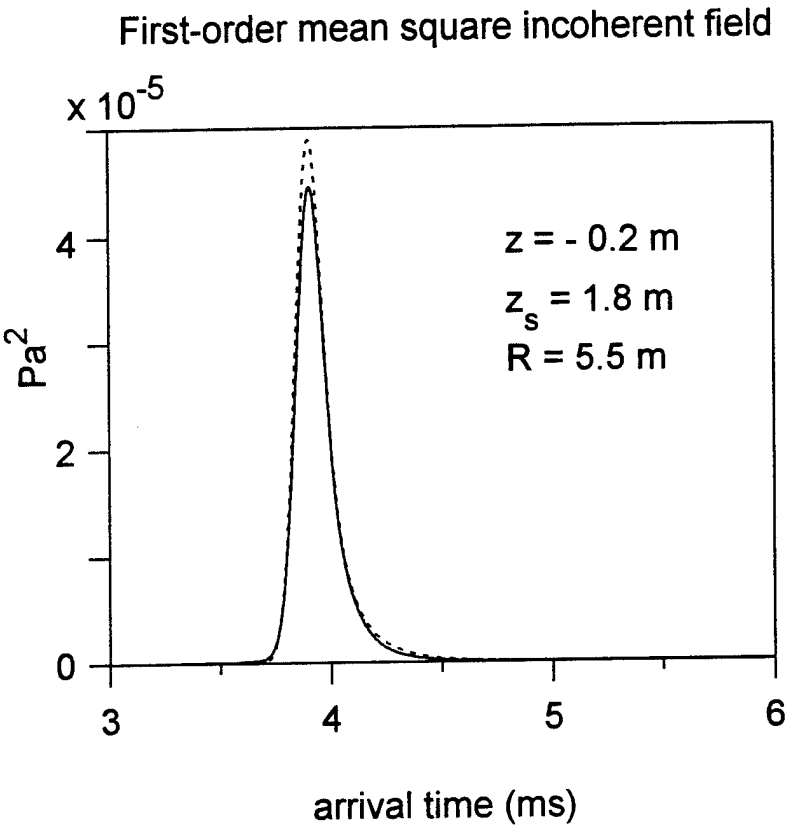

Figure 2.5b : Time-dependent mean square incoherent field at depth $0.2\,\mathrm{m}$ below the mean interface. Point source height above interface is $5.5\,\mathrm{m}$; transverse distance between source and receiver: $2\,\mathrm{m}$. Source frequency = $20\,\mathrm{kHz}$, $t_s = 100\mu s$. Solid line uses Eq. 2.85; dotted line is obtained from setting $g(t) = u(t)$. Same sediment parameters and incident angle as Figs. 2.4a, 2.5a.

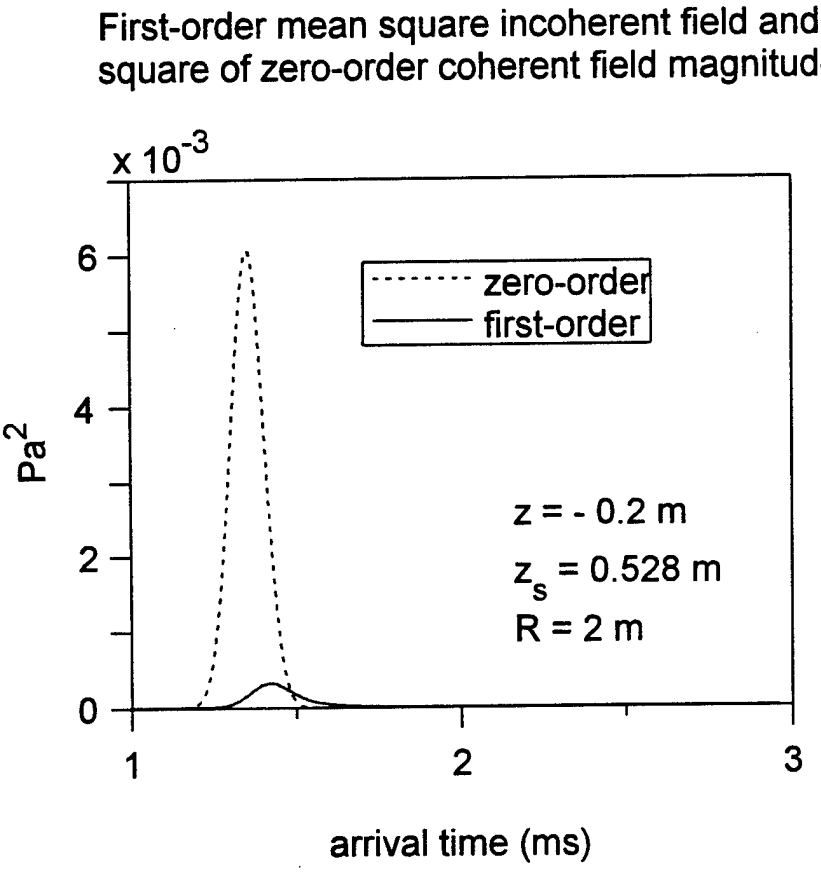

Figure 2.6a : Square of zero-order coherent field magnitude shown with dotted line, first-order mean square incoherent field shown with solid line. All parameters identical to Fig. 2.5a.

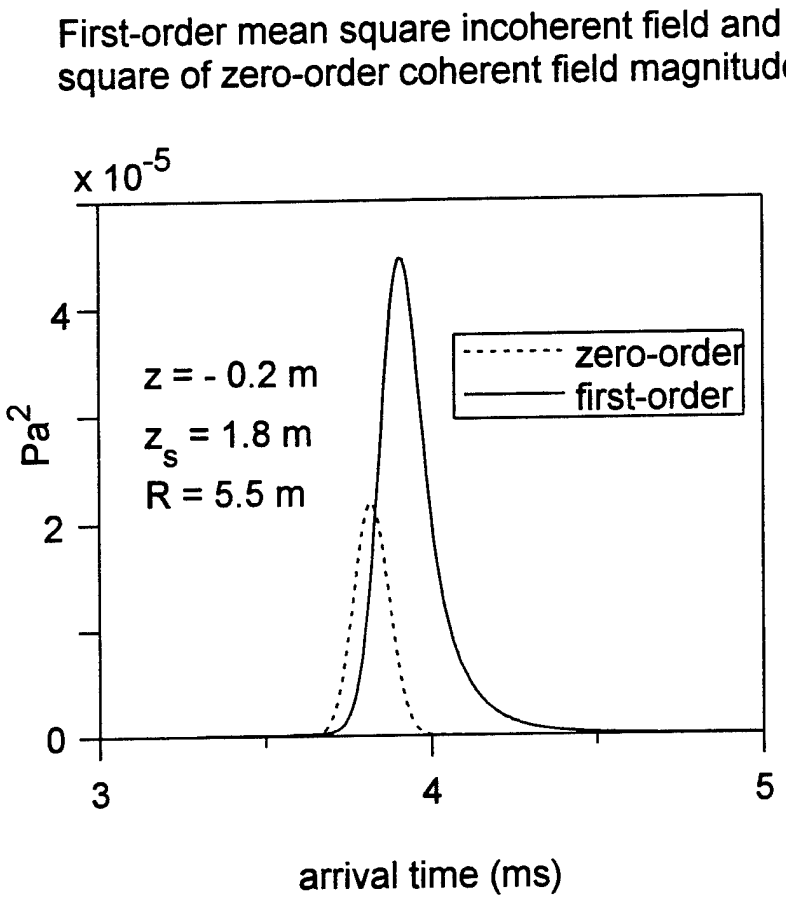

Figure 2.6b : Square of zero-order coherent field magnitude shown with dotted line, first-order mean square incoherent field shown with solid line. All parameters identical to Fig. 2.5b.

CHAPTER 3

First-order perturbation solution for rough fluid-fluid interface

3.1 Introduction to chapter 3

In the numerical computations in chapter 2, and in the simulation in chapter 4, the water above the seafloor is modeled as a homogenous fluid, and the sediment is modeled as a lossy homogenous fluid. The rough interface between the water and sediment is modeled as a 2-D random process with a truncated power-law roughness spectrum. The first-order fluid-fluid perturbation results used in chapters 2 and 4 are derived in this chapter. The power-law filter used in chapters 2 and 4 is also discussed in this chapter.

Perturbation derivations are also given in chapter 5. However, the derivations in chapter 5 allow the sediment bulk properties below the lowest point on the interface to be arbitrarily stratified, and the approach allows evaluation of higher orders. The goal of this chapter is to obtain the zero-order coherent field and the first-order incoherent field for the fluid-fluid rough interface problem with homogenous half spaces. In addition to derivation of an expression for the field scattered back into the water as in Kuo (1964) and Mourad and Jackson (1989), a solution for the field scattered into the sediment is also derived. Although the results in this chapter are derived for the two homogenous fluid case, the form of the first-order scattered field solution derived in this chapter is shown to be more general in chapter 5.

3.2 Scattering problem description

A 2-D slice of the 3-D scattering problem is shown in Fig. 2.1. An arbitrary pressure field, $\psi_i(\mathbf{r})$, is incident on a 2-D rough interface, $z = hf(\mathbf{R})$, separating

the homogenous lossless fluid in medium 1 (water) from a homogenous lossy fluid in medium 2 (sediment), resulting in the pressure field, $\psi_f(\mathbf{r})$, scattered back into the water and the pressure field, $\psi_{2-}(\mathbf{r})$, scattered into the sediment. The mean of $f(\mathbf{R})$ is taken to be zero for convenience and without loss of generality. Substituting the plane wave representations (Devaney and Sherman, 1973) for the field above the interface (Eqs. 2.5 and 2.6) and the field below the interface (Eq. 2.9) into the equation for the continuity of pressure (Eq. 2.3) yields

$$\int d^2K\left[\Psi_i(\mathbf{K})\mathrm{e}^{-ik_1\beta_1(\mathbf{K})f(\mathbf{R})}+\Psi_f(\mathbf{K})\mathrm{e}^{ik_1\beta_1(\mathbf{K})f(\mathbf{R})}\right]\mathrm{e}^{i\mathbf{K}\cdot\mathbf{R}}$$

$$=\int d^2K\Psi_{2-}(\mathbf{K})\mathrm{e}^{-i\kappa k_1\beta_2(\mathbf{K})f(\mathbf{R})}\mathrm{e}^{i\mathbf{K}\cdot\mathbf{R}}. \tag{3.1}$$

Substituting the plane wave representations for incident and scattered fields into the equation for continuity of normal velocity (Eq. 2.4) yields

$$\begin{aligned}
&\frac{1}{\rho_1}\int d^2K k_1\beta_1(\mathbf{K})\left[-\Psi_i(\mathbf{K})\mathrm{e}^{-ik_1\beta_1(\mathbf{K})hf(\mathbf{R})}+\Psi_f(\mathbf{K})\mathrm{e}^{ik_1\beta_1(\mathbf{K})hf(\mathbf{R})}\right]\mathrm{e}^{i\mathbf{K}\cdot\mathbf{R}}\\
&-\frac{1}{\rho_1}\int d^2K\mathbf{K}\cdot\nabla(hf(\mathbf{R}))\left[\Psi_i(\mathbf{K})\mathrm{e}^{-ik_1\beta_1(\mathbf{K})hf(\mathbf{R})}+\Psi_f(\mathbf{K})\mathrm{e}^{ik_1\beta_1(\mathbf{K})hf(\mathbf{R})}\right]\mathrm{e}^{i\mathbf{K}\cdot\mathbf{R}}\\
&=-\frac{1}{\rho_2}\int d^2K k_2\beta_2(\mathbf{K})\Psi_{2-}(\mathbf{K})\mathrm{e}^{-i\kappa k_1\beta_2(\mathbf{K})hf(\mathbf{R})}\mathrm{e}^{i\mathbf{K}\cdot\mathbf{R}}\\
&-\frac{1}{\rho_2}\int d^2K\mathbf{K}\cdot\nabla(hf(\mathbf{R}))\Psi_{2-}(\mathbf{K})\mathrm{e}^{-i\kappa k_1\beta_2(\mathbf{K})hf(\mathbf{R})}\mathrm{e}^{i\mathbf{K}\cdot\mathbf{R}}
\end{aligned} \tag{3.2}$$

where the unit vector normal to the interface in Eq. (2.4) is given by

$$\hat{n}=\frac{\hat{z}-\nabla hf(\mathbf{R})}{|\hat{z}-\nabla hf(\mathbf{R})|}, \tag{3.3}$$

and ∇ represents the gradient over the transverse coordinates.

$$\nabla f=\frac{\partial f}{\partial x}\hat{x}+\frac{\partial f}{\partial y}\hat{y}. \tag{3.4}$$

Since $\delta << 1$, the expressions in Eqs. 3.1 and 3.2 are valid (Landau and Lifshits, 1987).

The plane wave representation for the field scattered from the interface, given in Eq. (2.5), represents the scattered field above the highest point of the interface. Likewise, the plane wave representation for the field scattered through the interface, given in Eq. (2.9), represents the scattered field below the lowest point of the interface. Using Eqs. (2.5) and (2.9) to represent the field on the interface, $z = hf(\mathbf{R})$, in Eqs. (3.1) and (3.2) invokes the Rayleigh hypothesis (e.g., Jackson, Winebrenner, and Ishimaru, 1988).

The goal of this chapter is to find the scattered field in terms of the incident field. Since

$$\Psi_f(\mathbf{K}) = \int d^2K' T_{11}(\mathbf{K},\mathbf{K}')\Psi_i(\mathbf{K}'), \tag{3.5}$$

and

$$\Psi_{2-}(\mathbf{K}) = \int d^2K' T_{12}(\mathbf{K},\mathbf{K}')\Psi_i(\mathbf{K}'), \tag{3.6}$$

the scattering problem is solved when the T-matrices T_{11} and T_{12} are found from Eqs (3.1) and (3.2).

3.3 First-order and zero-order perturbation theory solution for scattered field

The perturbation theory approach assumes that the product of the wave number in the water and the RMS surface height, $k_1 h$, is small. The fields and T-matrices are expanded in a power series in $k_1 h$, and the problem is solved one order at a time. In this chapter, we are only interested in the first-order solution used in chapters 2 and 4, and therefore keep only the zero-order terms and the first-order terms of the scattered fields,

$$\Psi(\mathbf{K}) \cong \Psi^{(0)}(\mathbf{K}) + (k_1 h)\Psi^{(1)}(\mathbf{K}), \tag{3.7}$$

and the zero-order and first-order T-matrix components,

$$T(\mathbf{K},\mathbf{K}_i) \cong T^{(0)}(\mathbf{K},\mathbf{K}_i) + (k_1 h)T^{(1)}(\mathbf{K},\mathbf{K}_i). \tag{3.8}$$

Likewise, exponential terms In Eqs. (3.1) and (3.2) are also expanded in the first two terms of a power series,

$$e^{ik_1\beta_1(\mathbf{K})hf(\mathbf{R})} \cong 1 + ik_1\beta_1(\mathbf{K})hf(\mathbf{R}). \tag{3.9}$$

The Fourier transform of $f(\mathbf{R})$ is given by

$$F(\mathbf{K}) = \frac{1}{(2\pi)^2}\int d^2R f(\mathbf{R})e^{-i\mathbf{K}\cdot\mathbf{R}}. \tag{3.10}$$

Therefore $f(\mathbf{R})$ and $\nabla f(\mathbf{R})$ can be expressed as

$$f(\mathbf{R}) = \int d^2K' F(\mathbf{K}')e^{i\mathbf{K}'\cdot\mathbf{R}}, \tag{3.11}$$

$$\nabla f(\mathbf{R}) = \int d^2K' i\mathbf{K}' F(\mathbf{K}')e^{i\mathbf{K}'\cdot\mathbf{R}}. \tag{3.12}$$

Using Eqs. (3.9) and (3.11) in Eq. (3.1) yields an approximate expression for the continuity of pressure boundary condition appropriate for first-order and zero-order fields:

$$\begin{aligned}&\int d^2K\left[\Psi_i(\mathbf{K}) + \Psi_f(\mathbf{K})\right]e^{i\mathbf{K}\cdot\mathbf{R}} \\ &+\int d^2K i(k_1 h)\beta_1(\mathbf{K})\left[\Psi_i(\mathbf{K})(-1) + \Psi_f(\mathbf{K})\right]\int d^2K' F(\mathbf{K}')e^{i(\mathbf{K}+\mathbf{K}')\cdot\mathbf{R}} \\ &= \int d^2K\Psi_{2-}(\mathbf{K})e^{i\mathbf{K}\cdot\mathbf{R}} - \int d^2K i(\kappa k_1 h)\beta_2(\mathbf{K})\Psi_{2-}(\mathbf{K})\int d^2K' F(\mathbf{K}')e^{i(\mathbf{K}+\mathbf{K}')\cdot\mathbf{R}}.\end{aligned} \tag{3.13}$$

Multiplying both sides of the above expression by $e^{-i\mathbf{K}''\cdot\mathbf{R}}$, and integrating this equation over $\mathbf{R}$ by means of the operator $\int d^2R$, yields

$$\begin{aligned}
&\int d^2K\left[\Psi_i(\mathbf{K})+\Psi_f(\mathbf{K})\right]\delta(\mathbf{K}-\mathbf{K}'')\\
&+\int d^2K\, i(k_1h)\beta_1(\mathbf{K})\left[-\Psi_i(\mathbf{K})+\Psi_f(\mathbf{K})\right]\int d^2K' F(\mathbf{K}')\delta(\mathbf{K}+\mathbf{K}'-\mathbf{K}'')\\
&=\int d^2K\Psi_{2-}(\mathbf{K})\delta(\mathbf{K}-\mathbf{K}'')\\
&-\int d^2K\, i(\kappa k_1h)\beta_2(\mathbf{K})\Psi_{2-}(\mathbf{K})\int d^2K' F(\mathbf{K}')\delta(\mathbf{K}+\mathbf{K}'-\mathbf{K}''),
\end{aligned} \tag{3.14}$$

where $\delta(\mathbf{K})$ is the 2-D Dirac delta function. Integrating the above expression over $\mathbf{K}$ and over $\mathbf{K}'$ results in the following simplified expression for the continuity of pressure boundary condition appropriate for first-order and zero-order fields:

$$\begin{aligned}
&\Psi_i(\mathbf{K}'')+\Psi_f(\mathbf{K}'')\\
&+\int d^2K\, i(k_1h)\beta_1(\mathbf{K})\left[-\Psi_i(\mathbf{K})+\Psi_f(\mathbf{K})\right]F(\mathbf{K}''-\mathbf{K})\\
&=\Psi_{2-}(\mathbf{K}'')-\int d^2K\, i(\kappa k_1h)\beta_2(\mathbf{K})\Psi_{2-}(\mathbf{K})F(\mathbf{K}''-\mathbf{K})
\end{aligned} \tag{3.15}$$

Following the above procedure, we now use Eqs. (3.9), (3.11), and (3.12) in Eq. (3.2) and obtain an approximate expression for the continuity of pressure boundary condition appropriate for first-order and zero-order fields:

$$\begin{aligned}
&\int d^2K\beta_1(\mathbf{K})\left[-\Psi_i(\mathbf{K})+\Psi_f(\mathbf{K})\right]e^{i\mathbf{K}\cdot\mathbf{R}}\\
&+i\int d^2K\,(k_1h)\beta_1^2(\mathbf{K})\left[\Psi_i(\mathbf{K})+\Psi_f(\mathbf{K})\right]\int d^2K' F(\mathbf{K}')e^{i(\mathbf{K}+\mathbf{K}')\cdot\mathbf{R}}\\
&-i\int d^2K\,(k_1h)\left[\Psi_i(\mathbf{K})+\Psi_f(\mathbf{K})\right]\int d^2K'\frac{\mathbf{K}\cdot\mathbf{K}'}{k_1^2}F(\mathbf{K}')e^{i(\mathbf{K}+\mathbf{K}')\cdot\mathbf{R}}\\
&=-\frac{1}{\rho}\int d^2K\kappa\beta_2(\mathbf{K})\Psi_{2-}(\mathbf{K})e^{i\mathbf{K}\cdot\mathbf{R}}\\
&+\frac{i}{\rho}\int d^2K\,(k_1h)\kappa^2\beta_2^2(\mathbf{K})\Psi_{2-}(\mathbf{K})\int d^2K' F(\mathbf{K}')e^{i(\mathbf{K}+\mathbf{K}')\cdot\mathbf{R}}\\
&-\frac{i}{\rho}\int d^2K\,(k_1h)\Psi_{2-}(\mathbf{K})\int d^2K'\frac{\mathbf{K}\cdot\mathbf{K}'}{k_1^2}F(\mathbf{K}')e^{i(\mathbf{K}+\mathbf{K}')\cdot\mathbf{R}}.
\end{aligned} \tag{3.16}$$

Multiplying both sides of the above expression by $e^{-i\mathbf{K}''\cdot\mathbf{R}}$ and integrating this equation over $\int d^2R$ yields

$$
\begin{aligned}
&\int d^2K\beta_1(\mathbf{K})\left[-\Psi_i(\mathbf{K})+\Psi_f(\mathbf{K})\right]\delta(\mathbf{K}''-\mathbf{K})\\
&+i\int d^2K\left(k_1h\right)\beta_1^2(\mathbf{K})\left[\Psi_i(\mathbf{K})+\Psi_f(\mathbf{K})\right]\int d^2K'F(\mathbf{K}')\delta(\mathbf{K}+\mathbf{K}'-\mathbf{K}'')\\
&-i\int d^2K\left(k_1h\right)\left[\Psi_i(\mathbf{K})+\Psi_f(\mathbf{K})\right]\int d^2K'\frac{\mathbf{K}\cdot\mathbf{K}'}{k_1^2}F(\mathbf{K}')\delta(\mathbf{K}+\mathbf{K}'-\mathbf{K}'')\\
&=-\frac{1}{\rho}\int d^2K\kappa\beta_2(\mathbf{K})\Psi_{2-}(\mathbf{K})\delta(\mathbf{K}''-\mathbf{K})\\
&+\frac{i}{\rho}\int d^2K\left(k_1h\right)\kappa^2\beta_2^2(\mathbf{K})\Psi_{2-}(\mathbf{K})\int d^2K'F(\mathbf{K}')\delta(\mathbf{K}+\mathbf{K}'-\mathbf{K}'')\\
&-\frac{i}{\rho}\int d^2K\left(k_1h\right)\Psi_{2-}(\mathbf{K})\int d^2K'\frac{\mathbf{K}\cdot\mathbf{K}'}{k_1^2}F(\mathbf{K}')\delta(\mathbf{K}+\mathbf{K}'-\mathbf{K}'').
\end{aligned}
\tag{3.17}
$$

Integrating the above expression over $\mathbf{K}$ and $\mathbf{K}'$ results in the following simplified expression for the continuity of normal velocity boundary condition, appropriate for first-order and zero-order fields:

$$
\begin{aligned}
&\beta_1(\mathbf{K}'')\left[-\Psi_i(\mathbf{K}'')+\Psi_f(\mathbf{K}'')\right]\\
&+i\int d^2K\left(k_1h\right)\beta_1^2(\mathbf{K})\left[\Psi_i(\mathbf{K})+\Psi_f(\mathbf{K})\right]F(\mathbf{K}''-\mathbf{K})\\
&-i\int d^2K\left(k_1h\right)\left[\Psi_i(\mathbf{K})+\Psi_f(\mathbf{K})\right]\frac{\mathbf{K}\cdot(\mathbf{K}''-\mathbf{K})}{k_1^2}F(\mathbf{K}''-\mathbf{K})\\
&=-\frac{1}{\rho}\kappa\beta_2(\mathbf{K}'')\Psi_{2-}(\mathbf{K}'')\\
&+\frac{i}{\rho}\int d^2K\left(k_1h\right)\kappa^2\beta_2^2(\mathbf{K})\Psi_{2-}(\mathbf{K})F(\mathbf{K}''-\mathbf{K})\\
&-\frac{i}{\rho}\int d^2K\left(k_1h\right)\Psi_{2-}(\mathbf{K})\frac{\mathbf{K}\cdot(\mathbf{K}''-\mathbf{K})}{k_1^2}F(\mathbf{K}''-\mathbf{K}).
\end{aligned}
\tag{3.18}
$$

3.3.1 Zero-order field (flat surface reflected and transmitted field)

Substituting $\Psi_{2-}^{(0)}(\mathbf{K})$ for $\Psi_{2-}(\mathbf{K})$ and $\Psi_f^{(0)}(\mathbf{K})$ for $\Psi_f(\mathbf{K})$ into Eqs (3.15) and (3.18), and keeping only zero-order terms, yields the zero-order equations for continuity of pressure and continuity of normal velocity:

$$\Psi_i(\mathbf{K}'') + \Psi_f^{(0)}(\mathbf{K}'') = \Psi_{2-}^{(0)}(\mathbf{K}'') \tag{3.19}$$

$$\Psi_i(\mathbf{K}'') - \Psi_f^{(0)}(\mathbf{K}'') = \frac{\kappa\beta_2(\mathbf{K}'')}{\rho\beta_1(\mathbf{K}'')}\Psi_{2-}^{(0)}(\mathbf{K}''). \tag{3.20}$$

Solving Eqs. (3.19) and (3.20) for $\Psi_{2-}^{(0)}$ and $\Psi_f^{(0)}$ yields

$$\Psi_f^{(0)}(\mathbf{K}) = \Gamma(\mathbf{K})\Psi_i(\mathbf{K}) \tag{3.21}$$

and

$$\Psi_{2-}^{(0)}(\mathbf{K}) = \mathrm{T}(\mathbf{K})\Psi_i(\mathbf{K}), \tag{3.22}$$

where

$$\Gamma(\mathbf{K}) = \frac{1 - \kappa\beta_2(\mathbf{K})/\rho\beta_1(\mathbf{K})}{1 + \kappa\beta_2(\mathbf{K})/\rho\beta_1(\mathbf{K})} \tag{3.23}$$

is the flat surface reflection coefficient, and

$$\mathrm{T}(\mathbf{K}) = 1 + \Gamma(\mathbf{K}) = \frac{2}{1 + \kappa\beta_2(\mathbf{K})/\rho\beta_1(\mathbf{K})} \tag{3.24}$$

is the flat surface transmission coefficient. The zero-order field is therefore the field transmitted and reflected from the flat zero-mean surface. Comparing Eqs. (3.21) and (3.22) with Eqs. (3.5) and (3.6) shows that the reflection coefficient can be expressed in terms of the zero-order T-matrix, $T_{11}^{(0)}$,

$$\Gamma(\mathbf{K}) = T_{11}^{(0)}(\mathbf{K}', \mathbf{K})\delta(\mathbf{K}' - \mathbf{K}), \tag{3.25}$$

and the transmission coefficient can be expressed in terms of the zero-order T-matrix, $T_{12}^{(0)}$,

$$\mathrm{T}(\mathbf{K}) = T_{12}^{(0)}(\mathbf{K}', \mathbf{K})\delta(\mathbf{K}' - \mathbf{K}). \tag{3.26}$$

3.3.2 First-order scattered field

Substituting Eq. (3.7) into Eqs (3.15) and (3.18), and keeping only first-order terms (terms with a $k_1 h$ factor), yields the first-order equations for continuity of pressure,

$$\begin{aligned}&\Psi_f^{(1)}(\mathbf{K}'')+\int d^2K\, i\beta_1(\mathbf{K})\left[-\Psi_i(\mathbf{K})+\Psi_f^{(0)}(\mathbf{K})\right]F(\mathbf{K}''-\mathbf{K})\\&=\Psi_{2-}^{(1)}(\mathbf{K}'')-\int d^2K\, i\kappa\beta_2(\mathbf{K})\Psi_{2-}^{(0)}(\mathbf{K})F(\mathbf{K}''-\mathbf{K}),\end{aligned}\tag{3.27}$$

and continuity of normal velocity,

$$\begin{aligned}&\frac{\rho\beta_1(\mathbf{K}'')}{\kappa\beta_2(\mathbf{K}'')}\Psi_f^{(1)}(\mathbf{K}'')\\&+\frac{i\rho}{\kappa\beta_2(\mathbf{K}'')}\int d^2K\,\beta_1^2(\mathbf{K})\left[\Psi_i(\mathbf{K})+\Psi_f^{(0)}(\mathbf{K})\right]F(\mathbf{K}''-\mathbf{K})\\&-\frac{i\rho}{\kappa\beta_2(\mathbf{K}'')}\int d^2K\left[\Psi_i(\mathbf{K})+\Psi_f^{(0)}(\mathbf{K})\right]\frac{\mathbf{K}\cdot(\mathbf{K}''-\mathbf{K})}{k_1^2}F(\mathbf{K}''-\mathbf{K})\\&=-\Psi_{2-}^{(1)}(\mathbf{K}'')\\&+\frac{i}{\kappa\beta_2(\mathbf{K}'')}\int d^2K\,\kappa^2\beta_2^2(\mathbf{K})\Psi_{2-}^{(0)}(\mathbf{K})F(\mathbf{K}''-\mathbf{K})\\&-\frac{i}{\kappa\beta_2(\mathbf{K}'')}\int d^2K\,\Psi_{2-}^{(0)}(\mathbf{K})\frac{\mathbf{K}\cdot(\mathbf{K}''-\mathbf{K})}{k_1^2}F(\mathbf{K}''-\mathbf{K}).\end{aligned}\tag{3.28}$$

3.3.2.1 First-order field scattered from interface back into water

Equations (3.27) and (3.28) are added together to eliminate $\Psi_{2-}^{(1)}$; Eqs. (3.21), (3.22), and (3.24) are used to express $\Psi_f^{(0)}$ and $\Psi_{2-}^{(0)}$ in terms of Ψ_i.

$$
\begin{aligned}
&\Psi_f^{(1)}(\mathbf{K}'')\left(1+\frac{\rho\beta_1(\mathbf{K}'')}{\kappa\beta_2(\mathbf{K}'')}\right)\\
&=-\frac{i\rho}{\kappa\beta_2(\mathbf{K}'')}\int d^2K\beta_1^2(\mathbf{K})\Psi_i(\mathbf{K})(1+\Gamma(\mathbf{K}))F(\mathbf{K}''-\mathbf{K})\\
&+\frac{i\rho}{\kappa\beta_2(\mathbf{K}'')}\int d^2K\Psi_i(\mathbf{K})(1+\Gamma(\mathbf{K}))\frac{\mathbf{K}\cdot(\mathbf{K}''-\mathbf{K})}{k_1^2}F(\mathbf{K}''-\mathbf{K})\\
&+\frac{i}{\kappa\beta_2(\mathbf{K}'')}\int d^2K\kappa^2\beta_2^2(\mathbf{K})\Psi_i(\mathbf{K})(1+\Gamma(\mathbf{K}))F(\mathbf{K}''-\mathbf{K})\\
&-\frac{i}{\kappa\beta_2(\mathbf{K}'')}\int d^2K\Psi_i(\mathbf{K})(1+\Gamma(\mathbf{K}))\frac{\mathbf{K}\cdot(\mathbf{K}''-\mathbf{K})}{k_1^2}F(\mathbf{K}''-\mathbf{K})\\
&+\int d^2Ki\beta_1(\mathbf{K})\Psi_i(\mathbf{K})(1-\Gamma(\mathbf{K}))F(\mathbf{K}''-\mathbf{K})\\
&-\int d^2Ki\kappa\beta_2(\mathbf{K})\Psi_i(\mathbf{K})(1+\Gamma(\mathbf{K}))F(\mathbf{K}''-\mathbf{K}).
\end{aligned}
\tag{3.29}
$$

Noting Eq. (3.5), and multiplying the above equation by $\kappa\beta_2(\mathbf{K}'')/\rho$, we obtain an equivalent expression in terms of the first-order T-matrix:

$$
\begin{aligned}
\beta_1(\mathbf{K}'')\left(1+\frac{\kappa\beta_2(\mathbf{K}'')}{\rho\beta_1(\mathbf{K}'')}\right)T_{11}^{(1)}(\mathbf{K}'',\mathbf{K})=\Bigg\{&i(1-\Gamma(\mathbf{K}))\frac{\kappa\beta_2(\mathbf{K}'')}{\rho}\beta_1(\mathbf{K})\\
&-i(1+\Gamma(\mathbf{K}))\left(\beta_1^2(\mathbf{K})-\frac{1}{\rho}\kappa^2\beta_2^2(\mathbf{K})+\frac{\kappa\beta_2(\mathbf{K}'')}{\rho}\kappa\beta_2(\mathbf{K})\right)\\
&+i(1+\Gamma(\mathbf{K}))\frac{\mathbf{K}\cdot(\mathbf{K}''-\mathbf{K})}{k_1^2}\left(1-\frac{1}{\rho}\right)\Bigg\}F(\mathbf{K}''-\mathbf{K}).
\end{aligned}
\tag{3.30}
$$

For convenience, define H_{11} such that

$$
T_{11}^{(1)}(\mathbf{K}'',\mathbf{K})=H_{11}(\mathbf{K}'',\mathbf{K})F(\mathbf{K}''-\mathbf{K}). \tag{3.31}
$$

Substituting

$$
\frac{\mathbf{K}\cdot(\mathbf{K}''-\mathbf{K})}{k_1^2}=\frac{\mathbf{K}\cdot\mathbf{K}''}{k_1^2}-1+\beta_1^2(\mathbf{K}), \tag{3.32}
$$

$$
\beta_1^2(\mathbf{K})-(\kappa\beta_2(\mathbf{K}))^2=\frac{k_1^2-K^2}{k_1^2}-\frac{k_2^2-K^2}{k_1^2}=1-\kappa^2 \tag{3.33}
$$

into Eq. (3.30), and using Eq. (3.31), yields

$$\beta_1(\mathbf{K}'')\left(1+\frac{\kappa\beta_2(\mathbf{K}'')}{\rho\beta_1(\mathbf{K}'')}\right)H_{11}(\mathbf{K}'',\mathbf{K})=i\left(1-\Gamma(\mathbf{K})\right)\frac{\kappa\beta_2(\mathbf{K}'')\beta_1(\mathbf{K})}{\rho}$$

$$-i\left(1+\Gamma(\mathbf{K})\right)\left(\frac{\kappa\beta_2(\mathbf{K}'')\kappa\beta_2(\mathbf{K})}{\rho}+1-\frac{1}{\rho}+\frac{1}{\rho}\left(1-\kappa^2\right)\right)$$

$$+i\left(1+\Gamma(\mathbf{K})\right)\left(\left(1-\frac{1}{\rho}\right)\frac{\mathbf{K}\cdot\mathbf{K}''}{k_1^2}\right). \tag{3.34}$$

With the use of Eq. (3.24), the left side of Eq. (3.34) is expressed in terms of one plus the reflection coefficient:

$$H_{11}(\mathbf{K}'',\mathbf{K})=-\left(1+\Gamma(\mathbf{K}'')\right)\left(1-\Gamma(\mathbf{K})\right)\frac{\kappa\beta_2(\mathbf{K}'')\beta_1(\mathbf{K})}{2i\rho\beta_1(\mathbf{K}'')}$$

$$+\frac{\left(1+\Gamma(\mathbf{K}'')\right)\left(1+\Gamma(\mathbf{K})\right)}{i\beta_1(\mathbf{K}'')}\left(\frac{\kappa\beta_2(\mathbf{K}'')\kappa\beta_2(\mathbf{K})}{\rho}+1-\frac{1}{\rho}+\frac{1}{\rho}\left(1-\kappa^2\right)\right)$$

$$+\frac{\left(1+\Gamma(\mathbf{K}'')\right)\left(1+\Gamma(\mathbf{K})\right)}{2i\beta_1(\mathbf{K}'')}\left(\left(\frac{1}{\rho}-1\right)\frac{\mathbf{K}\cdot\mathbf{K}''}{k_1^2}\right). \tag{3.35}$$

The first factor on the right side of the above equation and the first two factors in the second term are converted from one plus the reflection coefficient to one minus the reflection coefficient through the following equality, obtained from Eq. (3.23):

$$\frac{1+\Gamma(\mathbf{K})}{1-\Gamma(\mathbf{K})}=\frac{\rho\beta_1(\mathbf{K})}{\kappa\beta_2(\mathbf{K})}. \tag{3.36}$$

The expression for H_{11} follows from Eq. (3.35):

$$H_{11}(\mathbf{K}'',\mathbf{K})=\frac{1}{2i\beta_1(\mathbf{K}'')}\left\{a(\mathbf{K}'',\mathbf{K})\left(1+\Gamma(\mathbf{K}'')\right)\left(1+\Gamma(\mathbf{K})\right)\right.$$

$$\left.+b(\mathbf{K}'',\mathbf{K})\left(1-\Gamma(\mathbf{K}'')\right)\left(1-\Gamma(\mathbf{K})\right)\right\}, \tag{3.37}$$

where

$$a(\mathbf{K}'',\mathbf{K}) = 1 - \frac{\kappa^2}{\rho} + \left(\frac{1}{\rho} - 1\right)\frac{\mathbf{K}''\cdot\mathbf{K}}{k_1^2} \tag{3.38}$$

and

$$b(\mathbf{K}'',\mathbf{K}) = \beta_1(\mathbf{K}'')\beta_1(\mathbf{K})(\rho - 1). \tag{3.39}$$

The first-order incoherent field is given by $k_1 h$ multiplied by the 2-D inverse Fourier transform of Eq. (3.5), where $T_{11}^{(1)}$ is given by Eq. (3.31) and H_{11} is given by Eq. (3.37).

3.3.2.2 First-order field scattered into sediment

The field scattered into the sediment follows from rearranging the terms in Eq. (3.27), and expressing the reflected and transmitted fields in terms of the incident field by using Eqs. (3.21) and (3.22),

$$\begin{aligned}\Psi_{2-}^{(1)}(\mathbf{K}'') = \Psi_f^{(1)}(\mathbf{K}'') &- \int d^2K\, i\beta_1(\mathbf{K})(1-\Gamma(\mathbf{K}))F(\mathbf{K}''-\mathbf{K}) \\ &+ \int d^2K\, i\kappa\beta_2(\mathbf{K})(1+\Gamma(\mathbf{K}))F(\mathbf{K}''-\mathbf{K}).\end{aligned} \tag{3.40}$$

As in Eq. (3.31), define H_{12} in terms of the first-order T-matrix, $T_{12}^{(1)}$, and 2-D Fourier transform of the interface profile function F,

$$T_{12}^{(1)}(\mathbf{K}'',\mathbf{K}) = H_{12}(\mathbf{K}'',\mathbf{K})F(\mathbf{K}''-\mathbf{K}), \tag{3.41}$$

where

$$H_{12}^{(1)}(\mathbf{K}'',\mathbf{K}) = H_{11}^{(1)}(\mathbf{K}'',\mathbf{K}) - i\beta_1(\mathbf{K})(1-\Gamma(\mathbf{K})) + i\kappa\beta_2(\mathbf{K})(1+\Gamma(\mathbf{K})) \tag{3.42}$$

follows from Eqs. (3.40) and (3.41). Substituting Eq. (3.37) for H_{11} into the above equation yields

$$H_{12}^{(1)}(\mathbf{K}'',\mathbf{K}) = \frac{1}{2i\beta_1(\mathbf{K}'')}\{a(\mathbf{K}'',\mathbf{K})(1+\Gamma(\mathbf{K}''))(1+\Gamma(\mathbf{K})) + b(\mathbf{K}'',\mathbf{K})(1-\Gamma(\mathbf{K}''))(1-\Gamma(\mathbf{K}))\} - i\beta_1(\mathbf{K})(1-\Gamma(\mathbf{K})) + i\kappa\beta_2(\mathbf{K})(1+\Gamma(\mathbf{K})). \quad (3.43)$$

The following identity is shown by using Eq. (3.36):

$$2i\beta_1(\mathbf{K}'')[-i\beta_1(\mathbf{K})(1-\Gamma(\mathbf{K})) + i\kappa\beta_2(\mathbf{K})(1+\Gamma(\mathbf{K}))] + b(\mathbf{K}'',\mathbf{K})(1-\Gamma(\mathbf{K}''))(1-\Gamma(\mathbf{K})) = -\beta_1(\mathbf{K})\beta_1(\mathbf{K}'')(\rho-1)(1-\Gamma(\mathbf{K}))(1+\Gamma(\mathbf{K}'')). \quad (3.44)$$

Substituting Eq. (3.44) into Eq. (3.43) yields

$$H_{12}(\mathbf{K}'',\mathbf{K}) = \frac{\mathcal{T}(\mathbf{K}'')}{2i\beta_1(\mathbf{K}'')}[a(\mathbf{K}'',\mathbf{K})(1+\Gamma(\mathbf{K})) - b(\mathbf{K}'',\mathbf{K})(1-\Gamma(\mathbf{K}))], \quad (3.45)$$

where $\mathcal{T}$ is the flat surface transmission coefficient given in Eq. (3.24). The first-order approximation to the T-matrix for forward scattering into the sediment is obtained from Eqs. (3.6), (3.41), and (3.45).

3.4 Time-dependent mean square incoherent field approximation

Since the first-order T-matrices are proportional to the 2-D Fourier transform of the zero-mean interface, their expected value over the rough interface ensemble is zero. In addition, the zero-order component of each T-matrix is only dependent on the zeroth moment of the rough interface ensemble. Therefore

$$\tilde{T}_{12}(\mathbf{K},\mathbf{K}_i) \cong (k_1 h)T_{12}^{(1)}(\mathbf{K},\mathbf{K}_i) = (k_1 h)H_{12}(\mathbf{K},\mathbf{K}_i)F(\mathbf{K}-\mathbf{K}_i) \quad (3.46)$$

and

$$\tilde{T}_{11}(\mathbf{K},\mathbf{K}_i) \cong (k_1 h)T_{11}^{(1)}(\mathbf{K},\mathbf{K}_i) = (k_1 h)H_{11}(\mathbf{K},\mathbf{K}_i)F(\mathbf{K}-\mathbf{K}_i) \quad (3.47)$$

are the first-order approximations for the incoherent T-matrices given in Eq. (2.18). Using the first-order approximation to the T-matrix in Eq. (3.41),

$$(k_1h)^2\left\langle T_{12}^{(1)}(\mathbf{K}',\mathbf{K}_i',\omega_1)T_{12}^{(1)*}(\mathbf{K}'',\mathbf{K}_i'',\omega_2)\right\rangle$$

$$=(k_1h)^2H_{12}(\mathbf{K}',\mathbf{K}_i',\omega_1)H_{12}^{*}(\mathbf{K}'',\mathbf{K}_i'',\omega_2)\left\langle F_1(\mathbf{K}'-\mathbf{K}_i')F_1(\mathbf{K}''-\mathbf{K}_i'')\right\rangle \tag{3.48}$$

is the first-order approximation to the incoherent T-matrix correlation function, given in Eq. (2.33), for forward scattering through a fluid-fluid interface. The dependence on angular frequency is shown explicitly in the T-matrix and H_{12}. Using the identity

$$h^2\left\langle F(\mathbf{K}''-\mathbf{K}_i)F(\mathbf{K}'-\mathbf{K}_i)\right\rangle = W(\mathbf{K}'-\mathbf{K}_i)\delta(\mathbf{K}''-\mathbf{K}') \tag{3.49}$$

together with Eq. (2.33) and Eq. (3.48) yields

$$\mathcal{C}_{12}(\mathbf{K}',\mathbf{K}'',\mathbf{K}_i',\mathbf{K}_i'',\omega_c+\omega',\omega_c+\omega'')$$

$$=k_1^2H_{12}(\mathbf{K}',\mathbf{K}_i',\omega_c+\omega')H_{12}^{*}(\mathbf{K}'',\mathbf{K}_i'',\omega_c+\omega'')W\left(\mathbf{K}-(\mathbf{K}_i'+\mathbf{K}_i'')/2\right), \tag{3.50}$$

where W is the roughness spectrum. For the case of a wide sense stationary process (WSS),

$$W(\mathbf{K})=\frac{1}{(2\pi)^2}\int d^2R\,C(\mathbf{R})e^{-i\mathbf{K}\cdot\mathbf{R}}, \tag{3.51}$$

where

$$C(\mathbf{R}_d)=\left\langle f(\mathbf{R}+\mathbf{R}_d)f(\mathbf{R})\right\rangle \tag{3.52}$$

is the surface autocorrelation function. For this special case, the identity in Eq. (3.49) is simply derived by making the substitutions

$$\mathbf{R}_d=\mathbf{R}_1-\mathbf{R}_2,\ \mathbf{R}_a=(\mathbf{R}_1+\mathbf{R}_2)/2 \tag{3.53}$$

in

$$\left\langle F(\mathbf{K}_1)F(\mathbf{K}_2)\right\rangle=\frac{1}{(2\pi)^4}\int d^2R_1\int d^2R_2\left\langle f(\mathbf{R}_1)f(\mathbf{R}_2)\right\rangle e^{i(\mathbf{K}_2\cdot\mathbf{R}_2+\mathbf{K}_1\cdot\mathbf{R}_1)} \tag{3.54}$$

and using Eqs. (3.51) and (3.52).

3.4.1 Seafloor roughness spectrum

The two dimensional Gaussian random process $f(\mathbf{R})$ describing the seafloor surface is assumed to be an isotropic power-law (Fox and Hayes, 1985; Goff, and Jordan, 1989; Briggs, 1989) with a roughness spectrum

$$W(\mathbf{K}) = \frac{w_2}{K^{\gamma}}. \tag{3.55}$$

In the notation of Mourad and Jackson (1989, 1993), the spectral strength and spectral exponent are represented by the parameters w_2 and γ, respectively. For $2 < \gamma < 4$, this surface random process is an example of a fractal (Mandelbrot, 1983), and the perturbation theory requirement that $k_1 h$ be small is not satisfied. In fact, the RMS height is infinite, and the random process is not WSS. However, since this random process is stationary in increments, Eq. (3.49) is valid (Ishimaru, 1978b), and the large scale roughness can be removed by a filtering operation (Jackson, Winebrenner, Ishimaru, 1986).

The power-law spectrum is an estimate of the roughness spectrum over all spatial frequencies. The seafloor roughness spectrum on scales over one meter is poorly known, and therefore assuming a roughness spectrum that is a power-law over all spatial frequencies (Eq. 3.55) may not be valid. Large scale components of the roughness spectrum are set by the spatial scale of the experiment. In the case of a tank experiment, moderate to large scale roughness will not be present. Removal of the large scale roughness in Eq. (3.55) is therefore appropriate.

Let $\tilde{f}(\mathbf{R})$ be the surface with the power-law roughness spectrum given in Eq. (3.55), with 2-D Fourier transform, $\tilde{F}(\mathbf{K})$. A filtered surface, $f(\mathbf{R})$, is obtained by subtracting a moving average (Papoulis, 1984) of $\tilde{f}(\mathbf{R})$ from itself:

$$f(\mathbf{R}) = \tilde{f}(\mathbf{R}) - \frac{1}{\pi a^2}\int_0^{2\pi} d\phi' \int_0^{a} dR' \tilde{f}(\mathbf{R}-\mathbf{R}'). \tag{3.56}$$

Equation (3.56) can be expressed as a 2-D convolution of $\tilde{f}(\mathbf{R})$ with a filter $s(\mathbf{R})$,

$$f(\mathbf{R}) = \frac{1}{(2\pi)^2}\int \tilde{f}(\mathbf{R}-\mathbf{R}')s(\mathbf{R}'), \tag{3.57}$$

or

$$f(\mathbf{R}) = \tilde{f}(\mathbf{R}) \otimes s(\mathbf{R}), \tag{3.58}$$

where $s(\mathbf{R})$ is of the form

$$s(\mathbf{R}) = (2\pi)^2 \delta(\mathbf{R}) - m(\mathbf{R}), \tag{3.59}$$

and

$$m_1(\mathbf{R}) = (2\pi)^2 \frac{\mathrm{circ}(R/a)}{\pi a^2} \tag{3.60}$$

is a moving average filter. The circ function is defined as (Goodman, 1968)

$$\mathrm{circ}(R) = \begin{cases} 1 & R \le 1 \\ 0 & \text{otherwise} \end{cases}. \tag{3.61}$$

Filtering the original power-law random process with roughness spectrum given in Eq. (3.57) with the filter $s(\mathbf{R})$ corresponds to subtracting from each point on the random surface, $\tilde{f}(\mathbf{R})$, an average of the surface over a radius a about each point. The filter's Fourier transform follows from Eq. (3.59),

$$\mathcal{S}(\mathbf{K}) = 1 - M(\mathbf{K}) \tag{3.62}$$

where

$$M(\mathbf{K}) = \frac{2J_1(Ka)}{Ka}. \tag{3.63}$$

The resulting roughness spectrum obtained by filtering the surface with the power-law roughness spectrum given in Eq. (3.55) using the filter in Eqs. (3.62) and (3.63) results in the 2-D surface random process given by

$$W(\mathbf{K}) = \frac{w_2}{K^\gamma}\left(1 - \frac{2J_1(Ka)}{Ka}\right)^2. \tag{3.64}$$

Instead of subtracting a uniformly averaged area around each surface point from the surface, subtracting a Gaussian weighted average around each surface point from the surface results in a roughness spectrum without the Bessel function oscillations. In this case

$$m_2(\mathbf{R}) = (2\pi)^2 \frac{e^{-R^2/2a^2}}{a\sqrt{2\pi}}, \tag{3.65}$$

and the filtered, or truncated, roughness spectrum is given by

$$W(\mathbf{K}) = \frac{w_2}{K^\gamma}\left(1 - e^{-(Ka)^2/2}\right)^2, \tag{3.66}$$

with RMS height (see Appendix C)

$$h = \sqrt{2\pi \int_0^\infty W(\mathbf{K}) K dK} = \sqrt{\frac{2\pi w_2 a^{\gamma-2}}{\gamma - 2}\Gamma(2 - \gamma/2)\left[2^{2-\gamma/2} - 1\right]}. \tag{3.67}$$

Here, Γ refers to the gamma function — not the reflection coefficient, and not the two-frequency mutual coherence function.

The roughness spectrum given in Eq. (3.66) is the roughness spectrum used in this dissertation. The choice of the filter parameter, a, is discussed for each numerical calculation. The larger this parameter is, the closer the filtered roughness spectrum is to the original power-law (Eq. 3.55). Subtracting a moving average of the power-law random process from itself results in removal of low frequency components of the original power-law roughness spectrum.

Plots of this roughness spectrum as a function of K for two different values of the filter parameter, a, are given in Fig. (3.1).

3.4.2 Incoherent T-matrix correlation function approximation in Eq. (2.37)

In order to evaluate the approximation in Eq. (2.37) using first-order perturbation theory, $\mathbf{K}-\mathbf{K}_d/2$ is substituted for $\mathbf{K}'$, and $\mathbf{K}+\mathbf{K}_d/2$ is substituted for $\mathbf{K}''$ in Eq. (3.50)

$$\begin{aligned}
&\mathcal{C}_{12}\left(\mathbf{K}-\mathbf{K}_d/2,\mathbf{K}+\mathbf{K}_d/2,\mathbf{K}_i',\mathbf{K}_i'',\omega_c+\omega',\omega_c+\omega''\right)\\
&\quad\cong k_1^2 H_{12}\left(\mathbf{K}-\mathbf{K}_d/2,\mathbf{K}_i',\omega_c+\omega'\right)H_{12}^*\left(\mathbf{K}+\mathbf{K}_d/2,\mathbf{K}_i'',\omega_c+\omega''\right)\\
&\qquad\times W\left(\mathbf{K}-\left(\mathbf{K}_i'+\mathbf{K}_i''\right)/2\right),
\end{aligned} \tag{3.68}$$

where $\mathbf{K}_d$ is given in Eq. (2.34) and is repeated here for convenience.

$$\begin{aligned}
\mathbf{K}_d &= \mathbf{K}_i''-\mathbf{K}_i'\\
&= \frac{\omega_c+\omega''}{c_1}\cos\theta_i\hat{\alpha}_i-\frac{\omega_c+\omega'}{c_1}\cos\theta_i\hat{\alpha}_i\\
&= \frac{\omega''-\omega'}{c_1}\cos\theta_i\hat{\alpha}_i,
\end{aligned} \tag{3.69}$$

where θ_i is the incident grazing angle and $\hat{\alpha}_i$ is the unit transverse direction vector of the incident field. From Eq. (2.37), $\mathcal{C}_{12}$ in Eq. (3.68) is approximated by

$$\begin{aligned}
&\mathcal{C}_{12}\left(\mathbf{K}-\mathbf{K}_d/2,\mathbf{K}+\mathbf{K}_d/2,\mathbf{K}_i',\mathbf{K}_i'',\omega_c+\omega',\omega_c+\omega''\right)\\
&\quad\cong \mathcal{C}_{12}\left(\mathbf{K},\mathbf{K}_i,\omega_c\right)\\
&\quad\cong k_1^2\left|H_{12}\left(\mathbf{K},\mathbf{K}_i,\omega_c\right)\right|^2 W\left(\mathbf{K}-\mathbf{K}_i\right),
\end{aligned} \tag{3.70}$$

where

$$\mathbf{K}_i=\left(\omega_c/c_1\right)\cos\theta_i\hat{\alpha}_i. \tag{3.71}$$

The roughness spectrum, $W\left(\mathbf{K}-\left(\mathbf{K}_i'+\mathbf{K}_i''\right)/2\right)$, is not a function of

$$\omega_d = \omega'' - \omega'. \tag{3.72}$$

For a narrowband signal, it is a slowly varying function of

$$\omega_a = \omega_c + \frac{\omega'+\omega''}{2}, \tag{3.73}$$

except for $K \cong k_1$. However, scattered energy with $K > k_2$ is evanescent. From inspection of Eqs. (3.38), (3.39), and (3.45), the quantity $H_{12}\left(\mathbf{K}-\mathbf{K}_d/2,\mathbf{K}_i',\omega_c+\omega'\right)H_{12}^{*}\left(\mathbf{K}+\mathbf{K}_d/2,\mathbf{K}_i'',\omega_c+\omega''\right)$ depends on ω_a only in the last term of Eq. (3.38). In addition, the dependency on ω_d is primarily in the factor $7/\beta$ outside the square brackets in Eq. (3.45).

$$\frac{7\left(\mathbf{K}+\mathbf{K}_d/2\right)}{\beta_1\left(\mathbf{K}+\mathbf{K}_d/2\right)} = \frac{2\rho}{\kappa\beta_2\left(\mathbf{K}+\mathbf{K}_d/2\right)+\rho\beta_1\left(\mathbf{K}+\mathbf{K}_d/2\right)}. \tag{3.74}$$

Although the magnitude of Eq. (3.68) varies slowly with frequency, the phase becomes very dependent on ω_d when either $\left|\mathbf{K}+\mathbf{K}_d/2\right|$ or $\left|\mathbf{K}-\mathbf{K}_d/2\right|$ is greater than both κk_1 and k_1. For a narrowband signal, this situation occurs for evanescent scattered waves and possibly scattered waves at shallow grazing angles. However, as shown in chapter 2, including the evanescent scattered field is only necessary within a wavelength or two of the interface, depending on the roughness.

Figure 3.2a is a plot of the magnitude of Eq. (3.68) (excluding the roughness spectrum, W) and Fig. 3.2b is a plot of its phase as a function of $K = |\mathbf{K}|$ and

$$\mathrm{f_d} = \omega_d/(2\pi). \tag{3.75}$$

The roughness spectrum is not included in these plots, because it is not a function of $\mathrm{f_d}$. The direction of $\mathbf{K}$ is the same as the incident transverse wave vector in this example. The center frequency is 20 kHz, and the sediment

parameters are the same as Fig 2.4b. Figure 3.2a shows that the magnitude becomes slightly dependent on f_d only for shallow grazing angles. Figure 3.2b shows that the phase of Eq. (3.68) becomes dependent on large f_d only for the evanescent scattered field and for scattering at shallow grazing angles — even for a relatively wideband signal. The simplifying approximation for $\mathscr{C}$ in Eq. (2.37) is valid for all values of K, except those values corresponding to evanescent waves and those corresponding to scattering at small grazing angles. Because of loss in the sediment, energy scattered at these small grazing angles is insignificant compared to energy scattered at larger grazing angles. Therefore, Eq. (3.68) can be considered to be independent of f_d.

3.4.3 First-order time-dependent mean square incoherent field

Substituting $\mathscr{C}_{12}(\mathbf{K},\mathbf{K}_i,\omega_c)$ in Eq. (3.70) into Eq. (2.50) yields the first-order expression for the time-dependent mean square incoherent field scattered through a rough fluid-fluid interface due to an incident plane wave:

$$I_2(\mathbf{r},t) \cong \int d^2K\, k_1^2 \left|H_{12}(\mathbf{K},\mathbf{K}_i,\omega_c)\right|^2 W(\mathbf{K}-\mathbf{K}_i) \mathrm{e}^{2k_1 \operatorname{Im}(\kappa\beta_2(\mathbf{K},\omega_c))z}\, g^2(t-t_d). \quad (3.76)$$

The differential cross section from first-order perturbation theory is found by substituting Eq. (3.70) into Eq. (2.61).

$$\sigma_{12}(\hat{\alpha},\hat{\alpha}_i) \cong \frac{k_1^4 \sin^2(\theta_2)}{\nu^2} \left|H_{12}(\mathbf{K},\mathbf{K}_i,\omega_c)\right|^2 W(\mathbf{K}-\mathbf{K}_i). \quad (3.77)$$

Although the differential cross section in this approximation is actually second order in $k_1 h$ (Thorsos and Jackson, 1989), we refer to it as the first-order differential cross section, and will refer to the corresponding mean square incoherent field in Eq. (3.76) ($I_2(\mathbf{r},t)$) as the first-order mean square incoherent field. Another first-order expression for $I_2(\mathbf{r},t)$ for an incident plane wave that neglects evanescent waves is obtained using Eq. (3.77) in Eq. (2.63). The effect

of neglecting evanescent waves is discussed in chapter 2. The first-order differential cross section is also substituted into Eq. (2.85) to obtain the first-order expression for $I_2(\mathbf{r},t)$ due to an incident field from a point source. This resulting expression is used in the simulations of experiments that are discussed in chapter 4.

3.5 Summary

First-order perturbation solutions of the scattered field from and through a rough interface between two homogenous fluids are derived in this chapter. These results are used to show the validity of approximating the incoherent T-matrix correlation function as only dependent on the center frequency of a narrowband source signal (Eq. 2.37). The results derived in this chapter are primarily used in chapters 2 and 4. The Gaussian weighted filtered power law (Eq. 3.66) is used for all numerical computations in this dissertation. The filter parameter, a, is chosen to create a spectrum appropriate for each particular example. For example, in the simulation of scattering into the sediment in a tank, discussed in chapter 4, a small value is used for this filter parameter. In ocean experiments, the value of this parameter is considerably larger.

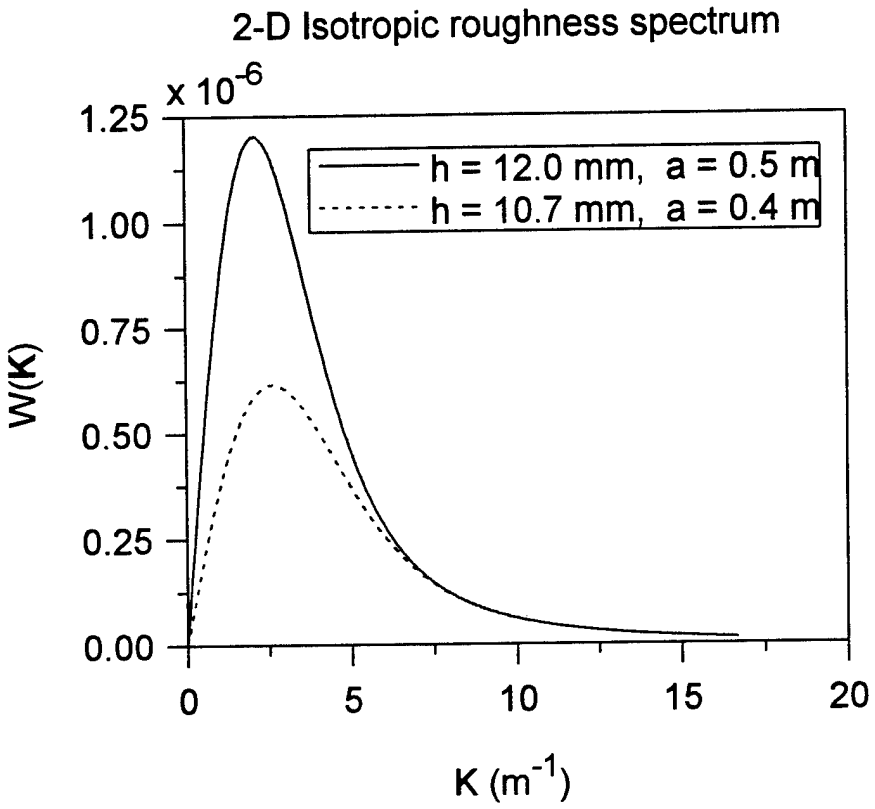

Figure 3.1 : Filtered power-law example with $w_2 = 6.2 \times 10^{-5}$, $\gamma = 3.0$.

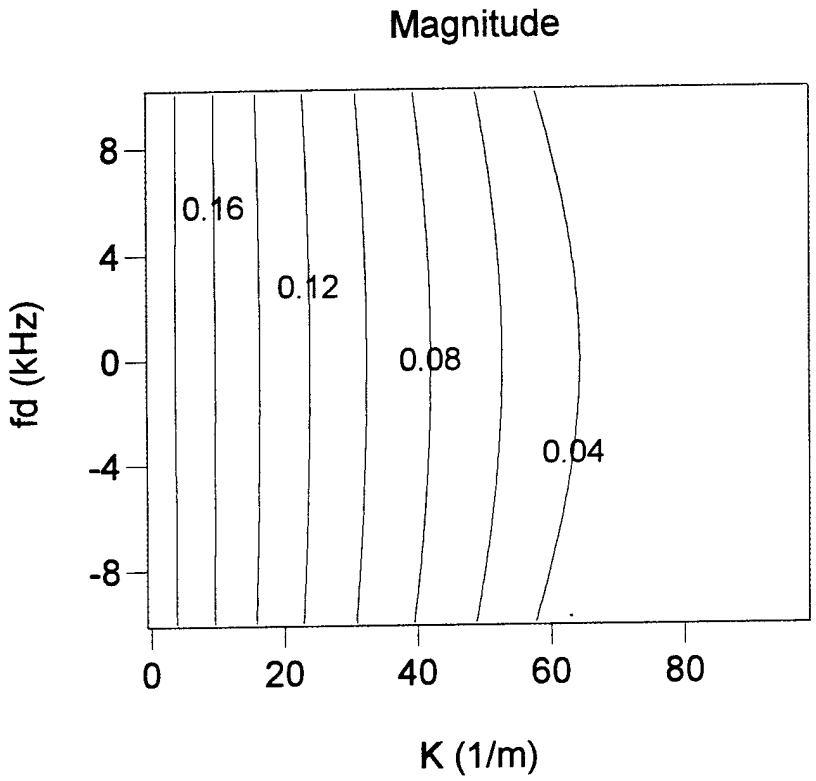

Figure 3.2a : Magnitude of Eq. (3.68), incoherent T-matrix correlation function (divided by the roughness spectrum), incident angle = 20°, $f_c = 20\,\text{kHz}$, $\rho = 1.9608$, $\delta = 0.0163$, $\nu = 1.12565$, $c_1 = 1536\ \text{m/s}$.

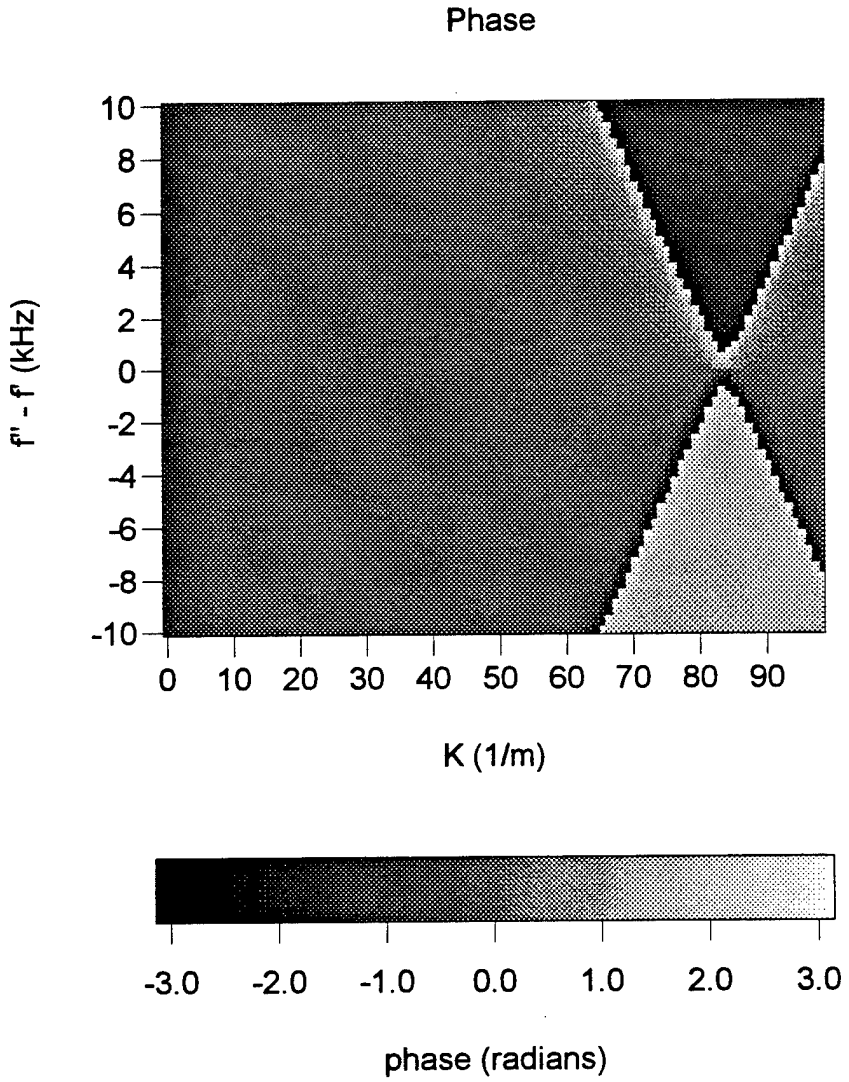

Figure 3.2b : Phase of Eq. (3.68), incoherent T-matrix correlation function (divided by the roughness spectrum), same parameters as Figure 3.2a.

CHAPTER 4

The effect of roughness on acoustic penetration of the seafloor as given by a fluid-fluid perturbation model and comparison with recent sediment penetration experiments

4.1 Introduction to chapter 4

Simulation results of a sediment penetration tank experiment by Boyle and Chotiros (1992) and an ocean penetration experiment by Chotiros (1995) are presented in this chapter. For the incoherent intensity calculations, the first-order perturbation theory results derived in chapter 3 are used in Eq. (2.85); the incoherent intensity in the sediment is obtained by dividing Eq. (2.85) by the characteristic impedance of the sediment ($\rho_2 c_2$). In the ocean experiment simulation, the time domain zero-order coherent intensity is calculated using Eq. (2.92) (divided by $\rho_2 c_2$). Note that the incoherent intensity calculated using first-order perturbation theory is proportional to the second power of $k_1 h$, and the coherent intensity is computed to an accuracy of only zero order. The contribution of the second-order coherent intensity contribution is derived and demonstrated in chapter 5. The effect of sound speed gradients in the vertical direction on the field scattered back into the water is considered in chapters 5 and 6. Although the influence of sound speed gradients on the field scattered through the interface is beyond the scope of this dissertation, possible effects are mentioned in chapter 6.

4.2 Background

Figure 4.1 depicts the scattering model derived in chapter 2. The source pulse originates at a point in the water (medium 1) and propagates to the nth

surface patch, its mean square incoherent field magnitude is multiplied by the differential cross section of the patch, and then it propagates to the receiver in the sediment (medium 2). In addition to spherical spreading from the source to the patch, and from the patch to the receiver, there is a sediment loss term. The contributions of all patches are summed up and divided by the characteristic impedance of the sediment, yielding the total incoherent intensity below the rough interface. Figure 4.1 includes the term $g(t)$ derived in chapter 2. We argue later that the baseband source signal, $u(t)$, can be substituted for $g(t)$ for both simulations. Substituting $u(t)$ for $g(t)$ in Eq. (2.85) yields:

$$I_2(\mathbf{r},t) \cong \Delta A \sum_n r_0^2 \frac{\sigma_n\left(\hat{\alpha}_{nf},\hat{\alpha}_{ni}\right)}{r_{1n}^2 r_{2n}^2} \left|u\left(t-t_{dn}\right)\right|^2 e^{-2\,\mathrm{Im}(k_2) r_{2n}} , \tag{4.1}$$

where t_{dn} is the sum of the propagation time from the source to the nth patch and the propagation time from the nth patch to the receiver. Note that the incoherent intensity is given by $I_2(\mathbf{r},t)/(\rho_2 c_2)$, where $\rho_2 c_2$ is the characteristic impedance of medium 2. The first-order perturbation expression for scattering into the sediment, σ_n, is derived in chapter 3 and given in Eq. (3.77). The exact expression for the time domain coherent intensity is given by Eq. (2.92) divided by the characteristic impedance of medium 2 (also see Fig. 4.1). Since we use the zero-order field to represent the coherent field, the transmission coefficient, $\mathcal{T}$ is substituted for $\mathcal{R}_{12}$ in this figure — which then becomes Eq. (2.92). Following the definition of the coherent reflection coefficient in Thorsos (1990), $\mathcal{R}_{12}$ is defined in chapter 5 to be the coherent transmission coefficient. The power spectrum used for both simulations is that of a filtered power law (Eq. 3.66).

4.3 Tank experiment simulation

This simulation determines the incoherent field scattered into the sand, assuming a small amount of roughness at the interface. A diagram of the tank experiment is shown in Fig 4.2.

4.3.1 Simulation parameters

A source in water just under one half meter above sand transmits a signal with Gaussian envelope and 60 kHz carrier frequency. The baseband source signal used in the simulation is

$$u(t) = \text{constant} \times \mathrm{e}^{-t^2/t_s^2}, \tag{4.2}$$

with $t_s = 33.3\,\mu\text{s}$. This signal approximates the time resolution achieved in the tank experiment. The water sound speed, $c_1 = 1489\,\text{m/s}$, and signal center frequency of 60 kHz correspond to a wavelength of $\lambda = 2.5\,\text{cm}$ in the water. In order to agree with the experiment described in Boyle and Chotiros (1992), the value for constant is chosen such that the field $1\,\text{m}$ from the source is $191\,\mu\text{Pa}$. The sound speed in sand is given by Boyle and Chotiros (1992) to be $c_2 = 1675\,\text{m/s}$. The loss parameter in the sand is not given, and is assumed to be a value appropriate for sand, $\delta = 0.015$, or $0.49\,\text{dB/m/kHz}$. No roughness parameters for the experiment characterizing the rough interface for the sand are given. We assume only a small amount of roughness, and set the filter parameter in Eq. (3.66) to $a = 0.01\,\text{m}$. The spectral exponent and spectral strength in Eq. (3.66) are chosen to be $\gamma = 3$ and $w_2 = 2.17 \times 10^{-5}$, respectively, resulting in an RMS height (Eq. 3.67) of $h = 1\,\text{mm}$ and $k_1 h = 0.25$. This roughness spectrum is well within the range of validity for first-order perturbation theory for scattering through a rough interface (Thorsos, 1996a). Of the three roughness

parameters (a,γ,w_2), $\gamma = 3$ was chosen arbitrarily, but it is consistent with observed seafloor roughness spectra. Values for w_2 and a in Eq. (3.66) are chosen to provide only a small amount of roughness while yielding scattering intensities close to those obtained by Boyle and Chotiros. The roughness spectrum is shown in Fig. 4.3.

4.3.2 Simulation results

As mentioned, the baseband source signal $u(t)$ is substituted for $g(t)$ in Eq. (2.85) for the simulations (Eq. 4.1). The justification for using this simpler model in the tank experiment simulation is shown in Figs 4.4a and 4.4b, where the time-dependent mean square incoherent fields using $u(t)$ and $g(t)$ are compared for two receiver depths, with 2 m transverse distance between source and receiver. At the lower depth, the two cases are almost indistinguishable; at the depth of $0.08\,\mathrm{cm}$, the differences become more noticeable, but are still negligible.

The incoherent intensity (first-order) as a function of time and horizontal distance between source and receiver is shown in Figs 4.5a, 4.5b, and 4.5c for receiver depths of 0.05 m, 0,33 m, and 0.614 m. Since the baseband source signal is Gaussian, the arrival time is the peak of the intensity pulse. The source level is given by Boyle and Chotiros (1992) to be at $191\,\mathrm{dB}$ referenced to $1\,\mu\mathrm{Pa}$ at $1\,\mathrm{m}$ (in the sediment). Figures 4.4a and 4.4b are vertical slices of Figs 4.5a and 4.5b, respectively (in Pa^2 instead of dB). The simulation results have been presented in Figs. 4.5a, 4.5b, and 4.5c for the purpose of direct comparison with Figs. 5, 6, and 7 of Boyle and Chotiros (1992). By choosing the appropriate roughness parameters, these simulations match measured intensity space - time behavior as presented by Boyle and Chotiros (1992), not only in terms of pulse arrival times, but also in terms of the resulting field strength. Although the simulation only contains the incoherent intensity, the coherent contribution, dominates only for incident grazing angles above critical. The curve plotted in

Fig 4.5 is the propagation time for the pulse, assuming the existence of a $1200\,\mathrm{m/s}$ refracted "slow wave." The arrival time of the incoherent intensity pulse coincides with this curve. This agreement occurs for all three depths, as well as over a wide range of incident angles. This model does not allow for slow wave propagation, and the "apparent slow wave" propagation can be accounted for by considering the diffraction path for the signal. A result due to Thorsos (1995) showing the relationship between an apparent slow wave and downward diffracted energy is presented in the next section.

4.4 How roughness can mimic a slow refracted wave

The purpose of this section is to determine the apparent slow wave speed for energy diffracted in a given direction. This derivation follows Thorsos (1995), and allows for the diffracted energy in the sediment to be in directions ranging from straight down to the compressional refracted direction (determined by Snell's law). Figure 4.6 shows a plane wave pulse propagating with a sound speed c_1 and at a sub-critical grazing angle θ_1, incident on a water sediment interface. Two rays strike the interface; the second intersects the interface at a distance d from the first, and at a time τ later than the first. Both rays are scattered by the rough interface, and propagate into the sediment at a grazing angle θ_2 and at a sediment sound speed c_2. The path AB, at a grazing angle

$$\theta_2' = \theta_2 - \theta', \tag{4.3}$$

represents the apparent slow wave refracted direction corresponding to the slow wave speed c_2'. All points perpendicular to this path are therefore taken to have the same total propagation time. From Fig. 4.6,

$$\cos\theta_1 = \frac{c_1\tau}{d} \tag{4.4}$$

and

$$\cos\theta_2' = \frac{c_2'\tau}{d}. \tag{4.5}$$

Solving Eqs. (4.4) and (4.5) for τ, and equating, results in Snell's law for the apparent refracted slow wave direction:

$$\frac{\cos\theta_1}{c_1} = \frac{\cos\theta_2'}{c_2'}. \tag{4.6}$$

Using Eq. (4.3) and

$$c_2' = c_2\cos\theta' \tag{4.7}$$

in Eq. (4.6), and solving for θ', yields

$$\theta' = \tan^{-1}\left[\left(\frac{c_2}{c_1}\cos\theta_1 - \cos\theta_2\right)\Big/\sin\theta_2\right]. \tag{4.8}$$

The apparent refracted grazing angle, θ_2', follows from the above result and Eq. (4.3). The apparent slow wave refracted speed is given by Eq. (4.7).

For the same sound speed ratio used in the simulation, Fig. 4.7 shows the dependence of the apparent slow wave velocity on the scattered grazing angle, θ_2. Figure 4.7 indicates that the apparent slow wave propagation speed of $1200\,\mathrm{m/s}$ in the tank experiment simulations (see Fig. 4.5) corresponds to an "average" scattered grazing angle of about $80°$. Because of loss in the sediment, the average diffraction path is at large grazing angles in a downward direction, as other directions suffer larger absorption loss.

Taking the scattered grazing angle to be $90°$ (straight down), we plot the effect of sediment sound speed and incident grazing angle on the apparent slow wave speed and apparent refracted angle in Fig. 4.8a and Fig. 4.8b, respectively. For this case, $\theta_2 = 90°$, the apparent refracted speed is equivalently expressed as

$$c_2' = \frac{c_2}{\sqrt{1+(c_2/c_1)^2 \cos^2\theta_1}}. \tag{4.9}$$

It is evident from this example that the apparent refracted slow wave speed and the apparent refracted grazing angle do not depend strongly on the sediment sound speed, even for these extreme sediment compressional sound speed examples. Although the apparent slow wave speed increases with increasing incident grazing angle, it is relatively constant for incidence below critical grazing. Below critical grazing is the region of interest, since the refracted component dominates above this angle.

Consequently, roughness can mimic a slow refracted wave ($\cong 1200\,\mathrm{m/s}$), even though the acoustic sound speed is considerably larger ($1675\,\mathrm{m/s}$ in this example). This tank experiment simulation shows that the effects of roughness must be considered in interpretation of penetration experiments.

4.5 Ocean experiment simulation

The tank experiment determines the arrival time of the pulse, but not the direction that the wave propagates. In considering the propagation of the penetrating acoustic field, an ocean experiment using a buried array of receivers (Panama City experiment, Chotiros, 1991, 1995) measures the direction and speed of the intensity front. The results of computer simulations of this experiment using Eq. (4.1) for the incoherent intensity and Eq. (2.92) for the coherent intensity are presented in this section.

4.5.1 Experiment simulation layout

The receiver locations used in the ocean simulation are taken from Fig. 3.3.1 of Chotiros (1991). This array layout is also shown in Fig. 3.4 of Chotiros (1995). As in their analysis of the experimental data, the receiver shown on the y axis

and the receiver farthest out on the x axis (see Fig 3.3.1 of Chotiros, 1991) are not used in the simulation. The layout used in the simulation is shown in Fig. 4.9. The source is at a height of $4\,\mathrm{m}$ above the sediment, positioned along the x axis at several different distances from the array corresponding to incident angles with respect to the array center of $\theta_i = 79°, 40°, 24.9°, 12.7°$, and $9.7°$.

As in Chotiros (1995), the center frequency for the ocean experiment simulations is $20\,\mathrm{kHz}$. The water sound speed, sediment sound speed, and sediment loss parameter are given by Chotiros (1995) to be $c_1 = 1536\,\mathrm{m/s}$, $c_2 = 1729\,\mathrm{m/s}$, and $\delta = 0.0163$ $(.514\,\mathrm{dB/m/kHz})$, respectively, resulting in a critical incident grazing angle of $\theta_i = 27.3°$. The spectral strength and spectral exponent are consistent with Stanic *et al.* (1988), which are from measurements in the vicinity of the experiment ($w_2 = 6.2\times10^{-5}\,\mathrm{m}$ and $\gamma = 3$). The filter truncation parameter (Eq. 3.66), $a = 0.5\,\mathrm{m}$, is chosen to be consistent with the scale of the experiment, resulting in $k_1 h = 0.98$ from Eq. (3.67). Note that the transverse distance between all receivers is within $2a = 1\,\mathrm{m}$. Thorsos (1996a) shows that perturbation theory is valid for scattering through the water-sediment interface with $k_1 h$ as high as 2.0.

4.5.2 First-order intensity model

As in the tank simulation, the baseband source signal $u(t)$ is also substituted for $g(t)$ in Eq. (2.85) for the ocean simulations. The baseband source signal is taken to be

$$u(t) = \mathrm{e}^{-t^2/t_s^2}, \tag{4.10}$$

with $t_s = 100\,\mu\mathrm{sec}$. This pulse width is comparable to that achieved in the actual experiment. As mentioned later, the signal at each receiver is normalized such that the signal peak is the inverse of the number of array elements. Therefore,

the magnitude of the source signal is irrelevant to the simulation. The justification for using this simpler model (Eq. 4.1) for the incoherent intensity is shown in Figs 4.10a and 4.10b, where the mean square incoherent field on the most shallow receiver ($0.05\,\mathrm{m}$ depth) is plotted using both the expression in Eq. (2.85) and Eq. (4.1), that is, $u(t)$ is substituted for $g(t)$ in Eq. (2.85). Although the mean square incoherent field magnitude using the simplification $g(t)=u(t)$ is 22% greater than the result obtained from Eq. (2.85) at a depth of $5\mathrm{cm}$, and 17% greater than the result obtained from Eq. (2.85) at a depth of $18\mathrm{cm}$, the arrival times are not affected by the approximation, $g(t)=u(t)$. Furthermore, the error in incoherent intensity resulting from this simplification does not affect the results presented in this chapter.

4.5.3 Coherent intensity model

Analytical approximations for the integral in Eq. (2.91) can be found (for example, Brekhovskikh, 1980; Ishimaru, 1991). When the incident field is above critical, steepest descent solutions agree closely with the exact numerical solution. Furthermore, for narrowband signals, the received zero-order signal amplitude is determined by the magnitude of the Green's function evaluated at the pulse center frequency. Therefore, the time domain zero-order received pulse can be determined by evaluating the steepest descent solution at the pulse center frequency. Although the approximate steepest descent analytical solutions agree with the numerical solution of Eq. (2.91) very closely for incidence above the critical angle, the solution near critical can differ significantly (Westwood, 1989). In addition, the Green's function is very frequency dependent when the incident field is at or below the critical angle. For this reason, the zero-order transfer function or Green's function is found by evaluating Eq. (2.91) numerically for a discrete range of angular frequencies, ω. In order to obtain the zero-order output pulse at a receiver, the discrete Fourier transform of the source

signal in Eq. (3.21) is multiplied by the corresponding Green's function, and the result is transformed back to the time domain. The resulting exact zero-order time-dependent field magnitude is squared and added to the time-dependent first-order mean square incoherent field. The simpler steepest descent solutions have been used for comparison purposes.

Although the zero-order field will be seen to be somewhat greater than the actual coherent signal (Rice, 1951; Thorsos, 1990) for the values of $k_1 h$ used in these simulations, Chotiros' intensity velocity algorithm is affected only if coherent and incoherent intensities are close in magnitude. As shown in chapter 5, using only the zero-order field to represent the coherent intensity results in coherent intensity calculations about 10% greater than calculations using both the zero-order and second-order contribution. Including the second-order component of the coherent intensity would not produce noticeably different simulation results.

4.5.4 Algorithm for estimating intensity front velocity

Since the receiver locations in Chotiros' ocean penetration experiment are not known precisely enough to use a coherent spatial spectral estimation technique, Chotiros (1995) proposed and used the following intensity speed and direction finding algorithm. This velocity finding algorithm assumes a direction and speed for a plane front of propagating energy, determines the corresponding delays for each receiver with respect to a reference receiver, and then adds normalized and delayed versions of all receiver intensities. If the position of the mth receiver is denoted by $\mathbf{r}_m$ and the reference receiver by $\mathbf{r}_1$, the relative signal delay at the mth receiver with respect to the reference receiver is given by

$$\Delta t_m = \hat{k}_2 \cdot \mathbf{r}_m / c_2' \tag{4.11}$$

for a plane wave traveling in a direction $\hat{k}_2$ and speed c_2'. For a given speed and propagation direction, the normalized received signals are delayed by Eq. (4.11), and then summed. The resulting magnitude is plotted as a function of grazing angle (depression angle) and wave speed values. A peak in the resulting plot occurs when the assumed direction and speed coincide with the actual intensity front. As can be deduced from section 4.4, this type of incoherent processing cannot unambiguously resolve wave velocity. In addition, the intensity front measurement will be off if the flat surface coherent component of the signal dominates at the reference receiver but incoherent diffracted energy dominates at the other receivers.

In order to determine the direction of the intensity front, an array is generally required to span 3-D space (see Appendix D). However, the direction of the intensity front is assumed to have no y component, and the receivers are therefore only required to span the xz plane.

4.5.5 Results

Speed-angle distributions for the five source locations for $\theta_i = 79°, 40°, 24.9°, 12.7°$, and $9.7°$ are shown in Figs. 4.11a, 4.11b, 4.11c, 4.11d, and 4.11e, respectively. Chotiros (1991) states that the receiver at $z = -0.05\,\mathrm{m}$ is usually taken to be the reference receiver. These plots are therefore obtained using the receiver at $z = -0.05\,\mathrm{m}$ for the reference. Figures 4.11a and 4.11b correspond to incidence above the critical grazing angle, and show energy propagating approximately at the sediment sound speed and at angles given approximately by Snell's Law. The curve in the figures obeys Snell's Law. Since the incident grazing angle is above critical in Figs. 4.11a and 4.11b, almost all of the energy penetrating into the sediment is due to the zero-order refracted energy. The coherent intensity due to the flat surface solution is also greater than the

incoherent intensity in Fig. 4.11c, but the first-order incoherent intensity is of comparable magnitude. At sub-critical angles (Figs 4.11d, 4.11e), the energy appears to be propagating at about $1400\,\mathrm{m/s}$, at angles that also agree with Snell's Law for this apparent slow wave speed. This model does not include slow wave propagation; this apparent slow wave propagation is explained by diffractive scattering. Equation (4.6) shows that the diffracted intensity front will always appear to obey Snell's Law.

Although Chotiros reports apparent slow wave propagation at speeds between $1100\,\mathrm{m/s}$ and about $1350\,\mathrm{m/s}$ (see Fig. 6, Chotiros, 1995), we observe an apparent slow wave speed of $1400\,\mathrm{m/s}$ in Figs 4.11c, 4.11d, and 4.11e. However, different choices of roughness spectrum will result in different apparent slow wave speeds. Although the roughness spectrum used in the simulation is suitable for the ocean experiment location, burying receivers into the sediment will likely alter the roughness spectrum at the interface above the receiver. Therefore, it is possible that the roughness spectrum used in the simulation is not an accurate representation of the seafloor at the experiment site. The effect of decreasing the roughness by changing the filter parameter in Eq. 3.66 is shown in section 4.5.7. In the next section, another factor that can affect the apparent slow wave speed is discussed.

4.5.6 Significance of reference receiver choice

The apparent slow wave speed as determined by Chotiros' sound speed and direction finding algorithm can be affected by reference receiver choice. Refraction is dominant when the incident angle is above critical, and diffraction can be dominant at subcritical incidence, depending on the receiver depth and incident grazing angle. Since the refracted path is much shorter for the receivers closest to the interface, the refracted coherent intensity will sometimes dominate over the incoherent intensity only at shallow receivers. In fact, the zero-order

field is negligible for the transverse distance of $19.19\,\mathrm{m}$ between source and receiver (incident grazing $= 12.7°$) at all receiver depths except for the depth of $0.05\,\mathrm{m}$ — the reference receiver. Figures 4.12a, and 4.12b show the mean square incoherent field and square of coherent field magnitude ($1\,\mathrm{Pa}$ at $1\,\mathrm{m}$ from source in water) for all receivers in the simulation as a function of time for the $12.7°$ incidence grazing example. For all receivers except the reference receiver, the mean square incoherent field is much greater than the square of the coherent field magnitude; at the reference receiver, the coherent field is much greater than the incoherent field. Since the refracted path is the fastest, the peak in the incoherent intensity pulse will always arrive after the zero-order component of the coherent pulse. As a result, the relative time delay is greater than would be the case if another receiver were chosen as the reference receiver and the receiver signal at $z = -0.05\,\mathrm{m}$ not included in the intensity velocity algorithm. The apparent slow wave speed using this reference receiver is therefore slightly slower than the apparent slow wave speed using any other receiver. For both incidence at $12.7°$ and $9.7°$, the first-order incoherent intensity is less than the zero-order coherent intensity for the receiver at depth $0.05\,\mathrm{m}$; for all other receivers, the opposite is true. The outputs for $12.7°$ incidence and $9.7°$ incidence are plotted in Figs. 4.13a and 4.13b using the receiver at $z = -0.18\,\mathrm{m}$ as the reference receiver and removing the receiver at $z = -0.05\,\mathrm{m}$. These simulation results show slightly faster apparent slow wave propagation ($1500\,\mathrm{m/s}$) than the results in Figs. 4.11d and 4.11e. Note that this speed is significantly smaller than the sediment sound speed of $1729\,\mathrm{m/s}$.

Note that if the apparent slow wave in the experiments is also due to diffraction, then using any other receiver as the reference than the one at $z = -0.05\,\mathrm{m}$ in the experiment would also result in observation of an apparent slow wave that is faster than would otherwise be observed. It is important to note that the slower the observed apparent slow wave, the greater is this discrepancy.

4.5.7 Effect of the filter parameter

The purpose of this section is to show the effect of the filter parameter a (see Eq. 3.66) on the apparent slow wave speed using Chotiros' speed and direction finding algorithm. In Figs 4.11 and 4.13, the filter parameter $a = 0.5\,\mathrm{m}$, resulting in $k_1 h = 0.5\,\mathrm{m}$, was chosen. Figures 4.14a and 4.14b show speed-angle distributions for the two source locations corresponding to $\theta_i = 12.7°$ and $9.7°$, respectively, for a filter parameter value of $a = 2.0\,\mathrm{m}$ — $k_1 h = 1.96$. As shown by Thorsos (1996a), perturbation theory is valid for this case. As in Fig. 4.13, the receiver at the depth of $0.18\,\mathrm{m}$ is used as the reference receiver, and the receiver at a depth of $0.05\,\mathrm{m}$ is discarded. The differences between Figs. 4.14a and 4.13a and Figs. 4.14b and 4.13b are negligible. Increasing the filter parameter beyond $a = 0.5\,\mathrm{m}$ to a value more than twice as large as the scale of the receiving array has negligible effect on the speed-angle distribution output.

Figs. 4.15a and 4.15b use a filter parameter $a = 0.02\,\mathrm{m}$, resulting in an apparent slow wave speed of about $1200\,\mathrm{m/s}$ — the same as the tank experiment simulation results. Since Chotiros' sound speed and direction finding algorithm measures the propagation of the intensity front, it does not determine the actual direction of propagation. The reason that this algorithm yields a direction and speed corresponding to an apparent refracted slow wave follows from the discussion in section 4.4 (Thorsos, 1995).

4.6 Summary

By modeling sand as a fluid, and including a small amount of roughness $h_{rms} = 1$, the tank simulation results match the acoustical penetration experimental results obtained by Boyle and Chotiros (1992), both in magnitude and in arrival time of the intensity pulse. The simulation results of this tank experiment show that roughness must be included in a sediment penetration

model, and that even a small amount of roughness can account for energy penetrating the interface measured in their experiments.

Although the measured results in the ocean array experiments (Chotiros, 1995) yield an apparent slow wave that is between $50\,\mathrm{m/s}$ and $300\,\mathrm{m/s}$ slower than the results obtained from the simulation, the assumed roughness spectrum may not be an appropriate representation of the experimental site after the receivers were buried. However, the results of this chapter show that diffraction results in apparent slow wave propagation that appears to obey Snell's Law.

Intensity time series simulation

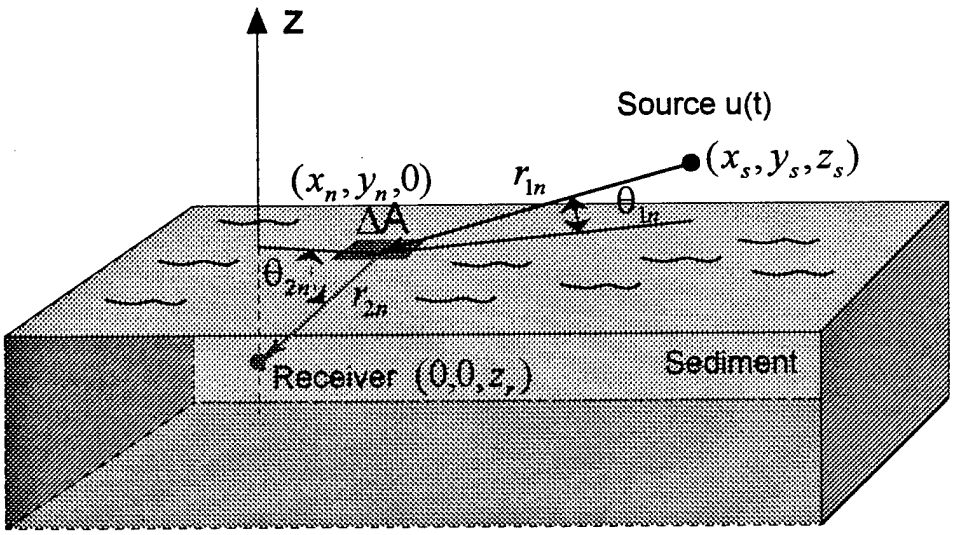

Mean square incoherent field

$$I_2(\mathrm{r},t) \cong \Delta A \sum_{\mathrm{n}} \frac{\sigma_n(\hat{\alpha}_{fn}, \hat{\alpha}_{in})}{r_{1n}^2 r_{2n}^2} r_0^2 g^2(t - t_{dn}) \mathrm{e}^{-2\,\mathrm{Im}(k_2) r_{2n}}$$

Square of coherent field magnitude

$$I_{2c}(\mathrm{r},t) = \left| \int_{-\infty}^{\infty} d\omega\, U(\omega) \mathrm{e}^{-i\omega t} \int_0^{\infty} dK \frac{K r_0 \mathcal{R}_{12}(\mathrm{K})}{k_1 \beta_1(\mathrm{K})} \mathrm{e}^{i(z_s k_1 \beta_1(\mathrm{K}) - z k_2 \beta_2(\mathrm{K}))} J_0(KR) \right|^2$$

Figure 4.1 : Scattering model diagram.

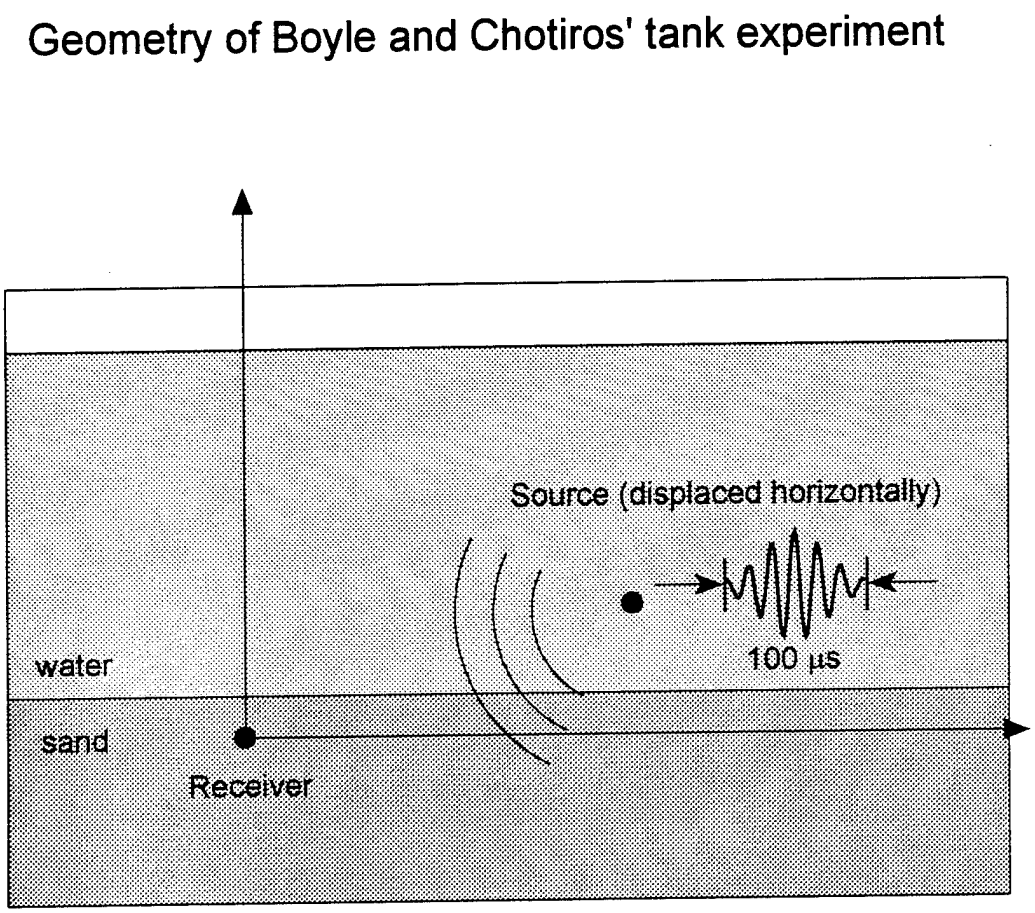

Figure 4.2 : Tank experiment simulation diagram.

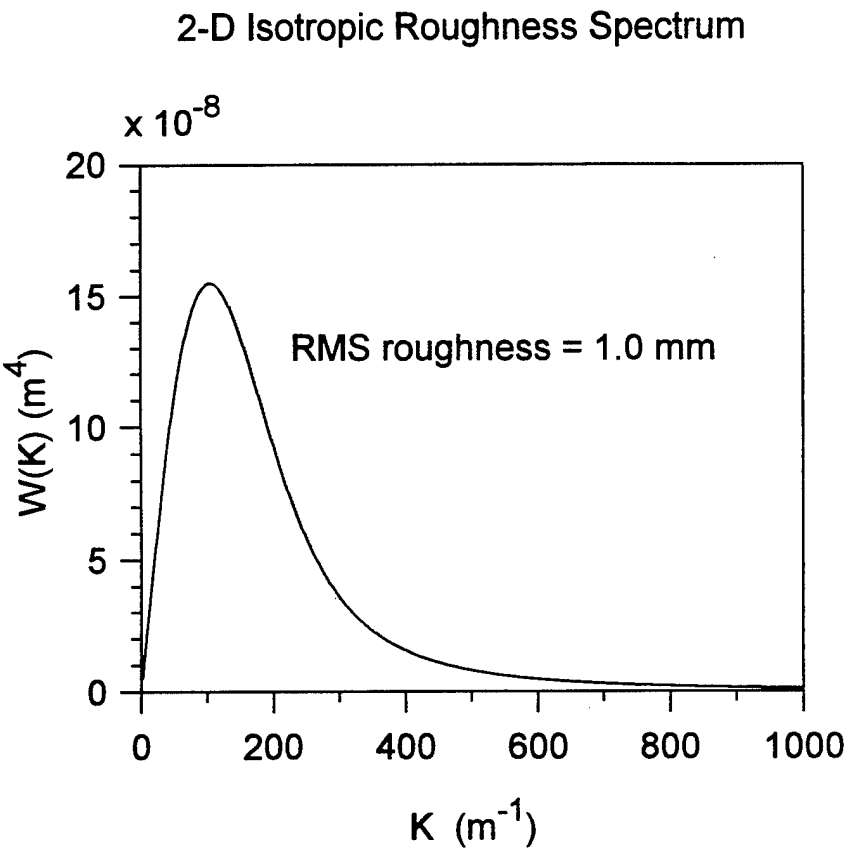

Figure 4.3 : Roughness spectrum used in tank simulation, $a = 0.01\,\mathrm{m}$, $\gamma = 3.0$, $w_2 = 2.17 \times 10^{-5}\,\mathrm{m}$, $h = 1\,\mathrm{mm}$.

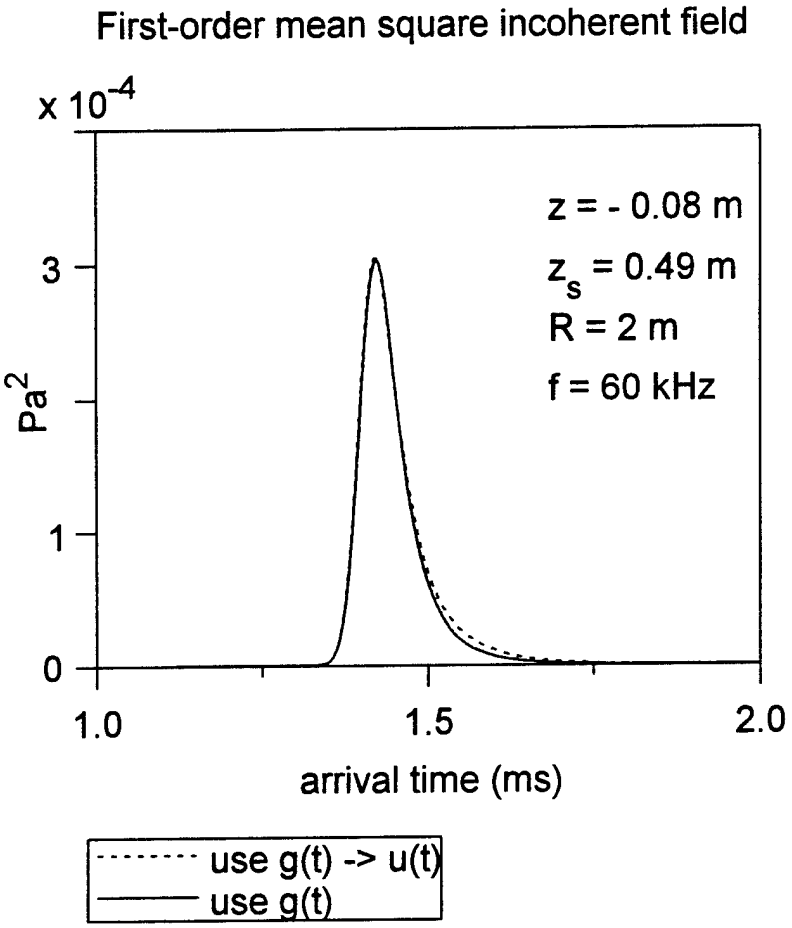

Figure 4.4a : Time-dependent mean square incoherent field determined in tank experiment simulation; solid line uses Eq. (2.85), dotted line uses Eq. (4.1). Roughness parameters are given in Fig. 4.3, frequency = 60 kHz, $\rho = 2.0$, $\delta = 0.015$, $\nu = 1.125$, $c_1 = 1489\,\mathrm{m/s}$, $t_s = 33.33\,\mu\mathrm{s}$. Source height $= 0.49\,\mathrm{m}$, receiver depth $= 0.08\,\mathrm{m}$, transverse distance between source, receiver $= 2\,\mathrm{m}$.

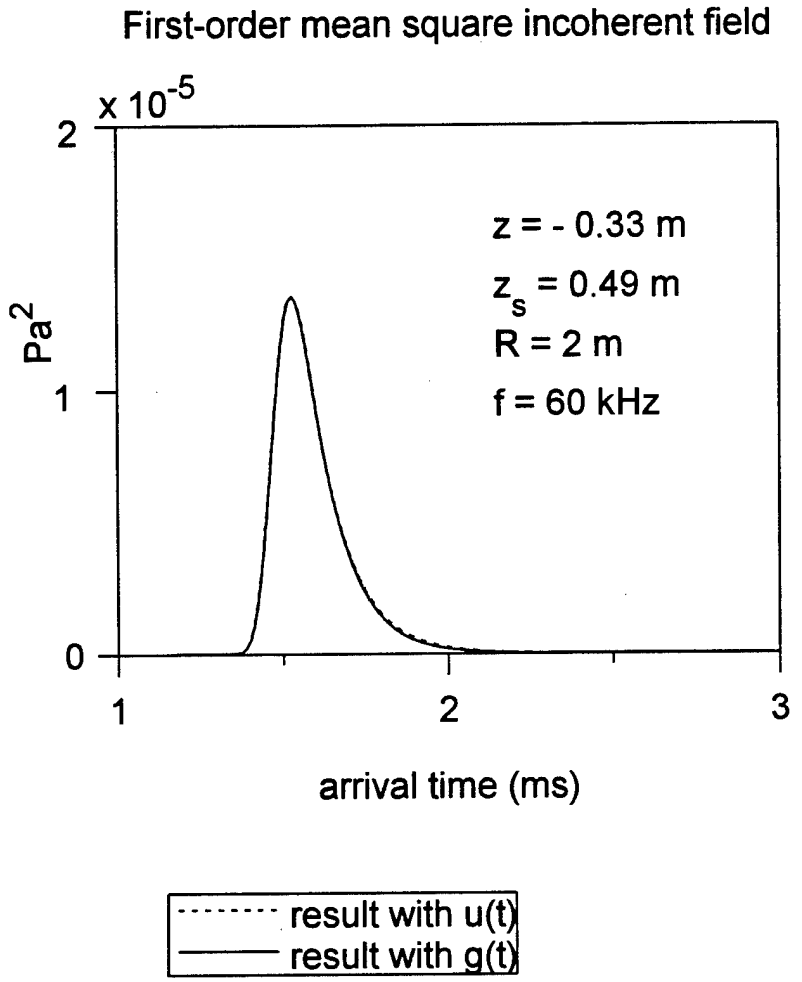

Figure 4.4b : Time-dependent mean square incoherent field determined in tank experiment simulation; solid line uses Eq. (2.85), dotted line uses Eq. (4.1). Receiver depth = 0.33 m , otherwise same parameters as Fig. 4.4a.

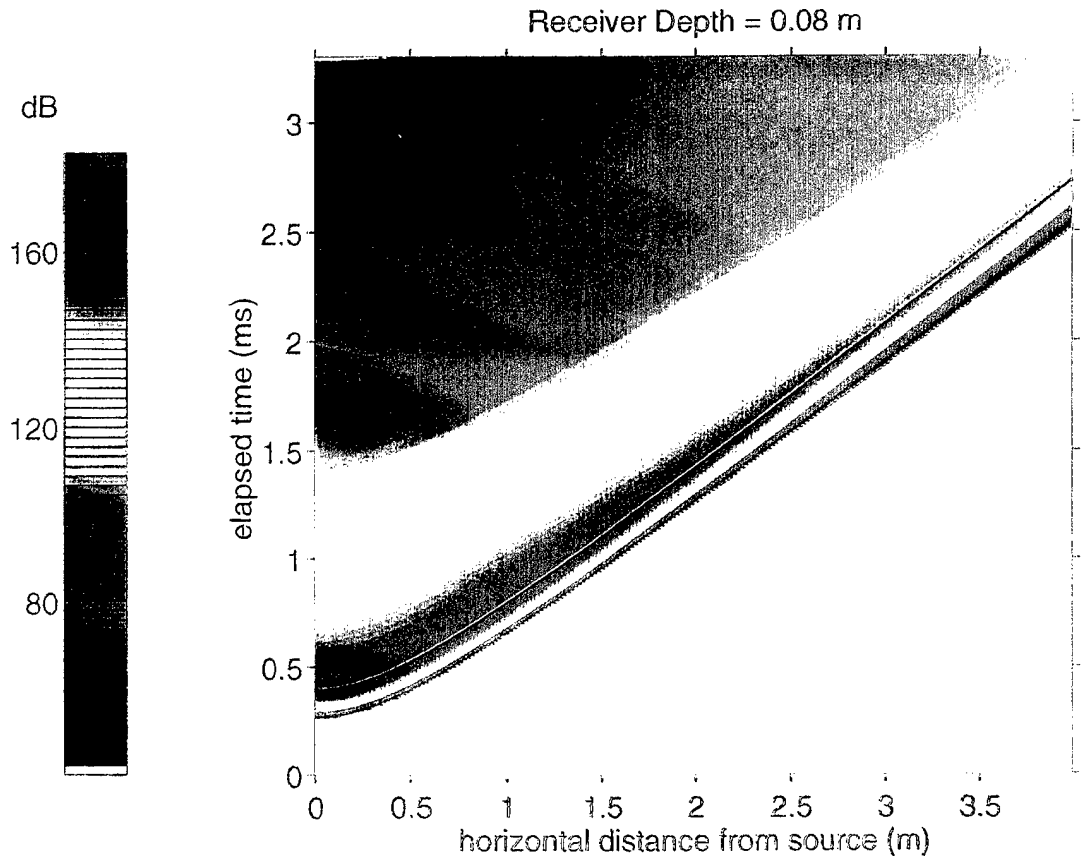

Figure 4.5a : First-order incoherent intensity as a function of time and transverse distance between source and receiver. Arrival time is at pulse peak; black curve corresponds to $1200\,\mathrm{m/s}$ arrival time of apparent slow wave. Same parameters as Figs 4.3, and 4.4 -- frequency $= 60\,\mathrm{kHz}$, $\rho = 2.0$, $\delta = 0.015$, $\nu = 1.125$, $c_1 = 1489\,\mathrm{m/s}$, $t_s = 33.33\,\mu\mathrm{s}$. Source height $= 0.49\,\mathrm{m}$, receiver depth $= 0.08\,\mathrm{m}$.

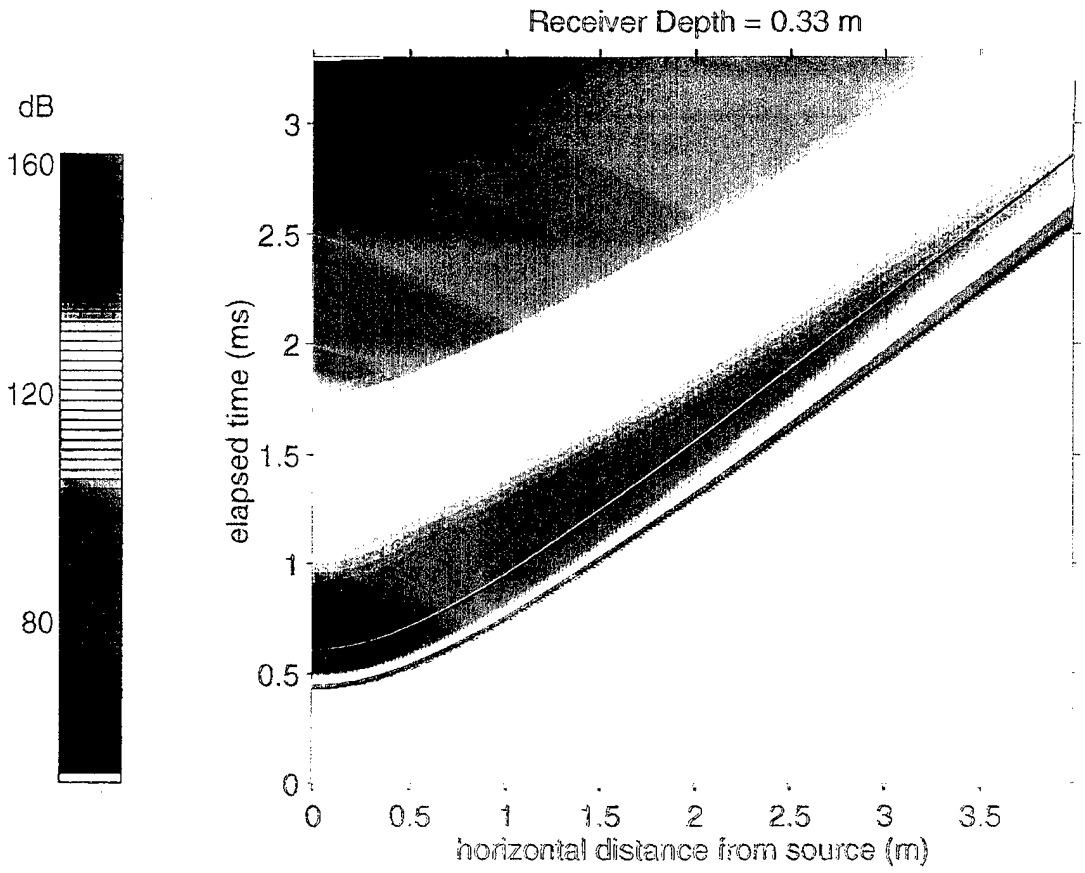

Figure 4.5b : First-order incoherent intensity as a function of time and transverse distance between source and receiver. Receiver depth $= 0.33\,\mathrm{m}$, otherwise same parameters as Fig. 4.5a.

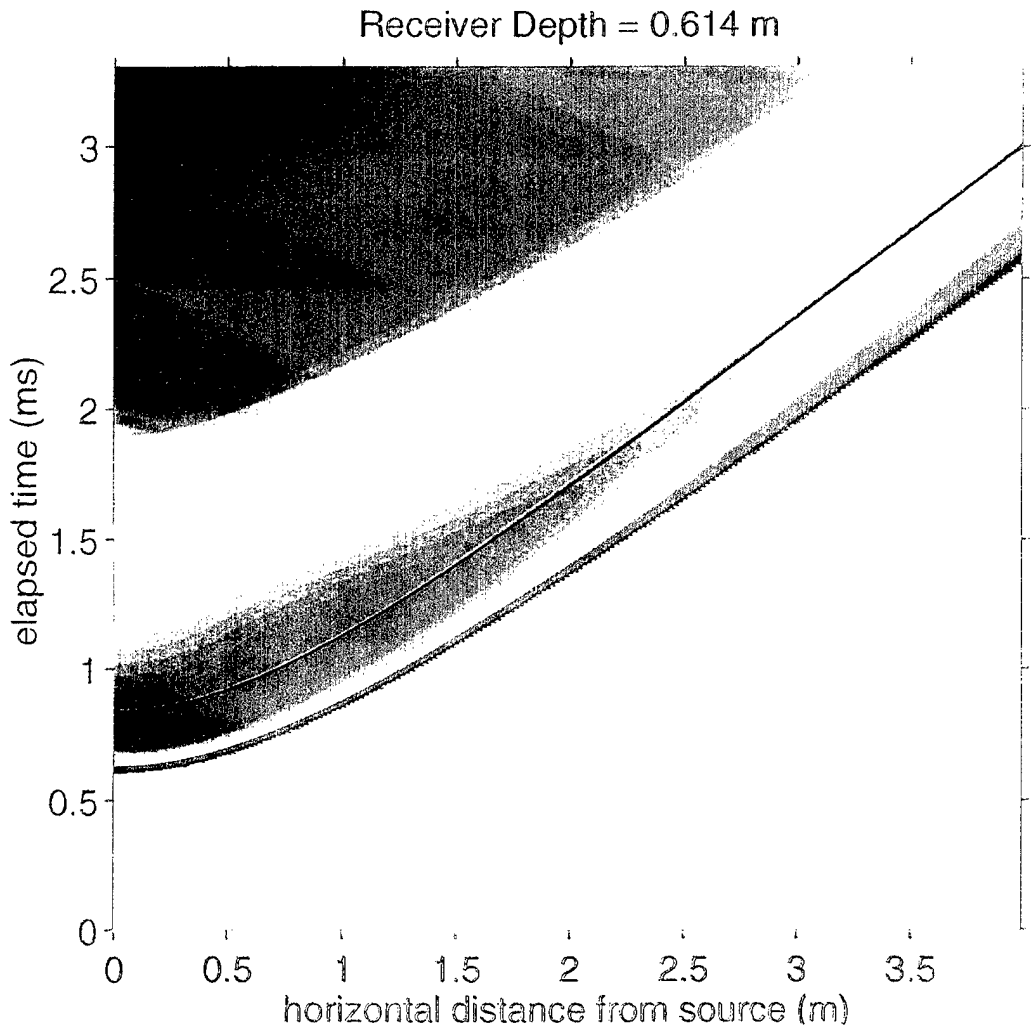

Figure 4.5c : First-order incoherent intensity as a function of time and transverse distance between source and receiver. Receiver depth $= 0.614\,\mathrm{m}$, otherwise same parameters as Fig. 4.5a.

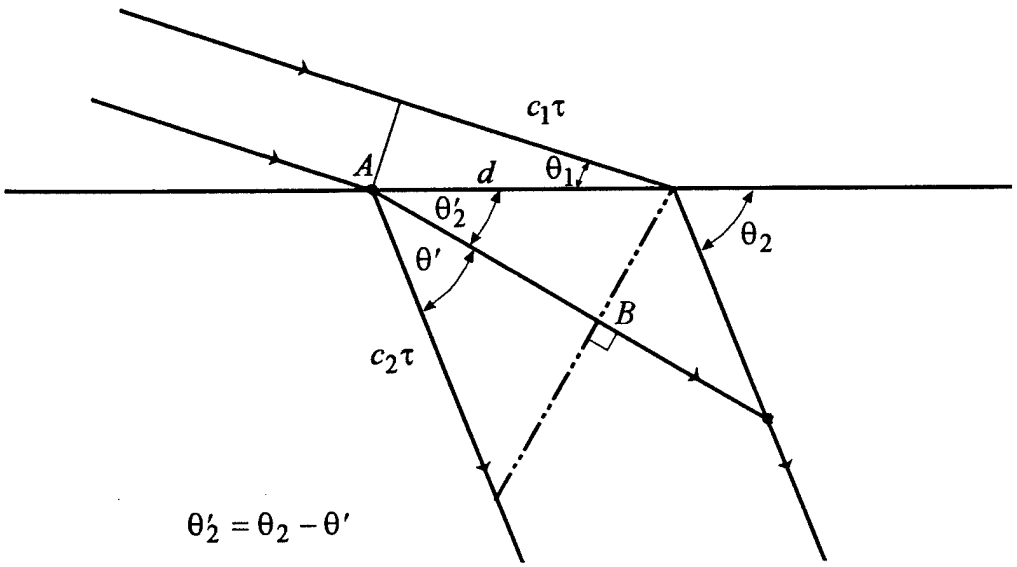

Figure 4.6 : Intensity front diagram; θ_2 represents direction of average diffracted energy propagation, θ_2' represents direction of apparent slow wave.

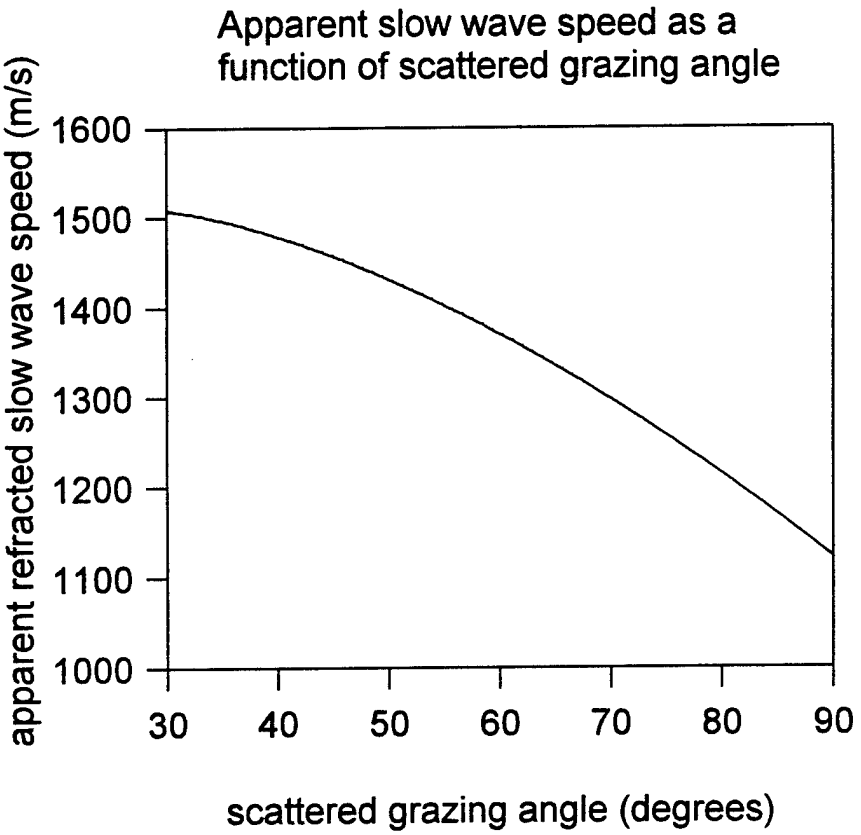

Figure 4.7 : Dependence of the apparent slow wave velocity on scattered grazing angle for incident grazing angle, $\theta_i = 10^\circ$.

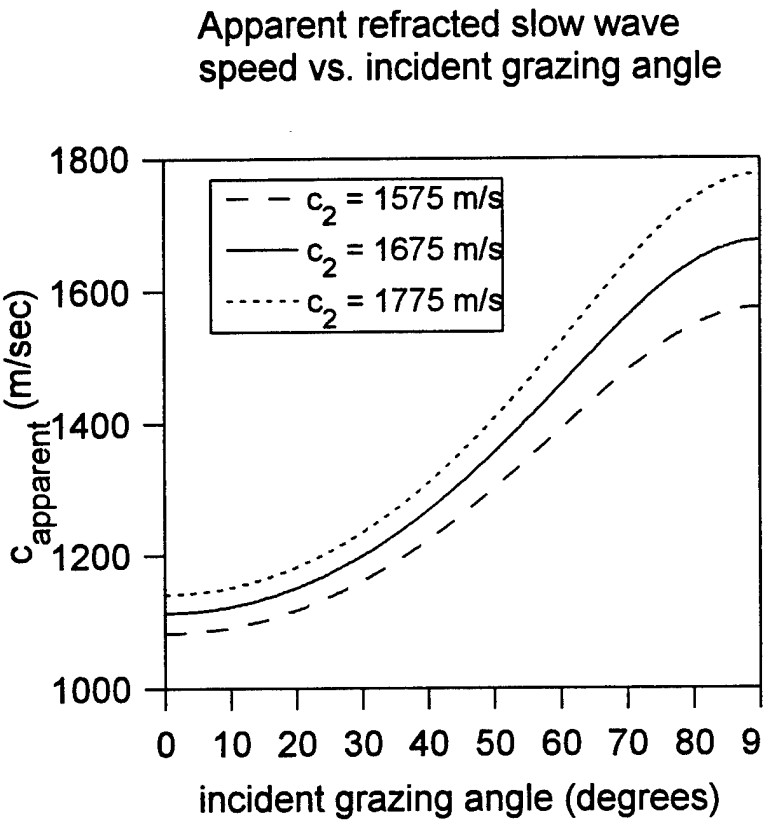

c_2 = compressional wave speed in sediment

Figure 4.8a : Dependence of the apparent slow wave velocity on incident grazing angle assuming average scattered field is straight down.

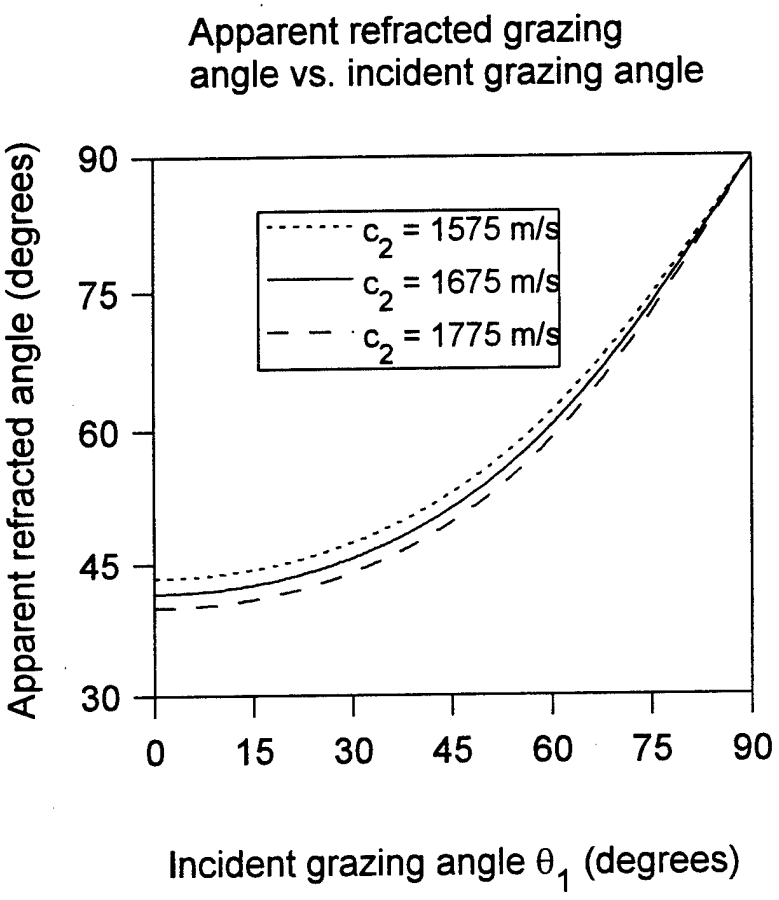

Figure 4.8b : Dependence of the apparent refracted grazing angle on incident grazing angle assuming average scattered field is straight down.

Simulation Layout

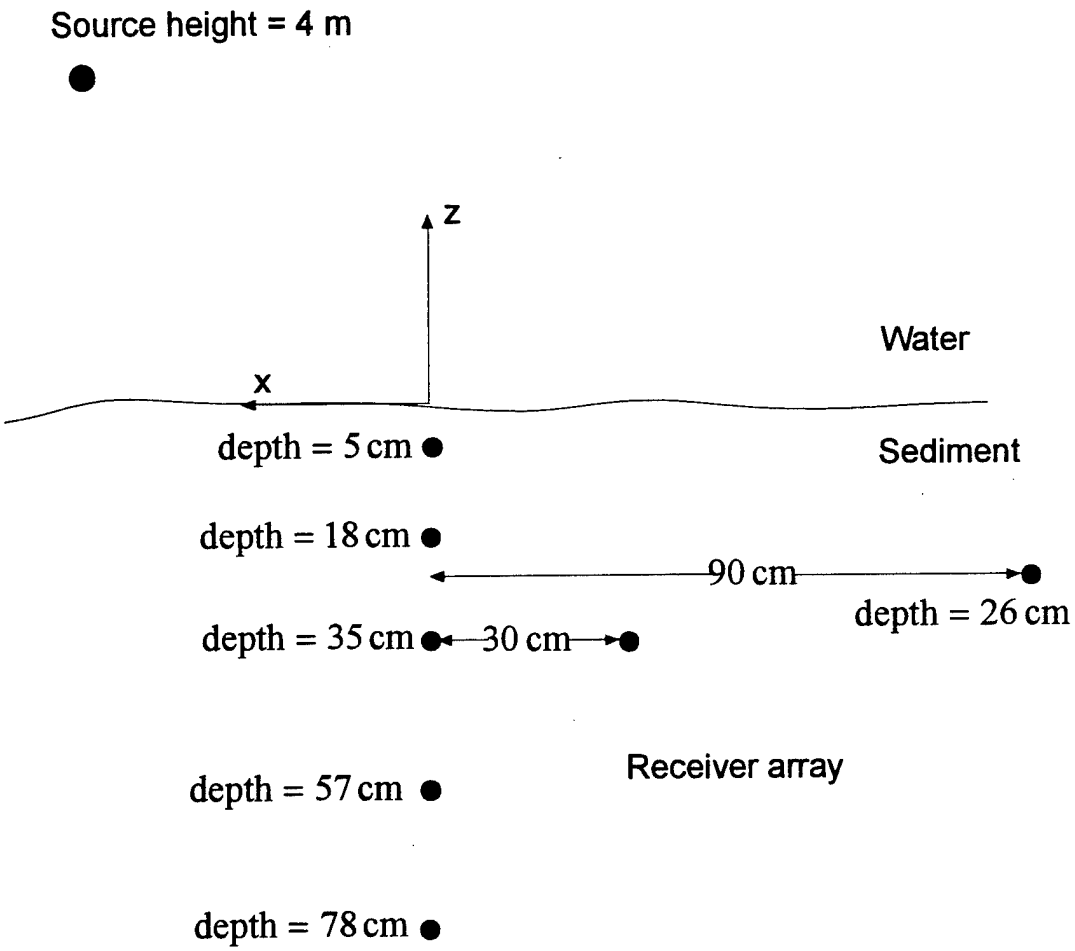

Figure 4.9 : Ocean experiment simulation layout.

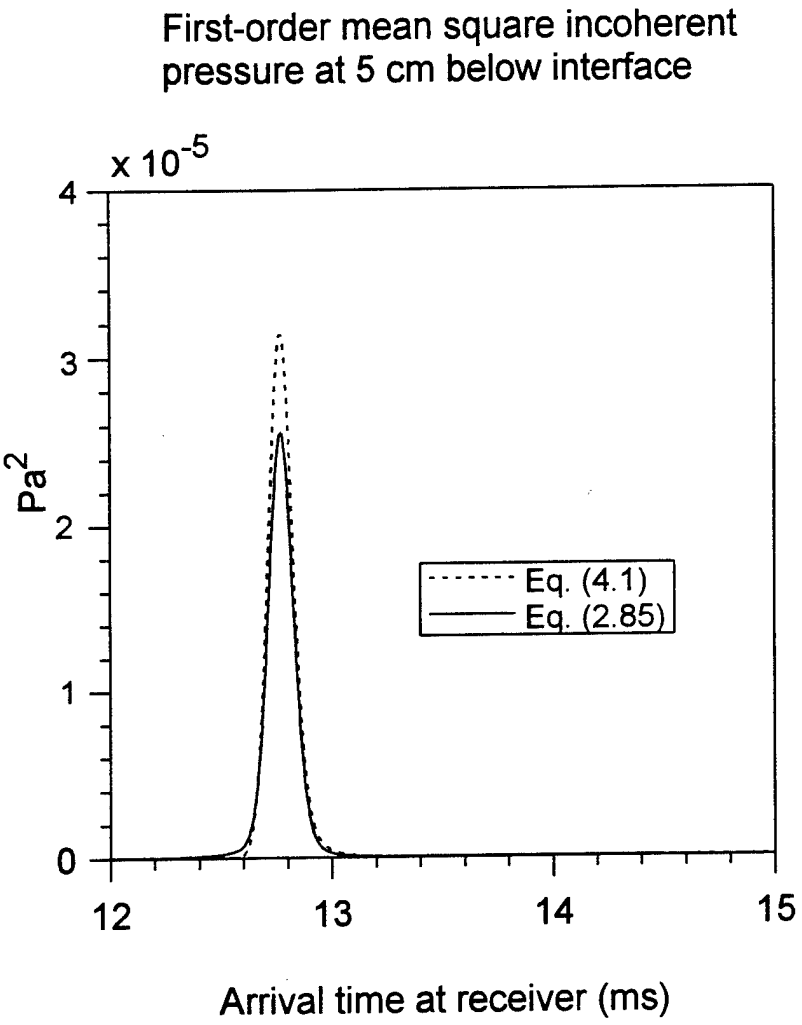

Figure 4.10a : Time-dependent mean square incoherent pressure in ocean experiment simulation for receiver depth = 0.05 m. Solid line uses Eq. (2.85), dotted line uses Eq. (4.1). Transverse distance between source and receiver = 19.19 m, $a = 0.5$ m, $\gamma = 3.0$, $w_2 = 6.2 \times 10^{-5}$ m, $h = 1.2$ cm, frequency = 20 kHz, $\rho = 1.9608$, $\delta = 0.0163$, $\nu = 1.1257$, $c_1 = 1536$ m/s, $t_s = 100\ \mu$s.

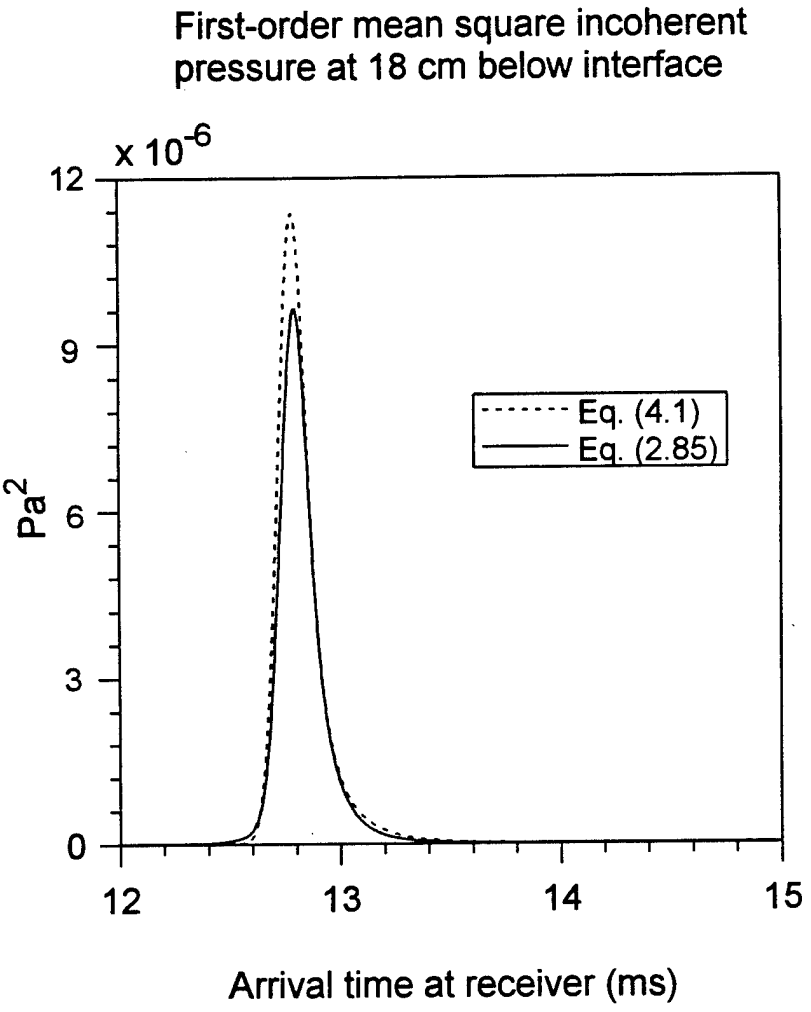

Figure 4.10b : Time-dependent mean square incoherent pressure in ocean experiment simulation for receiver depth $= 0.18\,\mathrm{m}$, otherwise same parameters as Fig. 4.10a.

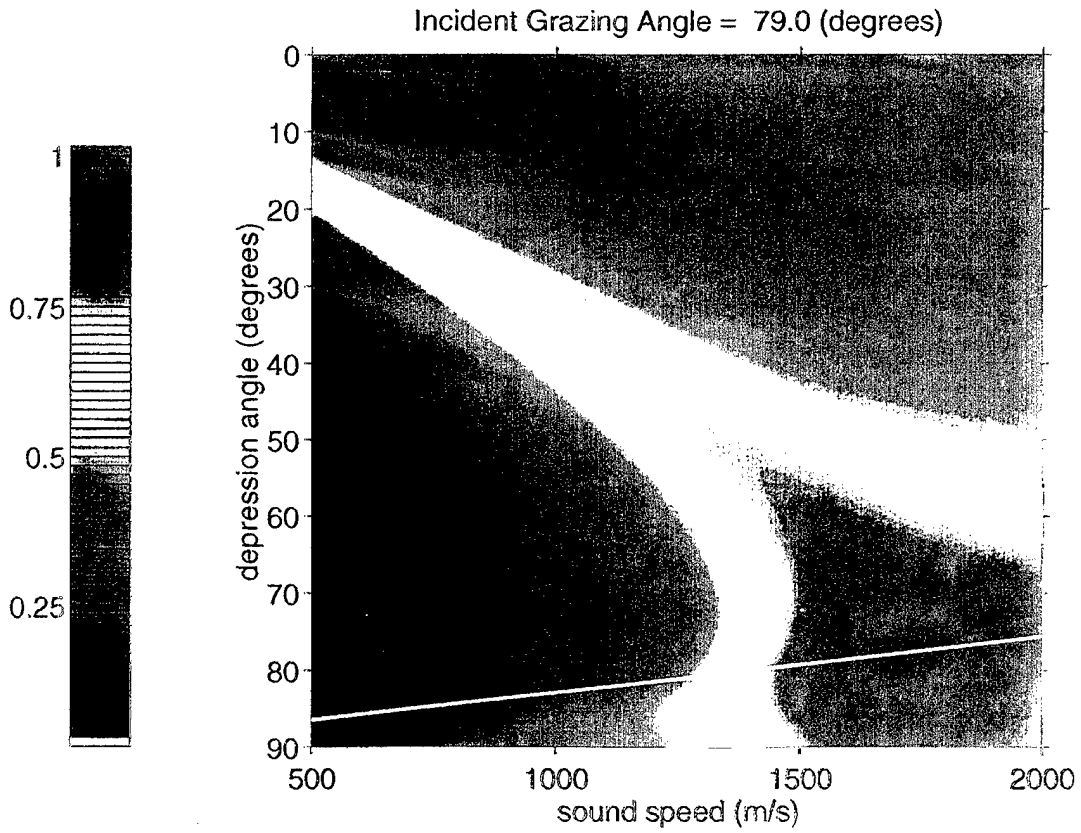

Figure 4.11a : Normalized output intensity of ocean simulation using intensity velocity finding algorithm given in Chotiros (1995). Velocity distribution for $\theta_i = 79^\circ$ (0.43 m transverse distance between source and reference receiver), same parameters as Fig. 4.10. White curve corresponds to energy propagating at speeds and directions coinciding with Snell's law.

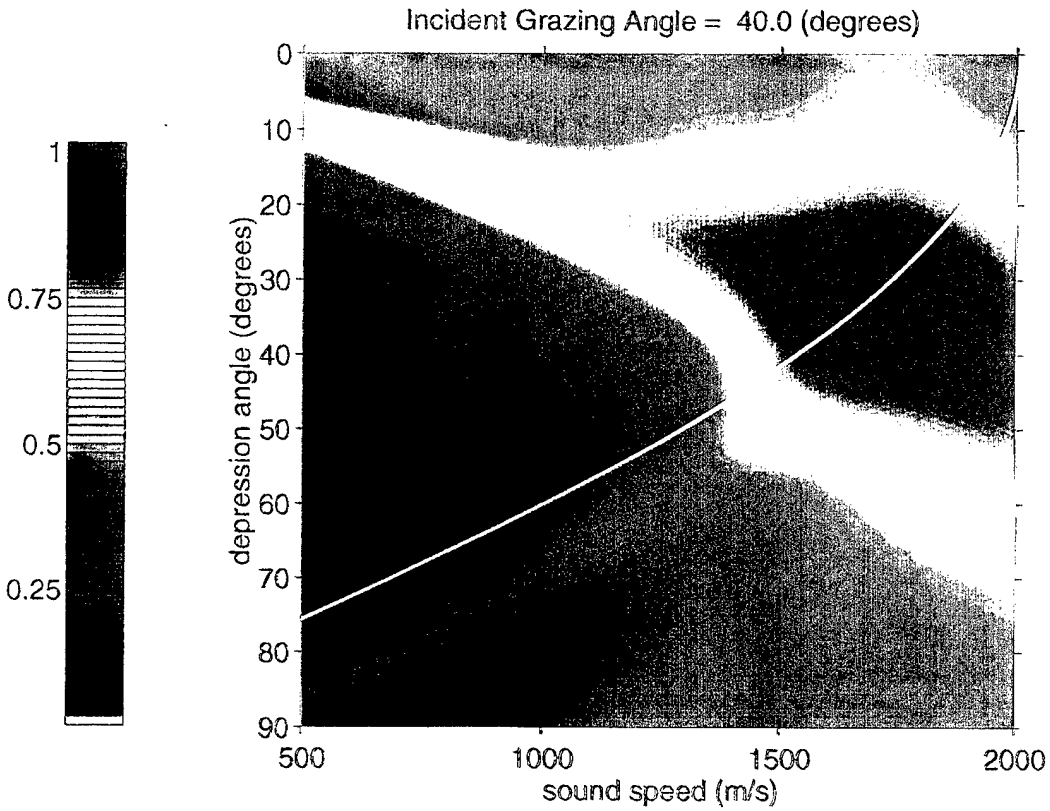

Figure 4.11b : Normalized output intensity of ocean simulation using intensity velocity finding algorithm given in Chotiros (1995). Velocity distribution for $\theta_i = 40^\circ$ (4.91 m transverse distance between source and reference receiver), otherwise same parameters as **Fig. 4.11a.** White curve corresponds to energy propagating at speeds and directions coinciding with Snell's law.

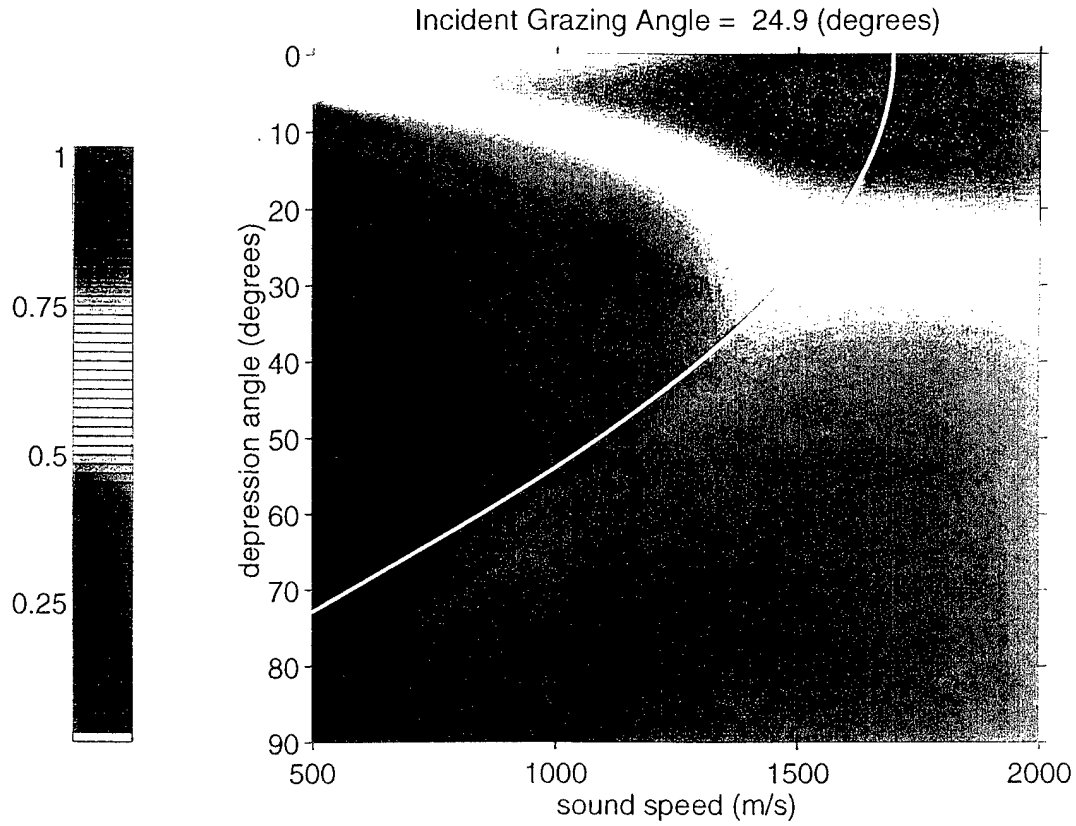

Figure 4.11c : Normalized output intensity of ocean simulation using intensity velocity finding algorithm given in Chotiros (1995). Velocity distribution for $\theta_i = 24.9^\circ$ (9.22 m transverse distance between source and reference receiver), otherwise same parameters as **Fig. 4.11a.** White curve corresponds to energy propagating at speeds and directions coinciding with Snell's law.

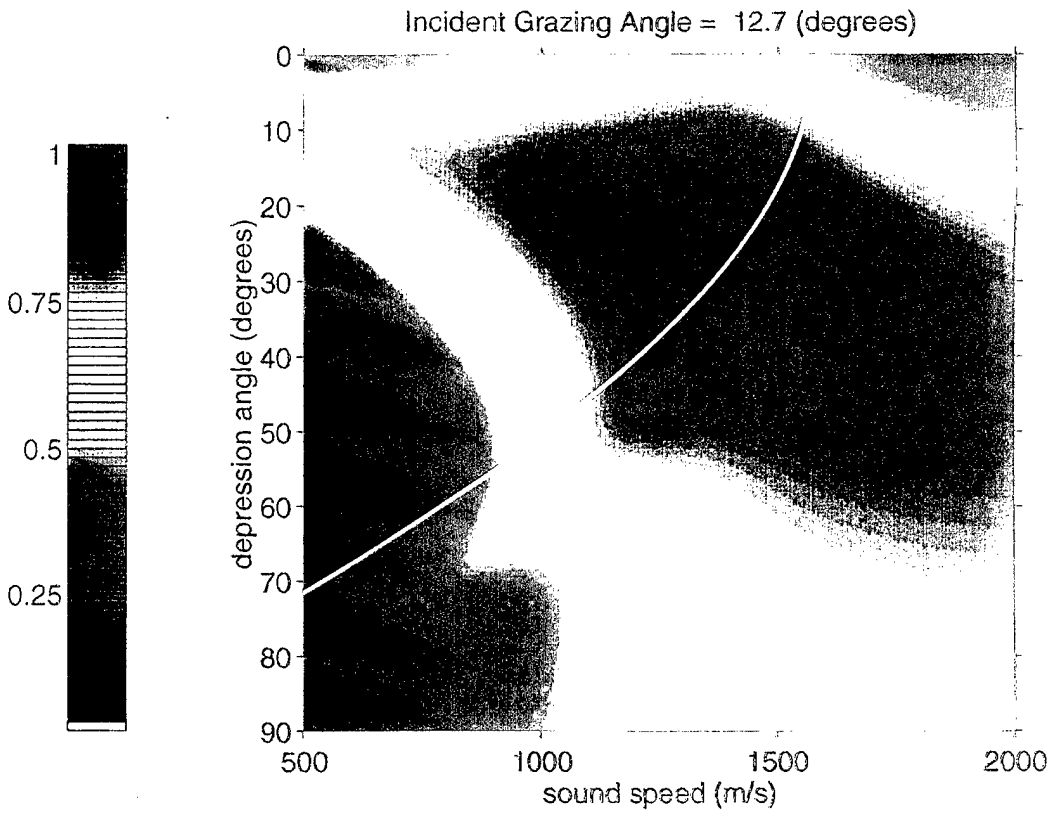

Figure 4.11d : Normalized output intensity of ocean simulation using intensity velocity finding algorithm given in Chotiros (1995). Velocity distribution for $\theta_i = 12.7^\circ$ (19.19 transverse distance between source and reference receiver), otherwise same parameters as Fig. 4.11a. White curve corresponds to energy propagating at speeds and directions coinciding with Snell's law.

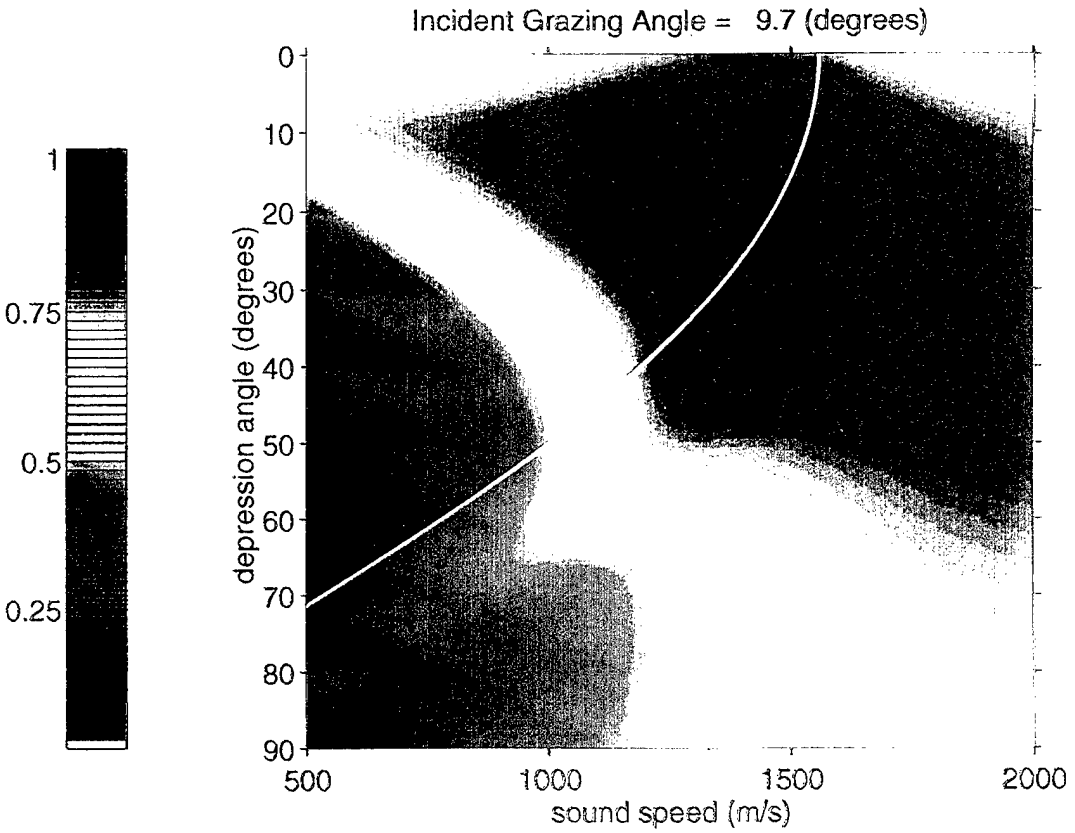

Figure 4.11e : Normalized output intensity of ocean simulation using intensity velocity finding algorithm given in Chotiros (1995). Velocity distribution for $\theta_i = 9.7^\circ$ (25.83 m transverse distance between source and reference receiver), otherwise same parameters as Fig. 4.11a. White curve corresponds to energy propagating at speeds and directions coinciding with Snell's law.

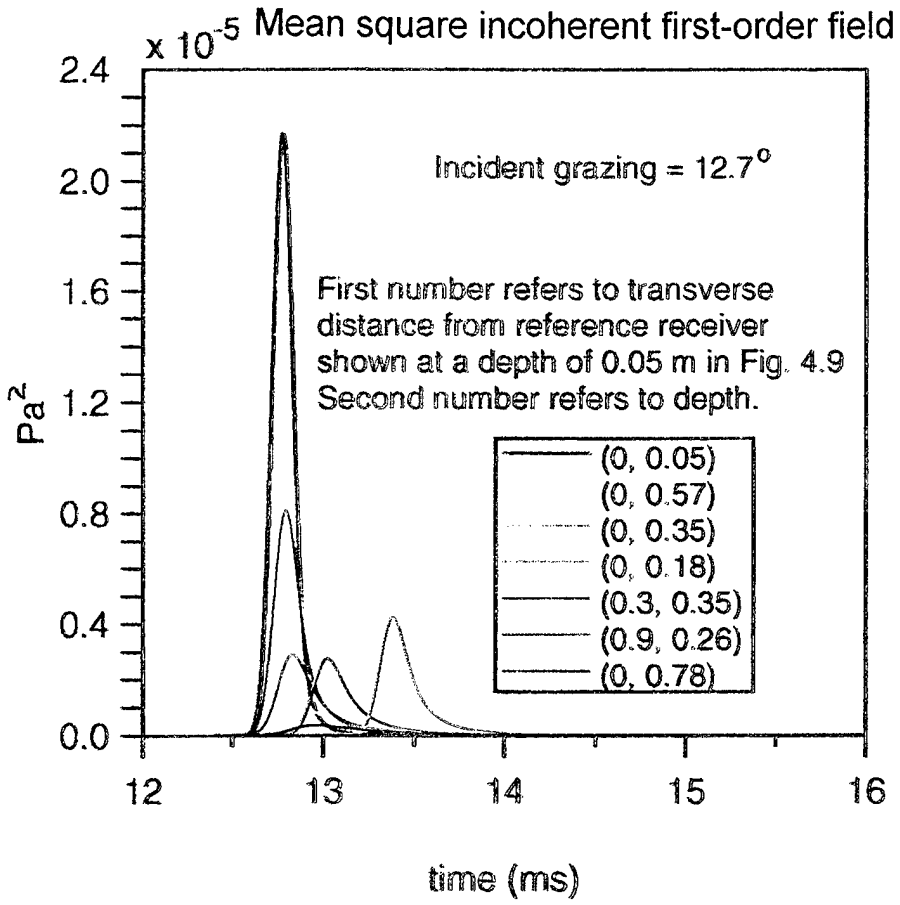

Figure 4.12a : Time dependent mean square incoherent pressure in ocean simulation at each receiver for the 12.7° incidence grazing (Fig. 4.11d example).

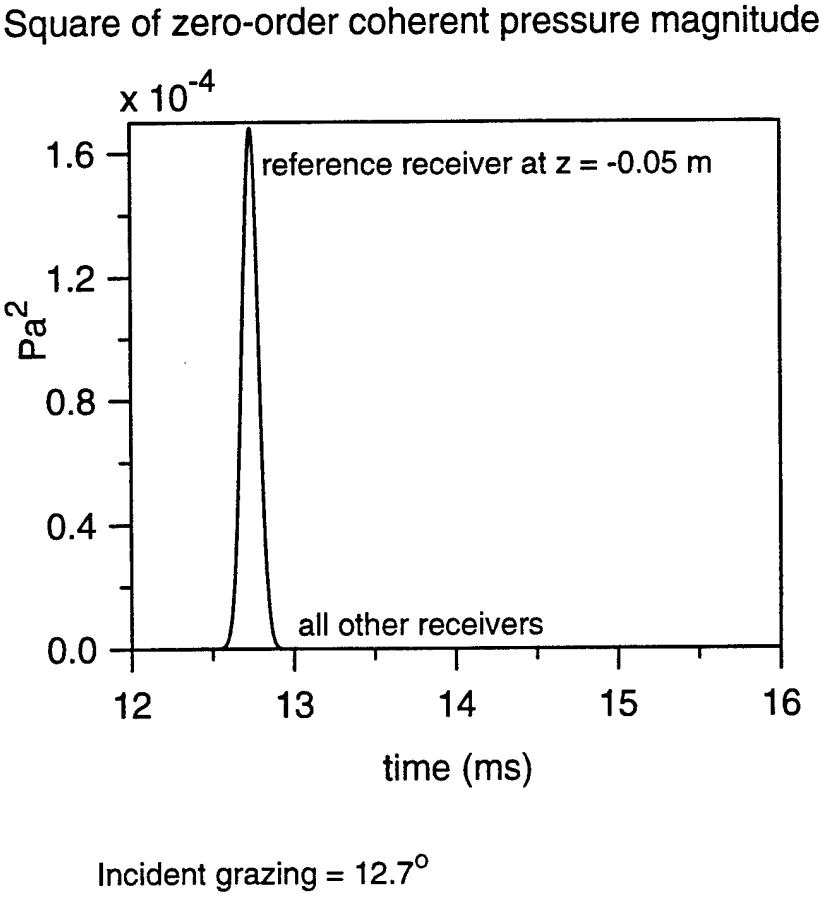

Figure 4.12b : Square of coherent pressure magnitude at each receiver in ocean simulation for the 2.7° incidence grazing (Fig. 4.11e example).

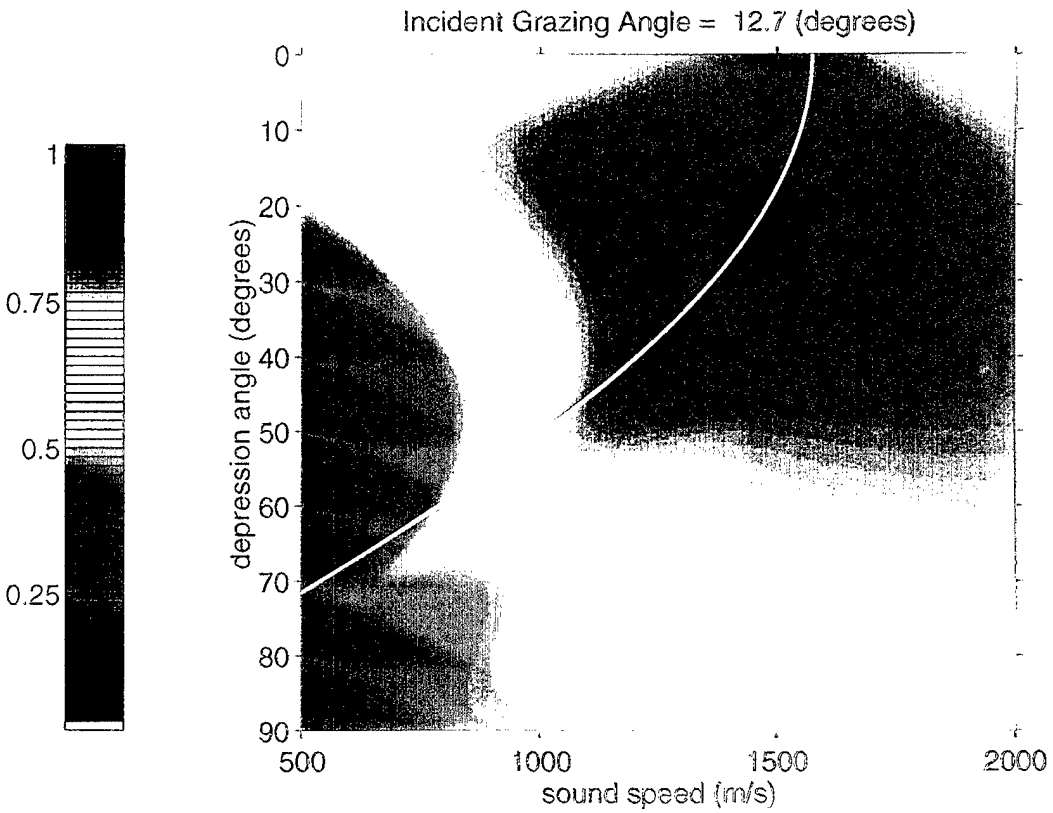

Figure 4.13a : Normalized output intensity of ocean simulation using intensity velocity finding algorithm given in Chotiros (1995). Same parameters as Fig 4.11d except receiver at $z = -0.05\,\mathrm{m}$ is removed, and receiver at $0.18\,\mathrm{m}$ depth (see Fig. 4.9) is used as reference receiver.

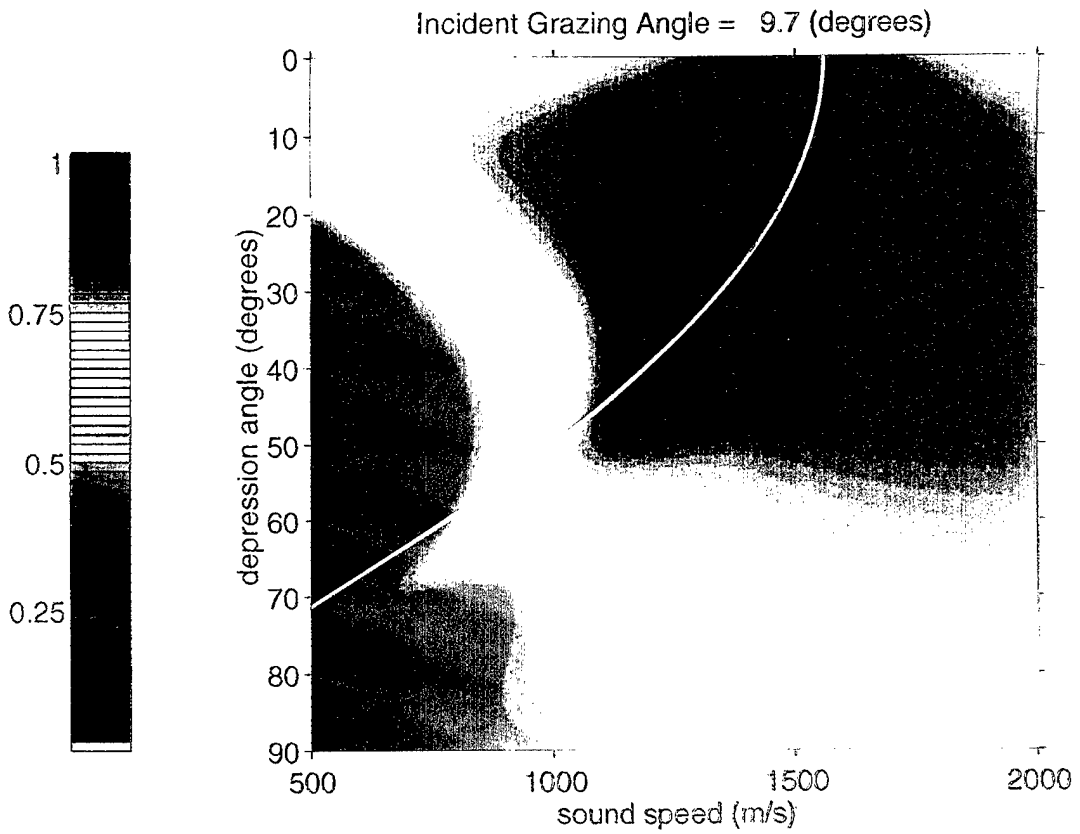

Figure 4.13b : Normalized output intensity of ocean simulation using intensity velocity finding algorithm given in Chotiros (1995). Same parameters as Fig 4.11e except receiver at $z = -0.05\,\mathrm{m}$ is removed, and receiver at $0.18\,\mathrm{m}$ depth (see Fig. 4.9) is used as reference receiver.

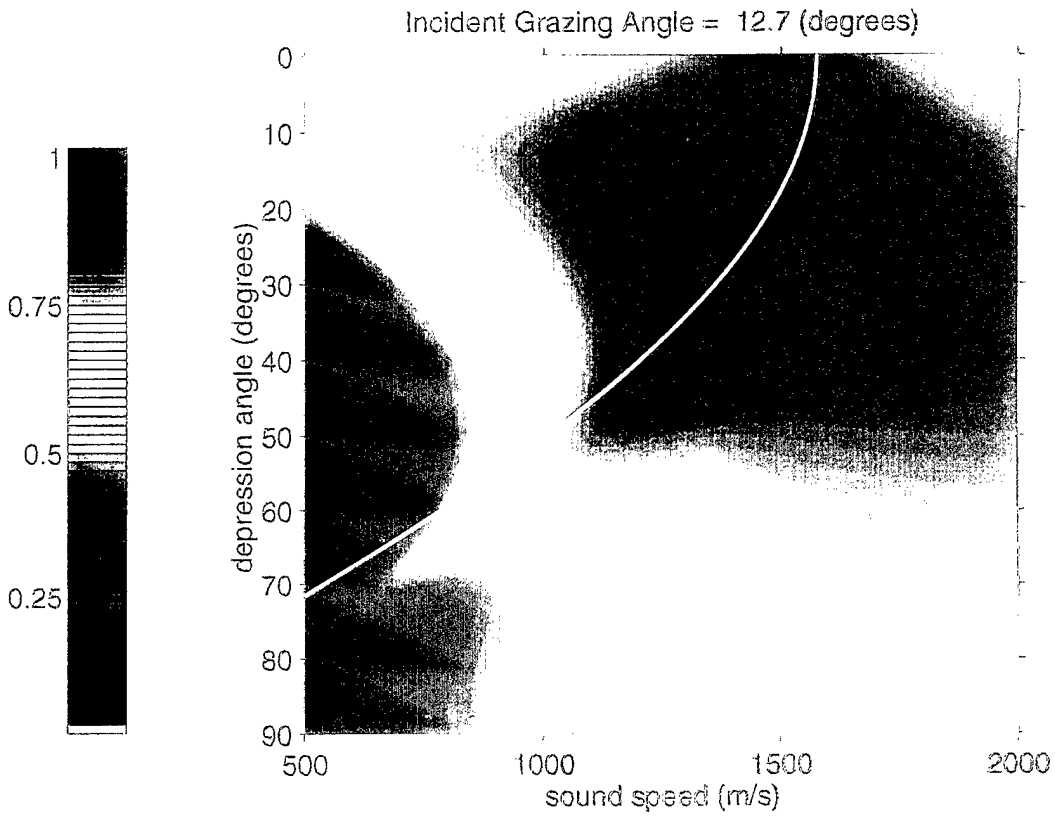

Figure 4.14a : Normalized output intensity of ocean simulation using intensity velocity finding algorithm given in Chotiros (1995). Same parameters as Fig 4.13a except roughness spectrum filter parameter $a = 2.0\,\mathrm{m}$, rather than $a = 0.5\,\mathrm{m}$.

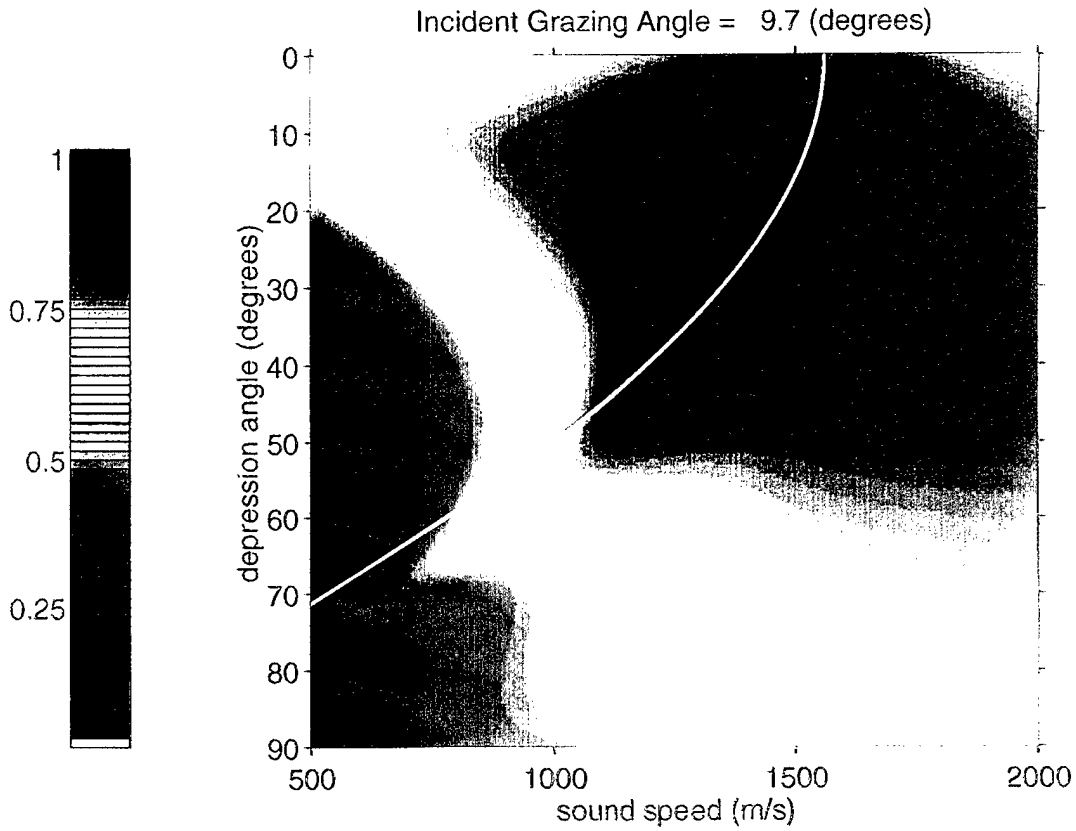

Figure 4.14b : Normalized output intensity of ocean simulation using intensity velocity finding algorithm given in Chotiros (1995). Same parameters as Fig 4.13b except roughness spectrum filter parameter $a = 2.0\,\mathrm{m}$, rather than $a = 0.5\,\mathrm{m}$.

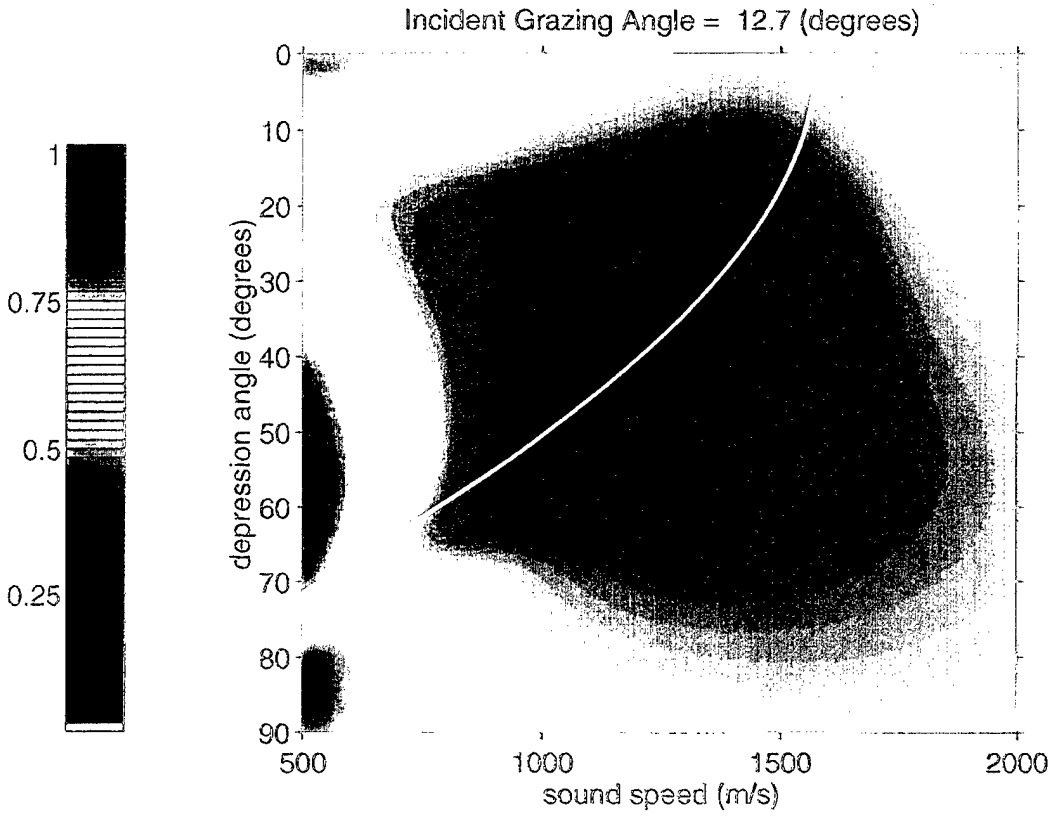

Figure 4.15a : Normalized output intensity of ocean simulation using intensity velocity finding algorithm given in Chotiros (1995). Same parameters as Fig 4.13a except roughness spectrum filter parameter $a = 0.02\,\mathrm{m}$, rather than $a = 0.5\,\mathrm{m}$.

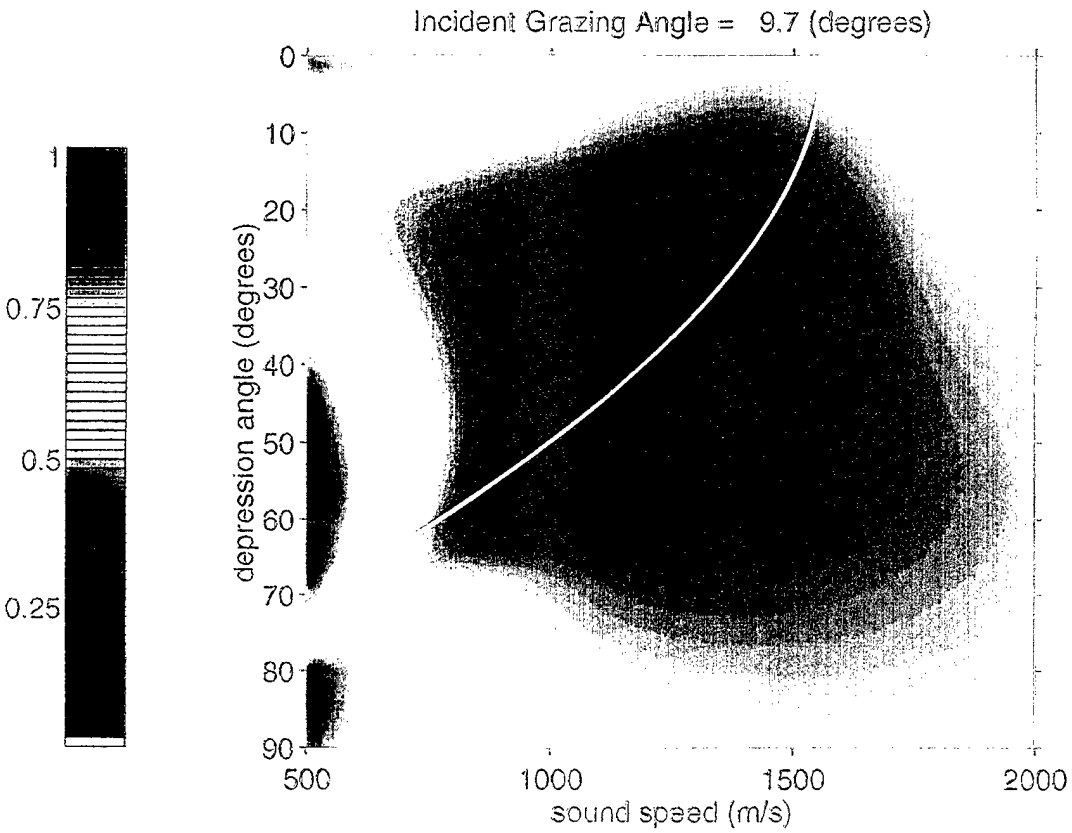

Figure 4.15b : Normalized output intensity of ocean simulation using intensity velocity finding algorithm given in Chotiros (1995). Same parameters as Fig 4.13b except roughness spectrum filter parameter $a = 0.02\,\mathrm{m}$, rather than $a = 0.5\,\mathrm{m}$.

CHAPTER 5

Perturbation derivation including the effect of gradients

5.1 Introduction to chapter 5

Solution to the first-order scattered field from and through a rough interface separating two homogenous fluids is derived in chapter 3. The simulations of the tank and ocean experiments in chapter 4 use first-order perturbation theory to calculate the incoherent scattered intensity, and the flat-surface (zero-order) results are used to calculate the coherent intensity. Although first-order perturbation theory results allow solution for the incoherent intensity proportional to the second power of $k_1 h$, the zero-order solution results in computation of the coherent intensity only to $(k_1 h)^0$. In order to calculate the coherent intensity component proportional to $(k_1 h)^2$, the second-order scattered field is required. The second-order field and second-order coherent field are calculated in this chapter, and compared with the zero-order component of the coherent field.

Since the sediment in both the tank and ocean experiment simulations is modeled as a homogenous fluid, the effect of sound-speed gradients on the scattered field is not included. In this chapter, the sound-speed gradients are included in the model. Moe and Jackson (1994a) take an approach suggested by Winebrenner *et al.* (1995) that allows for layering below the rough interface. Although the medium just below the rough interface is constrained to be a homogenous lossy fluid, the medium below the lowest point on the interface is constrained only to be vertically stratified (see Fig. 5.1), and its complexity is contained in the reflection coefficient for the corresponding flat-surface problem. This approach is used to derive recursion equations that allow for calculation of the Nth-order scattered field. The zero-order field and first-order scattered field

are derived and compared with the results in chapter 3. The second-order field is derived in order to obtain an expression for the second-order component of the coherent field. The second-order coherent field is compared to the flat surface transmitted field. The effect of including sound-speed gradients as well as a shear supporting medium is also discussed.

5.2 Scattering problem

The seafloor is represented as a two dimensional random rough fluid-fluid interface. The geometry of the scattering problem is shown in Fig. 5.1. A pressure field, $\psi_i(\mathbf{r})$, is incident on a 2-D rough interface separating the homogenous lossless fluid in medium 1 (water) from a homogenous lossy fluid in medium 2 (sediment). Unlike the problem in chapter 3, the region below the lowest point on the rough interface ($z=-d$) is arbitrary. As in chapter 3, the total field above the highest point of the rough interface in medium 1 is a sum of an arbitrary incident field, $\psi_i(\mathbf{r})$, and the resulting scattered pressure field, $\psi_f(\mathbf{r})$, and is expressed as

$$\psi_1(\mathbf{r}) = \int d^2K \left[\Psi_i(\mathbf{K}) e^{-ik_1\beta_1(\mathbf{K})z} + \Psi_f(\mathbf{K}) e^{ik_1\beta_1(\mathbf{K})z} \right] e^{i\mathbf{K}\cdot\mathbf{R}}. \tag{5.1}$$

A factor of $e^{-i\omega t}$ is suppressed. Because of the flat interface between medium 2 and medium 3, the field in medium 2, ψ_2, is expressed as a sum of plane waves traveling in the positive z direction, as well as a sum of a plane waves traveling in the negative z direction:

$$\psi_2(\mathbf{r}) = \int d^2K \left[\Psi_{2-}(\mathbf{K}) e^{-ik_2\beta_2(\mathbf{K})z} + \Psi_{2+}(\mathbf{K}) e^{ik_2\beta_2(\mathbf{K})z} \right] e^{i\mathbf{K}\cdot\mathbf{R}}. \tag{5.2}$$

Note that in the absence of upward refracted or reflected energy, $\Psi_{2+}=0$. The derivation proceeds similarly to the derivation in chapter 3. In Eq. (5.1), Ψ_f is unknown; in Eq. (5.2), both Ψ_{2-} and Ψ_{2+} are unknown. Three equations are

required to solve for these three unknowns. Two of the boundary conditions are the continuity of pressure on the interface, given in Eq. (2.2), and the continuity of normal velocity on the interface, given in Eq. (2.4). These boundary conditions are used in the scattered field derivation for the fluid-fluid model in chapter 3. An additional equation is supplied by a technique originated by Winebrenner *et al.* (1995) in their treatment of electromagnetic scattering from rough dielectric surfaces. This third equation uses the general boundary condition that relates Ψ_{2+} to Ψ_{2-} at $z=-d$ in terms of the reflection coefficient Γ_{23} at $z=-d$ for a wave incident from medium 2 to medium 3 (Bucker, 1970):

$$\Gamma_{23}(\mathbf{K})=\frac{\Psi_{2+}(\mathbf{K})}{\Psi_{2-}(\mathbf{K})}\mathrm{e}^{-2ik_2\beta_2(\mathbf{K})d}. \tag{5.3}$$

This equation is key to Winebrenner's approach. All of the complexity of medium 3 is contained in Γ_{23}. Note that media 2 and 3 can both be lossy, with a complex wave number, but the sediment in region 3 is not constrained to be a fluid, e.g., it could be viscoelastic or porous. Furthermore, arbitrary gradients in density and wave number are allowed in medium 3 provided variations are only in z.

The goal of this chapter is to find the scattered field in terms of the incident field. Since

$$\Psi_f(\mathbf{K})=\int d^2K' T_{11}(\mathbf{K},\mathbf{K}')\Psi_i(\mathbf{K}') \tag{5.4}$$

and

$$\Psi_{2-}(\mathbf{K})=\int d^2K' T_{12}(\mathbf{K},\mathbf{K}')\Psi_i(\mathbf{K}') \tag{5.5}$$

(Eq. 3.5 and Eq. 3.6), the scattering problem is solved when the T-matrices T_{11}, and T_{12} are found. Perturbation theory solves this problem by expanding the fields and each T-matrix in terms of a power series representation,

$$\Psi(\mathbf{K}) = \sum_{l=0}^{\infty} \frac{(k_1 h)^n}{n!} \Psi^{(n)}(\mathbf{K}) \tag{5.6}$$

$$T(\mathbf{K},\mathbf{K}_i) = \sum_{l=0}^{\infty} \frac{(k_1 h)^n}{n!} T^{(n)}(\mathbf{K},\mathbf{K}_i), \tag{5.7}$$

and solving one order at a time. Both the factorial and the factor $(k_1 h)^n$ do not need to be displayed, but this representation emphasizes that the perturbation expansion can be viewed as a power series expansion.

5.3 Derivation of Nth-order recursion relation

Although only the zero, first, and second-order fields are derived in this chapter, the results of this section can be used as a starting point to derive higher-order results. An immediate application of higher-order results would be to use the second-order field component as a correction to the first-order coherent field. Higher-order results serve as both a correction and measure of accuracy of lower-order results.

5.3.1 Background

Define the Fourier transform of the nth power of the surface,

$$F_n(\mathbf{K}) \equiv \frac{1}{(2\pi)^2} \int d^2K f^n(\mathbf{R}) \mathrm{e}^{-i\mathbf{K}\cdot\mathbf{R}}, \tag{5.8}$$

so that $F_n(\mathbf{K})$ is obtained from a convolution of $F_{n-1}(\mathbf{K})$ with $F(\mathbf{K})$,

$$F_n(\mathbf{K}) = F_{n-1}(\mathbf{K}) \otimes F(\mathbf{K}). \tag{5.9}$$

Also,

$$F_0(\mathbf{K}) \equiv \delta(\mathbf{K}), \tag{5.10}$$

and

$$F_1(\mathbf{K}) \equiv F(\mathbf{K}), \tag{5.11}$$

is the Fourier transform of the surface profile function. Taking the gradient (Eq. 3.4) of

$$f^{n+1}(\mathbf{R}) = \int d^2K F_{n+1}(\mathbf{K}) \mathrm{e}^{i\mathbf{K}\cdot\mathbf{R}} \tag{5.12}$$

and then dividing by $n+1$ yields

$$\frac{\nabla f^{n+1}(\mathbf{R})}{n+1} = \frac{i}{n+1} \int d^2K\, \mathbf{K} F_{n+1}(\mathbf{K}) \mathrm{e}^{i\mathbf{K}\cdot\mathbf{R}}. \tag{5.13}$$

The following identity,

$$f^n(\mathbf{R}) \nabla f(\mathbf{R}) = \frac{i}{n+1} \int d^2K\, \mathbf{K} F_{n+1}(\mathbf{K}) \mathrm{e}^{i\mathbf{K}\cdot\mathbf{R}}, \tag{5.14}$$

follows from Eq. (5.13) and

$$\nabla f^{n+1}(\mathbf{R}) = (n+1) f^n(\mathbf{R}) \nabla f(\mathbf{R}). \tag{5.15}$$

5.3.2 Continuity of pressure

Invoking the Rayleigh hypothesis, we use Eqs. (5.1) and (5.2) in Eq. (2.3) to obtain the equation of continuity of pressure:

$$\begin{aligned} &\int d^2K \left[\Psi_i(\mathbf{K}) \mathrm{e}^{-ik_1\beta_1(\mathbf{K})hf(\mathbf{R})} + \Psi_f(\mathbf{K}) \mathrm{e}^{ik_1\beta_1(\mathbf{K})hf(\mathbf{R})} \right] \mathrm{e}^{i\mathbf{K}\cdot\mathbf{R}} \\ &= \int d^2K \left[\Psi_{2-}(\mathbf{K}) \mathrm{e}^{-ik_2\beta_2(\mathbf{K})hf(\mathbf{R})} + \Psi_{2+}(\mathbf{K}) \mathrm{e}^{ik_2\beta_2(\mathbf{K})hf(\mathbf{R})} \right] \mathrm{e}^{i\mathbf{K}\cdot\mathbf{R}}. \end{aligned} \tag{5.16}$$

Expanding the exponential terms in a power series,

$$\mathrm{e}^{ik_1\beta_1(\mathbf{K})hf(\mathbf{R})} = \sum_{n=0}^{\infty} \left(i\beta_1(\mathbf{K}) f(\mathbf{R})\right)^n \frac{(k_1 h)^n}{n!}, \tag{5.17}$$

and using Eqs. (5.3), (5.12), and (5.13) yields

$$\int d^2K \sum_{n=0}^{\infty} (i\beta_1(\mathbf{K}))^n \frac{(k_1 h)^n}{n!} \left[\Psi_i(\mathbf{K})(-1)^n + \Psi_f(\mathbf{K})\right] \int d^2K' \, F_n(\mathbf{K}') e^{i(\mathbf{K}+\mathbf{K}')\cdot\mathbf{R}}$$
$$= \int d^2K \sum_{n=0}^{\infty} (i\beta_2(\mathbf{K}))^n \frac{(k_2 h)^n}{n!} \Psi_{2-}(\mathbf{K}) \left\{ \left[(-1)^n + \Gamma_{23} e^{i2k_2\beta_2(\mathbf{K})d}\right] \right.$$
$$\left. \times \int d^2K' F_n(\mathbf{K}') e^{i(\mathbf{K}+\mathbf{K}')\cdot\mathbf{R}} \right\}. \qquad (5.18)$$

After using the operator $\frac{1}{(2\pi)^2} \int d^2R \, e^{-i\mathbf{K}''\cdot\mathbf{R}}$, the above expression is integrated over $\mathbf{R}$, and over $\mathbf{K}$, to obtain

$$\int d^2K \sum_{n=0}^{\infty} (i\beta_1(\mathbf{K}))^n \frac{(k_1 h)^n}{n!} \left[\Psi_i(\mathbf{K})(-1)^n + \Psi_f(\mathbf{K})\right] F_n(\mathbf{K}'' - \mathbf{K})$$
$$= \int d^2K \sum_{n=0}^{\infty} (i\beta_2(\mathbf{K}))^n \frac{(k_2 h)^n}{n!} \Psi_{2-}(\mathbf{K}) \left[(-1)^n + \Gamma_{23} e^{i2k_2\beta_2(\mathbf{K})d}\right] F_n(\mathbf{K}'' - \mathbf{K}). \qquad (5.19)$$

Expanding fields in Eq. (5.19) in a power series (Eq. 5.6) yields

$$\int d^2K \sum_{n=0}^{\infty} (i\beta_1(\mathbf{K}))^n \frac{(k_1 h)^n}{n!} \Psi_i(\mathbf{K})(-1)^n F_n(\mathbf{K}'' - \mathbf{K}) \qquad (5.20)$$
$$+ \int d^2K \sum_{m=0}^{\infty} (i\beta_1(\mathbf{K}))^m \frac{(k_1 h)^m}{m!} \sum_{l=0}^{\infty} \frac{(k_1 h)^l}{l!} \Psi_f^{(l)}(\mathbf{K}) F_m(\mathbf{K}'' - \mathbf{K})$$
$$= \int d^2K \sum_{m=0}^{\infty} (i\beta_2(\mathbf{K}))^m \left\{ \frac{(k_2 h)^m}{m!} \right.$$
$$\left. \times \left[\sum_{l=0}^{\infty} \frac{(k_1 h)^l}{l!} \Psi_{2-}^{(l)}(\mathbf{K}) \left((-1)^m + \Gamma_{23} e^{i2k_2\beta_2(\mathbf{K})d}\right) \right] F_m(\mathbf{K}'' - \mathbf{K}) \right\}$$

Combining powers of $k_1 h$ results in the following expression for the continuity of pressure on the interface:

$$
\begin{aligned}
&\Psi_{2-}^{(N)}(\mathbf{K}'')(\gamma''+1) \\
&\quad = \int d^2K\,(-1)^N \left(i\beta_1(\mathbf{K})\right)^N F_N(\mathbf{K}''-\mathbf{K})\Psi_i(\mathbf{K}) \\
&\quad + \int d^2K \sum_{m=1}^{N} \binom{N}{m} \left(i\beta_1(\mathbf{K})\right)^m F_m(\mathbf{K}''-\mathbf{K})\Psi_f^{(N-m)}(\mathbf{K}) \\
&\quad - \int d^2K \sum_{m=1}^{N} \binom{N}{m} \left(i\kappa\beta_2(\mathbf{K})\right)^m F_m(\mathbf{K}''-\mathbf{K})\left[\gamma+(-1)^m\right]\Psi_{2-}^{(N-m)}(\mathbf{K}) \\
&\quad + \Psi_f^{(N)}(\mathbf{K}''),
\end{aligned}
\tag{5.21}
$$

where

$$
\gamma = \Gamma_{23}(\mathbf{K})\mathrm{e}^{i2k_2\beta_2(\mathbf{K})d}. \tag{5.22}
$$

5.3.3 Continuity of normal velocity

An expression for the equation for continuity of normal velocity on the interface is obtained by substituting Eq. (3.3),

$$
\hat{n} = \frac{\hat{z} - \nabla hf(\mathbf{R})}{|\hat{z} - \nabla hf(\mathbf{R})|}, \tag{5.23}
$$

into Eq. (2.4),

$$
\frac{1}{\rho_1}\hat{n}\cdot\nabla\psi_1(\mathbf{r}) = \frac{1}{\rho_2}\hat{n}\cdot\nabla\psi_2(\mathbf{r})\big|_{z=f(\mathbf{R})}, \tag{5.24}
$$

yielding an expression for the continuity of normal velocity,

$$
\frac{1}{\rho_1}\hat{n}\cdot\nabla\psi_1\Big|_{z=f(\mathbf{R})} = \frac{1}{\rho_1}\frac{1}{N(\mathbf{R})}\left[\frac{\partial\psi_1}{\partial z} - \nabla\psi_1\cdot\nabla hf(\mathbf{R})\right]_{z=f(\mathbf{R})}. \tag{5.25}
$$

Using Eqs. (5.1) and (5.2) in Eq. (5.25) results in the following expression:

$$\frac{1}{\rho_1}\int d^2K\, k_1\beta_1(\mathbf{K})\left[-\Psi_i(\mathbf{K})\mathrm{e}^{-ik_1\beta_1(\mathbf{K})hf(\mathbf{R})}+\Psi_f(\mathbf{K})\mathrm{e}^{ik_1\beta_1(\mathbf{K})hf(\mathbf{R})}\right]\mathrm{e}^{i\mathbf{K}\cdot\mathbf{R}}$$
$$-\frac{1}{\rho_1}\int d^2K\,\mathbf{K}\cdot\nabla(hf(\mathbf{R}))\left[\Psi_i(\mathbf{K})\mathrm{e}^{-ik_1\beta_1(\mathbf{K})hf(\mathbf{R})}+\Psi_f(\mathbf{K})\mathrm{e}^{ik_1\beta_1(\mathbf{K})hf(\mathbf{R})}\right]\mathrm{e}^{i\mathbf{K}\cdot\mathbf{R}}$$
$$=\frac{1}{\rho_2}\int d^2K\, k_2\beta_2(\mathbf{K})\left[-\Psi_{2-}(\mathbf{K})\mathrm{e}^{-ik_2\beta_2(\mathbf{K})hf(\mathbf{R})}+\Psi_{2+}(\mathbf{K})\mathrm{e}^{ik_2\beta_2(\mathbf{K})hf(\mathbf{R})}\right]\mathrm{e}^{i\mathbf{K}\cdot\mathbf{R}}$$
$$-\frac{1}{\rho_2}\int d^2K\,\mathbf{K}\cdot\nabla(hf(\mathbf{R}))\left[\Psi_{2-}(\mathbf{K})\mathrm{e}^{-ik_2\beta_2(\mathbf{K})hf(\mathbf{R})}+\Psi_{2+}(\mathbf{K})\mathrm{e}^{ik_2\beta_2(\mathbf{K})hf(\mathbf{R})}\right]\mathrm{e}^{i\mathbf{K}\cdot\mathbf{R}}, \tag{5.26}$$

which becomes

$$\frac{1}{\rho_1}\int d^2K\, k_1\beta_1(\mathbf{K})\sum_{n=0}^{\infty}\left(i\beta_1(\mathbf{K})f(\mathbf{R})\right)^n\frac{(k_1h)^n}{n!}\left[-\Psi_i(\mathbf{K})(-1)^n+\Psi_f(\mathbf{K})\right]\mathrm{e}^{i\mathbf{K}\cdot\mathbf{R}} \tag{5.27}$$
$$-\frac{1}{\rho_1}\int d^2K\,\mathbf{K}\cdot\nabla(hf(\mathbf{R}))\sum_{n=0}^{\infty}\left(i\beta_1(\mathbf{K})f(\mathbf{R})\right)^n\frac{(k_1h)^n}{n!}\left[\Psi_i(\mathbf{K})(-1)^n+\Psi_f(\mathbf{K})\right]\mathrm{e}^{i\mathbf{K}\cdot\mathbf{R}}$$
$$=\frac{1}{\rho_2}\int d^2K\, k_2\beta_2(\mathbf{K})\sum_{n=0}^{\infty}\left(i\beta_2(\mathbf{K})f(\mathbf{R})\right)^n\frac{(k_2h)^n}{n!}\left[-\Psi_{2-}(\mathbf{K})(-1)^n+\Psi_{2+}(\mathbf{K})\right]\mathrm{e}^{i\mathbf{K}\cdot\mathbf{R}}$$
$$-\frac{1}{\rho_2}\int d^2K\,\mathbf{K}\cdot\nabla(hf(\mathbf{R}))\sum_{n=0}^{\infty}\left(i\beta_2(\mathbf{K})f(\mathbf{R})\right)^n\frac{(k_2h)^n}{n!}\left[\Psi_{2-}(\mathbf{K})(-1)^n+\Psi_{2+}(\mathbf{K})\right]\mathrm{e}^{i\mathbf{K}\cdot\mathbf{R}}$$

with the use of Eqs. (5.6) and (5.17). Using Eqs. (5.3), (5.12), and (5.14) in the above expression yields

$$\frac{1}{\rho_1}\int d^2K\, k_1\beta_1(\mathbf{K})\sum_{n=0}^{\infty}\left(i\beta_1(\mathbf{K})\right)^n\frac{(k_1h)^n}{n!}\left[-(-1)^n\Psi_i(\mathbf{K})+\Psi_f(\mathbf{K})\right] \tag{5.28}$$
$$\times\int d^2K'\, F_n(\mathbf{K}')\mathrm{e}^{i(\mathbf{K}+\mathbf{K}')\cdot\mathbf{R}}$$
$$-\frac{1}{\rho_1}\int d^2Kh\sum_{n=0}^{\infty}\left(i\beta_1(\mathbf{K})\right)^n\frac{(k_1h)^n}{n!}\left[\Psi_i(\mathbf{K})(-1)^n+\Psi_f(\mathbf{K})\right]$$
$$\times\frac{i}{n+1}\int d^2K'\,\mathbf{K}\cdot\mathbf{K}'\,F_{n+1}(\mathbf{K}')\mathrm{e}^{i(\mathbf{K}+\mathbf{K}')\cdot\mathbf{R}}$$
$$=\frac{1}{\rho_2}\int d^2Kk_2\beta_2(\mathbf{K})\sum_{n=0}^{\infty}\left(i\beta_2(\mathbf{K})\right)^n\frac{(k_2h)^n}{n!}\Psi_{2-}(\mathbf{K})\left[-(-1)^n+\Gamma_{23}\mathrm{e}^{i2k_2\beta_2(\mathbf{K})d}\right]$$
$$\times\int d^2K'\,F_n(\mathbf{K}')\mathrm{e}^{i(\mathbf{K}+\mathbf{K}')\cdot\mathbf{R}}$$
$$-\frac{1}{\rho_2}\int d^2Kh\sum_{n=0}^{\infty}\left(i\beta_2(\mathbf{K})\right)^n\frac{(k_2h)^n}{n!}\Psi_{2-}(\mathbf{K})\left[(-1)^n+\Gamma_{23}\mathrm{e}^{i2k_2\beta_2(\mathbf{K})d}\right]$$
$$\times\frac{i}{n+1}\int d^2K'\mathbf{K}\cdot\mathbf{K}'\,F_{n+1}(\mathbf{K}')\mathrm{e}^{i(\mathbf{K}+\mathbf{K}')\cdot\mathbf{R}}.$$

Equation (5.28) is integrated over $\mathbf{R}$ using $\frac{1}{(2\pi)^2}\int d^2R\,\mathrm{e}^{-i\mathbf{K}''\cdot\mathbf{R}}$, and over $\mathbf{K}$. The substitution in Eq. (5.22) is made, yielding the equivalent expression,

$$\frac{1}{\rho_1}\int d^2K\, k_1\beta_1(\mathbf{K})\sum_{n=0}^{\infty}\left(i\beta_1(\mathbf{K})\right)^n\frac{(k_1h)^n}{n!}\left[-(-1)^n\Psi_i(\mathbf{K})+\Psi_f(\mathbf{K})\right]F_n(\mathbf{K}''-\mathbf{K}) \tag{5.29}$$
$$-\frac{i}{\rho_1}\int d^2Kh\sum_{n=0}^{\infty}\left(i\beta_1(\mathbf{K})\right)^n\frac{(k_1h)^n}{n!}\left[\Psi_i(\mathbf{K})(-1)^n+\Psi_f(\mathbf{K})\right]\frac{\mathbf{K}\cdot(\mathbf{K}''-\mathbf{K})}{n+1}F_{n+1}(\mathbf{K}''-\mathbf{K})$$
$$=\frac{1}{\rho_2}\int d^2K\, k_2\beta_2(\mathbf{K})\sum_{n=0}^{\infty}\left(i\beta_2(\mathbf{K})\right)^n\frac{(k_2h)^n}{n!}\Psi_{2-}(\mathbf{K})\left[-(-1)^n+\gamma\right]F_n(\mathbf{K}''-\mathbf{K})$$
$$-\frac{i}{\rho_2}\int d^2Kh\sum_{n=0}^{\infty}\left(i\beta_2(\mathbf{K})\right)^n\frac{(k_2h)^n}{n!}\Psi_{2-}(\mathbf{K})\left[(-1)^n+\gamma\right]\frac{\mathbf{K}\cdot(\mathbf{K}''-\mathbf{K})}{n+1}F_{n+1}(\mathbf{K}''-\mathbf{K}).$$

Dividing the above expression by k_1, multiplying by ρ_1, and expanding in a power series — Eq. (5.6) — yields

$$\int d^2K\beta_1(\mathbf{K})\sum_{n=0}^{\infty}(i\beta_1(\mathbf{K}))^n\frac{(k_1h)^n}{n!}\left[-(-1)^n\Psi_i(\mathbf{K})+\sum_{l=0}^{\infty}\frac{(k_1h)^l}{l!}\Psi_f^{(l)}(\mathbf{K})\right]F_n(\mathbf{K}''-\mathbf{K})$$

$$-i\int d^2K\sum_{n=0}^{\infty}(i\beta_1(\mathbf{K}))^n\frac{(k_1h)^{n+1}}{(n+1)!}$$

$$\times\left[\Psi_i(\mathbf{K})(-1)^n+\sum_{l=0}^{\infty}\frac{(k_1h)^l}{l!}\Psi_f^{(l)}(\mathbf{K})\right]\frac{\mathbf{K}\cdot(\mathbf{K}''-\mathbf{K})}{k_1^2}F_{n+1}(\mathbf{K}''-\mathbf{K})$$

$$=\frac{1}{\rho}\int d^2K\kappa\beta_2(\mathbf{K})\sum_{n=0}^{\infty}(i\beta_2(\mathbf{K}))^n\frac{(k_2h)^n}{n!}$$

$$\times\sum_{l=0}^{\infty}\frac{(k_1h)^l}{l!}\Psi_{2-}^{(l)}(\mathbf{K})\left[-(-1)^n+\gamma\right]F_n(\mathbf{K}''-\mathbf{K})$$

$$-\frac{i}{\rho}\int d^2K\sum_{n=0}^{\infty}(i\beta_2(\mathbf{K}))^n\frac{(k_2h)^{n+1}}{(n+1)!}\sum_{l=0}^{\infty}\frac{(k_1h)^l}{l!}\Psi_{2-}^{(l)}(\mathbf{K})$$

$$\times\left[(-1)^n+\gamma\right]\frac{\mathbf{K}\cdot(\mathbf{K}''-\mathbf{K})}{\kappa k_1^2}F_{n+1}(\mathbf{K}''-\mathbf{K}). \qquad (5.30)$$

Separating terms, renumbering indices (setting $n=l+m$), and equating like powers of k_1h yields

$$
\begin{aligned}
&-\int d^2K\,\beta_1(\mathbf{K})\frac{(-1)^N\left(i\beta_1(\mathbf{K})\right)^N}{N!}\Psi_i(\mathbf{K})F_N(\mathbf{K}''-\mathbf{K})\\
&+\int d^2K\,\beta_1(\mathbf{K})\sum_{m=0}^{N}\frac{\left(i\beta_1(\mathbf{K})\right)^m}{m!(N-m)!}\Psi_f^{(N-m)}(\mathbf{K})F_m(\mathbf{K}''-\mathbf{K})\\
&+\int d^2K\,\frac{(-1)^N\left(i\beta_1(\mathbf{K})\right)^N}{N!}\Psi_i(\mathbf{K})\frac{\mathbf{K}\cdot(\mathbf{K}''-\mathbf{K})}{\beta_1(\mathbf{K})k_1^2}F_N(\mathbf{K}''-\mathbf{K})\\
&-\int d^2K\sum_{m=1}^{N}\frac{\left(i\beta_1(\mathbf{K})\right)^m}{m!(N-m)!}\Psi_f^{(N-m)}(\mathbf{K})\frac{\mathbf{K}\cdot(\mathbf{K}''-\mathbf{K})}{\beta_1(\mathbf{K})k_1^2}F_m(\mathbf{K}''-\mathbf{K})\\
&=\frac{1}{\rho}\int d^2K\,\kappa\beta_2(\mathbf{K})\sum_{m=0}^{N}\frac{\left(i\kappa\beta_2(\mathbf{K})\right)^m}{m!(N-m)!}\Psi_{2-}^{(N-m)}(\mathbf{K})\left[-(-1)^m+\gamma\right]F_m(\mathbf{K}''-\mathbf{K})\\
&-\frac{1}{\rho}\int d^2K\sum_{m=1}^{N}\frac{\left(i\kappa\beta_2(\mathbf{K})\right)^m}{m!(N-m)!}\Psi_{2-}^{(N-m)}(\mathbf{K})\left[-(-1)^m+\gamma\right]\frac{\mathbf{K}\cdot(\mathbf{K}''-\mathbf{K})}{\kappa\beta_2(\mathbf{K})k_1^2}F_m(\mathbf{K}''-\mathbf{K}).
\end{aligned}
\tag{5.31}
$$

Corresponding to the definition in Eq. (5.22), define

$$
\gamma''=\Gamma_{23}(\mathbf{K}'')e^{i2k_2\beta_2(\mathbf{K}'')d}. \tag{5.32}
$$

The following definitions,

$$
\mathbf{A}_N=\frac{\left(i\beta_1(\mathbf{K})\right)^N}{N!}F_N(\mathbf{K}''-\mathbf{K}), \tag{5.33}
$$

$$
\mathbf{A}(\mathbf{K}'',\mathbf{K})=\begin{bmatrix}
i\beta_1(\mathbf{K})F(\mathbf{K}''-\mathbf{K})\\
\frac{\left(i\beta_1(\mathbf{K})\right)^2}{2!}F_2(\mathbf{K}''-\mathbf{K})\\
\cdot\\
\cdot\\
\frac{\left(i\beta_1(\mathbf{K})\right)^N}{N!}F_N(\mathbf{K}''-\mathbf{K})
\end{bmatrix}, \tag{5.34}
$$

$$\mathbf{B}_{+}(\mathbf{K}'',\mathbf{K}) = \begin{bmatrix} i\kappa\beta_2(\mathbf{K})F(\mathbf{K}''-\mathbf{K}) \\ \dfrac{(i\kappa\beta_2(\mathbf{K}))^2}{2!}F_2(\mathbf{K}''-\mathbf{K}) \\ \cdot \\ \dfrac{(i\kappa\beta_2(\mathbf{K}))^N}{N!}F_N(\mathbf{K}''-\mathbf{K}) \end{bmatrix}, \tag{5.35}$$

$$\mathbf{B}_{-}(\mathbf{K}'',\mathbf{K}) = \begin{bmatrix} -i\kappa\beta_2(\mathbf{K})F(\mathbf{K}''-\mathbf{K}) \\ \dfrac{(-i\kappa\beta_2(\mathbf{K}))^2}{2!}F_2(\mathbf{K}''-\mathbf{K}) \\ \cdot \\ \dfrac{(-i\kappa\beta_2(\mathbf{K}))^N}{N!}F_N(\mathbf{K}''-\mathbf{K}) \end{bmatrix}, \tag{5.36}$$

$$\mathbf{Y}_f^t(\mathbf{K}) = \begin{bmatrix} \dfrac{\Psi_f^{(N-1)}}{(N-1)!} & \dfrac{\Psi_f^{(N-2)}}{(N-2)!} & \cdots & \Psi_f^{(0)} \end{bmatrix}, \tag{5.37}$$

and

$$\mathbf{Y}_{2-}^t(\mathbf{K}) = \begin{bmatrix} \dfrac{\Psi_{2-}^{(N-1)}}{(N-1)!} & \dfrac{\Psi_{2-}^{(N-2)}}{(N-2)!} & \cdots & \Psi_{2-}^{(0)} \end{bmatrix}, \tag{5.38}$$

result in more concise forms of Eq. (5.21),

$$\begin{aligned} \frac{\Psi_f^{(N)}(\mathbf{K}'')}{N!} &= (\gamma''+1)\frac{\Psi_{2-}^{(N)}(\mathbf{K}'')}{N!} \\ &+ \int d^2K \left[\gamma \mathbf{B}_{+}^t(\mathbf{K}'',\mathbf{K}) + \mathbf{B}_{-}^t(\mathbf{K}'',\mathbf{K})\right]\mathbf{Y}_{2-}(\mathbf{K}) \\ &- \int d^2K\,(-1)^N A_N(\mathbf{K}'',\mathbf{K})\Psi_i(\mathbf{K}) \\ &- \int d^2K\,\mathbf{A}^t(\mathbf{K}'',\mathbf{K})\mathbf{Y}_f(\mathbf{K}), \end{aligned} \tag{5.39}$$

and Eq. (5.31),

$$
\begin{aligned}
&\beta_1(\mathbf{K}'')\frac{\Psi_f^{(N)}(\mathbf{K}'')}{N!} \\
&= \int d^2K\,\beta_1(\mathbf{K})(-1)^N A_N(\mathbf{K}'',\mathbf{K})\Psi_i(\mathbf{K}) \\
&-u(N-1)\int d^2K\,\frac{\mathbf{K}\cdot(\mathbf{K}''-\mathbf{K})}{\beta_1(\mathbf{K})k_1^2}(-1)^N A_N(\mathbf{K}'',\mathbf{K})\Psi_i(\mathbf{K}) \\
&+\int d^2K\,\frac{\mathbf{K}\cdot(\mathbf{K}''-\mathbf{K})}{\beta_1(\mathbf{K})k_1^2}\mathbf{A}^t(\mathbf{K}'',\mathbf{K})\mathbf{Y}_f(\mathbf{K}) \\
&-\int d^2K\,\beta_1(\mathbf{K})\mathbf{A}^t(\mathbf{K}'',\mathbf{K})\mathbf{Y}_f(\mathbf{K}) \\
&\frac{1}{\rho}\int d^2K\,\kappa\beta_2(\mathbf{K})\left[\gamma\mathbf{B}_+^t(\mathbf{K}'',\mathbf{K})-\mathbf{B}_-^t(\mathbf{K}'',\mathbf{K})\right]\mathbf{Y}_{2-}(\mathbf{K}) \\
&+\frac{1}{\rho}(\gamma''-1)\kappa\beta_2(\mathbf{K}'')\frac{\Psi_{2-}^{(N)}(\mathbf{K}'')}{N!} \\
&-\frac{1}{\rho}\int d^2K\,\frac{\mathbf{K}\cdot(\mathbf{K}''-\mathbf{K})}{\kappa\beta_2(\mathbf{K})k_1^2}\left[\gamma\mathbf{B}_+^t(\mathbf{K}'',\mathbf{K})-\mathbf{B}_-^t(\mathbf{K}'',\mathbf{K})\right]\mathbf{Y}_{2-}(\mathbf{K})
\end{aligned}
\tag{5.40}
$$

Adding Eq. (5.39) multiplied by $(\gamma''-1)\kappa\beta_2(\mathbf{K}'')$, and Eq. (5.40) multiplied by $\rho(\gamma''+1)$, eliminates $\Psi_{2-}^{(N)}$ and results in an expression for the Nth-order scattered field:

$$
\begin{aligned}
&\frac{\Psi_f^{(N)}(\mathbf{K}'')}{N!}\left[\rho(\gamma''+1)\beta_1(\mathbf{K}'')-(\gamma''-1)\kappa\beta_2(\mathbf{K}'')\right] \\
&=\rho(\gamma''+1)\int d^2K\,\beta_1(\mathbf{K})(-1)^N A_N(\mathbf{K}'',\mathbf{K})\Psi_i(\mathbf{K}) \\
&-\rho(\gamma''+1)\int d^2K\,\beta_1(\mathbf{K})\mathbf{A}^t(\mathbf{K}'',\mathbf{K})\mathbf{Y}_f(\mathbf{K}) \\
&-u(N-1)\rho(\gamma''+1)\int d^2K\,\frac{\mathbf{K}\cdot(\mathbf{K}''-\mathbf{K})}{\beta_1(\mathbf{K})k_1^2}(-1)^N A_N(\mathbf{K}'',\mathbf{K})\Psi_i(\mathbf{K}) \\
&+\rho(\gamma''+1)\int d^2K\,\frac{\mathbf{K}\cdot(\mathbf{K}''-\mathbf{K})}{\beta_1(\mathbf{K})k_1^2}\mathbf{A}^t(\mathbf{K}'',\mathbf{K})\mathbf{Y}_f(\mathbf{K}) \\
&+(\gamma''+1)\int d^2K\,\kappa\beta_2(\mathbf{K})\left[\gamma\mathbf{B}_+^t(\mathbf{K}'',\mathbf{K})-\mathbf{B}_-^t(\mathbf{K}'',\mathbf{K})\right]\mathbf{Y}_{2-}(\mathbf{K}) \\
&-(\gamma''+1)\int d^2K\,\frac{\mathbf{K}\cdot(\mathbf{K}''-\mathbf{K})}{\kappa\beta_2(\mathbf{K})k_1^2}\left[\gamma\mathbf{B}_+^t(\mathbf{K}'',\mathbf{K})-\mathbf{B}_-^t(\mathbf{K}'',\mathbf{K})\right]\mathbf{Y}_{2-}(\mathbf{K}) \\
&+(\gamma''-1)\kappa\beta_2(\mathbf{K}'')\int d^2K(-1)^N A_N(\mathbf{K}'',\mathbf{K})\Psi_i(\mathbf{K}) \\
&+(\gamma''-1)\kappa\beta_2(\mathbf{K}'')\int d^2K\,\mathbf{A}^t(\mathbf{K}'',\mathbf{K})\mathbf{Y}_f(\mathbf{K}) \\
&-(\gamma''-1)\kappa\beta_2(\mathbf{K}'')\int d^2K\left[\gamma\mathbf{B}_+^t(\mathbf{K}'',\mathbf{K})+\mathbf{B}_-^t(\mathbf{K}'',\mathbf{K})\right]\mathbf{Y}_{2-}(\mathbf{K}).
\end{aligned}
\tag{5.41}
$$

Define

$$
\xi''=\frac{\rho\beta_1(\mathbf{K}'')}{\kappa\beta_2(\mathbf{K}'')}\left(\frac{1+\gamma''}{1-\gamma''}\right)=\frac{1+\Gamma(\mathbf{K}'')}{1-\Gamma(\mathbf{K}'')},
\tag{5.42}
$$

where Γ in second equality in Eq. (5.42) is the total reflection coefficient of the corresponding flat surface problem at the zero-mean rough interface, obtained from the well known reflection coefficient expression (see for example Sec. 3.3 of Brekhovskikh and Lysanov).

$$
\Gamma(\mathbf{K})=\frac{\Gamma_{12}(\mathbf{K})+\Gamma_{23}(\mathbf{K})e^{i2k_2\beta_2(\mathbf{K})d}}{1+\Gamma_{12}(\mathbf{K})\Gamma_{23}(\mathbf{K})e^{i2k_2\beta_2(\mathbf{K})d}},
\tag{5.43}
$$

where

$$
\Gamma_{12}(\mathbf{K})=\frac{\rho\beta_1(\mathbf{K})-\kappa\beta_2(\mathbf{K})}{\rho\beta_1(\mathbf{K})+\kappa\beta_2(\mathbf{K})}
\tag{5.44}
$$

is the reflection coefficient corresponding to a flat surface fluid-fluid interface between medium 1 and medium 2 in the limit as the width of medium 2, d, becomes arbitrarily large, or medium 3 parameters are identical to medium 2 parameters. The term Γ_{23} is a general reflection coefficient corresponding to the medium 2 - medium 3 flat interface. Although medium 2 is constrained to be a fluid, medium 3 is only constrained to vary in the z direction. Dividing Eq. (5.41) by $(\gamma''-1)\kappa\beta_2$ and using Eq. (5.42) yields

$$\begin{aligned}
&\frac{\Psi_f^{(N)}(\mathbf{K}'')}{N!}[\xi''+1] \\
&=\int d^2K\left[\frac{\xi''\beta_1(\mathbf{K})}{\beta_1(\mathbf{K}'')}-1-\frac{\xi''\mathbf{K}\cdot(\mathbf{K}''-\mathbf{K})}{\beta_1(\mathbf{K}'')\beta_1(\mathbf{K})k_1^2}\right](-1)^N A_N(\mathbf{K}'',\mathbf{K})\Psi_i(\mathbf{K}) \\
&+\int d^2K\left[-\frac{\xi''\beta_1(\mathbf{K})}{\beta_1(\mathbf{K}'')}-1+\frac{\xi''\mathbf{K}\cdot(\mathbf{K}''-\mathbf{K})}{\beta_1(\mathbf{K}'')\beta_1(\mathbf{K})k_1^2}\right]\mathbf{A}^t(\mathbf{K}'',\mathbf{K})\mathbf{Y}_f(\mathbf{K}) \\
&+\int d^2K\left[\frac{\xi''\kappa\beta_2(\mathbf{K})}{\rho\beta_1(\mathbf{K}'')}-\frac{\xi''\mathbf{K}\cdot(\mathbf{K}''-\mathbf{K})}{\rho\beta_1(\mathbf{K}'')\kappa\beta_2(\mathbf{K})k_1^2}\right]\left[\gamma\mathbf{B}_+^t(\mathbf{K}'',\mathbf{K})-\mathbf{B}_-^t(\mathbf{K}'',\mathbf{K})\right]\mathbf{Y}_{2-}(\mathbf{K}) \\
&+\int d^2K\left[\gamma\mathbf{B}_+^t(\mathbf{K}'',\mathbf{K})+\mathbf{B}_-^t(\mathbf{K}'',\mathbf{K})\right]\mathbf{Y}_{2-}(\mathbf{K}).
\end{aligned} \tag{5.45}$$

Dividing the above expression by k_1, multiplying by ρ_1, substituting Eq (5.33) through Eq. (5.38) into the above expression, using the binomial coefficient notation,

$$\binom{N}{m}=\frac{N!}{(N-m)!m!}, \tag{5.46}$$

and collecting terms in the same power in k_1h yields

$$\Psi_f^{(N)}(\mathbf{K}'')[\xi''+1]=\int d^2K\left[\frac{\xi''\beta_1(\mathbf{K})}{\beta_1(\mathbf{K}'')}-1-\frac{\xi''\mathbf{K}\cdot(\mathbf{K}''-\mathbf{K})}{\beta_1(\mathbf{K}'')\beta_1(\mathbf{K})k_1^2}\right]$$
$$\times(-1)^N\left(i\beta_1(\mathbf{K})\right)^N F_N(\mathbf{K}''-\mathbf{K})\Psi_i(\mathbf{K})$$
$$+\int d^2K\left[-\frac{\xi''\beta_1(\mathbf{K})}{\beta_1(\mathbf{K}'')}-1+\frac{\xi''\mathbf{K}\cdot(\mathbf{K}''-\mathbf{K})}{\beta_1(\mathbf{K}'')\beta_1(\mathbf{K})k_1^2}\right]$$
$$\times\sum_{m=1}^{N}\binom{N}{m}\left(i\beta_1(\mathbf{K})\right)^m F_m(\mathbf{K}''-\mathbf{K})\Psi_f^{(N-m)}(\mathbf{K})$$
$$+\int d^2K\left[\frac{\xi''\kappa\beta_2(\mathbf{K})}{\rho\beta_1(\mathbf{K}'')}-\frac{\xi''\mathbf{K}\cdot(\mathbf{K}''-\mathbf{K})}{\rho\beta_1(\mathbf{K}'')\kappa\beta_2(\mathbf{K})k_1^2}\right]$$
$$\times\sum_{m=1}^{N}\binom{N}{m}\left(i\kappa\beta_2(\mathbf{K})\right)^m F_m(\mathbf{K}''-\mathbf{K})\left[\gamma-(-1)^m\right]\Psi_{2-}^{(N-m)}(\mathbf{K})$$
$$+\int d^2K\sum_{m=1}^{N}\binom{N}{m}\left(i\kappa\beta_2(\mathbf{K})\right)^m F_m(\mathbf{K}''-\mathbf{K})\left[\gamma+(-1)^m\right]\Psi_{2-}^{(N-m)}(\mathbf{K}) \qquad (5.47)$$

Apply Eq. (5.42) to Eq. (5.47),

$$
\begin{aligned}
&\Psi_f^{(N)}(\mathbf{K}'') \\
&= \int d^2K \left[\frac{1+\Gamma(\mathbf{K}'')}{2} \frac{\beta_1(\mathbf{K})}{\beta_1(\mathbf{K}'')} - \frac{1-\Gamma(\mathbf{K}'')}{2} - \frac{1+\Gamma(\mathbf{K}'')}{2} \frac{\mathbf{K}\cdot(\mathbf{K}''-\mathbf{K})}{\beta_1(\mathbf{K}'')\beta_1(\mathbf{K})k_1^2} \right] \\
&\times(-1)^N \left(i\beta_1(\mathbf{K})\right)^N F_N(\mathbf{K}''-\mathbf{K})\Psi_i(\mathbf{K}) \\
&+ \int d^2K \left[-\frac{1+\Gamma(\mathbf{K}'')}{2} \frac{\beta_1(\mathbf{K})}{\beta_1(\mathbf{K}'')} - \frac{1-\Gamma(\mathbf{K}'')}{2} + \frac{1+\Gamma(\mathbf{K}'')}{2} \frac{\mathbf{K}\cdot(\mathbf{K}''-\mathbf{K})}{\beta_1(\mathbf{K}'')\beta_1(\mathbf{K})k_1^2} \right] \\
&\times \sum_{m=1}^{N} \binom{N}{m} \left(i\beta_1(\mathbf{K})\right)^m F_m(\mathbf{K}''-\mathbf{K})\Psi_f^{(N-m)}(\mathbf{K}) \\
&+ \int d^2K \left[\frac{1+\Gamma(\mathbf{K}'')}{2} \frac{\kappa\beta_2(\mathbf{K})}{\rho\beta_1(\mathbf{K}'')} - \frac{1+\Gamma(\mathbf{K}'')}{2} \frac{\mathbf{K}\cdot(\mathbf{K}''-\mathbf{K})}{\rho\beta_1(\mathbf{K}'')\kappa\beta_2(\mathbf{K})k_1^2} \right] \\
&\times \sum_{m=1}^{N} \binom{N}{m} \left(i\kappa\beta_2(\mathbf{K})\right)^m F_m(\mathbf{K}''-\mathbf{K}) \left[\gamma - (-1)^m\right] \Psi_{2-}^{(N-m)}(\mathbf{K}) \\
&+ \int d^2K \sum_{m=1}^{N} \binom{N}{m} \frac{1-\Gamma(\mathbf{K}'')}{2} \left(i\kappa\beta_2(\mathbf{K})\right)^m F_m(\mathbf{K}''-\mathbf{K}) \left[\gamma + (-1)^m\right] \Psi_{2-}^{(N-m)}(\mathbf{K}) .
\end{aligned}
\tag{5.48}
$$

Equation (5.48) can be further simplified by using the identities

$$
\frac{\mathbf{K}\cdot(\mathbf{K}''-\mathbf{K})}{k_1^2} = \frac{\mathbf{K}\cdot\mathbf{K}''}{k_1^2} - 1 + \beta_1^2(\mathbf{K}) \tag{5.49}
$$

and

$$
\left(\beta_1(\mathbf{K})\right)^2 - \left(\kappa\beta_2(\mathbf{K})\right)^2 = \frac{k_1^2 - K^2}{k_1^2} - \frac{k_2^2 - K^2}{k_1^2} = 1 - \kappa^2 \tag{5.50}
$$

to give

$$
\begin{aligned}
&\Psi_f^{(N)}(\mathbf{K}'') \\
&= \frac{1}{2}\int d^2K\,(1+\Gamma(\mathbf{K}''))\frac{1}{\beta_1(\mathbf{K}'')\beta_1(\mathbf{K})}\left[-\frac{\mathbf{K}\cdot\mathbf{K}''}{k_1^2}+1-\beta_1(\mathbf{K}'')\beta_1(\mathbf{K})\frac{(1-\Gamma(\mathbf{K}''))}{(1+\Gamma(\mathbf{K}''))}\right] \\
&\times(-1)^N\left(i\beta_1(\mathbf{K})\right)^N F_N(\mathbf{K}''-\mathbf{K})\Psi_i(\mathbf{K}) \\
&+\frac{1}{2}\int d^2K\,(1+\Gamma(\mathbf{K}''))\frac{1}{\beta_1(\mathbf{K}'')\beta_1(\mathbf{K})}\left[\frac{\mathbf{K}\cdot\mathbf{K}''}{k_1^2}-1-\beta_1(\mathbf{K}'')\beta_1(\mathbf{K})\frac{(1-\Gamma(\mathbf{K}''))}{(1+\Gamma(\mathbf{K}''))}\right] \\
&\times\sum_{m=1}^{N}\binom{N}{m}\left(i\beta_1(\mathbf{K})\right)^m F_m(\mathbf{K}''-\mathbf{K})\Psi_f^{(N-m)}(\mathbf{K}) \\
&+\frac{1}{2}\int d^2K\,(1+\Gamma(\mathbf{K}''))\frac{1}{\rho}\frac{1}{\beta_1(\mathbf{K}'')\kappa\beta_2(\mathbf{K})}\left[\kappa^2-\frac{\mathbf{K}\cdot\mathbf{K}''}{k_1^2}\right] \\
&\times\sum_{m=1}^{N}\binom{N}{m}\left(i\kappa\beta_2(\mathbf{K})\right)^m F_m(\mathbf{K}''-\mathbf{K})\left[\gamma-(-1)^m\right]\Psi_{2-}^{(N-m)}(\mathbf{K}) \\
&+\frac{1}{2}\int d^2K\,(1-\Gamma(\mathbf{K}''))\sum_{m=1}^{N}\binom{N}{m}\left(i\kappa\beta_2(\mathbf{K})\right)^m F_m(\mathbf{K}''-\mathbf{K})\left[\gamma+(-1)^m\right]\Psi_{2-}^{(N-m)}(\mathbf{K}).
\end{aligned}
\tag{5.51}
$$

The Nth-order fields scattered away from the interface and through the interface are found from the recursion equations, Eq. (5.21) and Eq. (5.51). Each order field is found in terms of all lower-order fields. Although reciprocity is not obvious in Eqs. (5.21) and (5.51), nevertheless, it should be possible to show they are reciprocal when each order is calculated.

5.4 Zero-order

The flat surface reflected field follows from Eq. (5.51) by setting $N=0$.

$$
\begin{aligned}
\Psi_f^{(0)}(\mathbf{K}'') = \frac{1}{2}\int d^2K\Bigg\{&\delta(\mathbf{K}''-\mathbf{K})\Psi_i(\mathbf{K})\frac{(1+\Gamma(\mathbf{K}''))}{\beta_1(\mathbf{K}'')\beta_1(\mathbf{K})} \\
&\times\left[-\frac{\mathbf{K}\cdot\mathbf{K}''}{k_1^2}+1-\beta_1(\mathbf{K}'')\beta_1(\mathbf{K})\frac{(1-\Gamma(\mathbf{K}''))}{(1+\Gamma(\mathbf{K}''))}\right]\Bigg\}
\end{aligned}
\tag{5.52}
$$

$$
\Psi_f^{(0)}(\mathbf{K}'') = \int d^2K\,\delta(\mathbf{K}''-\mathbf{K})\Gamma(\mathbf{K}'')\Psi_i(\mathbf{K}) \tag{5.53}
$$

or

$$\Psi_f^{(0)}(\mathbf{K}) = \Gamma(\mathbf{K})\Psi_i(\mathbf{K}). \tag{5.54}$$

This result is the same as the zero-order result obtained in chapter 3, except that the reflection coefficient in this result, given by Eq. (5.43), includes medium 3 in the partial reflection coefficient, Γ_{23}, at the flat interface between medium 2 and medium 3. The zero-order T-matrix, $T_{11}^{(0)}$, is the flat surface reflection coefficient multiplied by a delta function;

$$T_{11}^{(0)}(\mathbf{K}'',\mathbf{K}) = \Gamma(\mathbf{K})\delta(\mathbf{K}''-\mathbf{K}), \tag{5.55}$$

where Γ is given in Eq. (5.43), representing the total reflection coefficient at $z=0$ when the rough interface is replaced by its mean. The zero-order field transmitted through the interface follows from Eq. (5.21) by setting $N=0$,

$$\Psi_{2-}^{(0)}(\mathbf{K}'')(\gamma''+1) = \int d^2K\,\delta(\mathbf{K}''-\mathbf{K})\Psi_i(\mathbf{K}) + \Psi_f^{(0)}(\mathbf{K}'') \tag{5.56}$$

or

$$\Psi_{2-}^{(0)}(\mathbf{K}) = \mathrm{T}(\mathbf{K})\Psi_i(\mathbf{K}), \tag{5.57}$$

where

$$\mathrm{T}(\mathbf{K}) = \frac{1+\Gamma(\mathbf{K})}{1+\gamma} \tag{5.58}$$

is the flat surface transmission coefficient. Note that this transmission coefficient relates the down-going transmitted field in medium 2 to the incident field. For the case of two homogenous fluids — medium 2 parameters are equal to medium 3 parameters, or $d\to\infty$, then $\gamma=0$, and

$$\mathrm{T}(\mathbf{K}) = 1+\Gamma(\mathbf{K}), \tag{5.59}$$

which agrees with Eq. (3.24).

5.5 First-order

The first-order incoherent field scattered back into medium 1 and the downward traveling field scattered into medium 2 are derived in this section and compared with the first-order fluid-fluid results of chapter 3.

5.5.1 Derivation of T-matrix

For the first-order field, set $N=1$ in Eq. (5.51):

$$
\begin{aligned}
&\Psi_f^{(1)}(\mathbf{K}'') \\
&= \frac{i}{2}\int d^2K \frac{(1+\Gamma(\mathbf{K}''))}{\beta_1(\mathbf{K}'')}\left[\frac{\mathbf{K}\cdot\mathbf{K}''}{k_1^2} - 1 + \beta_1(\mathbf{K}'')\beta_1(\mathbf{K})\frac{(1-\Gamma(\mathbf{K}''))}{(1+\Gamma(\mathbf{K}''))}\right] F(\mathbf{K}''-\mathbf{K})\Psi_i(\mathbf{K}) \\
&+ \frac{i}{2}\int d^2K \frac{(1+\Gamma(\mathbf{K}''))}{\beta_1(\mathbf{K}'')}\left[\frac{\mathbf{K}\cdot\mathbf{K}''}{k_1^2} - 1 - \beta_1(\mathbf{K}'')\beta_1(\mathbf{K})\frac{(1-\Gamma(\mathbf{K}''))}{(1+\Gamma(\mathbf{K}''))}\right] F(\mathbf{K}''-\mathbf{K})\Psi_f^{(0)}(\mathbf{K}) \\
&+ \frac{i}{2}\int d^2K \frac{1}{\rho}\frac{(1+\Gamma(\mathbf{K}''))}{\beta_1(\mathbf{K}'')\kappa\beta_2(\mathbf{K})}\left[\kappa^2 - \frac{\mathbf{K}\cdot\mathbf{K}''}{k_1^2}\right]\kappa\beta_2(\mathbf{K})F(\mathbf{K}''-\mathbf{K})[\gamma+1]\Psi_{2-}^{(0)}(\mathbf{K}) \\
&+ \frac{i}{2}\int d^2K (1-\Gamma(\mathbf{K}''))\kappa\beta_2(\mathbf{K})F(\mathbf{K}''-\mathbf{K})[\gamma-1]\Psi_{2-}^{(0)}(\mathbf{K}).
\end{aligned}
\tag{5.60}
$$

The first-order T-matrix then follows from Eq. (5.4), the zero-order quantities given in Eqs. (5.54) and (5.57), and from the above equation:

$$T_{11}^{(1)}(\mathbf{K}'',\mathbf{K})$$

$$\begin{aligned}
&= \frac{1}{2}\frac{i(1+\Gamma(\mathbf{K}''))}{\beta_1(\mathbf{K}'')}\left[\frac{\mathbf{K}\cdot\mathbf{K}''}{k_1^2} - 1 + \beta_1(\mathbf{K}'')\beta_1(\mathbf{K})\frac{(1-\Gamma(\mathbf{K}''))}{(1+\Gamma(\mathbf{K}''))}\right]F(\mathbf{K}''-\mathbf{K}) \\
&+ \frac{1}{2}\frac{i\Gamma(\mathbf{K})(1+\Gamma(\mathbf{K}''))}{\beta_1(\mathbf{K}'')}\left[\frac{\mathbf{K}\cdot\mathbf{K}''}{k_1^2} - 1 - \beta_1(\mathbf{K}'')\beta_1(\mathbf{K})\frac{(1-\Gamma(\mathbf{K}''))}{(1+\Gamma(\mathbf{K}''))}\right]F(\mathbf{K}''-\mathbf{K}) \\
&+ \frac{1}{2}\frac{1}{\rho}\frac{i(1+\Gamma(\mathbf{K}''))}{\beta_1(\mathbf{K}'')\kappa\beta_2(\mathbf{K})}\left[\kappa^2 - \frac{\mathbf{K}\cdot\mathbf{K}''}{k_1^2}\right]\kappa\beta_2(\mathbf{K})F(\mathbf{K}''-\mathbf{K})(1+\Gamma(\mathbf{K})) \\
&+ \frac{1}{2}(1-\Gamma(\mathbf{K}''))i\kappa\beta_2(\mathbf{K})F(\mathbf{K}''-\mathbf{K})\frac{[\gamma-1]}{[\gamma+1]}(1+\Gamma(\mathbf{K})).
\end{aligned} \tag{5.61}$$

By applying the second equality in Eq. (5.42), the above equation simplifies to

$$T_{11}^{(1)}(\mathbf{K}'',\mathbf{K}) \equiv H_{11}(\mathbf{K}'',\mathbf{K})F(\mathbf{K}''-\mathbf{K}), \tag{5.62}$$

where

$$H_{11}(\mathbf{K}'',\mathbf{K}) = \frac{1}{2i\beta_1(\mathbf{K}'')}\left\{b(1-\Gamma(\mathbf{K}''))(1-\Gamma(\mathbf{K})) + a(1+\Gamma(\mathbf{K}''))(1+\Gamma(\mathbf{K}))\right\}, \tag{5.63}$$

$$a = 1 - \frac{\kappa^2}{\rho} + \left(\frac{1}{\rho} - 1\right)\frac{\mathbf{K}''\cdot\mathbf{K}}{k_1^2}, \tag{5.64}$$

and

$$b = \beta_1(\mathbf{K}'')\beta_1(\mathbf{K})(\rho - 1). \tag{5.65}$$

Reciprocity is manifest here. Also note that this result is identical to the fluid-fluid first-order result in chapter 3. In this result, the complexity of medium 3 is included in the reflection coefficient given in Eq. (5.43). Although it appears as though Eq. (5.63) follows from the two-homogenous fluid result in Eq. (3.37), one would not typically be able to generalize the two fluid result to Eq. (5.63) simply by substituting the general expression for the reflection coefficient given in Eq. (5.43) for the two-fluid reflection coefficient given in Eq. (3.23). Using Eq. (3.36)

in Eq. (3.35) to eliminate the $\kappa\beta_2$ was necessary to obtain the expression identical to Eq. (5.63). If this substitution were not made, then the first-order results in chapter 3 would not generalize to the results in this chapter — simply by using the general reflection coefficient given in Eq. (5.43).

The first-order field scattered through the surface is found by setting $N=1$ in Eq. (5.21):

$$\begin{aligned}\Psi_{2-}^{(1)}(\mathbf{K}'')(\gamma''+1) = &-\int d^2K i\beta_1(\mathbf{K})F(\mathbf{K}''-\mathbf{K})\Psi_i(\mathbf{K}) \\ &+\int d^2K i\beta_1(\mathbf{K})F(\mathbf{K}''-\mathbf{K})\Psi_f^{(0)}(\mathbf{K}) \\ &-\int d^2K i\kappa\beta_2(\mathbf{K})F(\mathbf{K}''-\mathbf{K})[\gamma-1]\Psi_{2-}^{(0)}(\mathbf{K}) \\ &+\Psi_f^{(1)}(\mathbf{K}'').\end{aligned} \tag{5.66}$$

Using the zero-order results in Eqs. (5.54), (5.57), (5.58), and (5.62) in the above equation results in the following expression for the first-order field scattering through the rough interface:

$$\begin{aligned}\Psi_{2-}^{(1)}(\mathbf{K}'')(\gamma''+1) = &\int d^2K i\beta_1(\mathbf{K})F(\mathbf{K}''-\mathbf{K})\Gamma(\mathbf{K})\Psi_i(\mathbf{K}) \\ &-\int d^2K i\beta_1(\mathbf{K})F(\mathbf{K}''-\mathbf{K})\Psi_i(\mathbf{K}) \\ &+\int d^2K i\rho\beta_1(\mathbf{K})F(\mathbf{K}''-\mathbf{K})(1-\Gamma(\mathbf{K}))\Psi_i(\mathbf{K}) \\ &+\int d^2K H_{11}(\mathbf{K}'',\mathbf{K})F(\mathbf{K}''-\mathbf{K})\Psi_i(\mathbf{K}).\end{aligned} \tag{5.67}$$

The first-order T-matrix $T_{12}^{(1)}$ follows from the above equation and Eq. (5.5):

$$\begin{aligned}T_{12}^{(1)}(\mathbf{K}'',\mathbf{K})(\gamma''+1) = &\, i(\rho-1)\beta_1(\mathbf{K})(1-\Gamma(\mathbf{K}))F(\mathbf{K}''-\mathbf{K}) \\ &+H_{11}(\mathbf{K}'',\mathbf{K})F(\mathbf{K}''-\mathbf{K}).\end{aligned} \tag{5.68}$$

Similar to Eq. (5.62), define

$$T_{12}^{(1)}(\mathbf{K}'',\mathbf{K}) \equiv H_{12}(\mathbf{K}'',\mathbf{K})F(\mathbf{K}''-\mathbf{K}). \tag{5.69}$$

If we use the representation for the transmission coefficient in Eq. (5.58), and the definitions of a, and b in Eqs. (5.64) and (5.65), H_{12} follows from Eq. (5.68) and its definition in Eq. (5.69):

$$H_{12}(\mathbf{K}'',\mathbf{K}) = \frac{\mathrm{T}(\mathbf{K}'')}{2i\beta_1(\mathbf{K}'')}\left\{a(1+\Gamma(\mathbf{K})) - b(1-\Gamma(\mathbf{K}))\right\}. \tag{5.70}$$

This result is a generalization of the result in Eq. (3.45), where the transmission coefficient relates the downward traveling field below the zero-mean rough surface to the incident field on the rough surface. For scattering back into medium 1, the complexity of medium 3 is contained in the reflection coefficient; for scattering through the sediment, the complexity of medium 3 is contained in both the transmission and reflection coefficients.

5.5.2 The effect of shear waves on the differential cross section

As a check of the formalism developed in this chapter, we reproduce a result from Essen (1994) that includes shear supporting sediment below a rough fluid-fluid interface. This particular example is an appropriate check, because the medium immediately below the rough surface is a fluid and Essen uses perturbation theory to calculate the differential cross section.

The differential cross section obtained from first-order perturbation theory for scattering back into the water (medium 1) follows from Eq. (3.77) by replacing H_{12} from Eq. (5.70) with H_{11} from Eq. (5.63) and setting the speed ratio, ν, to one.

$$\sigma_{11}\left(\hat{\alpha}_f,\hat{\alpha}_i\right) = k_1^4 \sin^2(\theta_2)\left|H_{11}\left(\mathbf{K}_f,\mathbf{K}_i\right)\right|^2 W\left(\mathbf{K}_f - \mathbf{K}_i\right). \tag{5.71}$$

Here, θ_2 is the scattered grazing angle measured from the mean surface, and $\mathbf{K}_f$ and $\mathbf{K}_i$ are the transverse components of the scattered field and incident

field wave vectors, respectively. This example is concerned with the backscattering strength, $10\log(\sigma_{11})$, where $\mathbf{K}_f = -\mathbf{K}_i$.

In Eq. (5.63), the complexity of medium 3 is characterized by the flat surface reflection coefficient, Γ. Eq. (5.43) is used to find the reflection coefficient from the partial reflection coefficients, Γ_{12} and Γ_{23}. The partial reflection coefficient Γ_{12} is the fluid-fluid reflection coefficient at the interface between medium 2 and medium 3 ($z = 0$). The partial reflection coefficient Γ_{23} is the fluid-solid reflection coefficient at the interface between medium 2 and medium 3 at $z = -d$. When medium 3 is shear supporting, but gradient free, the partial reflection coefficient Γ_{23} is given by (Brekhovskikh, 1980; Brekhovskikh and Lysanov, 1991)

$$\Gamma_{23} = \frac{Z_{in} - Z_2}{Z_{in} + Z_2}, \tag{5.72}$$

where

$$Z_{in} = Z_{3\ell}\cos^2(2\gamma_3) + Z_{3t}\sin^2(2\gamma_3), \tag{5.73}$$

$$Z_2 = \frac{\rho_2}{\kappa\beta_2}, \tag{5.74}$$

$$Z_{3\ell} = \frac{\rho_3}{\kappa_l\beta_{3\ell}}, \tag{5.75}$$

and

$$Z_{3t} = \frac{\rho_3}{\kappa_t\beta_{3t}}. \tag{5.76}$$

The parameter κ_l is the ratio of the compressional wave number of medium 3 to k_1, and the parameter κ_t is the ratio of the shear wave number of medium 3 to k_1. The complex angle γ_3 is determined from

$$\cos(\gamma_3) = \beta_{3t}(\mathbf{K}), \tag{5.77}$$

where

$$\beta_{3l,3t} = \sqrt{1 - K^2 / \left(k_1 \kappa_{l,t}\right)^2}\,. \tag{5.78}$$

In Fig. 5.2, the parameters given in Fig. 5c of Essen (1994) are used to plot the backscattered field strength, $10\log_{10}\left(\sigma_{11}\left(\mathbf{K}_f, \mathbf{K}_i\right)\right)$, $\mathbf{K}_f = -\mathbf{K}_i$, as a function of grazing angle. In this example, medium 2 consists of a very fine sand and has thickness $d = \lambda$. The wave number and density ratios are taken to be $\kappa = 1/(1.12 - 0.004i)$ and $\rho = 1.85$. The sedimentary rock in medium 3 supports both shear and compressional waves with wave number ratios $\kappa_\ell = 1/(2.3 - 0.004i)$ and $\kappa_t = 1/(1.3 - 0.11i)$. The ratio of the density in the sedimentary rock (medium 3) to that of the fluid in medium 2 is equal to 2.5. This example also uses the power-law roughness spectrum given in Eq. (3.55) or Eq. (3.66) with $a = \infty$. Using a finite value for the filter parameter, a, would only affect the result at larger grazing angles than those plotted. Since $\gamma = 4.0$, the backscattering strength does not depend on frequency. The spectral strength is given to be $w_2 = 0.04/(2\pi)$. This result is identical to the result obtained by Essen.

5.5.3 The effect of sound-speed gradient on incoherent backscattered field

In order to illustrate that gradients in sound speed can have a significant effect on the intensity scattered back into the water, the backscattered field strength, $10\log_{10}\left(\sigma_{11}\left(\mathbf{K}_f, \mathbf{K}_i\right)\right)$, $\mathbf{K}_f = -\mathbf{K}_i$, is computed as a function of grazing angle for a sediment with a sound-speed gradient in medium 3, and is contrasted with the no sound-speed gradient case — all medium parameters in medium 3 are identical to those of medium 2. In this example, we have followed Mourad and Jackson (1993) in assuming that the square of the wave number in the

medium below the rough seafloor decreases linearly with depth. The choice of linear decrease in squared wave number with depth,

$$k_3^2(\zeta) = (1 - \alpha\zeta)k_1^2\kappa^2, \tag{5.79}$$

where

$$\zeta = -(z + d) \tag{5.80}$$

yields the well known solution for the field in medium 3 proportional to the Airy function, $Ai(\tau)$, and solution for the reflection coefficient in terms of Airy functions (Brekhovskikh, 1980):

$$\Gamma_{23}(\mathbf{K}) = \frac{ik_2\beta_2(\mathbf{K})HAi(t_0) - Ai'(t_0)}{ik_2\beta_2(\mathbf{K})HAi(t_0) + Ai'(t_0)} \tag{5.81}$$

with

$$H = \left(k_2^2 a\right)^{-1/3}, \tag{5.82}$$

$$t_0 = H^2\left(K^2 - k_2^2\right), \tag{5.83}$$

and

$$\tau = H^2 a\zeta k_2^2 + H^2\left(K^2 - k_2^2\right). \tag{5.84}$$

The parameter a is expressed in terms of the sound-speed gradient, g, the sound-speed ratio, ν, and the sound velocity in medium 1, c_1:

$$a = 2g/(\nu c_1), \tag{5.85}$$

where

$$g = \left.\frac{dc(\zeta)}{d\zeta}\right|_{\zeta=0}. \tag{5.86}$$

The parameter g is taken to be the sound-speed gradient at the interface between medium 2 and medium 3. An example that shows the effect of a sound-

speed gradient on scattering back into the water is given below. In this example, medium 2 is taken to be arbitrarily thin; the reflection coefficient Γ can be found from substituting Eq. (5.81) into Eq. (5.43), and setting $d = 0$.

$$\Gamma(\mathbf{K}) = \frac{ik_1\beta_1(\mathbf{K})\rho H\, Ai(t_0) - Ai'(t_0)}{ik_1\beta_1(\mathbf{K})\rho H\, Ai(t_0) + Ai'(t_0)}. \tag{5.87}$$

Since the medium above $z = -d$ must be medium 2, $z = -d$ must be at or below the lowest point on the rough interface. However the sound-speed gradient is small enough in this example that setting $d = 0$ results in a negligible difference in scattering strength. Since the backscattered field strength is plotted only to a grazing angle of $70°$, values of the filter parameter $a > 1.5\,\mathrm{m}$ in the power-law roughness spectrum given in Eq. (3.66) result in the same scattered field strength.

Figure (5.3) compares computations of seafloor backscattered field strength made with and without a sound-speed gradient for a frequency of $300\mathrm{Hz}$ and a water sound speed of 1545 m^{-1}, with parameters appropriate to a soft silty or clayey bottom ($\rho_{21} = 1.548$, $v_{21} = 0.96$, and $\delta = 0.1445\times10^{-3}$) and an upward refracting sound-speed gradient at the interface of $1.3\ \mathrm{s}^{-1}$. This example shows that the sound-speed gradient can cause an appreciable change in the seafloor scattering strength. The gradient in this example is high enough, and the loss is low enough, so that much of the energy that is transmitted through the interface is refracted upward to the interface to strike it again, resulting in constructive or destructive interference. The significance of this interference is discussed further in chapter 6. While this example illustrates the effect of large-scale gradients on low frequency scattering, very steep gradients on centimeter scales can result from biological reworking of sediments (Richardson, 1986) and may influence high frequency scattering. Gradients in porosity are equivalent to gradients in density (Hamilton, 1974), which can have strong effects on the reflection coefficient (Rutherford and Hawker, 1978; Holthusen and Vidmar, 1982).

Since the sound-speed profile at the experimental site is not known, the effect of gradients in sound speed on the incoherent and coherent intensity scattered through a rough interface is not included in the model used in the simulations (chapter 4).

5.6 Second-order field

For the ocean experiment simulation (Chotiros, 1995) we use a zero-order approximation in the coherent intensity calculation. There is a slight inconsistency in this approach, in that the incoherent intensity is proportional to the second power of $k_1 h$, while the coherent intensity is only computed to an accuracy of $k_1 h$ to the zeroth power. The second-order field is found in the next section. Using this result, we obtain an expression for the second-order coherent field.

5.6.1 Derivation of T-matrix

The procedure for finding the second-order field is similar to finding the first-order field. However, both first-order and zero-order results are required in order to obtain the second-order field. Setting N=2 in Eq. (5.51), substituting $\mathbf{K}'$ for $\mathbf{K}$ in the F_1 terms, and using Eqs. (5.54), (5.57), (5.58), and (5.69) and

$$F_2(\mathbf{K}'' - \mathbf{K}) = \int d^2K' F(\mathbf{K}'' - \mathbf{K}') F(\mathbf{K}' - \mathbf{K}) \tag{5.88}$$

from Eq. (5.9) yields

$$2\Psi_f^{(2)}(\mathbf{K}'') = \int d^2K' \int d^2K\, F(\mathbf{K}''-\mathbf{K}')F(\mathbf{K}'-\mathbf{K})\Psi_i(\mathbf{K}) \tag{5.89}$$
$$\times\Bigg\{(1+\Gamma(\mathbf{K}''))\frac{\beta_1(\mathbf{K})}{\beta_1(\mathbf{K}'')}\left[\frac{\mathbf{K}\cdot\mathbf{K}''}{k_1^2}-1+\beta_1(\mathbf{K}'')\beta_1(\mathbf{K})\frac{(1-\Gamma(\mathbf{K}''))}{(1+\Gamma(\mathbf{K}''))}\right]$$
$$+(1+\Gamma(\mathbf{K}''))\frac{\beta_1(\mathbf{K})}{\beta_1(\mathbf{K}'')}\left[-\frac{\mathbf{K}\cdot\mathbf{K}''}{k_1^2}+1+\beta_1(\mathbf{K}'')\beta_1(\mathbf{K})\frac{(1-\Gamma(\mathbf{K}''))}{(1+\Gamma(\mathbf{K}''))}\right]\Gamma(\mathbf{K})\Bigg\}$$
$$+(1+\Gamma(\mathbf{K}''))(1+\Gamma(\mathbf{K}))\frac{(1-\gamma)}{(1+\gamma)}\frac{\kappa\beta_2(\mathbf{K})}{\rho\beta_1(\mathbf{K}'')}\left[\kappa^2-\frac{\mathbf{K}\cdot\mathbf{K}''}{k_1^2}\right]$$
$$-(1-\Gamma(\mathbf{K}''))(1+\Gamma(\mathbf{K}))(\kappa\beta_2(\mathbf{K}))^2\Bigg\}$$
$$+2i\int d^2K' \int d^2K\, F(\mathbf{K}''-\mathbf{K}')F(\mathbf{K}'-\mathbf{K})\Psi_i(\mathbf{K})$$
$$\times\Bigg\{H_{11}(\mathbf{K}',\mathbf{K})(1+\Gamma(\mathbf{K}''))\frac{1}{\beta_1(\mathbf{K}'')}\left[\frac{\mathbf{K}'\cdot\mathbf{K}''}{k_1^2}-1-\beta_1(\mathbf{K}'')\beta_1(\mathbf{K}')\frac{(1-\Gamma(\mathbf{K}''))}{(1+\Gamma(\mathbf{K}''))}\right]$$
$$+H_{12}(\mathbf{K}',\mathbf{K})(1+\Gamma(\mathbf{K}''))(1+\gamma')\frac{1}{\rho}\frac{1}{\beta_1(\mathbf{K}'')}\left[\kappa^2-\frac{\mathbf{K}'\cdot\mathbf{K}''}{k_1^2}\right]$$
$$-H_{12}(\mathbf{K}',\mathbf{K})(1-\Gamma(\mathbf{K}''))\kappa\beta_2(\mathbf{K}')(1-\gamma')\Bigg\}.$$

Define $G_{11}(\mathbf{K}'',\mathbf{K}',\mathbf{K})$, such that

$$\Psi_f^{(2)}(\mathbf{K}'') = \int d^2K' \int d^2K\, F(\mathbf{K}''-\mathbf{K}')F(\mathbf{K}'-\mathbf{K})\Psi_i(\mathbf{K})G_{11}(\mathbf{K}'',\mathbf{K}',\mathbf{K}). \tag{5.90}$$

With much work and use of the second identity in Eq. (5.42), the above expression is equivalent to

$$
\begin{aligned}
&G_{11}(\mathbf{K}'',\mathbf{K}',\mathbf{K}) \\
&= \frac{1}{2}\left(\kappa^2 - 1\right)\left[(1+\Gamma(\mathbf{K}''))(1-\Gamma(\mathbf{K}))\frac{\beta_1(\mathbf{K})}{\beta_1(\mathbf{K}'')} - (1-\Gamma(\mathbf{K}''))(1+\Gamma(\mathbf{K}))\right] \\
&+ \frac{iH_{11}(\mathbf{K}',\mathbf{K})}{\beta_1(\mathbf{K}'')}\left[\left(\frac{\mathbf{K}'\cdot\mathbf{K}''}{k_1^2} - 1\right)(1+\Gamma(\mathbf{K}'')) - \beta_1(\mathbf{K}'')\beta_1(\mathbf{K}')(1-\Gamma(\mathbf{K}''))\right] \\
&+ iH_{12}(\mathbf{K}',\mathbf{K})(1+\Gamma(\mathbf{K}''))\frac{(1+\gamma')}{\beta_1(\mathbf{K}'')} \\
&\times\left[\frac{\kappa^2}{\rho} - \frac{1}{\rho}\frac{\mathbf{K}'\cdot\mathbf{K}''}{k_1^2} - \rho\beta_1(\mathbf{K}'')\beta_1(\mathbf{K}')\frac{(1-\Gamma(\mathbf{K}''))}{(1+\Gamma(\mathbf{K}''))}\frac{1-\Gamma(\mathbf{K}')}{1+\Gamma(\mathbf{K}')}\right].
\end{aligned}
\tag{5.91}
$$

In order to find the second-order field scattering through the interface, set $N = 2$ in Eq. (5.21).

$$
\begin{aligned}
\Psi_-^{(2)}(\mathbf{K}'')(1+\gamma'') = &-\int d^2K\left(\beta_1(\mathbf{K})\right)^2 F_2(\mathbf{K}''-\mathbf{K})\Psi_i(\mathbf{K}) \\
&+\int d^2K\, 2i\beta_1(\mathbf{K})F(\mathbf{K}''-\mathbf{K})\Psi_f^{(1)}(\mathbf{K}) \\
&-\int d^2K\left(\beta_1(\mathbf{K})\right)^2 F_2(\mathbf{K}''-\mathbf{K})\Psi_f^{(0)}(\mathbf{K}) \\
&+\int d^2K\,\kappa\beta_2(\mathbf{K})F(\mathbf{K}''-\mathbf{K})[1-\gamma]\Psi_{2-}^{(1)}(\mathbf{K}) \\
&+\int d^2K\left(\kappa\beta_2(\mathbf{K})\right)^2 F_2(\mathbf{K}''-\mathbf{K})[1+\gamma]\Psi_{2-}^{(0)}(\mathbf{K}) \\
&+\Psi_f^{(2)}(\mathbf{K}'').
\end{aligned}
\tag{5.92}
$$

The expressions

$$
\Psi_f^{(1)}(\mathbf{K}) = \int d^2K' H_{11}(\mathbf{K},\mathbf{K}')F(\mathbf{K}-\mathbf{K}')\Psi_i(\mathbf{K}') \tag{5.93}
$$

and

$$
\Psi_-^{(1)}(\mathbf{K}) = \int d^2K' H_{12}(\mathbf{K},\mathbf{K}')F(\mathbf{K}-\mathbf{K}')\Psi_i(\mathbf{K}') \tag{5.94}
$$

are obtained by combining Eqs. (5.4), (5.62) and Eqs. (5.5), (5.69). Combining Eqs. (5.57) and (5.58) yields

$$\Psi_{-}^{(0)}(\mathbf{K}) = \frac{1+\Gamma(\mathbf{K})}{(1+\gamma)}\Psi_i(\mathbf{K}). \tag{5.95}$$

Using Eqs (5.88), (5.93), (5.94), and (5.95) in Eq. (5.92) yields

$$\begin{aligned}
&\Psi_{-}^{(2)}(\mathbf{K}'')(1+\gamma'') \\
&= \int d^2K \int d^2K' F(\mathbf{K}''-\mathbf{K}')F(\mathbf{K}'-\mathbf{K})\Psi_i(\mathbf{K}) \\
&\times\Big\{-\beta_1^2(\mathbf{K})(1+\Gamma(\mathbf{K})) + (\kappa\beta_2(\mathbf{K}))^2(1+\Gamma(\mathbf{K})) + 2iH_{11}(\mathbf{K}',\mathbf{K})\beta_1(\mathbf{K}') \\
&+2iH_{12}(\mathbf{K}',\mathbf{K})\kappa\beta_2(\mathbf{K}')(1-\gamma') + G_{11}(\mathbf{K}'',\mathbf{K}',\mathbf{K})\Big\}.
\end{aligned} \tag{5.96}$$

Using the following definition for $G_{12}(\mathbf{K}'',\mathbf{K}',\mathbf{K})$,

$$\Psi_{-}^{(2)}(\mathbf{K}'') = \int d^2K \int d^2K' F(\mathbf{K}''-\mathbf{K}')F(\mathbf{K}'-\mathbf{K})\Psi_i(\mathbf{K}')G_{12}(\mathbf{K}'',\mathbf{K}',\mathbf{K}), \tag{5.97}$$

in Eq. (5.96) yields

$$\begin{aligned}
G_{12}(\mathbf{K}'',\mathbf{K}',\mathbf{K})(1+\gamma'') = \Big\{&-\beta_1^2(\mathbf{K})(1+\Gamma(\mathbf{K})) + (\kappa\beta_2(\mathbf{K}))^2(1+\Gamma(\mathbf{K})) \\
&+2iH_{11}(\mathbf{K}',\mathbf{K})\beta_1(\mathbf{K}') \\
&+2iH_{12}(\mathbf{K}',\mathbf{K})\kappa\beta_2(\mathbf{K}')(1-\gamma') + G_{11}(\mathbf{K}'',\mathbf{K}',\mathbf{K})\Big\}.
\end{aligned} \tag{5.98}$$

By noting the following identities,

$$(\beta_1(\mathbf{K}))^2 - (\kappa\beta_2(\mathbf{K}))^2 = \frac{k_1^2-K^2}{k_1^2} - \frac{k_2^2-K^2}{k_1^2} = 1-\kappa^2, \tag{5.99}$$

Eq. (5.98) simplifies to

$$\begin{aligned}
(1+\gamma'')G_{12}(\mathbf{K}'',\mathbf{K}',\mathbf{K}) = &\left(\kappa^2-1\right)(1+\Gamma(\mathbf{K})) + 2iH_{11}(\mathbf{K}',\mathbf{K})\beta_1(\mathbf{K}') \\
&+2iH_{12}(\mathbf{K}',\mathbf{K})\kappa\beta_2(\mathbf{K}')(1-\gamma') + G_{11}(\mathbf{K}'',\mathbf{K}',\mathbf{K}).
\end{aligned} \tag{5.100}$$

5.6.2 Second-order coherent field

In order to check the zero-order approximation for the coherent intensity, the goal in this section is to find the coherent component of the second-order T-matrix, $\left\langle T^{(2)}(\mathbf{K}'',\mathbf{K})\right\rangle$. If we allow G to represent both G_{11} in Eq. (5.91) and G_{12} in Eq. (5.98), it can be expressed as the sum:

$$G(\mathbf{K}'',\mathbf{K}',\mathbf{K}) \equiv G_a(\mathbf{K}'',\mathbf{K}) + G_b(\mathbf{K}'',\mathbf{K}',\mathbf{K}). \tag{5.101}$$

The T-matrix is found from Eq. (5.90) or Eq. (5.97):

$$\begin{aligned} T^{(2)}(\mathbf{K}'',\mathbf{K}) = &\int d^2K' F(\mathbf{K}''-\mathbf{K}')F(\mathbf{K}'-\mathbf{K})G_a(\mathbf{K}'',\mathbf{K}) \\ &+\int d^2K' F(\mathbf{K}''-\mathbf{K}')F(\mathbf{K}'-\mathbf{K})G_b(\mathbf{K}'',\mathbf{K}',\mathbf{K}). \end{aligned} \tag{5.102}$$

Substituting

$$f_1(\mathbf{R}) = f(\mathbf{R}) \tag{5.103}$$

and

$$f_2(\mathbf{R}) = f(\mathbf{R})\mathrm{e}^{i\mathbf{K}_i\cdot\mathbf{R}} \tag{5.104}$$

into the identity

$$\frac{1}{(2\pi)^2}\int d^2R f_1(\mathbf{R})f_2(\mathbf{R})\mathrm{e}^{-i\mathbf{K}\cdot\mathbf{R}} = \int d^2K' F_1(\mathbf{K}-\mathbf{K}')F_2(\mathbf{K}') \tag{5.105}$$

yields

$$\frac{1}{(2\pi)^2}\int d^2R f^2(\mathbf{R})\mathrm{e}^{-i(\mathbf{K}''-\mathbf{K})\cdot\mathbf{R}} = \int d^2K' F(\mathbf{K}''-\mathbf{K}')F(\mathbf{K}'-\mathbf{K}). \tag{5.106}$$

Note that f is a WSS process with unit variance. Therefore, taking the expected value of Eq. (5.106) over the ensemble of interfaces results in the following identity:

$$\delta(\mathbf{K}''-\mathbf{K})=\left\langle\int d^2K' F_1(\mathbf{K}''-\mathbf{K}')F_2(\mathbf{K}'-\mathbf{K})\right\rangle. \tag{5.107}$$

Consequently, the expected value of the first term on the right side of (5.81) results in the following expression for the coherent second-order T-matrix:

$$\left\langle\int d^2K' F(\mathbf{K}''-\mathbf{K}')F(\mathbf{K}'-\mathbf{K})\right\rangle G_a(\mathbf{K}'',\mathbf{K})=\delta(\mathbf{K}''-\mathbf{K})G_a(\mathbf{K},\mathbf{K}). \tag{5.108}$$

Define Int2 to be the second term on the right side of Eq. (102).

$$\text{Int2}=\int d^2K' F(\mathbf{K}''-\mathbf{K}')F(\mathbf{K}'-\mathbf{K})G_b(\mathbf{K}'',\mathbf{K}',\mathbf{K}). \tag{5.109}$$

Substituting

$$F(\mathbf{K})=\frac{1}{(2\pi)^2}\int d^2K f(\mathbf{R})\mathrm{e}^{-i\mathbf{K}\cdot\mathbf{R}} \tag{5.110}$$

for both $F(\mathbf{K}''-\mathbf{K}')$ and $F(\mathbf{K}'-\mathbf{K})$ in Eq. (5.109), and taking the expected value, yields

$$\begin{aligned}\langle\text{Int2}\rangle=\int d^2K' G_b(\mathbf{K}'',\mathbf{K}',\mathbf{K})\Big\{\int d^2R\,\mathrm{e}^{-i(\mathbf{K}'-\mathbf{K})\cdot\mathbf{R}}\\ \times\frac{1}{(2\pi)^4}\int d^2R'\,\mathrm{e}^{-i(\mathbf{K}''-\mathbf{K}')\cdot\mathbf{R}'}C(\mathbf{R}'-\mathbf{R})/h^2\Big\},\end{aligned} \tag{5.111}$$

where

$$C(\mathbf{R}'-\mathbf{R})\equiv h^2\langle f(\mathbf{R}')f(\mathbf{R})\rangle \tag{5.112}$$

is the surface autocorrelation function. By noting

$$\begin{aligned}\frac{1}{(2\pi)^2}\int d^2R'\,\mathrm{e}^{-i(\mathbf{K}''-\mathbf{K}')\cdot\mathbf{R}'}C(\mathbf{R}'-\mathbf{R})&=\mathrm{e}^{-i(\mathbf{K}''-\mathbf{K}')\cdot\mathbf{R}}\\ &\quad\times\frac{1}{(2\pi)^2}\int d^2U\,\mathrm{e}^{-i(\mathbf{K}''-\mathbf{K}')\cdot\mathbf{U}}C(\mathbf{U})\\ &=\mathrm{e}^{-i(\mathbf{K}''-\mathbf{K}')\cdot\mathbf{R}}W(\mathbf{K}''-\mathbf{K}')/h^2\end{aligned} \tag{5.113}$$

and

$$\frac{1}{(2\pi)^2}\int d^2R\, \mathrm{e}^{-i(\mathbf{K}'-\mathbf{K})\cdot\mathbf{R}}\mathrm{e}^{-i(\mathbf{K}''-\mathbf{K}')\cdot\mathbf{R}}\, W(\mathbf{K}''-\mathbf{K}') = \delta(\mathbf{K}-\mathbf{K}'')W(\mathbf{K}''-\mathbf{K}'), \quad (5.114)$$

Eq. (5.111) simplifies to

$$\langle \mathrm{Int2}\rangle = \delta(\mathbf{K}-\mathbf{K}'')\int d^2K' G_b(\mathbf{K}'',\mathbf{K}',\mathbf{K})W(\mathbf{K}''-\mathbf{K}')/h^2 . \quad (5.115)$$

By using Eqs. (5.107) and (5.115), the expected value of Eq. (5.102) simplifies to

$$\left\langle T^{(2)}(\mathbf{K}'',\mathbf{K})\right\rangle$$

$$= \delta(\mathbf{K}''-\mathbf{K})\left\{G_a(\mathbf{K},\mathbf{K}) + \int d^2K' G_b(\mathbf{K},\mathbf{K}',\mathbf{K})W(\mathbf{K}-\mathbf{K}')/h^2\right\}. \quad (5.116)$$

By making an approximation suggested by Thorsos and Jackson (private communication), Eq. (5.116) is approximately

$$\begin{aligned}\left\langle T^{(2)}(\mathbf{K}'',\mathbf{K})\right\rangle &\cong \delta(\mathbf{K}''-\mathbf{K})\left\{G_a(\mathbf{K},\mathbf{K}) + G_b(\mathbf{K},\mathbf{K},\mathbf{K})\int d^2K'\, W(\mathbf{K}-\mathbf{K}')/h^2\right\} \\ &= \delta(\mathbf{K}''-\mathbf{K})\left\{G_a(\mathbf{K},\mathbf{K}) + G_b(\mathbf{K},\mathbf{K},\mathbf{K})\right\}. \quad (5.117)\end{aligned}$$

To second-order, the expected value of the T-matrix is given by

$$\langle T(\mathbf{K}'',\mathbf{K})\rangle \cong \left\langle T^{(0)}(\mathbf{K}'',\mathbf{K})\right\rangle + \frac{1}{2}(k_1h)^2\left\langle T^{(2)}(\mathbf{K}'',\mathbf{K})\right\rangle. \quad (5.118)$$

The intensity reflection or transmission coefficient, $\mathcal{R}_I$, (Thorsos, 1990) follows from Eq. (5.118).

$$\mathcal{R}_I = |\mathcal{R}(\mathbf{K})|^2 \cong |\mathcal{R}_0(\mathbf{K})|^2 + (k_1h)^2\,\mathrm{Re}\left\{\mathcal{R}_0^*(\mathbf{K})\mathcal{R}_2(\mathbf{K})\right\}, \quad (5.119)$$

where

$$\mathcal{R}(\mathbf{K}) \cong \mathcal{R}_0(\mathbf{K}) + \frac{1}{2}(k_1h)^2\mathcal{R}_2(\mathbf{K}), \quad (5.120)$$

$$\langle T(\mathbf{K}'',\mathbf{K})\rangle = \delta(\mathbf{K}''-\mathbf{K})\mathcal{R}(\mathbf{K}), \quad (5.121)$$

and (see also Berman, 1992)

$$\left\langle T^{(2)}(\mathbf{K}'',\mathbf{K})\right\rangle = \delta(\mathbf{K}''-\mathbf{K})\mathcal{R}_2(\mathbf{K}). \tag{5.122}$$

For the case of scattering from an interface, substitute the flat-surface reflection coefficient $\Gamma(\mathbf{K})$ for $\mathcal{R}_0(\mathbf{K})$ and $\mathcal{R}_{11}(\mathbf{K})$ for $\mathcal{R}(\mathbf{K})$; for the case of scattering through an interface, substitute the flat surface transmission coefficient $\mathcal{T}(\mathbf{K})$ for $\mathcal{R}_0(\mathbf{K})$, and $\mathcal{R}_{12}(\mathbf{K})$ for $\mathcal{R}(\mathbf{K})$.

For scattering from the interface, Eq. (5.91) along with the definition in Eq. (5.101) yields

$$G_{11a}(\mathbf{K}'',\mathbf{K})$$

$$= \frac{1}{2}\left(\kappa^2-1\right)\left[(1+\Gamma(\mathbf{K}''))(1-\Gamma(\mathbf{K}))\frac{\beta_1(\mathbf{K})}{\beta_1(\mathbf{K}'')} - (1-\Gamma(\mathbf{K}''))(1+\Gamma(\mathbf{K}))\right] \tag{5.123}$$

and

$$G_{11b}(\mathbf{K}'',\mathbf{K}',\mathbf{K}) = \frac{iH_{11}(\mathbf{K}',\mathbf{K})}{\beta_1(\mathbf{K}'')}$$

$$\times\left[\left(\frac{\mathbf{K}'\cdot\mathbf{K}''}{k_1^2}-1\right)(1+\Gamma(\mathbf{K}''))-\beta_1(\mathbf{K}'')\beta_1(\mathbf{K}')(1-\Gamma(\mathbf{K}''))\right]$$

$$+iH_{12}(\mathbf{K}',\mathbf{K})\frac{(1+\gamma')}{\beta_1(\mathbf{K}'')}$$

$$\times\left[\left(\frac{\kappa^2}{\rho}-\frac{1}{\rho}\frac{\mathbf{K}'\cdot\mathbf{K}''}{k_1^2}\right)(1+\Gamma(\mathbf{K}''))-\rho\beta_1(\mathbf{K}'')\beta_1(\mathbf{K}')(1-\Gamma(\mathbf{K}''))\left(\frac{1-\Gamma(\mathbf{K}')}{1+\Gamma(\mathbf{K}')}\right)\right]. \tag{5.124}$$

Likewise, for scattering through the interface, using Eq. (5.100) and the definition in Eq. (5.101) yields

$$G_{12a}(\mathbf{K}'',\mathbf{K}) = \frac{1}{1+\gamma''}\left(\kappa^2-1\right)(1+\Gamma(\mathbf{K}))+\frac{1}{1+\gamma''}G_{11a}(\mathbf{K}'',\mathbf{K}) \tag{5.125}$$

and

$$G_{12b}(\mathbf{K}'',\mathbf{K}',\mathbf{K})(1+\gamma'')$$

$$= 2iH_{11}(\mathbf{K}',\mathbf{K})\beta_1(\mathbf{K}') + 2iH_{12}(\mathbf{K}',\mathbf{K})\kappa\beta_2(\mathbf{K}')(1-\gamma') + G_{11b}(\mathbf{K}'',\mathbf{K}',\mathbf{K}). \tag{5.126}$$

5.6.3 Second-order coherent field calculations for incident plane wave

In Eq. (5.119), $\mathcal{R}_I$ consists of the zero-order term and the second-order term; the first-order T-matrix is zero mean. In order to compare the second-order term to that of the zero-order term, the second term on the right side of Eq. (5.119) divided by the first term on the right side the equation is plotted in Fig. 5.4 as a function of the RMS (root mean square) surface height. The grazing angle is $20°$ in Fig. 5.4a, and it is $40°$ in Fig. 5.4b. The solid curve results from using Eq. (5.116), the dashed curve is due to Eq. (5.117).

5.6.4 Modification of coherent field calculation

Taking the expected value of both sides of Eq. (5.5) and using Eq. (5.121) yields

$$\langle \Psi_{2-}(\mathbf{K}) \rangle = \mathcal{R}_{12}(\mathbf{K})\Psi_i(\mathbf{K}). \tag{5.127}$$

For the case in which medium 3 parameters are identical to medium 2 parameters,

$$\psi_{2-}(\mathbf{r}) = \int d^2K \Psi_{2-}(\mathbf{K}) e^{-ik_1\beta_1(\mathbf{K})z} e^{i\mathbf{K}\cdot\mathbf{R}}. \tag{5.128}$$

Taking the expected value of the above equation and using Eq. (5.127) results in an expression for the coherent field penetrating the rough interface.

$$\langle \psi_{2-}(\mathbf{r}) \rangle = \int d^2K \mathcal{R}_{12}(\mathbf{K})\Psi_i(\mathbf{K}) e^{-ik_1\beta_1(\mathbf{K})z} e^{i\mathbf{K}\cdot\mathbf{R}}. \tag{5.129}$$

Likewise, the coherent field scattered from the interface is given by

$$\langle \psi_f(\mathbf{r}) \rangle = \int d^2K \mathcal{R}_{11}(\mathbf{K})\Psi_i(\mathbf{K}) e^{ik_1\beta_1(\mathbf{K})z} e^{i\mathbf{K}\cdot\mathbf{R}}. \tag{5.130}$$

Note that $\mathcal{R}_{12}(\mathbf{K})$ in Eq. (5.129) is a coherent *transmission* coefficient, but $\mathcal{R}_{11}(\mathbf{K})$ in Eq. (5.130) is a coherent *reflection* coefficient. Referring to Eq. (2.91), the exact expression for the zero-order field is easily modified by substituting $\mathcal{R}_{12}(\mathbf{K})$ for the transmission coefficient.

$$\langle \psi_{2-}(\mathbf{r}) \rangle = i \int_0^\infty dK \frac{r_0 K \mathcal{R}_{12}(\mathbf{K})}{k_1 \beta_1(\mathbf{K})} e^{i(z_s k_1 \beta_1(\mathbf{K}) - z k_2 \beta_2(\mathbf{K}))} J_0(KR). \tag{5.131}$$

The square of the time-dependent coherent field magnitude scattered through the rough interface due to an incident point source with baseband source signal $U(\omega)$ is therefore

$$I_{2c}(\mathbf{r},t) = \left| \int_{-\infty}^\infty d\omega U(\omega) e^{-i\omega t} \int_0^\infty dK \frac{r_0 K \mathcal{R}_{12}(\mathbf{K})}{k_1 \beta_1(\mathbf{K})} e^{i(z_s k_1 \beta_1(\mathbf{K}) - z k_2 \beta_2(\mathbf{K}))} J_0(KR) \right|^2. \tag{5.132}$$

5.7 Summary

Nth-order perturbation recursion equations are derived in this chapter that allow for simple computation of the first and second-order fields for scattering through and from a fluid-fluid rough interface. An expression for the second-order coherent field is derived that illustrates when it is necessary to include the second-order field in the coherent intensity calculations for scattering through rough interfaces. In the ocean experiment simulations, $k_1 h \cong 1$, and including the second-order component reduces the coherent field calculated with the zero-order result by almost ten percent. Since the peak incoherent intensity and coherent intensity typically differ by over an order of magnitude for all incident angles, and at all receivers, the difference in the calculated coherent field by excluding the second-order correction does not affect the intensity velocity algorithm output.

The results in this chapter are general in that the medium below the lowest point on the rough interface is allowed to be vertically stratified, viscoelastic, or porous, and is contained in the reflection coefficient of the corresponding flat surface problem. For the case of increasing sound speed with depth, these results show that an interference effect can occur when enough energy is redirected back toward the interface. Since the sediment parameters such as sound speed, sound-speed gradient, and density are not everywhere constant, the effect of treating the sediment parameters as random is discussed in the next chapter.

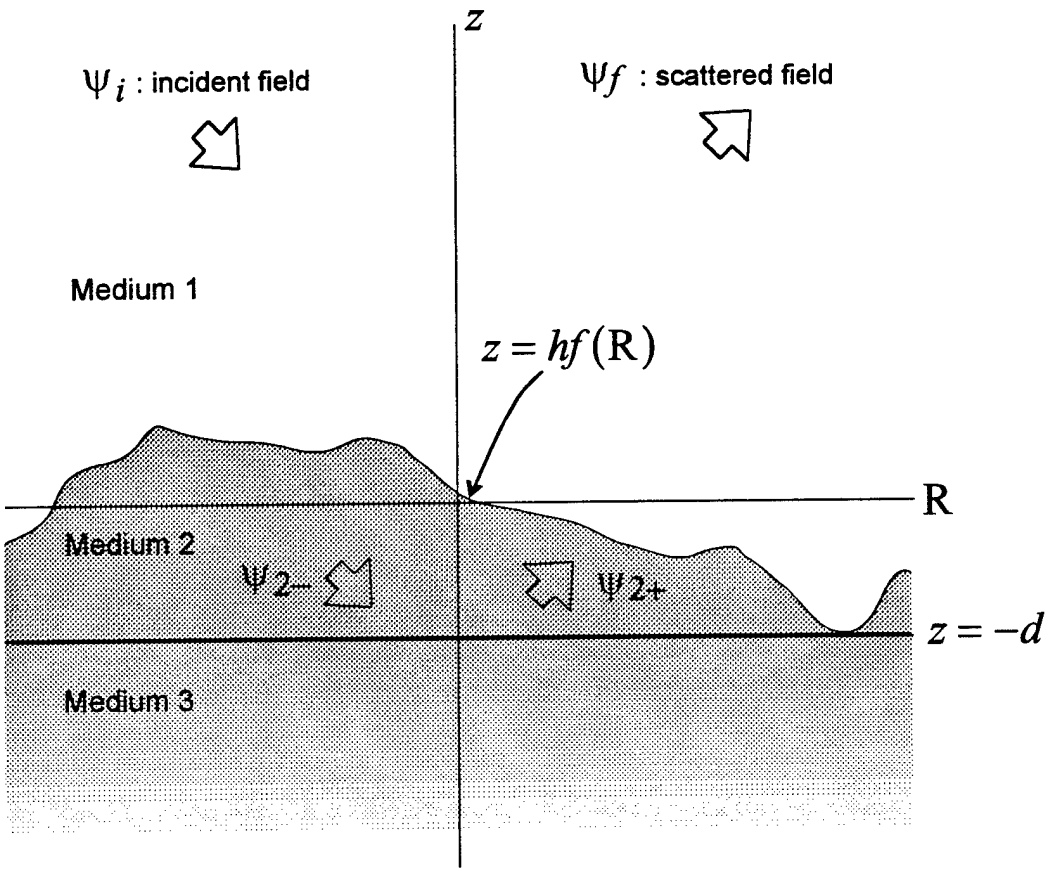

Figure 5.1 : Definition of the scattering problem for an arbitrary two-dimensional rough interface. Medium 1 $\left(z > hf(\mathbf{R})\right)$ and medium 2 $\left(-d < z < hf(\mathbf{R})\right)$ are homogenous fluids; the medium parameters can be a function of z for $(z < -d)$. This diagram can be viewed as a slice through a two-dimensional interface.

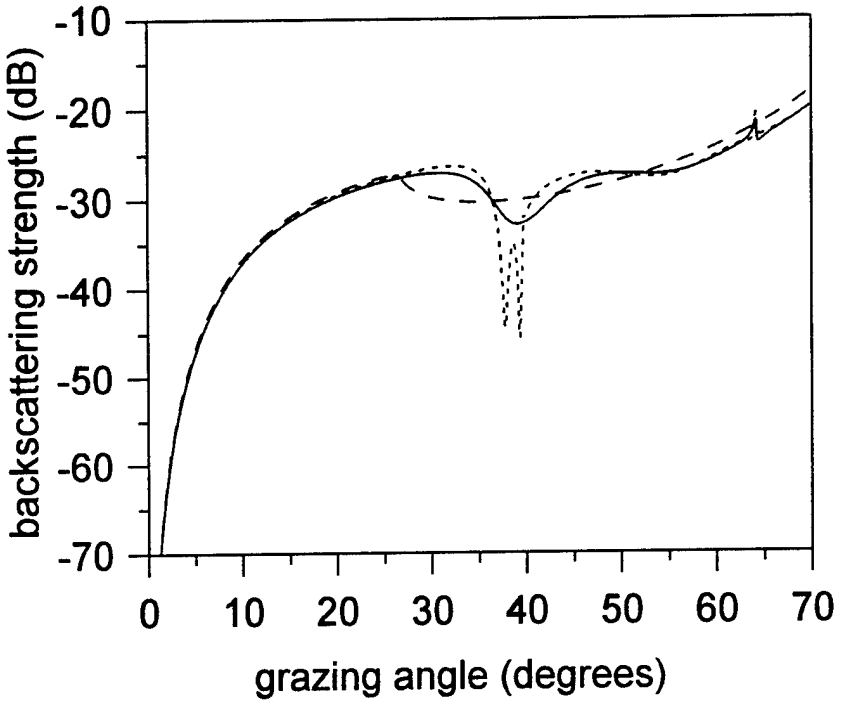

Figure 5.2 : Medium 2 is very fine sand with $d = \lambda$, $\kappa = 1/(1.12 - i \cdot 0.004)$, and $\rho = 1.85$. Medium 3 is sedimentary rock with $\kappa_\ell = 1/(2.3 - i \cdot 0.004)$, $\kappa_t = 1/(1.3 - i \cdot 0.11)$, and $\rho_3 / \rho_1 = 2.5$. Surface: $w_2 = 0.04/(2\pi)$, $\gamma = 4.0$. The solid curve uses these parameters. For the dashed curve, $\kappa_t = 1/1.13$. For the dotted curve, there is no layering, i.e., $d \to \infty$.

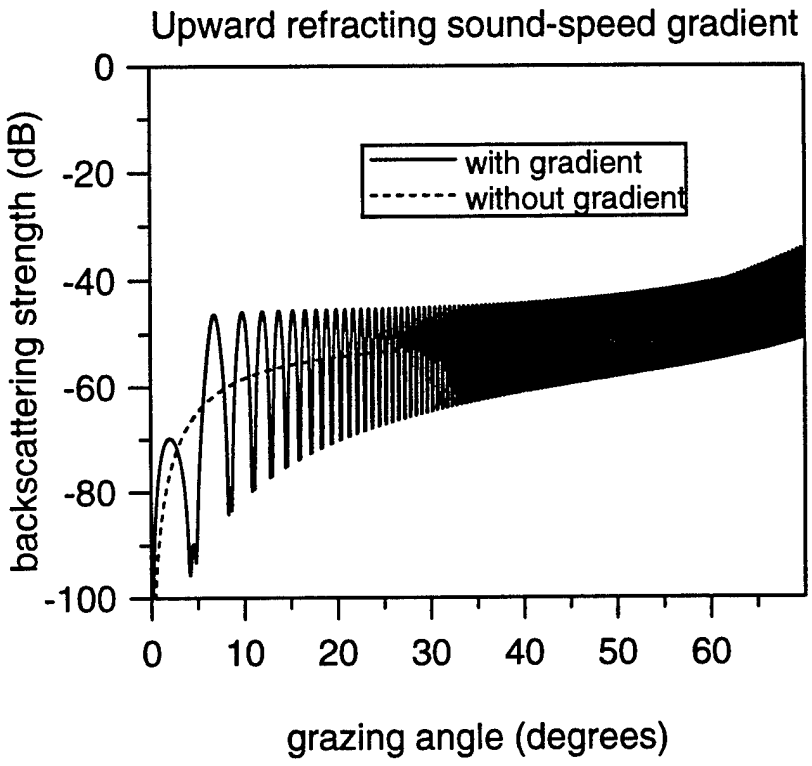

Figure 5.3 : Bottom backscattering strength with and without a sound-speed gradient for soft, silty, or clayey bottom: $\gamma = 3.25$, $w_2 = 1.636 \times 10^{-4}\ \mathrm{m}^{3/4}$, frequency = 300 kHz, $\rho = 1.548$, $\delta = 1.445 \times 10^{-4}$, $\nu = 0.96$, $c_1 = 1545\ \mathrm{m/s}$, gradient = $1.3\ \mathrm{s}^{-1}$.

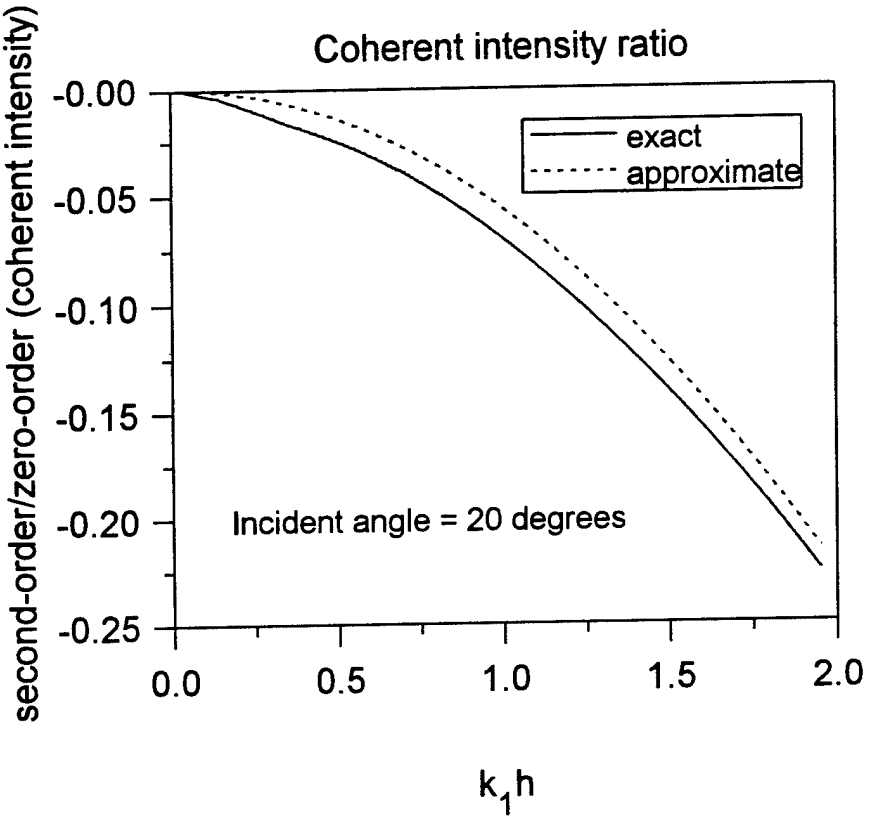

Figure 5.4a : Ratio of second-order coherent term to zero-order term, $(k_1 h)^2 \,\mathrm{Re}\left\{\mathcal{R}_0^*(\mathbf{K})\mathcal{R}_2(\mathbf{K})\right\}\Big/\left|\mathcal{R}_0(\mathbf{K})\right|^2$ with frequency $= 20\,\mathrm{kHz}$, $\rho = 2.0$, $\delta = 0.0163$, $\gamma = 3.0$, $w_2 = 6.2\times10^{-5}\,\mathrm{m}$, $\nu = 1.13$, $c_1 = 1536\,\mathrm{m/s}$, and incident grazing angle, $\theta_i = 20^\circ$.

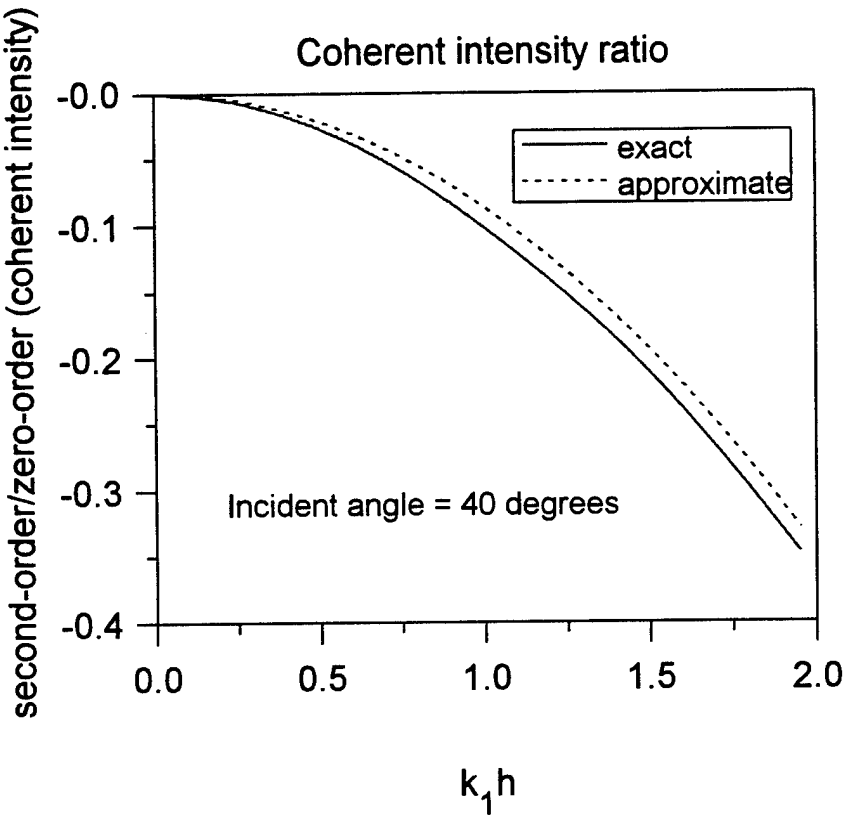

Figure 5.4b : Ratio of second-order coherent term to zero-order term: $(k_1 h)^2 \,\mathrm{Re}\{\mathcal{R}_0^*(\mathbf{K})\mathcal{R}_2(\mathbf{K})\}/|\mathcal{R}_0(\mathbf{K})|^2$ with $\theta_i = 40°$, otherwise same parameters as Fig. 5.4a (frequency = 20 kHz, $\rho = 2.0$, $\delta = 0.0163$, $\gamma = 3.0$, $w_2 = 6.2 \times 10^{-5}$ m, $\nu = 1.13$, $c_1 = 1536$ m/s).

CHAPTER 6

First-order perturbation solution for scattering from a rough seafloor including the effects of random subsurface stratification

6.1 Introduction to chapter 6

The example in Fig. 5.3 shows that upward refraction due to a sound-speed gradient in the sediment results in constructive and destructive interference in the field scattered back into the water. This example assumes the sound-speed gradient and other seafloor parameters are not random. Since seafloor parameters such as sound-speed gradient and density actually vary with position, a more suitable model may be one that takes into account the inherent randomness of the seafloor parameters. In the last chapter, a first-order expression for the scattering cross section per unit area per unit solid angle (differential cross section) is derived that includes the complexity of the medium below the lowest point on the rough interface (medium 3) in the flat surface reflection coefficient. In this chapter, the reflection coefficient, Γ_{23}, is modeled as a random variable. The expected value of the differential cross section over the random sediment parameters is then expressed analytically in terms of reflection coefficient moments. Analytical expressions for the reflection coefficient moments are found using ray theory. These analytical results are compared with modeling the sound-speed gradient as a random variable with Gaussian probability distribution (Moe and Jackson, 1994b), where the expected value of the differential cross section is calculated by means of a numerical integration.

6.2 Averaged scattering strength with random sound-speed gradient

The first-order perturbation solution for the differential cross section for scattering from the rough interface can be found by combining Eqs. (5.71) and (5.63).

$$\sigma_{11}(\hat{\alpha}_f,\hat{\alpha}_i)=\frac{k_1^4}{4}W(\mathbf{K}_f-\mathbf{K}_i) \times\left|a(1+\Gamma(\mathbf{K}_f))(1+\Gamma(\mathbf{K}_i))+b(1-\Gamma(\mathbf{K}_f))(1-\Gamma(\mathbf{K}_i))\right|^2, \tag{6.1}$$

where

$$a(\mathbf{K}_f,\mathbf{K}_i)=1-\frac{\kappa^2}{\rho}+\left(\frac{1}{\rho}-1\right)\frac{\mathbf{K}_f\cdot\mathbf{K}_i}{k_1^2} \tag{6.2}$$

and

$$b(\mathbf{K}_f,\mathbf{K}_i)=\beta_1(\mathbf{K}_f)\beta_1(\mathbf{K}_i)(\rho-1) \tag{6.3}$$

are given by Eqs. (5.64) and (5.65). The vectors $\mathbf{K}_f$ and $\mathbf{K}_i$ are the transverse components of the scattered field and incident field wave vectors, respectively. The mean (flat) surface reflection coefficient, Γ, is written explicitly in terms of the reflection coefficients Γ_{12} and Γ_{23} in Eq. (5.43), where Γ_{12} represents the mean surface reflection coefficient at $z=0$ as $d\to\infty$ and Γ_{23} is the reflection coefficient corresponding to the interface between medium 2 and medium 3 ($z=-d$). All of the complexity of the lower medium is contained in Γ_{23}. As shown in Fig. 5.3, the lower medium, characterized in Eq. (5.43) by Γ_{23}, can have a notable effect on the scattered field strength if it redirects a significant amount of the downward propagating energy in the sediment back up towards the rough interface. Two first-order effects as depicted in Fig. 6.1 can result in scattering energy away from the interface, resulting in destructive or constructive interference.

Since sediment parameters are typically not constant, the interference effects in Fig. 5.3 may not actually be observable. By treating the gradient as a random variable, the expression for the differential cross section given in Eq. (6.1), weighted by a Gaussian probability distribution for the sound-speed gradient (linear increase in squared wave number with depth) with variance $\left\langle \left| g - \langle g \rangle \right|^2 \right\rangle = 0.1 \mathrm{sec}^{-2}$ and mean $\langle g \rangle = 1.3 \mathrm{sec}^{-1}$, is numerically integrated. The resulting averaged backscattering strength is plotted in Fig. 6.2 as a function of grazing angle and compared with the backscattered field strength due only to the rough seafloor surface with no gradient, $\Gamma_{23} = 0$. In this example, a sound-speed gradient in the sediment results in a substantial increase in the average backscattered field strength. This scattering gain occurs at all grazing angles, but is greater at smaller grazing angles. Large grazing angles result in long refracted paths in the lossy sediment, and therefore contribute less to this gain than small grazing angles with shorter paths.

Using the same parameters as in the above example, we plot the bistatic scattering strength in Fig. 6.3 as a function of scattered grazing angle for an incident grazing angle $\theta_i = 15°$. The scattered direction in all plots is chosen such that the incident transverse wave vector, $\mathbf{K}_i$, and the scattered transverse wave vector, $\mathbf{K}_f$, are in the same line, and the scattered grazing angle, θ_f, is measured from the horizontal in the backward direction. In this case, backscattering ($\mathbf{K}_f = -\mathbf{K}_i$) corresponds to an angle of $\theta_f = 15°$. Scattering gain due to the upwardly refracting sediment occurs in all scattered directions, including the backscattered direction, where a local scattering gain maximum, or backscattering enhancement, is apparent. The reason for this backscattered peak, as illustrated in Fig. 6.4, is that the coherent sum of the two paths corresponding to the incident and scattered direction occurs only in the backscattered direction, because only in this direction are the paths $ABCD$ and

$D'CBA'$ of equal length. This effect is illustrated for similar scattering problems by Lang and Khadr (1992) in their analysis of remote sensing of a vegetation canopy over a flat ground, and in Hanson and Zavorotny (1995) in their analysis of backscattering from an ocean-like surface. The width of the peak depends on the sound-speed gradient variance, $\left\langle |g - \langle g \rangle|^2 \right\rangle$. The larger the sound-speed gradient variance, the narrower this peak. Another oscillation that depends on the sound-speed gradient can be observed just below a scattered grazing angle of 10°. At these angles, the oscillations in the scattering strength are not quite as rapid as those at larger grazing angles, and the variance chosen for the gradient is not sufficient to completely wash out the dependency of scattering strength on scattered grazing angle.

6.3 Formally averaged differential cross section with random sediment parameters

Rather than using numerical integration as in the last example, using a general approach to this problem leads to a formally averaged analytic expression for the differential cross section per unit area that includes the randomness of seafloor parameters below $f(\mathbf{R})$, in addition to the randomness of the interface. All of the complexity of the lower medium in Eq. (6.1) is contained in the reflection coefficient, Γ. Consequently, the inherent randomness of the sediment is equivalently represented in the random reflection coefficient, Γ. This point of view implies that the expression in Eq. (6.1) is actually a conditional expected value over the rough interface given deterministic sediment parameters below the interface, or a deterministic reflection coefficient, and the goal is to find the expected value of Eq. (6.1) over the random fluctuations in the seafloor parameters below $z = f(\mathbf{R})$,

$$\tilde{\sigma}_{11} \equiv \frac{k_1^4}{4} W(\mathbf{K}_f - \mathbf{K}_i) \left\langle \left| a(1+\Gamma_f)(1+\Gamma_i) + b(1-\Gamma_f)(1-\Gamma_i) \right|^2 \right\rangle. \tag{6.4}$$

The approach is to express Eq. (6.4) in terms of moments of the flat surface reflection coefficients. The notation $\Gamma_f = \Gamma(\mathbf{K}_f)$ and $\Gamma_i = \Gamma(\mathbf{K}_i)$ is used for the reflection coefficient in Eq. (6.1). Expanding the square in Eq. (6.4) yields

$$\begin{aligned} \tilde{\sigma}_{11} = \frac{k_1^4}{4} W(\mathbf{K}_f - \mathbf{K}_i) \Big[& \left\langle \left| a(1+\Gamma_f)(1+\Gamma_i) \right|^2 \right\rangle + b^2 \left\langle \left| (1-\Gamma_f)(1-\Gamma_i) \right|^2 \right\rangle \\ & + 2b \operatorname{Re} \left\langle a(1+\Gamma_f)(1+\Gamma_i)(1-\Gamma_f^*)(1-\Gamma_i^*) \right\rangle \Big]. \end{aligned} \tag{6.5}$$

For monostatic scattering, the random variables Γ_f and Γ_i are equal ($\mathbf{K}_f = -\mathbf{K}_i$), and Eq. (6.5) becomes

$$\begin{aligned} \tilde{\sigma}_{11} = & \frac{k_1^4}{4} W(\mathbf{K}_f - \mathbf{K}_i) \\ & \times \Big\{ |a|^2 \left[1 + 4\left\langle |\Gamma|^2 \right\rangle + \left\langle |\Gamma|^4 \right\rangle + 2\operatorname{Re}\left\langle \Gamma^2 \right\rangle + 4\operatorname{Re}\langle \Gamma \rangle + 4\operatorname{Re}\left\langle \Gamma |\Gamma|^2 \right\rangle \right] \\ & + b^2 \left[1 + 4\left\langle |\Gamma|^2 \right\rangle + \left\langle |\Gamma|^4 \right\rangle + 2\operatorname{Re}\left\langle \Gamma^2 \right\rangle - 4\operatorname{Re}\langle \Gamma \rangle - 4\operatorname{Re}\left\langle \Gamma |\Gamma|^2 \right\rangle \right] \\ & + b \operatorname{Re}(a) \left[2 - 8\left\langle |\Gamma|^2 \right\rangle + 2\left\langle |\Gamma|^4 \right\rangle + 4\operatorname{Re}\left\langle \Gamma^2 \right\rangle \right] \\ & + 8b \operatorname{Im}(a) \left[\operatorname{Im}\left\langle \Gamma |\Gamma|^2 \right\rangle - \operatorname{Im}\langle \Gamma \rangle \right] \Big\}. \end{aligned} \tag{6.6}$$

Small changes in medium parameters result in rapid changes in phase of the reflection coefficient. The reflection coefficients, Γ_f and Γ_i, are therefore assumed to be independent random variables for bistatic scattering. However, for scattering in directions close to the backscattered direction, the reflection coefficients corresponding to the incident and scattered directions are neither equal or independent (see Fig. 6.3). For independent reflection coefficients, Eq. (6.5) becomes

$$\tilde{\sigma}_{11} = \frac{k_1^4}{4} W(\mathbf{K}_f - \mathbf{K}_i)$$
$$\times \Big\{ |a|^2 \Big[1 + 2\,\mathrm{Re}\langle \Gamma_f \rangle + \big\langle |\Gamma_f|^2 \big\rangle \Big] \Big[1 + 2\,\mathrm{Re}\langle \Gamma_i \rangle + \big\langle |\Gamma_i|^2 \big\rangle \Big]$$
$$+ b^2 \Big[1 - 2\,\mathrm{Re}\langle \Gamma_f \rangle + \big\langle |\Gamma_f|^2 \big\rangle \Big] \Big[1 - 2\,\mathrm{Re}\langle \Gamma_i \rangle + \big\langle |\Gamma_i|^2 \big\rangle \Big]$$
$$+ 2b\,\mathrm{Re}(a) \Big[\Big(1 - \big\langle |\Gamma_f|^2 \big\rangle \Big) \Big(1 - \big\langle |\Gamma_i|^2 \big\rangle \Big) - 4\,\mathrm{Im}\langle \Gamma_f \rangle \mathrm{Im}\langle \Gamma_i \rangle \Big]$$
$$- 4b\,\mathrm{Im}(a) \Big[\mathrm{Im}\langle \Gamma_i \rangle \Big(1 - \big\langle |\Gamma_f|^2 \big\rangle \Big) + \mathrm{Im}\langle \Gamma_f \rangle \Big(1 - \big\langle |\Gamma_i|^2 \big\rangle \Big) \Big] \Big\}. \tag{6.7}$$

In order to find expressions for the moments $\langle \Gamma \rangle$, $\langle \Gamma^2 \rangle$, $\langle |\Gamma|^2 \rangle$, $\langle \Gamma |\Gamma|^2 \rangle$, and $\langle |\Gamma|^4 \rangle$, an equivalent form of Eq. (5.43) is used to express the reflection coefficient, Γ, in terms of the partial reflection coefficients Γ_{12}, and Γ_{23} as a geometric sum,

$$\Gamma = \Gamma_{12} + \left(1 - \Gamma_{12}^2\right) \Gamma_{23}\, e^{2ik_2\beta_2 d} \sum_{n=0}^{\infty} \left(-\Gamma_{12}\Gamma_{23}\, e^{2ik_2\beta_2 d} \right)^n. \tag{6.8}$$

Small variations in medium parameters result in small deviations of the magnitude of the reflection coefficient Γ_{23} from its mean, but result in large fluctuations of its phase. The partial reflection coefficient Γ_{23} is assumed to have the form

$$\Gamma_{23}(\mathbf{K}) e^{2ik_2\beta_2 d} = \eta(\mathbf{K}) e^{i\phi}, \tag{6.9}$$

where ϕ is a uniformly distributed random variable between 0 and 2π, and $\eta^2(\mathbf{K})$ is approximated as the mean square reflection coefficient $\big\langle |\Gamma_{23}(\mathbf{K})|^2 \big\rangle$. With much work, Eqs. (6.8) and (6.9) yield

$$\langle \Gamma \rangle = \Gamma_{12}, \tag{6.10}$$

$$\langle \Gamma^2 \rangle = \Gamma_{12}^2, \tag{6.11}$$

$$\left\langle |\Gamma|^2 \right\rangle = |\Gamma_{12}|^2 + \left|1-\Gamma_{12}^2\right|^2 \frac{\eta^2}{1-|\Gamma_{12}|^2\eta^2}, \tag{6.12}$$

$$\begin{aligned}\left\langle \Gamma|\Gamma|^2 \right\rangle = {} & \Gamma_{12}|\Gamma_{12}|^2 + 2\Gamma_{12}\left|1-\Gamma_{12}^2\right|^2 \frac{\eta^2}{1-|\Gamma_{12}|^2\eta^2} \\ & -\Gamma_{12}^*\left(1-\Gamma_{12}^2\right)\left|1-\Gamma_{12}^2\right|^2 \frac{\eta^4}{\left(1-|\Gamma_{12}|^2\eta^2\right)^2},\end{aligned} \tag{6.13}$$

$$\begin{aligned}\left\langle |\Gamma|^4 \right\rangle = {} & |\Gamma_{12}|^4 + 4|\Gamma_{12}|^2\left|1-\Gamma_{12}^2\right|^2 \frac{\eta^2}{1-|\Gamma_{12}|^2\eta^2} \\ & +\left|1-\Gamma_{12}^2\right|^4 \eta^4 \frac{1+|\Gamma_{12}|^2\eta^2}{\left(1-|\Gamma_{12}|^2\eta^2\right)^3} \\ & -4\,\mathrm{Re}\left(\Gamma_{12}^2\left(1-\Gamma_{12}^{*2}\right)\right)\left|1-\Gamma_{12}^2\right|^2 \frac{\eta^2}{1-|\Gamma_{12}|^2\eta^2}.\end{aligned} \tag{6.14}$$

The derivations for Eqs. (6.12), (6.13), and (6.14) are given in Appendix E; Eqs. (6.10) and (6.11) follow immediately from Eqs. (6.8) and (6.9).

6.4 Effect of sound-speed gradient

The above formalism is now applied to the case of a linear decrease in squared wave number with depth introduced earlier (Figs. 5.3, 6.2, and 6.3). In order to use the differential cross section expressions in Eqs. (6.6) and (6.7), the value for $\eta^2(\mathbf{K}) = \left\langle |\Gamma_{23}(\mathbf{K})|^2 \right\rangle$ $(d_2 = 0)$ is computed and used in Eqs. (6.10) through (6.14). These equations are then substituted in Eq. (6.6) to obtain the monostatic differential cross section, or in Eq. (6.7) to obtain the bistatic differential cross section for scattered directions not close to the backscattered and specular directions. Rather than use Eq. (5.81) to determine $\eta^2(\mathbf{K})$ exactly, a computationally efficient, yet accurate, ray theory expression (Appendix F) is used to obtain the following analytical expression for $\left\langle |\Gamma_{23}(\mathbf{K})|^2 \right\rangle$:

$$\left\langle \left|\Gamma_{23}(\mathbf{K})\right|^2 \right\rangle = \eta^2(\mathbf{K}) = \exp\left(-\frac{4\pi}{q}\left[\frac{2}{3}\sin^3(\theta_2) + 2\cos^2(\theta_2)\sin(\theta_2) \right] \right), \tag{6.15}$$

where θ_2 is the grazing angle just below the mean surface,

$$\cos(\theta_2) = \frac{K}{\mathrm{Re}(k_2)}. \tag{6.16}$$

The gain parameter, q, is the sound-speed gradient, $g = dc/dz$ evaluated at $z = 0$, divided by the product of the frequency, f, and the loss parameter, δ:

$$q \equiv \frac{g}{f\delta} = \frac{1}{\delta}\frac{d\lambda}{dz}. \tag{6.17}$$

This parameter will be shown to determine the average gain of the scattered field strength due to gradients and discontinuities below the rough water-sediment interface as compared to the scattered field strength due solely to the rough water-sediment interface. For example, a small value of q due to a relatively large loss at a high frequency will result in the attenuation of much of the signal energy before it strikes the rough interface again from below, resulting in little scattering gain over the homogenous fluid-fluid case. Also, a small sound-speed gradient results in large path lengths, and attenuation of much of the signal energy before it strikes the rough interface for the second time. When q is small, only the sediment properties at the water-sediment interface are of importance in the scattered field strength calculation .

An expression for $\eta^2(\mathbf{K})$ for the linear increase in sound speed with depth case is also derived in Appendix F.

6.4.1 Effect of sound-speed gradient on backscattered field strength

As a check of the analytical results, the backscattering strength using Eq. (6.6) is plotted in Fig. 6.5 along with the numerically obtained result from Fig. 6.2, and the bistatic scattering strength obtained from Eq. (6.7) is plotted in Fig. 6.6. It is evident that the scattered field strength obtained by numerically averaging the expression in Eq. (6.1) over a Gaussian probability distribution function for the gradient is indistinguishable from the result due to the formally averaged differential cross section in the backscattered direction and for bistatic scattering at least a few degrees from the backscattered direction. In this example, the gradient gain parameter has the relatively large value $q = 30$. Equation (6.6) is used to find the point on the plot corresponding to backscattering.

When $\mathbf{K}_f = -\mathbf{K}_i$, then $\Gamma(\mathbf{K}_f) = \Gamma(\mathbf{K}_i)$, resulting in a peak in the backscattered direction. Depending on the value of the sound-speed gradient variance in the numerical calculation, the reflection coefficients $\Gamma(\mathbf{K}_f)$ and $\Gamma(\mathbf{K}_i)$ are correlated when K_f is close to K_i, and therefore the bistatic scattered field strength is dependent on the gradient variance in the region close to the backscattered direction. However, even for a small variances in seafloor parameters, this region is very small.

The moments obtained in Eqs. (6.10) through (6.14) using the representation for the random reflection coefficient in Eq. (6.9) also agree very closely with the corresponding reflection coefficient moments obtained numerically with a Gaussian probability distribution function for the sound-speed gradient.

Figure 6.7a illustrates the dependency of the scattering gain, $10\log_{10}(\tilde{\sigma}_{11}/\sigma_{11})$, $(\mathbf{K}_i = -\mathbf{K}_f)$, where σ_{11} is given by Eq. (5.71), on the mean density ratio and mean sound-speed ratio for $q = 30$. This value for q is the same as that of Figs. 6.2, 6.3, 6.5, and 6.6. Fig. 6.7b is an identical plot, but with a lower gain parameter, $q = 10$, resulting in correspondingly lower values for the

scattering gain. For a density ratio close unity, the scattering gain can be very large. However, the density ratio must always be greater than one for the seafloor.

The dependence of the scattering gain on q and grazing angle is shown in Fig. 6.7c. As can be seen in Fig. 6.3 and Fig. 6.7c, the scattering gain is strongly dependent on the grazing angle. A low grazing angle results in a significantly higher scattering gain because the resulting ray path length in the lower sediment is much shorter and therefore attenuated much less than the large grazing angle case. The dependency of the scattering gain on q is greater for larger grazing angles.

6.4.2 Bistatic scattering and backscattering enhancement

Figures 6.8a, 6.8b, 6.8c, and 6.8d use Eqs. (6.6) and (6.7) to show backscattering enhancement corresponding to the same sediment parameters in Figs. 6.7a, 6.7b, 6.7c, and 6.7d. Note that these results do not depend on interface roughness. Since the two first-order paths through the sediment add coherently only for monostatic scattering (see Fig. 6.4), the field strength scattered back in the direction of the transmitter is greater than the field strength scattered in other nearby directions. As is clear from Fig 6.8c, the dependency of backscattering enhancement on q is negligible.

6.5 Conclusion

A formally averaged expression for the scattered field that includes the random stratification below the rough seafloor surface as well as the randomness of the rough seafloor is derived in this chapter. Although this formalism can be applied to a rough interface above any arbitrary vertically stratified sediment, ray theory is put to use to obtain formally averaged closed form analytical expressions for the special case of linear decrease of squared wave number with depth sound-speed gradient. This result shows that the scattering gain due to

upward refracting sound-speed gradients is determined by the quantity $q = g/(f\delta)$, the sediment parameters (speed ratio, and density ratio), and also the incident angle.

Gradients and layering below the seafloor can strongly affect the scattering from the interface if a significant amount of the energy that penetrates the interface is redirected back up towards the interface. The effect of gradients in sound-speed on scattering can be significant even for incident energy at large grazing angles (for situations with large q — large gradient, low frequency, low loss), but the effect of gradients on the scattered field strength is most significant at small grazing angles. Backscattering enhancement is also shown to occur in sediments that exhibit a relatively large scattering gain. By using numerical solutions for the flat surface reflection coefficient, the monostatic and bistatic differential cross sections of a rough interface above an arbitrarily complicated vertically stratified sediment that includes the randomness of the sediment parameters below the interface, in addition to the randomness of the interface, can be solved using the formalism in this chapter.

The results of this chapter can also be used to obtain expressions for the field scattered through the rough interface when the sound speed is depth dependent. These results could then be incorporated in the model used in the ocean experiment simulation discussed in chapter 4. Except for downward propagating energy, sound-speed gradients would increase the path length of energy scattering into the sediment. Consequently, sound-speed gradients would seem to favor downward propagating energy, resulting in a slower apparent slow wave propagation than that predicted by the model used in chapter 4. The effect of sound-speed gradients on the scattered field through the interface is, however, beyond the scope of this dissertation, and a subject for future investigation.

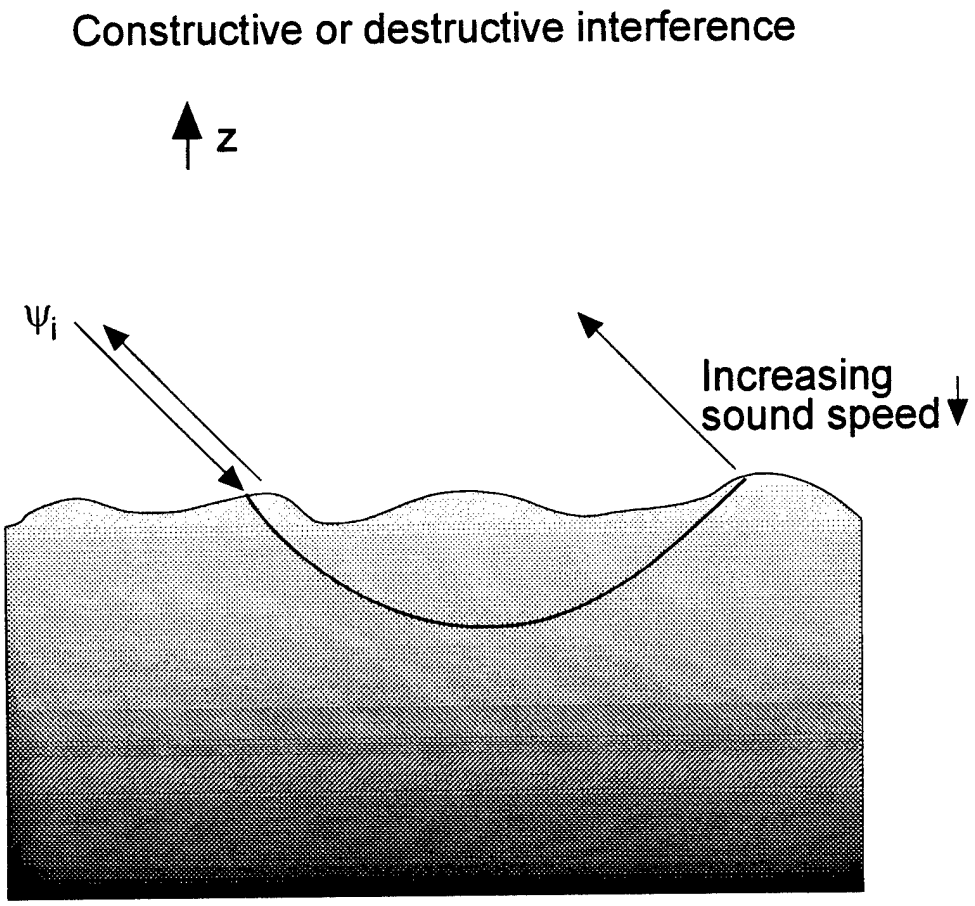

Figure 6.1 : Two first-order effects that can result in destructive or constructive interference.

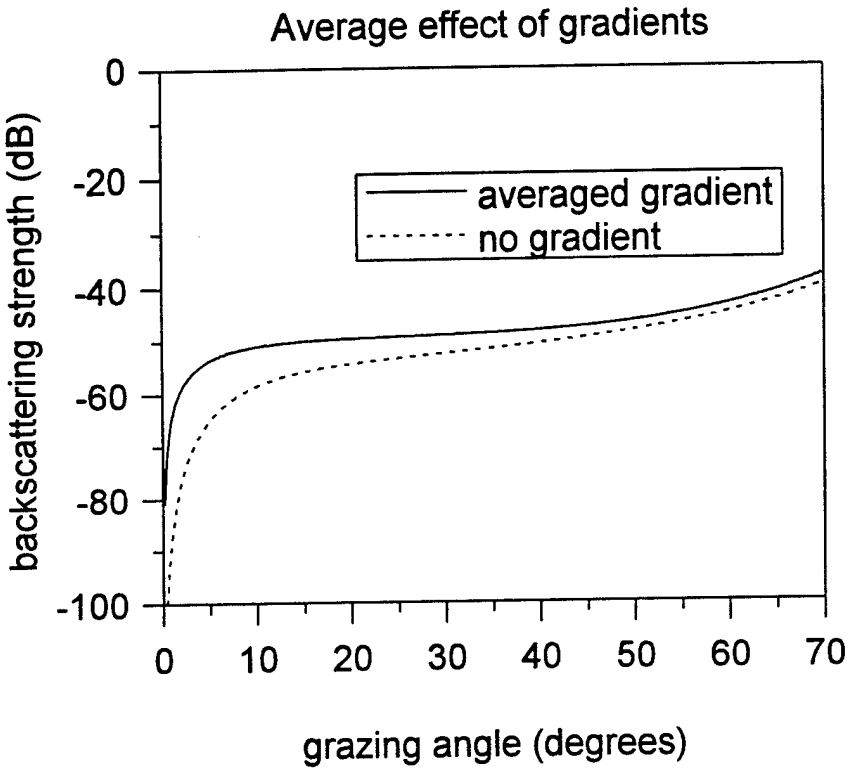

Figure 6.2 : Averaged backscattering strength. Linear decrease in squared wave number with depth sound-speed gradient, g, with Gaussian probability function ($\langle g \rangle = 1.3\,\mathrm{s}^{-1}$, $\left\langle |g|^2 - \langle g \rangle \right\rangle = 0.1\,\mathrm{s}^{-2}$). All other parameters same as Fig. 5.3.

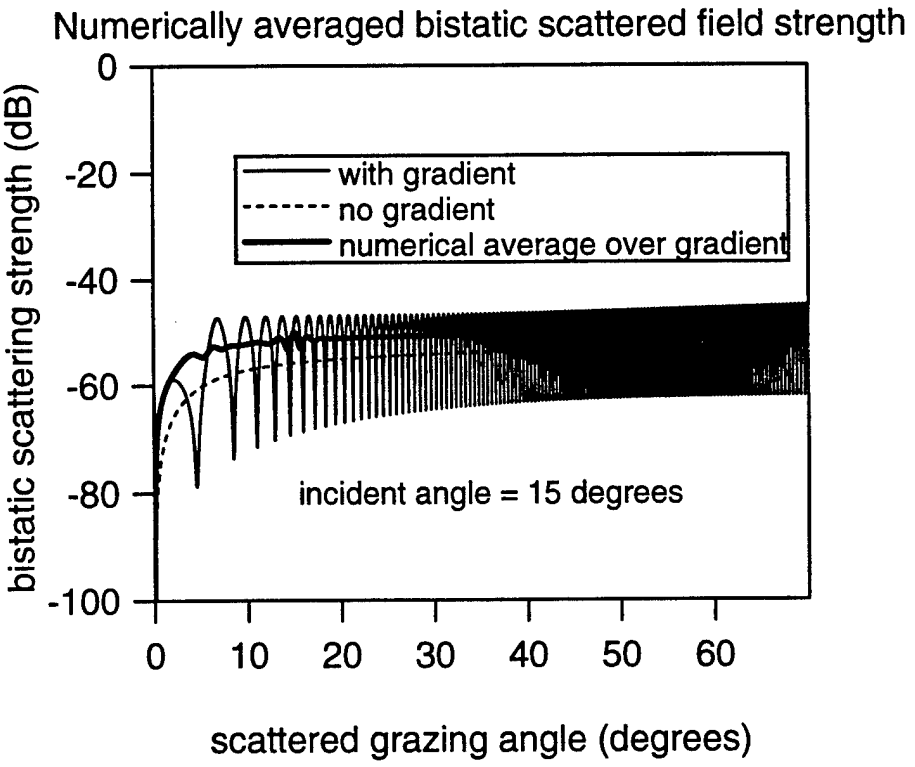

Figure 6.3 : Numerically averaged bistatic scattering strength; same parameters as Fig. 6.2 and Fig. 5.3.

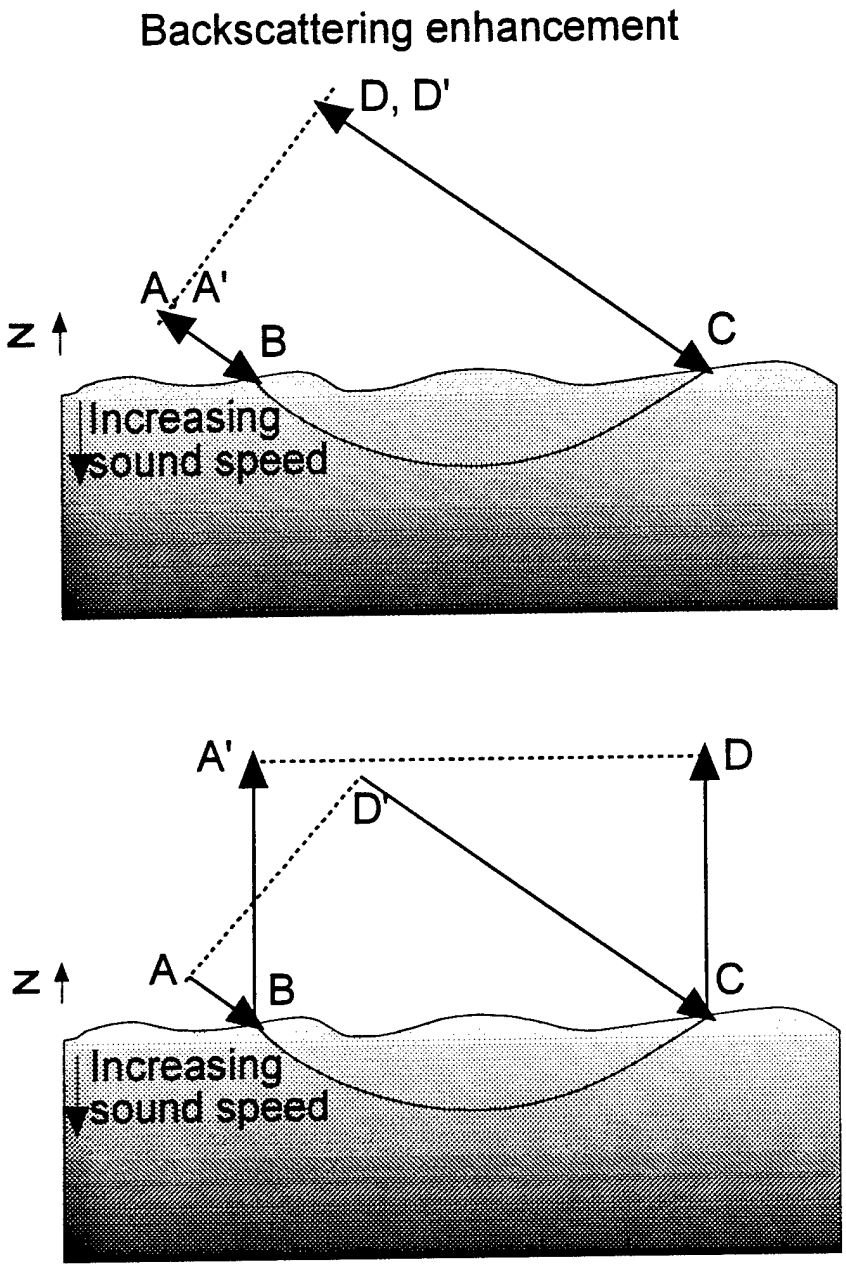

Figure 6.4 : Backscattering enhancement. If paths ABCD and D′CBA′ are equal (A = A′ and D = D′), then backscattering enhancement due to the sound-speed gradient occurs.

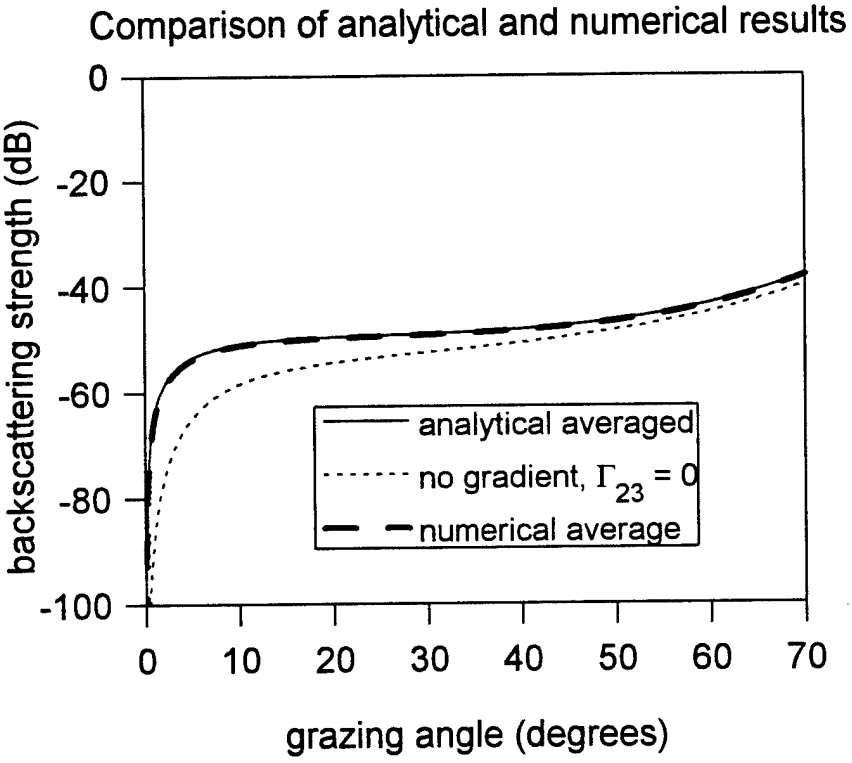

Figure 6.5 : Average backscattering strength: comparison of numerical average obtained with random sound-speed gradient (Fig. 6.2) with analytical formal average approximation. Same parameters as Fig. 6.3.

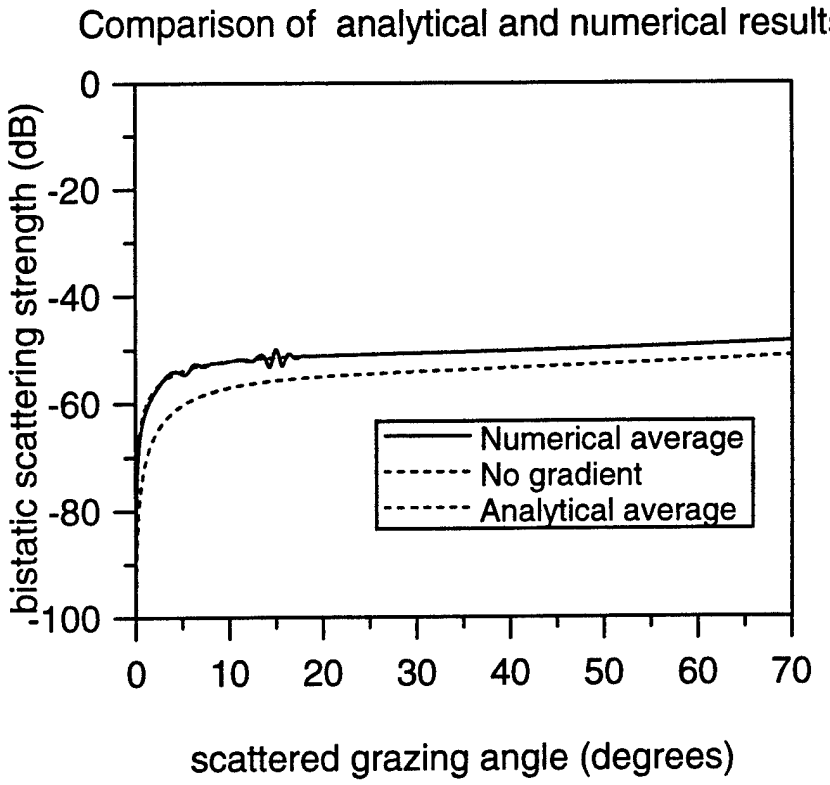

Figure 6.6 : Average bistatic scattering strength: comparison of numerical average obtained with random sound-speed gradient (Fig. 6.3) with analytical formal average approximation. Same parameters as Fig. 6.3.

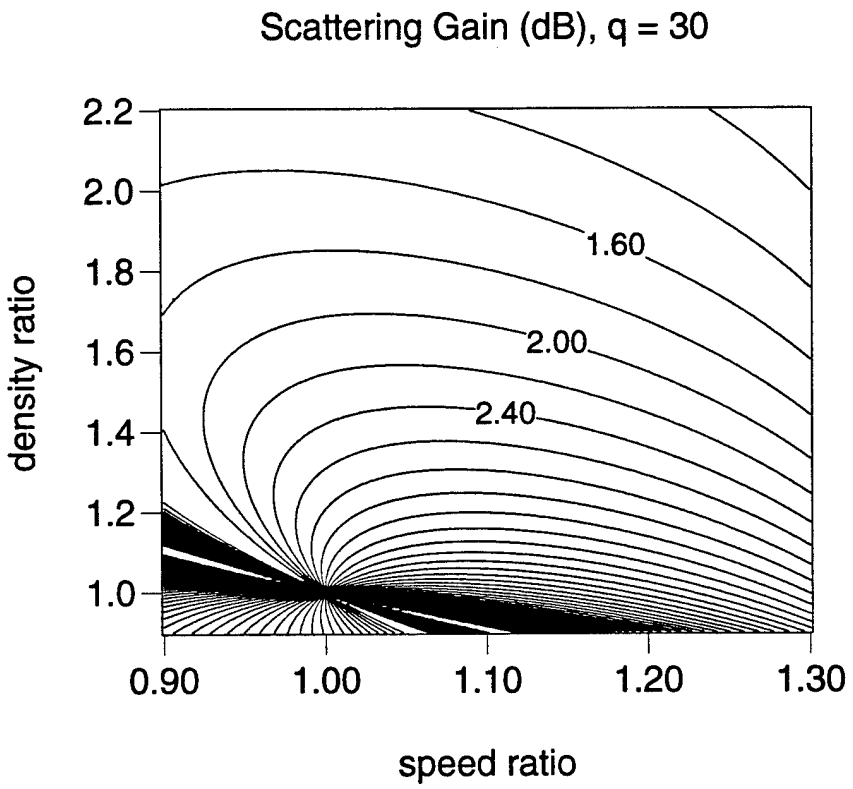

Figure 6.7a : Dependency of scattering gain, $10\log_{10}(\tilde{\sigma}/\sigma), (\mathbf{K}_i = -\mathbf{K}_f)$, on the mean density ratio and mean sound speed ratio for q = 30 (frequency = 1 kHz, g = 30 s^{-1}, $\delta = 0.001$, incident angle = 45°)

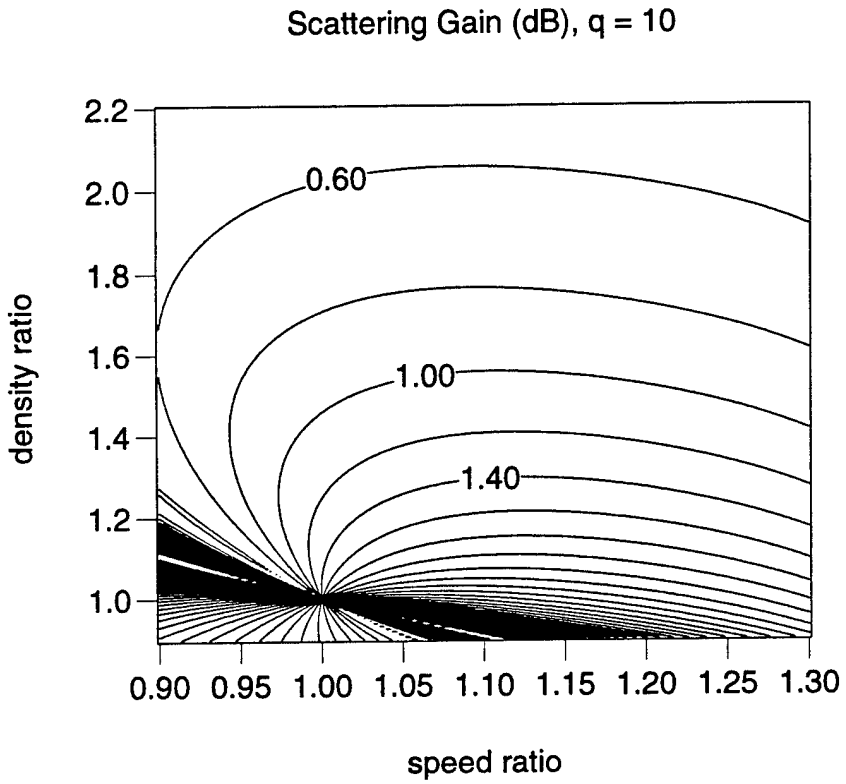

Figure 6.7b : Same parameters as Fig. 6.7a except $g = 10\,\mathrm{s}^{-1}$, resulting in $q = 10$.

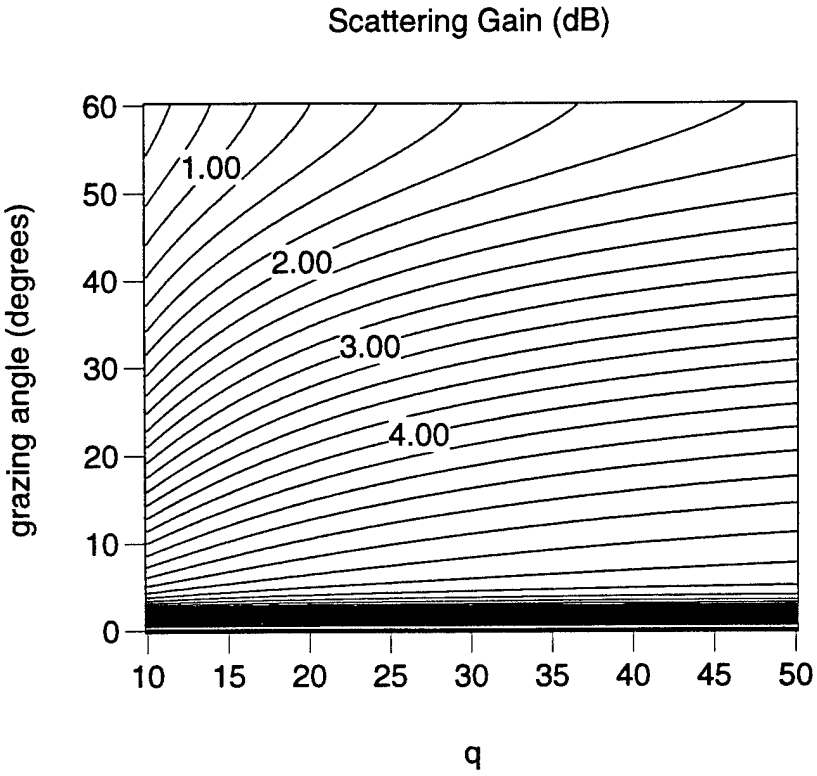

Figure 6.7c : The dependence of the scattering gain on q and grazing angle: frequency = 1 kHz, $\delta = 0.001$, $\nu = 1$, $c_1 = 1500$ m/s, $\rho = 1.5$.

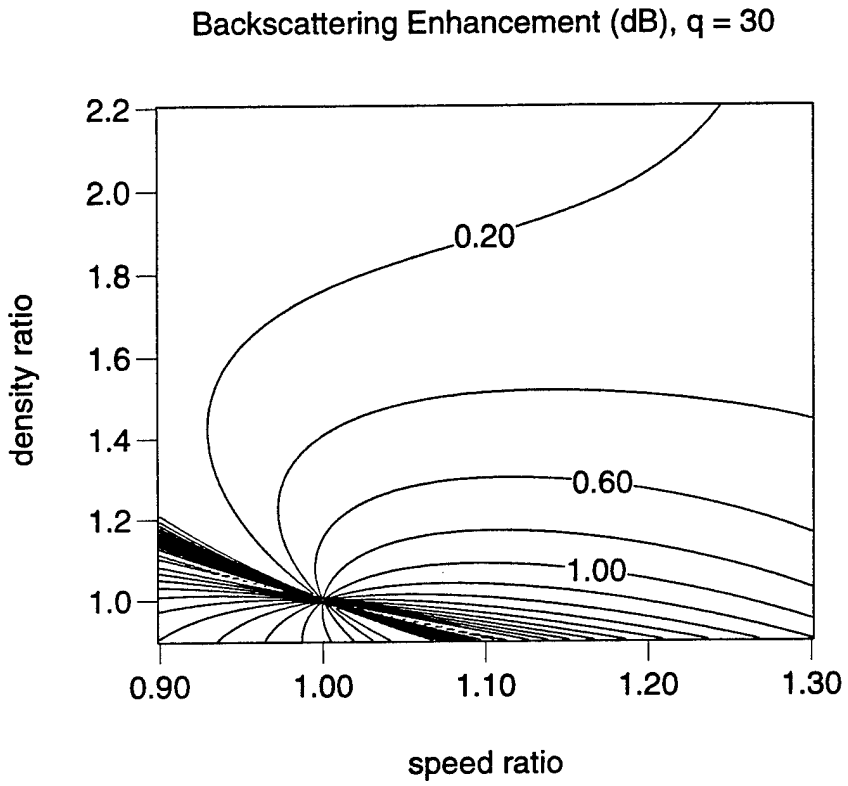

Figure 6.8a : Backscattering enhancement as a function of ρ and ν using same parameters as Fig. 6.7a ($q = 30$).

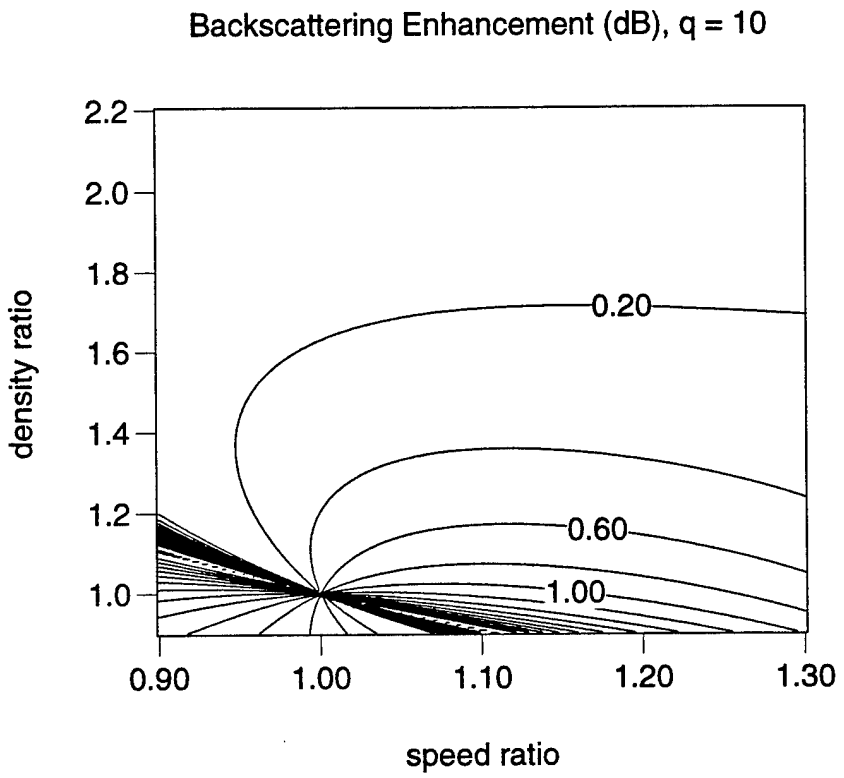

Figure 6.8b : Backscattering enhancement as a function of ρ and ν using same parameters as Fig. 6.7b ($q = 10$).

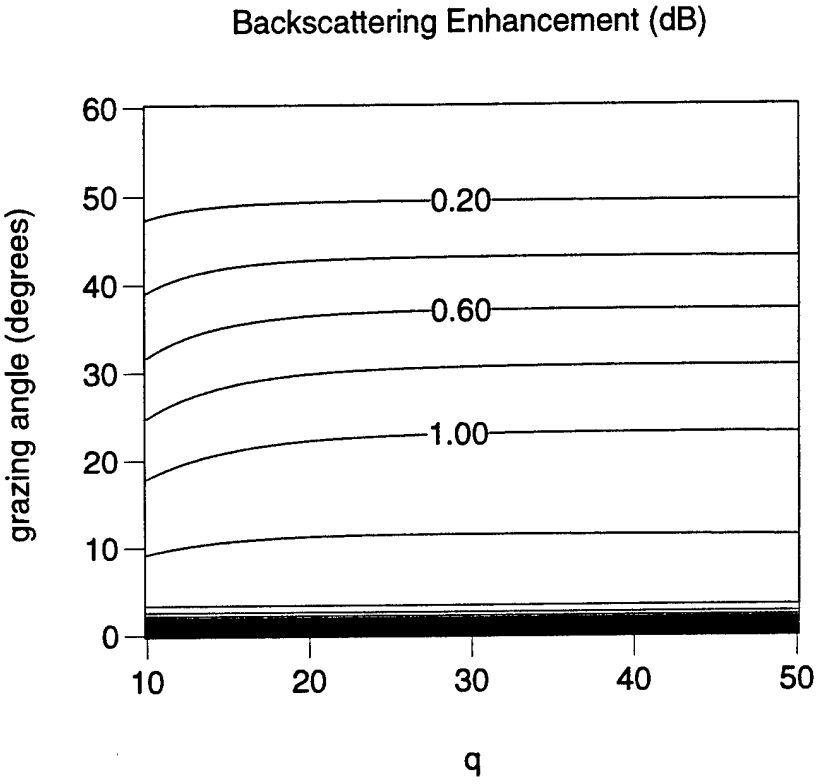

Figure 6.8c : Backscattering enhancement as a function of grazing angle and q; $\rho = 1.5$, $f = 1\,\text{kHz}$, $\delta = 0.001$, $\nu = 1.0$, $c_1 = 1500\,\text{m/s}$.

CHAPTER 7

Dissertation Summary and Proposed Future Work

7.1 Introduction to chapter 7

By means of analytical models for seafloor scattering derived in this dissertation, roughness is shown to be an important mechanism for penetration of acoustical energy into the sediment at subcritical grazing angles. Experimental results (Boyle and Chotiros, 1992; Chotiros, 1995) showing acoustic penetration from water into sandy sediments at grazing angles below the compressional critical angle in relation to the mean surface are explained in terms of diffraction of an ordinary longitudinal wave, rather than refraction of a slow wave.

Since the transmitted signal in the experiments is a pulse, formalism for scattering of a pulse through a rough interface as well as from a rough interface is derived in terms of the scattering cross section per unit area per unit solid angle (differential cross section). This analytical result for the time-dependent scattered field intensity is used to show that the CW approximation is appropriate for simulations of both experiments. First-order perturbation theory is used to obtain an approximate expression for the differential cross section. Since using the zero-order field to represent the coherent intensity is only valid for small amounts of interface roughness, the second-order component of the coherent field intensity is derived, and compared with the zero-order component of the coherent intensity for the sediment roughness parameters used in the ocean experiment simulation. These analytical results justify using the flat surface field to represent the coherent component of the field. Although the main problem is acoustic scattering *through* the water-sediment interface for an incident field in

the water, analytical results derived in this work also include scattering *from* the interface. Furthermore, these analytical results are general, and can be applied to other rough interface scattering problems.

Gradients in sediment sound speed are also allowed in the perturbation results. A novel approach for finding the differential cross section, given vertically stratified random sediment parameters, yields analytical results that show the average effect of sound speed gradients in the sediment on the field scattered back into the water. Although gradients in sound speed may affect the apparent slow wave speed, this effect is not calculated in this dissertation. However, the formalism in this dissertation can be generalized to include the effect of sound-speed gradients on the field penetrating the surface.

7.2 Time dependent scattered intensity — chapter 2

An original expression for the two-frequency mutual coherence function for scattering *from* and *through* a 2-D fluid-fluid rough interface due to a narrowband incident plane wave is derived and expressed in terms of the second moment of the T-matrix, resulting in a general analytical expression for the time dependent incoherent intensity due to a narrowband incident plane wave.

Two approximations are made to the two-frequency mutual coherence function when obtaining the results of chapter 2.

- The T-matrix correlation function is assumed to vary slowly over the source frequency range. This assumption is shown to be valid in chapter 3 for a narrowband source signal.
- The phase terms are expanded in a power series in frequency.

An equivalent expression, omitting evanescent waves, is obtained in terms of the differential cross section. It has been demonstrated that the evanescent component of the scattered incoherent field is insignificant compared to the

propagating component of the incoherent field for distances as small as one or two wavelengths from the interface, depending on the surface roughness spectrum. In the limit as the narrowband signal approaches the CW (continuous wave) case, the result in terms of the T-matrix correlation function is exact, and the result in terms of the differential cross section approaches the exact solution for distances sufficiently far from the interface. This result is interesting, because the differential cross section is defined as a far-field entity.

This expression for the incoherent time dependent scattered field intensity in terms of the differential cross section is used to heuristically obtain the corresponding expression for the scattered field due to a narrowband point source. A simple analytical expression is obtained for the case of a Gaussian shaped source pulse, also in terms of the differential cross section. The analytical results and calculations in this chapter show that the sonar equation is appropriate for the simulations of the experiments.

7.3 First-order perturbation theory — chapter 3

Derivations for the first-order perturbation expressions used for the numerical computations in chapter 2 and in the computer simulations (chapter 4) for scattering both from and through a rough fluid-fluid interface separating two homogenous fluids are presented in chapter 3. These first-order perturbation theory results are also used to show that the T-matrix correlation function varies sufficiently slowly over the source frequency range so that its dependence on frequency can be ignored in the time dependent scattered field derivation.

7.4 Computer simulations of recent experiments — chapter 4

The results of computer simulations of recent experiments, presented in chapter 4, show the effect of roughness on acoustic penetration of the seafloor

and are compared with recent sediment penetration experiments. These results show that the incoherent intensity scattered through the rough seafloor can mimic a slow refracted wave.

By assuming a small amount of roughness at the water-sediment interface, and using the 3-D scattering model developed in chapter 2 and the first-order perturbation theory results for 2-D fluid-fluid interfaces derived in chapter 3, it is possible to reproduce the results of the tank experiments of Boyle and Chotiros (1992), both in magnitude and arrival time of the incoherent intensity pulse (apparent slow wave). These results indicate that the acoustic penetration of the surface may be due to scattering (diffraction) from low levels of roughness rather than slow-wave refraction.

Simulations of the ocean sediment penetration experiments (Chotiros, 1995) are presented and compared with Chotiros' experimental results. Assuming roughness parameters appropriate to the experiment location and using the intensity propagation speed and direction finding algorithm used by Chotiros, these simulations also show propagation of energy at speeds slower than the compressional speed of the sediment, in a direction concurring with Snell's law. Although the simulations yield an apparent slow wave that is between $50\,\mathrm{m/s}$ and $300\,\mathrm{m/s}$ faster than the results presented by Chotiros, the apparent slow wave speed is dependent on the roughness spectrum. Because of the potential for disturbance of the sediment above the receivers, the roughness spectrum measured in the area of the experiment is not the same as that of the actual roughness spectrum at the experiment site.

7.5 Perturbation theory results for a fluid-fluid interface including gradients — chapter 5

Using Rayleigh-Rice perturbation theory, Nth order recursion equations are derived in chapter 5 that provide a starting point for evaluating the Nth order

scattered field in terms of lower orders. The sediment below the lowest point on the interface can be viscoelastic, or porous, supporting shear or Biot slow waves as well as gradients in physical properties (e.g., sound speed can vary with depth), and is represented by the corresponding flat surface reflection coefficient. For the case of increasing sound speed with depth, these results (first-order) show that constructive and destructive interference in the field strength can occur for scattering back into the water when a significant amount of energy is redirected back toward the surface.

An expression for the second-order coherent field is derived from the Nth order recursion equations that illustrates the necessity of including the second-order component in the coherent intensity calculations for $k_1 h > 1$.

7.6 Formal average of sediment parameters — chapter 6

Since the sediment parameters such as sound speed, sound speed gradient, and density generally show variability in lateral direction, the effect of treating the sediment parameters as random is shown in chapter 6. The first-order expression for the differential cross section derived in chapters 2 and 5 is generalized to account for randomness in the medium below the lowest point on the rough interface by expressing the differential cross section in terms of moments of the stochastic flat surface reflection coefficient. This approach results in a formally averaged expression for the scattered field that includes the random stratification in the sediment, in addition to the randomness of the rough water-sediment interface.

Although this formalism can be applied to a rough surface above any arbitrary vertically stratified sediment, ray theory is used to obtain formally averaged closed form analytical expressions for a few special cases that include sound speed gradients. This result shows that the scattering gain due to upward refracting sound speed gradients is determined by the quantity $q = g/(f\delta)$, the

sediment parameters (speed ratio and density ratio), and also the incident angle. Upward refraction or reflection due to large sound speed gradients in the sediment results in increased scattering strength over the non-gradient case. Backscattering enhancement is demonstrated in this first-order result, since the scattering gain has a relative maximum when the incident and scattered grazing angles are equal.

Summary and ideas for future work

The tank and ocean experiment simulation results presented in this experiment show that surface roughness is a mechanism for subcritical penetration of sediment. Although the issue of the dominant mechanism for subcritical penetration of the seafloor can only be resolved by experiment, further improvements on the scattering model can be made. For example, the effect of sound speed gradients on the scattered field through the interface is a subject for future investigation. The results of chapters 5 and 6 can be used to obtain analytical expressions for the field scattered through the rough interface when the sound speed is depth dependent. These results could then be incorporated in the model used in the ocean experiment simulation.

The Nth order recursion equations provide a starting point to solve higher orders. Solving for the third-order scattered field would provide a means of obtaining the differential cross section to $(k_1 h)^4$. This result could then be used to determine the accuracy of the first-order results for scattering through and from 2-D surfaces.

The results in chapter 5 provide a straightforward approach for obtaining the first-order scattered field from multiple rough interfaces in terms of partial reflection coefficients. The effect of multiple rough interfaces could then be compared with the results of chapter 6.

BIBLIOGRAPHY

Aki, K., and Richards, P. G. (**1980**). *Quantitative Seismology, Theory and Methods* (W. H. Freeman and Company, New York).

Berkhoff, A. P., Thijssen, J. M., and van den Berg, P. M. (**1996**). "Ultrasound wave propagation through rough interfaces: Iterative methods," J. Acoust. Soc. Am. **99,** 1306-1314.

Berman, D. H. (**1992**). "Renormalization of propagation in a waveguide with rough boundaries," J. Acoust. Soc. Am. **92**, 309-314.

Biot, M. A. (**1956a**). "Theory of propagation of elastic waves in a fluid-saturated porous sold. I. Low frequency range," J. Acoust. Soc. Am. **28**, 168-178.

Biot, M. A. (**1956b**). "Theory of propagation of elastic waves in a fluid-saturated porous sold. II. Higher frequency range," J. Acoust. Soc. Am. **28**, 179-191.

Biot, M. A. (**1962a**). "Mechanics of deformation and acoustic propagation in porous media," J. Appl. Phys. **33**, 1492-1498.

Biot, M. A. (**1962b**). "Theory of propagation of elastic waves in a fluid-saturated porous sold. II. Higher frequency range," J. Acoust. Soc. Am. **28,**179-191.

Boyle, F. A., and Chotiros, N. P. (**1992**). "Experimental detection of a slow acoustic wave in sediment at shallow grazing angles," J. Acoust. Soc. Am. **91**, 2615-2619.

Brekhovskikh, L. M. (**1952**). "Diffraction of waves at an uneven surface, I and II," J. Exptl.-Theoret. Phys. (USSR) **23**, 275-304.

Brekhovskikh, L. M. (**1980**). *Waves in Layered Media* (Academic Press, San Diego).

Brekhovskikh, L. M., and Lysanov, Y. P. (**1991**). *Fundamentals of Ocean Acoustics* (Springer-Verlag, Berlin).

Briggs, K. B. (**1989**). "Microtopographical roughness of shallow-water continental shelves," IEEE J. Oceanic Eng. **14**, 360-367.

Briggs, K. B., Richardson, M. D., and Young, D. K. (**1985**). "Variability in geoacoustic and related properties of surface sediments from the Venezuela Basin, Caribbean Sea," Marine Geol. **68**, 73-106.

Broschat, S. L., Tsang, L., Ishimaru, A., and Thorsos, E. I. (**1987**). "A numerical comparison of the phase perturbation technique with the classical field perturbation and Kirchhoff approximations for random rough surface scattering," J. Electromagnetic Waves Applic. **2**, 85-102.

Broschat, S. L., Thorsos, E. I., and Ishimaru, A. (**1989**). "The phase perturbation technique vs. an exact numerical method for random rough surface scattering," J. Electromagnetic Waves Applic. **3**, 237-256.

Bucker, H. P. (**1970**). "Sound propagation in a channel with lossy boundaries," J. Acoust. Soc. Am. **48**, 1187-1194.

Burdic, W. S. (**1991**). *Underwater Acoustic System Analysis* (Prentice Hall, Englewood Cliffs).

Chen, M. F., and Fung, M. F. (**1988**). "A numerical study of the regions of validity of the Kirchhoff and small-perturbation rough surface scattering models," Radio Sci. **23**, 163-170.

Chotiros, N. P. (**1991**). "High frequency bottom penetration: Panama City experiment analysis III," ARL-TR-91-18.

Chotiros, N. P. (**1995**). "Biot model of sound propagation in water-saturated sand," J. Acoust. Soc. Am. **97**, 199-214.

Crowther, P. A. (**1983**). "Some statistics of the sea-bed and scattering therefrom," in *Acoustics and the Sea-Bed*, edited by N. G. Pace (Bath University Press, Bath), pp. 147-155.

Devaney, A. J., and Sherman, G. C. (**1973**). "Plane-wave representations for scalar wave fields," SIAM Rev. **15**, 765-786.

Dacol, D. K., and Berman, D. H. (**1988**). "Sound scattering from a randomly rough fluid-solid interface," J. Acoust. Soc. Am. **84**, 292-302.

Eckart, C. (**1953**). "The scattering of sound from the sea surface," J. Acoust. Soc. Am. **25**, 566-570.

Essen, H. H. (**1994**). "Scattering from a rough sediment seafloor containing shear and layering," J. Acoust. Soc. Am. **95**, 1299-1310.

Fox, C. G., and Hayes, D. E. (**1985**). "Quantitative methods for analyzing the roughness of the seafloor," Rev. Geophys. **23**, 1-48.

Goff, J. A., and Jordan, T. H. (**1989**). "Stochastic modeling of seafloor morphology: Resolution of topographic parameters by sea beam data," IEEE J. of Oceanic Eng. **14**, 326-337.

Goodman, J. W. (**1968**). *Introduction to Fourier Optics* (McGraw-Hill, New York).

Hamilton, E. L. (**1974**). "Prediction of deep-sea properties: State of the art," in *Deep-Sea Sediments, Physical and Mechanical Properties*, edited by A. L. Inderbitzen (Plenum, New York), pp. 1-43.

Hamilton, E. L. (**1979**). "Sound velocity gradients in marine sediments," J. Acoust. Soc. Am. **65**, 909-922.

Hamilton, E. L. (**1980**). "Geoacoustic modeling of the sea floor," J. Acoust. Soc. Am. **68**, 1313-1341.

Hanson, S. G., and Zavorotny, V. U. (**1995**). "Polarization dependency of enhanced multipath radar backscattering from an ocean-like surface," Waves in Random Media **5**, 159-165.

Holthusen, H., and Vidmar, P. J. (**1982**). "The effect of near-surface layering on the reflectivity of the ocean bottom," J. Acoust. Soc. Am. **72**, 226-234.

Ishimaru, A. (**1978a**). *Wave Propagation and Scattering in Random Media, I* (Academic, San Diego).

Ishimaru, A. (**1978b**). *Wave Propagation and Scattering in Random Media, II* (Academic, San Diego).

Ishimaru, A. (**1991**). *Electromagnetic Wave Propagation, Radiation, and Scattering* (Prentice Hall, Englewood Cliffs).

Ishimaru, A., Ailes-Sengers, L., Phu, P., and Winebrenner, D. (**1994a**). "Pulse broadening and two-frequency mutual coherence function of the scattered wave from rough surfaces," Waves in Random Media **4**, 139-148.

Ishimaru, A., Ailes-Sengers, L., Phu, P., and Winebrenner, D. (**1994b**). "Pulse broadening of enhanced backscattering from rough surfaces," Waves in Random Media **4**, 453-465.

Ishimaru, A., and Chen, J. S. (**1990**). "Scattering from very rough surfaces based on the modified second-order Kirchhoff approximation with angular and propagation shadowing," J. Acoust. Soc. Am. **88**, 1887-1888.

Ishimaru, A., and Chen, J. S. (**1991**). "Scattering from very rough metallic and dielectric surfaces: A theory based on the modified Kirchhoff approximation," Waves in Random Media **1**, 21-34.

Ivakin, A. N. (**1994**). "Sound scattering by rough interfaces of layered media," Third international congress on air and structure borne sound and vibration, Montreal.

Ivakin, A. N., and Lysanov, Y. P. (**1981**). "Underwater sound scattering by volume inhomogeneities of a bottom medium bounded by a rough surface," Sov. Phys. Acoust. **27**, 212-215.

Ivakin, A. N., and Jackson, D. R. "Effects of shear elasticity on high-frequency bottom backscattering," in preparation.

Jackson, D. R., and Briggs, K. B. (**1992**). "High-frequency bottom backscattering: Roughness versus sediment volume scattering," J. Acoust. Soc. Am. **92**, 962-977.

Jackson, D. R., Briggs, K. B., Williams, K. L., and Richardson, M. D. (**1996**). "Test of models for high-frequency sea-floor backscattering," submitted.

Jackson, D. R., Moe, J. E., Thorsos, E. I., and Williams, K. L. (**1996**). "Sub-critical penetration of sandy sediments due to interface roughness," J. Acoust. Soc. Am. **99**, 2474.

Jackson, D. R., Winebrenner, D. P., and Ishimaru, A. (**1986**). "Application of the composite roughness model to high-frequency bottom backscattering," J. Acoust. Soc. Am. **79**, 1410-1422.

Jackson, D. R., Winebrenner, D. P., and Ishimaru, A. (**1988**). "Comparison of perturbation theories for rough surface scattering," J. Acoust. Soc. Am. **83**, 961-969.

Kaczkowski, P. J. (**1994**). "A study of the operator expansion method and its application to scattering from randomly rough Dirichlet surfaces," Ph.D. dissertation, Univ. of Washington, Seattle.

Kaczkowski, P. J., and Thorsos, E. I. (**1994**). "Application of the operator expansion method to scattering from one-dimensional moderately rough Dirichlet random surfaces," J. Acoust. Soc. Am. **96**, 957-972.

Kuo, E. Y. (**1964**). "Wave scattering and transmission at irregular surfaces," J. Acoust. Soc. Am. **36**, 2135-2142.

Kuperman, W. A., and Ingenito, F. (**1977**). "Attenuation of the coherent component of sound propagating in shallow water with rough boundaries," J. Acoust. Soc. Am. **61**(5), 1178-1187.

Kuperman, W. A., and Schmidt, H. (**1986**). "Rough surface elastic wave scattering in a horizontally stratified ocean," J. Acoust. Soc. Am. **79**, 1767-1777.

Landau, L. D., and Lifshits, E. M. (**1987**). *Fluid Mechanics* (Pergamon Press, Oxford, England; New York).

Lang, R. H., and Khadr, N. (**1992**). "Effects of backscattering enhancement on soil moisture sensitivity," IEEE International Geoscience and remote sensing symposium, Houston, 916-919.

Liu, J., Schmidt, H., and Kuperman, W. A. (**1993**). "Effect of a rough seabed on the spectral composition of deep ocean infrasonic ambient noise," J. Acoust. Soc. Am. **93** (2), 753-769.

Lyons, A. P., Anderson, A. L., and Dwan, F. S. (**1994**). "Acoustic scattering from the seafloor: Modeling and data comparison," J. Acoust. Soc. Am. **95** (5), 2441-2451.

Mandelbrot, B. B. (**1983**). *The Fractal Geometry of Nature* (W. H. Freeman, San Francisco)

Maradudin, A. A., and Mendez, E. R. (**1993**). "Enhanced backscattering of light from weakly rough, random metal surfaces," Appl. Opt. **32**, 3335-3343.

Milder, D. M. (**1991**). "An improved formalism for wave scattering from rough surfaces," J. Acoust. Soc. Am. **89**, 529-541.

Moe, J. E., and Jackson, D. R. (**1994a**). "First order perturbation solution for rough surface scattering cross section including the effects of gradients," J. Acoust. Soc. Am. **96**, 1748-1754.

Moe, J. E., and Jackson, D. R. (**1994b**) "The effect of gradients on high-frequency bottom scattering," J. Acoust. Soc. Am. **96**, 3286.

Moe, J. E., and Jackson, D. R. (**1994c**) "The effect of roughness on acoustic penetration of the ocean bottom," J. Acoust. Soc. Am. **96**, 3265.

Moe, J. E., and Jackson, D. R. (**1996a**). "Near field scattering through and from a 2-D fluid-fluid rough interface" submitted.

Moe, J. E., and Jackson, D. R. (**1996b**). "Near field scattering through and from a 2-D fluid-fluid rough interface" J. Acoust. Soc. Am., **99**, 2475.

Moe, J. E., Thorsos, E. I., Jackson, D. R., and Williams, K. L. (**1995**). "The effect of roughness on acoustic penetration of the seafloor as given by a fluid-fluid perturbation model and comparison with recent sediment penetration experiments", J. Acoust. Soc. Am. **97**(5), 3315.

Mourad, P. D., and Jackson, D. R. (**1989**). "High frequency sonar equation models for bottom backscatter and forward loss," in *Proceedings of OCEANS '89* (Marine Technology Society and IEEE), pp. 1168-1175.

Mourad, P. D., and Jackson, D. R. (**1993**). "A model/data comparison for low-frequency bottom backscatter," J. Acoust. Soc. Am. **94**, 344-358.

Nagy, P. B., and Rose, J. H. (**1993**). "Surface roughness and the ultrasonic detection of subsurface scatters," J. Appl. Phys. **73,** 566-580.

Nieto-Vesperinas, M., and Garcia, N. (**1981**) "A detailed study of the scattering of scalar waves from random rough surfaces," Optica Acta, vol. 28, no 12, 1651-1672.

Pak, K. Tsang, L. Chan, C. H., Kuga, Y., and Johnson, J. (**1995**). "Backscattering enhancement of electromagnetic waves from two-dimensional perfectly conducting random rough surfaces based on Monte Carlo simulations," J. Opt. Soc. of Am. **12**, pp. 2491-2499.

Papoulis, A. (**1984**). *Probability, Random Variables, and Stochastic Processes* (McGraw-Hill, New York).

Proakis, J. G. (**1989**). *Digital Communications* (McGraw-Hill, New York).

Rayleigh, Lord (Strutt, J. W.) (**1945**). *The Theory of Sound* (Dover, New York).

Rice, S. O. (**1951**). "Reflection of electromagnetic waves from slightly rough surfaces," Commun. Pure Appl. Math. **4**, 351-378.

Richardson, M. D. (**1986**). "Spatial variability of surficial shallow water sediment geoacoustic properties," *in Ocean Seismo Acoustics: Low Frequency Underwater Acoustics*, edited by T. Akal and J. M. Berkson (Plenum, New York), pp. 527-536.

Rutherford, S. R., and Hawker, K. E. (**1978**). "Effects of density gradients on bottom reflection loss for a class of marine sediments," J. Acoust. Soc. Am. **63**(3), 750-757.

Stanic, S., Briggs, K. B., Fleischer, P., Ray, R. I., and Sawyer, W. B. (**1988**). "Shallow-water high-frequency bottom scattering off Panama City, Florida," J. Acoust. Soc. Am. **83**, 2134-2144.

Stanic, S., Briggs, K. B., Fleischer, P., Sawyer, W. B., and Ray, R. I. (**1989**). "High-frequency acoustic backscattering from a coarse shell ocean bottom," J. Acoust. Soc. Am. **85**, 125-136.

Thorsos, E. I. (**1988a**). "Exact numerical methods vs the Kirchhoff approximation for rough surface scattering," in *Computational Acoustics, Vol. II, Algorithms and Applications*, edited by D. Lee, R. L. Sternberg, and M. L. Schultz (North-Holland, Amsterdam).

Thorsos, E. I. (**1988b**). "The validity of the Kirchhoff approximation for rough surface scattering using a Gaussian roughness spectrum," J. Acoust. Soc. Am. **83**, 78-92.

Thorsos, E. I. (**1990**). "Acoustic scattering from a 'Pierson-Moskowitz' sea surface," J. Acoust. Soc. Am. **88**, 335-349.

Thorsos, E. I. (**1995**). (Notes on speed of diffracted intensity front) (personal communication).

Thorsos, E. I. (**1996a**). "The accuracy of perturbation theory for acoustic penetration of sediment due to interface," J. Acoust. Soc. Am. **99**(4), 2475.

Thorsos, E. I. (**1996b**). (Notes on coherent transmission coefficient) (personal communications).

Thorsos, E. I., and Broschat, S. L. (**1995**). "An investigation of the small slope approximation for scattering from rough surfaces, Part I, Theory," J. Acoust. Soc. Am. **97**(4), 2082-2093.

Thorsos, E. I., and Jackson, D. R. (**1989**). "The validity of the perturbation approximation for rough surface scattering using a Gaussian roughness spectrum," J. Acoust. Soc. Am. **86**, 261-277.

Thorsos, E. I., and Jackson, D. R. (**1991**). "Studies of scattering theory using numerical methods," Waves in Random Media **3**, S165-S190.

Thorsos, E. I., and Jackson, D. R. (**1996**). (Roughness spectrum approximation) private communications.

Tsang, L., Chan, C. H., and Pak, K. (**1994**). "Backscattering enhancement of a two-dimensional random rough surface (three-dimensional scattering) based on Monte Carlo simulations", J. Opt. Soc. Am. (Optics and Image Science). **11**, 711-15.

Tsang, L., Chan, C. H., and Pak, K. (**1993**). "Monte Carlo simulation of a two-dimensional random rough surface using the sparse-matrix flat-surface iterative approach," Electronics Letters **29**, 1153-1154.

Urick, R. J. (**1975**). *Principles of Underwater Sound* (McGraw-Hill, New York).

Voronovich, A. G. (**1985**). "Small slope approximation in wave scattering by rough surfaces," Sov. Phys. JETP **62**, 65-70.

Voronovich, A. G. (**1994**). *Wave Scattering From Rough Surfaces* (Springer-Verlag, Berlin).

Westwood, E. K. (**1989**). "Complex ray methods for acoustic interaction at a fluid-fluid interface," J. Acoust. Soc. Am. **85**, 1872-1884.

Williams, K. L., Satkowiak, L. J., and Bugler, D. R. (**1989**) "Linear and parametric array transmission across a water-sand interface: Theory, experiment, and observation of beam displacement," J. Acoust. Soc. Am. **86**, 311-325.

Winebrenner, D. P. (**1985**). "A surface field phase-perturbation technique for scattering from rough surfaces," Ph.D. dissertation, Univ. of Washington, Seattle.

Winebrenner, D., and Ishimaru, A. (**1985a**). "Investigation of a surface field phase perturbation technique for scattering from rough surfaces," Rad. Sci. **20**, 161-170.

Winebrenner, D., and Ishimaru, A. (**1985b**). "Application of the phase-perturbation technique to randomly rough surfaces," J. Opt. Soc. Am. **2**, 2285-2294.

Winebrenner, D., and Ishimaru, A. (**1986**). "On the far-field approximation for scattering from randomly rough surfaces," IEEE Trans. Antennas Propag. **AP-34**(6), 847-849.

Winebrenner, D. P., Farmer, L. D., and Joughin, I. R. (**1995**). "On the response of polarimetric synthetic aperture radar signatures at 24-cm wavelength to sea ice thickness in Arctic leads," Radio Sci. **30**, 373-402.

Wingham, D. J. (**1985**). "The dispersion of sound in sediment," J. Acoust. Soc. Am. **78**, 1757-1760.

Yang, T., and Broschat, S. L. (**1994**). "Acoustic scattering from a fluid-elastic-solid interface using the small slope approximation," J. Acoust. Soc. Am. **96**, 1796-1804.

Ziomek, L. J. (**1982a**). "Generalized Kirchhoff approach to the ocean surface scatter communications channel. Part I. Transfer function of the ocean surface," J. Acoust. Soc. Am. **71**, 116-126.

Ziomek, L. J. (**1982b**). "Generalized Kirchhoff approach to the ocean surface scatter communications channel. Part II. Second-order functions," J. Acoust. Soc. Am. **71**, 1487-1495.

Zipfel, G. G., and J. A. DeSanto (**1972**). "Scattering of scalar waves from a random rough surface: A diagrammatic approach," J. Math. Phys. **13**, 1903–1911.

APPENDIX A

Derivation of narrowband dispersion coefficients

Equations (2.38) - (2.41) (expressions for t_1, t_2, P, and Q) are derived in this section. For convenience, define

$$\begin{aligned}\omega_t' &= \omega_c + \omega' \\ \omega_t'' &= \omega_c + \omega''.\end{aligned} \tag{A1}$$

From Eqs. (2.10), (2.36), and (A1),

$$\begin{aligned}B_2(K,\omega_t',\omega_t'') &= (\omega_t'/c_1)\kappa\beta_2(|\mathbf{K}-\mathbf{K}_d/2|,\omega_t') \\ &= \sqrt{\kappa\left(\frac{\omega_t'}{c_1}\right)^2 - K^2 + \mathbf{K}\cdot\mathbf{K}_d - \frac{1}{4}\mathbf{K}_d\cdot\mathbf{K}_d}\,.\end{aligned} \tag{A2}$$

Substituting Eq. (2.34) for $\mathbf{K}_d$ in the above expression yields

$$B_2(K,\omega_t',\omega_t'') = \sqrt{\kappa\left(\frac{\omega_t'}{c_1}\right)^2 - K^2 + K\left(\frac{\omega_t''-\omega_t'}{c_1}\right)\cos\theta_i\cos\phi - \left(\frac{\omega_t''-\omega_t'}{c_1}\right)^2\left(\frac{\cos\theta_i}{2}\right)^2}\,. \tag{A3}$$

Equation (2.42) is included below for convenience:

$$\begin{aligned}B_2(K,\omega_c+\omega',\omega_c+\omega'') \equiv\; & B_{2c}(K) + \frac{\partial B_2}{\partial\omega'}\omega' + \frac{\partial B_2}{\partial\omega''}\omega'' \\ & + \frac{1}{2}\left[\frac{\partial^2 B_2}{\partial\omega'^2}\omega'^2 + 2\frac{\partial^2 B_2}{\partial\omega\partial\omega''}\omega'\omega'' + \frac{\partial^2 B_2}{\partial\omega''^2}\omega''^2\right].\end{aligned} \tag{A4}$$

The derivatives in (A4) are found from (A3),

$$\frac{\partial B_2}{\partial\omega_t'} = \frac{1}{2B_2}\left[\frac{2\kappa^2\omega_t'}{c_1^2} - \frac{\hat{\alpha}_i\cdot\mathbf{K}}{c_1}\cos\theta_i + 2\left(\frac{\omega''-\omega'}{c_1^2}\right)\left(\frac{\cos\theta_i}{2}\right)^2\right], \tag{A5}$$

and

$$\frac{\partial B_2}{\partial \omega_t''} = \frac{1}{2B_2}\left[\frac{\hat{\alpha}_i \cdot \mathbf{K}}{c_1}\cos\theta_i - 2\left(\frac{\omega'' - \omega'}{c_1^2}\right)\left(\frac{\cos\theta_i}{2}\right)^2\right]. \tag{A6}$$

Note that

$$\frac{\partial (B_2)^{-1}}{\partial \omega_t'} = -\frac{1}{B_2^2}\frac{\partial B_2}{\partial \omega_t'}. \tag{A7}$$

Using (A5) and (A7),

$$\begin{aligned}\frac{\partial^2 B_2}{\partial \omega_t'^2} = &-\frac{1}{4B_2^3}\left[\frac{2\kappa^2\omega_t'}{c_1^2} - \frac{\hat{\alpha}_i \cdot \mathbf{K}}{c_1}\cos\theta_i + 2\left(\frac{\omega'' - \omega'}{c_1^2}\right)\left(\frac{\cos\theta_i}{2}\right)^2\right]^2 \\ &+\frac{1}{2B_2}\left[\frac{2\kappa^2}{c_1^2} - \frac{2}{c_1^2}\left(\frac{\cos\theta_i}{2}\right)^2\right],\end{aligned} \tag{A8}$$

or equivalently,

$$\frac{\partial^2 B_2}{\partial \omega_t''^2} = -\frac{1}{4B_2^3}\left[\frac{\hat{\alpha}_i \cdot \mathbf{K}}{c_1}\cos\theta_i - 2\left(\frac{\omega'' - \omega'}{c_1^2}\right)\left(\frac{\cos\theta_i}{2}\right)^2\right]^2 - \frac{1}{c_1^2 B_2}\left(\frac{\cos\theta_i}{2}\right)^2. \tag{A9}$$

Also,

$$\begin{aligned}\frac{\partial^2 B_2}{\partial \omega_t' \partial \omega_t''} = &-\frac{1}{4B_2^3}\left[\frac{2\kappa^2\omega_t'}{c_1^2} - \frac{\hat{\alpha}_i \cdot \mathbf{K}}{c_1}\cos\theta_i + 2\left(\frac{\omega'' - \omega'}{c_1^2}\right)\left(\frac{\cos\theta_i}{2}\right)^2\right] \\ &\times\left[\frac{\hat{\alpha}_i \cdot \mathbf{K}}{c_1}\cos\theta_i - 2\left(\frac{\omega'' - \omega'}{c_1^2}\right)\left(\frac{\cos\theta_i}{2}\right)^2\right] \\ &+\frac{1}{c_1^2 B_2}\left(\frac{\cos\theta_i}{2}\right)^2.\end{aligned} \tag{A10}$$

Evaluating the derivatives at $\omega' = \omega'' = 0$ or

$$\omega_t' = \omega_t'' = \omega_c \tag{A11}$$

yields

$$B_{2c}(K) \equiv B_2(K, \omega_c + \omega', \omega_c + \omega'')\big|_{\omega' = \omega'' = 0} = \kappa k_{1c}\beta_2(K, \omega_c), \tag{A12}$$

$$\left.\frac{\partial B_2}{\partial \omega_t'}\right|_{\omega_t'=\omega_t''=\omega_c} = \frac{1}{2B_{2c}}\left[\frac{2\kappa^2\omega_c}{c_1^2} - \frac{\hat{\alpha}_i\cdot\mathbf{K}}{c_1}\cos\theta_i\right], \tag{A13}$$

$$\left.\frac{\partial B_2}{\partial \omega_t''}\right|_{\omega_t'=\omega_t''=\omega_c} = \frac{\hat{\alpha}_i\cdot\mathbf{K}}{2c_1B_{2c}}\cos\theta_i, \tag{A14}$$

$$\left.\frac{\partial^2 B_2}{\partial \omega_t'^2}\right|_{\omega_t'=\omega_t''=\omega_c}$$

$$= -\frac{1}{4B_{2c}^3}\left[\frac{2\kappa^2\omega_c}{c_1^2} - \frac{\hat{\alpha}_i\cdot\mathbf{K}}{c_1}\cos\theta_i\right]^2 + \frac{1}{2B_{2c}}\left[\frac{2\kappa^2}{c_1^2} - \frac{2}{c_1^2}\left(\frac{\cos\theta_i}{2}\right)^2\right], \tag{A15}$$

$$\left.\frac{\partial^2 B_2}{\partial \omega_t''^2}\right|_{\omega_t'=\omega_t''=\omega_c} = -\frac{1}{4B_{2c}^3}\left[\frac{\hat{\alpha}_i\cdot\mathbf{K}}{c_1}\cos\theta_i\right]^2 - \frac{1}{c_1^2B_{2c}}\left(\frac{\cos\theta_i}{2}\right)^2, \tag{A16}$$

and

$$\left.\frac{\partial^2 B_2}{\partial \omega_t'\omega_t''}\right|_{\omega_t'=\omega_t''=\omega_c}$$

$$= -\frac{\hat{\alpha}_i\cdot\mathbf{K}}{4c_1B_{2c}^3}\cos\theta_i\left(\frac{2\kappa^2\omega_c}{c_1^2} - \frac{\hat{\alpha}_i\cdot\mathbf{K}}{c_1}\cos\theta_i\right) + \frac{1}{c_1^2B_{2c}}\left(\frac{\cos\theta_i}{2}\right)^2. \tag{A17}$$

Substituting (A12) - (A17) into (A4) yields an approximate expression for B_2.

$$B_2\left(K,\omega_c+\omega',\omega_c+\omega''\right)\equiv B_{2c}(K)$$

$$+\omega'\frac{1}{2B_{2c}}\left(\frac{2\kappa^2\omega_c}{c_1^2}-\frac{\hat{\alpha}_i\cdot\mathbf{K}}{c_1}\cos\theta_i\right)$$
$$+\omega''\frac{\hat{\alpha}_i\cdot\mathbf{K}}{2c_1B_{2c}}\cos\theta_i$$
$$-\frac{1}{2}\omega'^2\left[\frac{1}{4B_{2c}^3}\left(\frac{2\kappa^2\omega_c}{c_1^2}-\frac{\hat{\alpha}_i\cdot\mathbf{K}}{c_1}\cos\theta_i\right)^2-\frac{1}{2B_{2c}}\left(\frac{2\kappa^2}{c_1^2}-\frac{2}{c_1^2}\left(\frac{\cos\theta_i}{2}\right)^2\right)\right] \qquad \text{(A18)}$$
$$-\omega'\omega''\left[\frac{\hat{\alpha}_i\cdot\mathbf{K}}{4c_1B_{2c}^3}\cos\theta_i\left(\frac{2\kappa^2\omega_c}{c_1^2}-\frac{\hat{\alpha}_i\cdot\mathbf{K}}{c_1}\cos\theta_i\right)-\frac{1}{c_1^2B_{2c}}\left(\frac{\cos\theta_i}{2}\right)^2\right]$$
$$-\frac{1}{2}\omega''^2\left[\frac{1}{4B_{2c}^3}\left(\frac{\hat{\alpha}_i\cdot\mathbf{K}}{c_1}\cos\theta_i\right)^2+\frac{1}{c_1^2B_{2c}}\left(\frac{\cos\theta_i}{2}\right)^2\right].$$

Similarly,

$$B_2\left(K,\omega_c+\omega'',\omega_c+\omega'\right)\equiv B_{2c}(K)$$

$$+\omega''\frac{1}{2B_{2c}}\left(\frac{2\kappa^2\omega_c}{c_1^2}-\frac{\hat{\alpha}_i\cdot\mathbf{K}}{c_1}\cos\theta_i\right)$$
$$+\omega'\frac{\hat{\alpha}_i\cdot\mathbf{K}}{2c_1B_{2c}}\cos\theta_i$$
$$-\frac{1}{2}\omega''^2\left[\frac{1}{4B_{2c}^3}\left(\frac{2\kappa^2\omega_c}{c_1^2}-\frac{\hat{\alpha}_i\cdot\mathbf{K}}{c_1}\cos\theta_i\cos\phi\right)^2-\frac{1}{2B_{2c}}\left(\frac{2\kappa^2}{c_1^2}-\frac{2}{c_1^2}\left(\frac{\cos\theta_i}{2}\right)^2\right)\right]$$
$$-\omega'\omega''\left[\frac{\hat{\alpha}_i\cdot\mathbf{K}}{4c_1B_{2c}^3}\cos\theta_i\left(\frac{2\kappa^2\omega_c}{c_1^2}-\frac{\hat{\alpha}_i\cdot\mathbf{K}}{c_1}\cos\theta_i\cos\phi\right)\frac{1}{c_1^2B_{2c}}\left(\frac{\cos\theta_i}{2}\right)^2\right]$$
$$-\frac{1}{2}\omega'^2\left[\frac{1}{4B_{2c}^3}\left(\frac{\hat{\alpha}_i\cdot\mathbf{K}}{c_1}\cos\theta_i\right)^2+\frac{1}{c_1^2B_{2c}}\left(\frac{\cos\theta_i}{2}\right)^2\right]. \qquad \text{(A19)}$$

Subtracting Eq. (A18) from the conjugate of (A19) yields an approximation for

$$B_2^*(K,\omega_c+\omega'',\omega_c+\omega')-B_2(K,\omega_c+\omega',\omega_c+\omega'')\cong$$

$$\begin{aligned}
&\omega''\left\{\frac{\kappa^{*2}\omega_c}{c_1^2B_{2c}^*}-\frac{\hat{\alpha}_i\cdot\mathbf{K}}{2c_1B_{2c}^*}\cos\theta_i-\frac{\hat{\alpha}_i\cdot\mathbf{K}}{2c_1B_{2c}}\cos\theta_i\right\}\\
&+\omega'\left\{\frac{\hat{\alpha}_i\cdot\mathbf{K}}{2c_1B_{2c}^*}\cos\theta_i-\frac{\kappa^2\omega_c}{c_1^2B_{2c}}+\frac{\hat{\alpha}_i\cdot\mathbf{K}}{2c_1B_{2c}}\cos\theta_i\right\}\\
&+\frac{1}{2}\omega''^2\left\{\frac{1}{4B_{2c}^3}\left(\frac{\hat{\alpha}_i\cdot\mathbf{K}}{c_1}\cos\theta_i\right)^2+\frac{1}{c_1^2B_{2c}}\left(\frac{\cos\theta_i}{2}\right)^2\right.\\
&\qquad\left.-\frac{1}{4B_{2c}^{3\,*}}\left(\frac{2\kappa^{*2}\omega_c}{c_1^2}-\frac{\hat{\alpha}_i\cdot\mathbf{K}}{c_1}\cos\theta_i\right)^2+\frac{1}{2B_{2c}^*}\left(\frac{2\kappa^{*2}}{c_1^2}-\frac{2}{c_1^2}\left(\frac{\cos\theta_i}{2}\right)^2\right)\right\}\\
&+\frac{1}{2}\omega'^2\left\{\frac{1}{4B_{2c}^3}\left(\frac{2\kappa^2\omega_c}{c_1^2}-\frac{\hat{\alpha}_i\cdot\mathbf{K}}{c_1}\cos\theta_i\right)^2-\frac{1}{2B_{2c}}\left(\frac{2\kappa^2}{c_1^2}-\frac{2}{c_1^2}\left(\frac{\cos\theta_i}{2}\right)^2\right)\right.\\
&\qquad\left.-\frac{1}{4B_{2c}^{3\,*}}\left(\frac{\hat{\alpha}_i\cdot\mathbf{K}}{c_1}\cos\theta_i\right)^2-\frac{1}{c_1^2B_{2c}^*}\left(\frac{\cos\theta_i}{2}\right)^2\right\}\\
&+\omega'\omega''2i\,\mathrm{Im}\left\{\frac{\hat{\alpha}_i\cdot\mathbf{K}}{4c_1B_{2c}^3}\cos\theta_i\left(\frac{2\kappa^2\omega_c}{c_1^2}-\frac{\hat{\alpha}_i\cdot\mathbf{K}}{c_1}\cos\theta_i\right)-\frac{1}{c_1^2B_{2c}}\left(\frac{\cos\theta_i}{2}\right)^2\right\}.
\end{aligned}\tag{A20}$$

Combining the ω' terms in (A20),

$$\begin{aligned}
&\left\{\frac{\hat{\alpha}_i\cdot\mathbf{K}}{c_1}\cos\theta_i\,\mathrm{Re}(1/B_c)-\frac{\kappa^2\omega_c}{B_cc_1^2}\right\}i\omega' z\\
&\quad=\left\{\frac{\hat{\alpha}_i\cdot\mathbf{K}}{\omega_c}\cos\theta_i\,\mathrm{Re}\left(\frac{1}{\kappa\beta_2(K,\omega_c)}\right)-\frac{\kappa}{c_1\beta_2(K,\omega_c)}\right\}i\omega' z,
\end{aligned}\tag{A21}$$

and making the definitions

$$t_2=\frac{-z\,\kappa/c_1}{\beta_2(K,\omega_c)}\tag{A22}$$

$$t_1=\frac{\mathbf{R}\cdot\hat{\alpha}_i}{c_1}\cos\theta_i+\frac{z_s}{c_1}\sin\theta_i+z\frac{\hat{\alpha}_i\cdot\mathbf{K}\cos\theta_i}{c_1k_1}\mathrm{Re}\left(\frac{1}{\kappa\beta_2(K,\omega_c)}\right)-\frac{-z\,\kappa/c_1}{\beta_2(K,\omega_c)}\tag{A23}$$

leads to Eq. (2.45).

Starting with the ω'^2 terms in (A22), define

$$P = 2\left\{\frac{1}{4B_{2c}^3}\left(\frac{2\kappa^2\omega_c}{c_1^2} - \frac{\hat{\alpha}_i \cdot \mathbf{K}}{c_1}\cos\theta_i\right)^2 - \frac{1}{2B_{2c}}\left(\frac{2\kappa^2}{c_1^2} - \frac{2}{c_1^2}\left(\frac{\cos\theta_i}{2}\right)^2\right)\right.$$
$$\left. - \frac{1}{4B_{2c}^{3\,*}}\left(\frac{\hat{\alpha}_i \cdot \mathbf{K}}{c_1}\cos\theta_i\right)^2 - \frac{1}{c_1^2 B_{2c}^*}\left(\frac{\cos\theta_i}{2}\right)^2\right\} \qquad \text{(A24)}$$

Equation (2.47) is obtained by rearranging terms in (A24), and Eq. (2.48) is obtained from the cross term, $\omega''\omega'$.

APPENDIX B

Dispersion of a Gaussian pulse

Beginning with the baseband source term in Eq. (2.73), $u(t)=\mathrm{e}^{-t^2/t_s^2}$, and the definition of $g^2(t)$ in Eq. (2.42), Eq. (2.68) is derived. Using the well known identity

$$\frac{1}{\sigma\sqrt{2\pi}}\int_{-\infty}^{\infty}\mathrm{e}^{-x^2/2\sigma^2}\mathrm{e}^{i\omega x}=\mathrm{e}^{-\sigma^2\omega^2/2} \tag{B1}$$

in the second integral of Eq. (2.49) yields

$$\int_{-\infty}^{\infty}d\omega' U(\omega')\mathrm{e}^{-i\omega'(t-iP\omega'')}\mathrm{e}^{-i\omega'^2P/4}=\frac{t_s}{q}\mathrm{e}^{-(\tau-iP\omega'')^2/q^2}, \tag{B2}$$

where

$$U(\omega')=\frac{t_s}{q}\mathrm{e}^{-(t-iP\omega'')^2/q^2} \tag{B3}$$

and

$$q\equiv\sqrt{t_s^2+iP}\,. \tag{B4}$$

Using (B2), the expression for $g^2(t)$ becomes

$$g^2(t)=\frac{t_s}{q}\mathrm{e}^{-t^2/q^2}\int_{-\infty}^{\infty}d\omega'' U^*(\omega'')\mathrm{e}^{i\omega''\left(t^*+2tP/q^2\right)}\mathrm{e}^{i\omega'^2P''/4}, \tag{B5}$$

where

$$P''\equiv P^*-i(2P/q')^2. \tag{B6}$$

Using the identify in (B1) to evaluate (B5) yields Eq. (2.75).

APPENDIX C

RMS height : Subtracted Gaussian weighted moving average

The RMS height of the surface is the surface correlation function evaluated at $\mathbf{R} = \mathbf{0}$.

$$h^2 = \int d^2K\, W(\mathbf{K}). \tag{C1}$$

Substituting Eq. (3.66) for the roughness spectrum into (C1) yields

$$\begin{aligned} h^2 &= 2\pi w \int_0^\infty dKK \left|1 - \mathrm{e}^{-K^2a^2/2}\right|^2 \frac{1}{K^\gamma} \\ &= 2\pi w \int_0^\infty dKK^{1-\gamma}\left[1 - 2\mathrm{e}^{-K^2a^2/2} + \mathrm{e}^{-K^2a^2}\right]. \end{aligned} \tag{C2}$$

Evaluate

$$S(\varepsilon) = \lim_{\varepsilon \to 0} \int_\varepsilon^\infty dKK^{1-\gamma}\left[1 - 2\mathrm{e}^{-K^2a^2/2} + \mathrm{e}^{-K^2a^2}\right]. \tag{C3}$$

Let

$$I_1 = \int_\varepsilon^\infty dKK^{1-\gamma} = \frac{\varepsilon^{2-\gamma}}{\gamma - 2}, \tag{C4}$$

$$I_2 = \int_\varepsilon^\infty dKK^{1-\gamma}\mathrm{e}^{-K^2a^2/2}, \tag{C5}$$

and

$$I_3 = \int_\varepsilon^\infty dKK^{1-\gamma}\mathrm{e}^{-K^2a^2}. \tag{C6}$$

The integral I_2 is solved first. Using integration by parts (let $u = e^{-K^2a^2/2}$), this integral simplifies to

$$I_2 = \frac{e^{-\varepsilon^2 a^2/2}\varepsilon^{2-\gamma}}{\gamma-2} - \frac{a^2}{\gamma-2}\int_\varepsilon^\infty dK\, K^{3-\gamma} e^{-K^2a^2/2}. \tag{C7}$$

Next, I_3 from (C6) is evaluated using the solution for I_2. Let $b^2 = 2a^2$; then

$$I_3 = \frac{e^{-\varepsilon^2 b^2/2}\varepsilon^{2-\gamma}}{\gamma-2} - \frac{b^2}{\gamma-2}\int_\varepsilon^\infty dK\, K^{3-\gamma} e^{-K^2b^2/2}, \tag{C8}$$

or

$$I_3 = \frac{e^{-\varepsilon^2 a^2}\varepsilon^{2-\gamma}}{\gamma-2} - \frac{2a^2}{\gamma-2}\int_\varepsilon^\infty dK\, K^{3-\gamma} e^{-K^2a^2}. \tag{C9}$$

Therefore

$$\begin{aligned} S(\varepsilon) &= I_1 - 2I_2 + I_3 \\ &= \frac{\varepsilon^{2-\gamma}}{\gamma-2} - 2\frac{e^{-\varepsilon^2a^2/2}\varepsilon^{2-\gamma}}{\gamma-2} + \frac{e^{-\varepsilon^2a^2}\varepsilon^{2-\gamma}}{\gamma-2} \\ &\quad + 2\frac{a^2}{\gamma-2}\int_\varepsilon^\infty dK\, K^{3-\gamma} e^{-K^2a^2/2} \\ &\quad - \frac{2a^2}{\gamma-2}\int_\varepsilon^\infty dK\, K^{3-\gamma} e^{-K^2a^2}. \end{aligned} \tag{C10}$$

The first three terms in (C10) sum to zero in the limit; the last two terms can be evaluated using the identity

$$\int_0^\infty dK\, K^{3-\gamma} e^{-K^2a^2} = \frac{1}{2a^{4-\gamma}}\Gamma(2-\gamma/2), \tag{C11}$$

or equivalently,

$$\int_0^\infty dK\, K^{3-\gamma} e^{-K^2a^2/2} = \frac{2^{1-\gamma/2}}{a^{4-\gamma}}\Gamma(2-\gamma/2). \tag{C12}$$

Using Eqs. (C11) and (C12) in (C10) and (C2) yields

$$h^2 = \frac{2\pi w_2 a^{\gamma-2}}{\gamma-2}\Gamma(2-\gamma/2)\left[2^{2-\gamma/2}-1\right]. \qquad \text{(C13)}$$

The RMS surface height is therefore

$$h = \sqrt{\frac{2\pi w_2 a^{\gamma-2}}{\gamma-2}\Gamma(2-\gamma/2)\left[2^{2-\gamma/2}-1\right]}. \qquad \text{(C14)}$$

APPENDIX D

Number and placement of array elements

Using the intensity front velocity algorithm (Chotiros, 1995), determine the number of receivers that are required to obtain a point solution in speed-depression angle space.

Define the reference sensor $\mathbf{r}_0$ to be at the origin

$$\mathbf{r}_0 = \mathbf{0}. \tag{D1}$$

The signal arrives at the jth receiver located at $\mathbf{r}_j = (x_j, y_j, z_j)$ at time t_j.

$$t_j = \frac{\mathrm{a} \cdot \mathbf{r}_j}{c'}, \tag{D2}$$

where $\mathrm{a} = \alpha_x \hat{\mathbf{x}} + \alpha_y \hat{\mathbf{y}} + \alpha_z \hat{\mathbf{z}}$ is the unit magnitude direction vector of the plane wave, and c' is the propagation speed. Equation (D2) for receivers $\mathbf{r}_0, \mathbf{r}_1, \ldots, \mathbf{r}_n$ can be written as

$$\begin{bmatrix} x_1 & y_1 & z_1 \\ x_2 & y_2 & z_2 \\ . & . & . \\ . & . & . \\ x_n & y_n & z_n \end{bmatrix} \begin{bmatrix} \alpha_x \\ \alpha_y \\ \alpha_z \end{bmatrix} = c' \begin{bmatrix} t_1 \\ t_2 \\ . \\ . \\ t_n \end{bmatrix}. \tag{D3}$$

There are $n+1$ receivers including the reference receiver $\mathbf{r}_0$. Note that all of the receiver locations $\mathbf{r}_1, \mathbf{r}_2, \ldots \mathbf{r}_n$ and the receiver times $t_1, t_2, \ldots t_n$ are assumed to be known. The vector α and the propagation speed c' are unknown — three unknowns. In order to have a unique solution, the receiver position matrix $\mathbf{r}$ is required to have rank 3, requiring a minimum of three receivers ($\mathbf{r}_1, \mathbf{r}_2, \mathbf{r}_3$) that span 3-dimensional space. Including the reference receiver, a minimum of four receivers are required that are not in the same plane.

However, Chotiros' speed-depression angle solution space need only be a slice of the 3-D solution space since the plane wave direction has no y component ($\alpha_y = 0$). Therefore, the receiver matrix $\mathbf{r}$ is required only to have rank 2, spanning only the x,z plane. Including the reference receiver, a minimum of three receivers ($n = 2$) are required.

The following example shows that a linear array results on a curve in the speed-depression angle solution space. Assume a four element linear array, such that

$$\begin{aligned} \mathbf{r}_1 &= (0,0,z_1) \\ \mathbf{r}_2 &= (0,0,z_2) \\ \mathbf{r}_3 &= (0,0,z_3) \end{aligned}. \tag{D4}$$

The reference receiver is $\mathbf{r}_0 = (0,0,0)$. Equation (D3) results in

$$\alpha_z = c' \frac{t_1}{z_1} = c' \frac{t_2}{z_2} = c' \frac{t_3}{z_3} \tag{D5}$$

$$\alpha_x^2 = 1 - \left(c' \frac{t_1}{z_1} \right)^2 - \alpha_y^2 = 1 - \left(c' \frac{t_1}{z_1} \right)^2 \tag{D6}$$

because of the assumption $\alpha_y = 0$. A linear array therefore results in a curve (2-D solution) in speed-depression angle (velocity) solution space.

APPENDIX E

Calculation of reflection coefficient moments

The moments of the reflection coefficient (Γ) are obtained by multiplying Eq. (6.8) by the conjugate of itself. To simplify Eq. (6.8), let

$$\alpha = \Gamma_{12}, \tag{E1}$$

$$\gamma = 1 - \Gamma_{12}^2, \tag{E2}$$

$$\zeta = \Gamma_{23}\, e^{i2k_2\beta_2 d}, \tag{E3}$$

so that

$$\Gamma = \alpha + \gamma\zeta \sum_{n=0}^{\infty} (-\alpha\zeta)^n. \tag{E4}$$

Taking the expected value of (E4) multiplied by its conjugate yields

$$\left\langle |\Gamma|^2 \right\rangle = \left\langle |\alpha|^2 \right\rangle + \left\langle |\gamma\zeta|^2 \sum_{\ell=0}^{\infty}\sum_{m=0}^{\infty} (-\alpha\zeta)^{\ell} \left(-\alpha^*\zeta^*\right)^m \right\rangle + \left\langle 2\,\mathrm{Re}\left\{ \alpha^*\gamma\zeta \sum_{n=0}^{\infty} (-\alpha\zeta)^n \right\} \right\rangle. \tag{E5}$$

Noting that

$$\left\langle \zeta^{\ell} \left(\zeta^*\right)^m \right\rangle = \eta^2 \delta_{\ell m} \tag{E6}$$

and summing the geometric series results in

$$\left\langle |\Gamma|^2 \right\rangle = \left\langle |\alpha|^2 \right\rangle + \frac{|\gamma|^2 \eta^2}{1 - |\alpha|^2 \eta^2}. \tag{E7}$$

Equation (6.12) is obtained by substituting (E1) - (E3) into (E7). Multiply (E4) by (E5) and take the expected value to obtain the moment

$$\begin{aligned}\left\langle \Gamma|\Gamma|^2\right\rangle &= \alpha\left\langle|\Gamma|^2\right\rangle + |\alpha|^2\gamma\left\langle \zeta\sum_{n=0}^{\infty}(-\alpha\zeta)^n\right\rangle \\ &+\gamma|\gamma|^2\left\langle|\zeta|^2\sum_{\ell=0}^{\infty}\sum_{m=0}^{\infty}\sum_{n=0}^{\infty}\zeta^{\ell+n+1}\left(\zeta^*\right)^m(-\alpha)^{\ell+n}\left(-\alpha^*\right)^m\right\rangle \\ &+\gamma\left\langle\zeta\sum_{m=0}^{\infty}(-\alpha\zeta)^m\left\{\alpha^*\gamma\zeta\sum_{n=0}^{\infty}(-\alpha\zeta)^n+\alpha\gamma^*\zeta^*\sum_{n=0}^{\infty}\left(-\alpha^*\zeta^*\right)^n\right\}\right\rangle.\end{aligned} \tag{E8}$$

Making of use (E6),

$$\begin{aligned}\left\langle \Gamma|\Gamma|^2\right\rangle &= \alpha\left\langle|\Gamma|^2\right\rangle + \gamma|\gamma|^2\eta^2\sum_{\ell=0}^{\infty}\sum_{n=0}^{\infty}\eta^{2(\ell+n+1)}(-\alpha)^{\ell+n}\left(-\alpha^*\right)^{\ell+n+1} \\ &+\alpha|\gamma|^2|\eta|^2\sum_{m=0}^{\infty}|-\alpha\eta|^{2m},\end{aligned} \tag{E9}$$

or

$$\begin{aligned}\left\langle \Gamma|\Gamma|^2\right\rangle &= \alpha\left\langle|\Gamma|^2\right\rangle - \frac{\gamma|\gamma|^2|\alpha|^2\eta^4}{\alpha}\frac{1}{\left(1-|\alpha|^2\eta^2\right)^2} \\ &+\alpha|\gamma|^2|\eta|^2\frac{1}{1-|\alpha|^2\eta^2}.\end{aligned} \tag{E10}$$

Substituting (E7) into (E10) yields

$$\left\langle \Gamma|\Gamma|^2\right\rangle = \alpha|\alpha|^2 + 2\alpha|\gamma|^2\frac{|\eta|^2}{1-|\alpha|^2\eta^2} - \alpha^*\gamma|\gamma|^2\frac{\eta^4}{\left(1-|\alpha|^2\eta^2\right)^2}. \tag{E11}$$

Using the relations in (E1)-(E3), the above equation is equivalent to Eq. (6.13).

Taking the magnitude of (E4) to the fourth power gives an expression for the moment

$$\begin{aligned}\left\langle |\Gamma|^4 \right\rangle &= |\alpha|^2 \left\langle |\Gamma|^2 \right\rangle + |\alpha|^2|\gamma|^2 \left\langle |\zeta|^2 \sum_{\ell=0}^{\infty}\sum_{m=0}^{\infty} (-\alpha\zeta)^{\ell} \left(-\alpha^*\zeta^*\right)^m \right\rangle \\ &+2|\alpha|^2 \left\langle \mathrm{Re}\left\{ \alpha^*\gamma\zeta \sum_{n=0}^{\infty} (-\alpha\zeta)^n \right\} \right\rangle \\ &+|\gamma|^4 \left\langle |\zeta|^4 \left(\sum_{\ell=0}^{\infty}\sum_{m=0}^{\infty} (-\alpha\zeta)^{\ell} \left(-\alpha^*\zeta^*\right)^m \right) \left(\sum_{n=0}^{\infty}\sum_{p=0}^{\infty} (-\alpha\zeta)^n \left(-\alpha^*\zeta^*\right)^p \right) \right\rangle \\ &+4 \left\langle \left(\mathrm{Re}\left\{ \alpha^*\gamma\zeta \sum_{n=0}^{\infty} (-\alpha\zeta)^n \right\} \right)^2 \right\rangle \\ &+2|\gamma|^2 \left\langle |\zeta|^2 \left[\alpha^*\gamma\zeta \sum_{n=0}^{\infty} (-\alpha\zeta)^n + \alpha\gamma^*\zeta^* \sum_{n=0}^{\infty} \left(-\alpha^*\zeta^*\right)^n \right] \sum_{\ell=0}^{\infty}\sum_{m=0}^{\infty} (-\alpha\zeta)^{\ell} \left(-\alpha^*\zeta^*\right)^m \right\rangle .\end{aligned} \tag{E12}$$

We use (E7) for the first term on the right side and use the relation (E6) for the second, fourth, and sixth terms. The third term evaluates to zero, and the fifth term uses the identity

$$\left\langle \left(\mathrm{Re}\left\{ \sum_{n=0}^{\infty} (-\zeta)^n \right\} \right)^2 \right\rangle = \frac{1}{2} \sum_{n=0}^{\infty} \left(\eta^2\right)^n . \tag{E13}$$

With much work, the fourth order moment of the reflection coefficient can be shown to be

$$\begin{aligned}\left\langle |\Gamma|^4 \right\rangle &= |\alpha|^4 + 4|\alpha|^2|\gamma|^2 \frac{\eta^2}{1-|\alpha|^2\eta^2} + |\gamma|^4\eta^4 \frac{|\alpha|^2\eta^2+1}{\left(1-|\alpha|^2\eta^2\right)^3} \\ &-4\,\mathrm{Re}\left(\alpha^2\gamma^*\right)|\gamma|^2 \frac{\eta^4}{\left(1-|\alpha|^2\eta^2\right)^2} .\end{aligned} \tag{E14}$$

Using the relations in (E1)-(E3), the above equation is equivalent to Eq. (6.14).

APPENDIX F

Ray approximation calculation of reflection coefficient magnitude

F.1 Linear decrease in squared wave number with depth

The ray paths for propagation into the lower medium are parabolic. If the lower medium were lossless, then all of the energy propagating into the lower medium would be redirected upward, and the magnitude of the reflection coefficient, Γ_{23}, would be unity. However, loss in the lower medium results in a magnitude squared reflection coefficient equal to the energy that reaches the surface. The square of the wave number in medium 3 is given by

$$k_3(\zeta) = k_2(1 - a\zeta), \tag{F1}$$

where k_2 is the constant wave number in the arbitrarily thin layer below the mean surface, and the depth coordinate

$$\zeta = -z \tag{F2}$$

increases with depth. By defining the sound-speed gradient as the change in sound speed with respect to depth at a point just below the mean surface, a can be expressed in terms of the sound-speed gradient g at $\zeta = 0$, the speed ratio ν, and the sound speed in medium 1, c_1.

$$a = \frac{2g}{\nu c_1}. \tag{F3}$$

Since energy propagating through the sediment will be attenuated by an amount determined by the line integral over the ray path, we can approximate the expected value of the magnitude squared of the partial reflection coefficient Γ_{23} as

$$\left\langle \left|\Gamma_{23}\right|^2 \right\rangle = \exp\left(-2\,\mathrm{Im} \int_{\zeta=0}^{\zeta=Z_{max}} k_2 \sqrt{1-a\zeta}\, \frac{d\zeta}{\sin(\theta(\zeta))} \right), \tag{F4}$$

where the path of integration in over the ray path, $\theta(\zeta)$ is the grazing angle of the ray as it propagates through the lower medium, and k_2 is the wave number just below the surface (medium 2). In this example, the mean depth of medium 2, d_2, is allowed to be arbitrarily small. The turning point of the ray, Z_{max}, is found from Snell's law noting that the grazing angle is zero at this point:

$$\frac{\cos(\theta)}{c_3(\zeta)} = \frac{\cos(\theta_2)}{c_2}, \tag{F5}$$

where θ_2 is the grazing angle of the field just below the mean surface, related to the incident field grazing angle θ_1, and speed ratio ν_{21} is by Snell's law

$$\frac{\cos(\theta_2)}{\cos(\theta_1)} = \nu_{21}. \tag{F6}$$

Evaluating the integral in (F4) yields Eq. (6.15).

F.2 Linear increase in sound speed velocity with depth

The sound speed in medium 3 is set equal to the sound speed in medium 2 at the medium 2 - medium 3 interface; it increases linearly with depth, and is given by

$$c_3(\zeta) = (1 + a\zeta)c_2. \tag{F7}$$

The lower medium reflection coefficient follows from the following line integral:

$$\left\langle \left|\Gamma_{23}\right|^2 \right\rangle = \exp\left(-2\,\mathrm{Im}\left\{ k_2 \int_{\zeta=0}^{\zeta=Z_{max}} \frac{1}{1+a\zeta}\, \frac{d\zeta}{\sin(\theta(\zeta))} \right\} \right). \tag{F8}$$

By using Snell's law, the ray turning point, Z_{max} for this constant sound-speed gradient profile is easily shown to be

$$Z_{max} = \frac{1}{a}\left(\frac{1}{\cos(\theta_2)} - 1\right). \tag{F9}$$

The parameter a can be expressed in terms of the sound-speed gradient and the medium 1 sound speed.

$$a = \frac{g}{\nu_{21} c_1}. \tag{F10}$$

Evaluating the integral in (F8) yields an expression similar to Eq. (6.15) for the magnitude squared reflection coefficient:

$$\left\langle |\Gamma_{23}|^2 \right\rangle = \exp\left(-\frac{8\pi}{q}\ln\left(\frac{1+\sin(\theta_2)}{\cos(\theta_2)}\right)\right), \tag{F11}$$

where

$$q = \frac{g}{f\delta} \tag{F12}$$

is the sediment gain parameter.

F.3 Linear increase in sound speed over discontinuous interface

In the next case, the sediment sound speed is assumed to increase linearly down to a depth d_3, where the sediment parameters are discontinuous. When the maximum depth of the ray in medium 3, Z_{max}, is less than the depth of the surface separating medium 3 and medium 4, the loss due to the path in the sediment above the discontinuous interface is given by (F8). However, when $Z_{max} > d_3$, the ray intersects and reflects off of the medium 3 - medium 4 interface, resulting in

$$\eta^2 = |\Gamma_{34}|^2 \exp\left(-2\,\mathrm{Im}\left\{k_2 \int_{\zeta=0}^{\zeta=d_3} \frac{1}{1+a\zeta}\frac{d\zeta}{\sin(\theta(\zeta))}\right\}\right) \quad Z_{max} > d_3. \tag{F13}$$

The above equation is the same as (F8) except the upper limit of the integral is d_3, rather than Z_{max}, and the magnitude of the partial reflection coefficient $|\Gamma_{34}|^2$ is included. Setting $a = g/(\nu_{21} c_1)$ and evaluating the above integral, we get

$$\eta^2 = \exp\left(-\frac{8\pi}{q}\ln\left(\frac{1+\sin(\theta_2)}{\cos(\theta_2)}\right)\right) \qquad Z_{max} \le d_3$$

$$= \exp\left(-\frac{8\pi}{q}\left[\ln\left(\frac{1+\sin(\theta_2)}{\cos(\theta_2)}\right) - \ln\left(\frac{1+\sqrt{1-(1+ad_2)^2\cos^2(\theta_2)}}{(1+ad_2)\cos(\theta_2)}\right)\right]\right)|\Gamma_{34}|^2 \qquad \text{(F14)}$$

$$Z_{max} > d_3 .$$

REPORT DOCUMENTATION PAGE

Form Approved
OPM No. 0704-0188

1. AGENCY USE ONLY *(Leave blank)*	2. REPORT DATE	3. REPORT TYPE AND DATES COVERED
	October 1996	Technical

4. TITLE AND SUBTITLE
Near and Far-Field Acoustic Scattering through and from Two Dimensional Fluid-Fluid Rough Interfaces

5. FUNDING NUMBERS
ONR Grant N00014-96-1-0121

6. AUTHOR(S)
by John Einar Moe

7. PERFORMING ORGANIZATION NAME(S) AND ADDRESS(ES)
Applied Physics Laboratory
University of Washington
1013 NE 40th Street
Seattle, WA 98105-6698

8. PERFORMING ORGANIZATION REPORT NUMBER
APL-UW TR 9606

9. SPONSORING / MONITORING AGENCY NAME(S) AND ADDRESS(ES)
Dr. Jeffrey Simmen, Code 321OA
Office of Naval Research
800 N. Quincy St.
Arlington, VA 22217-5660

10. SPONSORING / MONITORING AGENCY REPORT NUMBER

11. SUPPLEMENTARY NOTES

12a. DISTRIBUTION / AVAILABILITY STATEMENT
Distribution unlimited.

12b. DISTRIBUTION CODE

13. ABSTRACT *(Maximum 200 words)*

Recent experimental results [F. E. Boyle and N. P. Chotiros, J. Acoust Soc. Am. 91, 2615-2619, 1992; N. P. Chotiros, J. Acoust Soc. Am. 97, 199-214, 1995] reveal acoustic penetration from water into sandy sediments at grazing angles below the compressional critical angle in relation to the mean surface. These authors interpret their results to indicate the excitation of a Biot slow wave in the sediment. Another explanation is considered here. Modeling the ocean as a homogenous fluid and the sediment as a lossy homogenous fluid, computer simulations of these experiments based on analytical derivations in this work show that roughness of the water-sediment interface causes propagation of acoustical energy from water into the sediment at grazing angles below the compressional critical grazing angle; these simulations indicate that the experimental results can be explained in terms of diffraction of an ordinary longitudinal wave. These simulations use an analytical expression for the time-dependent mean square incoherent field scattered through (and from) a rough 2-D fluid-fluid interface that is derived in terms of the bistatic scattering cross section per unit area per unit solid area (differential cross section) of the rough interface. First-order perturbation theory is used to derive an expression for the differential cross section. The coherent field is calculated using the flat-surface result (zero-order perturbation theory) and compared to the coherent component of the second-order perturbation theory result. Effects of sound-speed gradients on the field scattered from the rough water-sediment interface are also shown using the first-order perturbation derivations.

14. SUBJECT TERMS
Bottom Acoustic Scattering, Mine Countermeasures, Acoustic Interaction with Seafloor, Rough Surface Perturbation Theory

15. NUMBER OF PAGES
224

16. PRICE CODE

17. SECURITY CLASSIFICATION OF REPORT	18. SECURITY CLASSIFICATION OF THIS PAGE	19. SECURITY CLASSIFICATION OF ABSTRACT	20. LIMITATION OF ABSTRACT
Unclassified	Unclassified	Unclassified	SAR